SODAR Echograms Based Model Development for Atmospheric Boundary Layer Characterization

A Thesis submitted in fulfilment of the requirements for the Degree

of

Doctor of Philosophy

in

Electrical And Instrumentation Engineering Department

Submitted by

Nishant Kumar
Reg No. - 901504015

Under the Guidance of

Dr. Kirti Soni
Principal Scientist, A&V Metrology
CSIR-NPL, New Delhi

Dr. Ravinder Agarwal
Professor, EIED
TIET, Patiala

June 2021

Electrical and Instrumentation Engineering Department
Thapar Institute of Engineering & Technology
(Declared as Deemed-to-be-University u/s 3 of the UGC Act., 1956)
Post Bag No. 32, Patiala – 147004
Punjab (India)

Dedicated to

My Family

DECLARATION

I hereby certify that the work which is presented in dissertation entitled, "**SODAR Echograms Based Model Development for Atmospheric Boundary Layer Characterization**", in partial fulfillment of the requirements for the award of the degree of Doctor of Philosophy submitted to Electrical & Instrumentation Engineering Department of Thapar Institute of Engineering and Technology, Patiala is as authentic record of my own work carried under the supervision of Dr. Ravinder Agarwal and Dr. Kirti Soni.

The matter contained in this thesis has not been submitted elsewhere for award of any other degree in India or Abroad.

Nishant Kumar

Place: Patiala (Nishant Kumar)
Date: 07/10/2021 Reg No.: 901504015

It is certified that the above statement made by the student is correct to the best of my knowledge and belief.

(Kirti Soni) (Ravinder Agarwal)
Principal Scientist Professor

ACKNOWLEDGEMENT

The goal can be attained with firm determination and guidance. Consistent efforts with zeal and desire are the only way to achieve success and knowledge. Nature plays a role in this journey by providing sources of light and illuminating the correct path. I'd like to thank everyone who assisted me in reaching my goals.

Before expressing my heartfelt gratitude, I'd like to thank all of my mentors and, of course, all of them: GOD. They gave me the confidence to believe in myself and my passion for this research. I couldn't have done it without its blessings. Throughout my life, I have been extremely fortunate to have their blessings.

I am grateful to my Ph.D. supervisor ***Dr. Ravinder Agarwal***, Professor, Department of Electrical and Instrumentation Engineering Department, Thapar Institute of Engineering and Technology, Patiala, and ***Dr. Kirti Soni***, Principal Scientist, Council of Scientific and Industrial Research-National Physical Laboratory, New Delhi whose help, stimulating suggestions and encouragement helped me in all the time of research and writing of this thesis. I could not have imagined having a better advisor and mentor for my Ph.D.

I would like to thank ***Prof. Prakash Gopalan***, Director TIET, Patiala, and ***Dr. Dinesh K. Aswal***, Director, CSIR-NPL, New Delhi for providing facilities for current research work. I am also highly thankful to ***Prof. R. S. Kaler***, Head of Department, the members of my doctoral research committee for providing valuable suggestions throughout this research work. I am also thankful to my venerable faculty, of the Electrical and Instrumentation Engineering Department, TIET, Patiala for their invaluable suggestions and caring concern at every stage during the entire stretch of studies. I am also highly thankful to ***Dr. Sanjay Yadav***, Head of Division, and my venerable scientists, of Physico-Mechanical Metrology, CSIR-NPL, New Delhi for their invaluable suggestions and caring concern at every stage during the entire stretch of studies.

I am deeply indebted to ***Dr. Mahavir Singh***, Head, Acoustics and Vibration Metrology, CSIR-NPL, New Delhi for his dynamic support, keen interest, and special attention during the entire stretch of research pursuit. My heartiest thanks are due to ***Mr. Gurbir Singh, Dr. Y.K. Yadav*** and ***Dr. Kulwinder Singh Parmar*** for all help rendered to me besides taking personal pains to see the completion of my research. I am also highly thankful to all lab mates of Biomedical Research Lab, TIET, Patiala and A&V Metrology, CSIR-NPL, New Delhi for their support and constant encouragement.

I feel immense pleasure in expressing my regard, sincere appreciation, and a deep sense of gratitude to my family, I am sure, without their support, and this would have never been a reality in my life.

I express my sincere gratitude to my all friends for their generous help and continuous support.

Thank you all for your insights, guidance, and support.

(Nishant Kumar)

Table of Contents

Summary

SOnic Detection And Ranging (SODAR) is a well-known and widely accepted meteorological tool for supplying continuous real-time and critical Atmospheric Boundary Layer (ABL) data. Data is critical for evaluating environmental impact assessments and city-specific carrying capacity for pollutants. Existing SODAR technology was improved, which included, acoustic antenna advancements, virtual instrumentation, and improved data processing approaches. This advancement will affect the observed data, and data will be more accurate as a result of calibration and testing of equipment and materials. An acoustic antenna was designed using moving-coil transducers, parabolic dish, and acoustic baffle. Several types of Aluminium Composite Panel (ACP) for acoustic baffle were tested to their characteristics like Sound Transmission Coefficient (STC) and Noise Reduction Coefficient (NRC) in the reverberation chamber. A comparison investigation was carried out on transmission loss and absorption. It was concluded that baffle (ACP with foam) is the suitable material with STC (34) and NRC (0.98) for an acoustic antenna.

The SODAR echogram for the ABL structure was derived and successfully applied in a highly accurate and reliable machine-learning method. In terms of performance, five functional selection procedures and eight classification methods were examined. From 1698 SODAR echograms, 133 statistic features were calculated. Machine-learning methods were used to ensure the unbiased estimation of different structures. Ten cross-validations were used to determine accuracy. The boosted tree classifier was given the strongest prognostic presentation with 133 features (total prediction rating of 52.02%). After applying the Laplacian method for feature selection, the classifier (overall prediction performance 62.19%) showed the highest prognostic presentation with 20 features. The large variability analysis indicates the choice of a classification method for performance variation. The development of optimal machine-learning methods for SODAR echogram applications was a critical step toward the ABL structure identification, which provides an automatic structure classification method for atmospheric and pollutants studies.

A deep learning new model was then employed in temporary/seasonal and annual prediction of ABL height. It presents the outcomes of the Long-Short Term Memory (LSTM) models, based on SODAR observations from December 2018 to February 2020. The LSTM model

was used to predict the ABL height and analyse the model's performance. The analysis shows when the number of neurons was 32 it was possible to achieve optimal results in a short period of training when the epoch was 500. To achieve an acceptable prediction accuracy, various types of errors for the measured time-series data were calculated. The relative Root Mean Square Error (rRMSE) and Mean Absolute Percentage Error (MAPE) values for the update network state with predicted values were 7.33 % and 17.3 %, respectively, and for the update network state with observed values, rRMSE and MAPE are 5.95 % and 10.62 %, respectively. This model was also used to compare annual and seasonal predictions of ABL height, as the rRMSE values (7.49 % and 5.59 %) were lowest during post-monsoon prediction and highest (10.29 % and 5.86 %) during annual prediction.

Then, during the fireworks (Diwali festival), it deals with the impact on ABL height of pollutants and meteorological parameters. In 2014-2017, ABL height and Ventilation Coefficients (VC) were debated on the effect of firecrackers on air quality. The Forward Section (FS) technique was employing the major parameters affected by the ABL height. The main purpose of this study was to identify the highly effecting parameter for the ABL height regarding air pollution. On the day of Diwali festival, the average ABL height was approximately 25%, 15%, and 6% lower in 2014, 2016, and 2017, respectively, as compared to Pre-Diwali day, but 15% higher in 2015 due to high wind speed associated with elevated pollution levels. The burning of firecrackers during the Diwali festival is a very strong source of air pollution, according to mean comparisons and correlations, contributing significantly to the number of particulate matter and gaseous pollutants in the environment.

NOMENCLATURE

The main symbols and notations used in this study are listed below. Sometimes a symbol may have an alternate meaning but in such a case; the context is sufficient to avoid confusion.

SODAR	SOnic Detection and Ranging
ABL	Atmospheric Boundary Layer
VC	Ventilation Coefficient
FS	Forward Selection
LSTM	Long-Short Term Memory
ACP	Aluminium Composite Panel
STC	Sound Transmission Coefficient
NRC	Noise Reduction Coefficient
KNN	K-Nearest Neighbours
SVM	Support Vector Machine
NAR	Non-linear Auto-Regressive
C_v^2	Wind Structure
C_T^2	Temperature Structure

Chapter 1
Introduction to Atmospheric Boundary Layer and SODAR

1.1. Atmospheric Boundary Layer

The troposphere is the lowest portion of the atmosphere shown in Fig. 1.1. It is the domain of weather, cyclones, and anticyclones [1]. It stretches from the earth's surface to a height of roughly *15* x 10^3 *m*, with the highest limit varied depending on the region (i.e., from pole to the equator). The Earth's current environment is most likely not its only atmosphere. The current atmosphere is classified as an oxidative environment by chemists, whereas the previous atmosphere is classified as a reducing atmosphere. It is unlikely to carry oxygen. Plants have produced almost all the oxygen that makes up our atmosphere (cyanobacteria or, more colloquially, blue-green algae). As a result, the earth's atmosphere now contains *79%*, nitrogen, *20%* oxygen, and *1%* other gases.

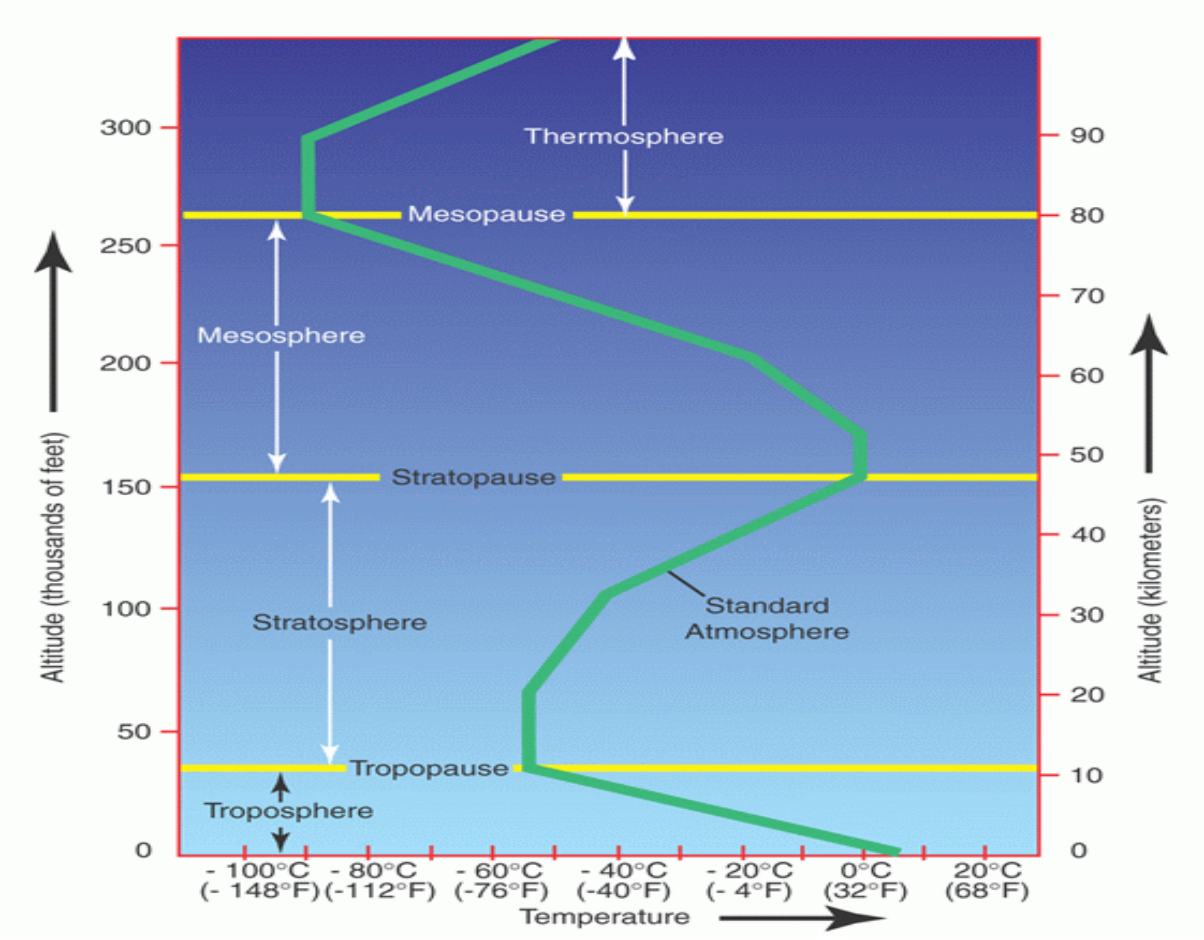

Figure 1.1. The vertical temperature profile in the atmosphere [1]

The Atmospheric Boundary Layer (ABL) is the lowest part of the troposphere where the direct effect of surface heating and cooling has been seen [2]. It is in this layer all biological and human activities take place [3]. Under the conditions of strong upward heat flux i.e., during daytime unstable conditions, the ABL extends to a height of convective mixing of buoyant parcels of air or the base of an elevated inversion layer and during night-time i.e., stable conditions, the level of surface-based inversions decides the height of the ABL. Moreover, turbulence is one of the essential ingredients of ABL [1]. It facilitates the transfer of water vapour, heat, momentum, diffusion of pollutants, and other tracer elements from place to place. In the ABL, the wind speed normally increases with height while pressure decreases regularly with height, temperature decreases less regularly and humidity very irregularly [1, 4]., Derived parameter refractivity, normally decreases exponentially although, sharp gradients also occur sometimes depending on weather conditions.

The ABL is in a convective equilibrium with the sun-warmed surface of the earth [5]. The sun acts as a primary source of energy for the Earth's atmospheric system. The exact amount of this energy depends upon the time of the year, time of the day, latitude, topography, and weather conditions. The amount of energy reflected, absorbed, or transmitted from the earth's surface is determined by the nature of the soil and the type of surface [1]. The absorbed energy is converted into heat energy either directly through a rise in temperature of the Earth's surface or indirectly through evaporation or conversion to mechanical, electrical, or chemical energy. The direct heating of the surface of the earth sets up convective motions in the atmosphere while the indirect heat energy gets stored in the earth for long periods in the form of chemical energy (say as fossil fuels) before being converted back into heat energy.

1.1.1. Need for ABL studies

Air quality management and environment protection are global issues of concern and inviting attention and action jointly at the international level, individual, national level and even going up to the grass-root level of domestic human activities. In different ways, the troposphere, particularly the bottom 2×10^3 m, plays a critical role in important human endeavours such as communication, aviation, and air pollution [6]. These situations require complete information of wind velocity, humidity, and thermal structure at a place to monitor the hazardous situations. Therefore, it is essential to have complete knowledge of its microscale details and their distribution in real-time and space.

1.1.2. Monitoring techniques for ABL

Various types of monitoring techniques have been developed from time to time to monitor atmospheric parameters such as temperature, pressure, humidity, wind speed and direction, and their distribution in space, which provide information about atmospheric structures and various dynamical processes active at a local scale [1, 5]. The schematic arrangement to use the various techniques for obtaining information about a particular atmospheric volume is shown in Table 1.1 [6]. All the techniques have their relevance to monitoring any parameter.

Table 1.1. Different techniques for measurement of ABL or atmospheric volume

	Continuous Data Output	*Range Covered well*			*Determination of Turbulence Parameters*
		10 – 100 m (Low SBL)	100 – 500 m (SBL/CBL)	0.5 – 3 km (CBL)	
In-Situ Techniques					
Aircraft	-	-	X	√	√
Radiosonde	-	-	√	√	.
Mast	√	√	-	-	√
Tethered Balloon	.	√	√	-	X
Remote Sensing Techniques					
SODAR	√	-	√	√	√
RASS	X	-	X	X	X
RADAR	√	-	X	√	√
Mini-SODAR	√	√	-	-	√
LIDAR	√	-	X	√	√
Numerical Models	X	X	-	√	√

Note: - √ means fulfilled, X partially fulfilled, and - not fulfilled

These techniques are broadly classified according to their mode of operation as in-situ techniques and remote sensing techniques. In-situ techniques require the measuring sensors or instruments to carry aloft to the height range of interest. In-situ techniques like the radiosonde and the microwave refractometer have the advantage of providing detailed height and space profiles but they are not continuous as required for some of the applied purposes [4]. Furthermore, the radiosonde's sensitivity and reaction time are frequently insufficient for communication, aviation, and air pollution research, where comprehensive information from lower heights, often up to *1000* or *2000 m*, is required. Measurements have been made with these techniques to make the inversion/ducts look wider than they are. The measurements are over a limited geometry using point sensors giving poor reliability and discontinuity of data. Besides instruments like the microwave refractometer are expensive and difficult to build although they can provide dependable information on ducts, turbulence, and occurrence of the layer structure in the lower atmosphere.

In addition, a recent report of national needs for improved communication networks, aviation, and air pollution monitoring has highlighted the need for improved ABL parameters [1]. The needs are mostly in the field of short-term local weather forecasting, such as predicting for a limited area ranging from *1* to 100×10^3 *m* in size for short time intervals. These better short-term local weather forecasts will demand a far greater set of meteorological data than the standard radiosonde can supply [6]. It has been anticipated that the required increase in time and spatial density of relevant observations will be tremendous. According to cost estimates, the only way to achieve the necessary increase in observing density will be to expand existing radiosonde networks.

As a result, the need for sensors can provide data on meteorological variables remotely and consistently in both space and time has been identified. Aside from providing continuous data in time and/or space, remote sensing techniques have several other advantages [1, 4, 6], like

a. The observations are taken without carrying the in-situ instrumentation to the region of interest
b. Remote sensing allows measurements of important atmospheric characteristics in all spatial dimensions as a function of time
c. Excellent resolution of data in time and space is attainable
d. An increasingly broad range of atmospheric parameters like temperature, humidity, wind, cloud particles, precipitation, gaseous pollutants, turbulence spectrum, and momentum flux can be measured
e. The medium being measured is not altered by the measurement system
f. In contrast to other methods, remote sensing measurements provide a line, area, or volume integration instead of only a single point sensor
g. The remote sensing measurements can be made automatic
h. The human eye and weather RADAR receive no information when the sky is clear, but these new remote sensing techniques allow the interior structure of the ABL to be monitored continually even when the sky is clear

It is essential to recall, rather than duplicating the kind of quantitative data to which meteorologists are familiar, the value of remote sensing techniques resides in its ability to deliver and display whole new forms of information in real-time. The strength of certain parameters, such as thermal plumes, breaking waves, gravity waves, and Kelvin-Helmholtz instabilities, has been displayed as maps or two-dimensional representations. The utilisation of these two-dimensional displays will rely mostly on pattern recognition rather than

complete quantitative analysis. Their application is expected to substantially change the nature and scope of atmospheric and meteorological services.

Different types of remote sensing techniques have been developed in recent years using acoustic and optical and radio waves are, SOnic Detection And Ranging (SODAR), Light Detection And Ranging (LiDAR), and RAdio Detection And Ranging (RADAR) respectively [6]. Also using radio and acoustic wave Radio And Sounding System (RASS) has been developed. This thesis only focused on acoustics wave and SODAR.

1.2. SODAR as a Monitoring Technique

SODAR is based on the principle of active echo sounding utilizing acoustic waves for probing the lower atmosphere. The propagation of these waves through the medium is a function of meteorological parameters like temperature, relative humidity, and wind. These parameters show their degree of variability through fluctuations in the refractive index of the medium and thus as a result causes acoustic waves to be refractive, scattering, and attenuated. The fluctuations in phase and amplitude of sound waves have been evaluated in terms of spatial and temporal fluctuations of atmospheric temperature, wind velocity, and humidity in a way very much like that of electromagnetic waves. Table 1.2 shows that acoustic waves are considerably more sensitive to atmospheric fluctuations than are electromagnetic waves and further that wind and temperature fluctuations dominate for sound waves [3, 7-9]. The strong interaction of acoustic waves with fluctuations in temperature and wind velocity compared to electromagnetic and optical waves makes it possible to monitor the presence and behaviour of various atmospheric structures more effectively using sound waves.

Table. 1.2. The sensitivity of remote-sensing equipment to atmospheric parameters

Parameter	Magnitude changes of the parameter	Corresponding change in refractive index		
		Acoustic	Radio	Optical
Temperature	1^0 K	1700	1	1
Humidity	1 mb	140	4	0.04
Wind	1 m s^{-1}	3000	2×10^{-6}	2×10^{-6}

SODAR has been one of the best remote sensing techniques for providing continuous real-time data of air quality, meteorological variables such as mixing height/inversion height, ABL stability, and wind profile [1-2]. It is recognized internationally and proven cost-effective. For air quality dispersion modeling in Environment Impact Assessment (EIA), it is recognized internationally and recommended by the EPA. This technique is used in a variety

of practical and ABL research applications all over the world. SODAR records can easily identify the occurrence of thermal convection, inversion, elevated inversion, advection, subsiding air mass, sudden gust, waves, and so on. SODAR provides valuable information on the evolution of coastal boundary layer occurrences (Sea/Land breeze) [10]. Information has been used to assess/understand the real-time signal performance of communication links. In sunny weather, the air warms considerably higher than air in the atmosphere close to the surface of the earth. This makes it lighter and rising. This vertical movement has been observed on SODAR in the form of thermal plumes (dense inverted cones). SODAR is one of the most effective ABL approaches in real-time and space up to a height of *3000* m [6].

1.3. Objectives and Outline of the Chapter

Delhi is experiencing environmental stress on several fronts due to exponentially growing population coupled with rapid urbanization, increasing vehicular density, increasing municipal wastage coupled with lack of dumping sites, overflowing wastage dumping ground, dumping of untreated sewage into the city river (Yamuna), illegal settlements residential colonies, *etc* [4]. All these factors are putting tremendous pressure on environmental stress and posing challenges of management for environment protection. Due to the interdependence of population growth, pollution-related activities, environmental stress presents management challenges on air, water, and soil pollution fronts. The troposphere, particularly lower than 1000 m, is a significant parameter in the characterization of air pollution because it limits the vertical space for rapid mixing of near-surface contaminants [1]. In the last decade, the determination and modeling of ABL, especially in urban meteorology, have been of great interest. The use of ground-based remote sensing equipment to monitor the structure of the ABL revealed that the ABL has various layering on occasion (*e.g.,* internal boundary layers, near-surface inversions, and residual layers at night-time and in the morning hours). The use of site-specific SODAR data on inversion/mixing height is recommended for environment protection agencies for EIA and planning strategies for disaster management under the accidental release of pollutants.

SODAR has faced several challenges in recent years, including:

a. greater accuracy of ABL height and structure in pollution studies
b. operation in metropolitan areas without disturbing the public
c. increased need for better data availability
d. Non-experts may install and operate it more easily.

e. The desire for a more "turn-key" autonomous operation that eliminates the requirement for filters to filter out rain and spurious echoes from SODARs.

The study exploits the potential applicability of SODAR to tackle ABL and its structures in Delhi's, National Capital Region (NCR). The objectives are listed below:

a. To collect the data of Atmospheric Boundary Layer (ABL) height and meteorological parameters
b. Enhancement in signal to noise ratio
c. Extraction of useful information from SODAR echograms
d. Prediction of models considering different meteorological conditions

The work addresses four aspects to achieve the goal: development of SODAR system with new acoustics antenna design, analysis of the ABL height, atmospheric pollutants and meteorological data during Diwali period, development of a new model of identification ABL structure using feature selection and classifier method and LSTM model for prediction of ABL height using SODAR data.

The subject matter is covered under eight chapters, besides chapter 1, there are seven more chapter

Chapter 1. Introduction to Atmospheric Boundary Layer and SODAR

The first chapter is an introduction to the subject, the troposphere, ABL, and its need for studies, monitoring techniques, and a comparison of various technologies. In this context, the current chapter highlights the use of the SODAR system in ABL studies, as well as the thesis's objective.

Chapter 2. Literature Review

The literature review gives a clear picture of the underlying concept that drives technological advancement and various future environmental applications for SODAR. SODAR has been shown to be very effective at controlling air pollutants at a low cost for site-specific dispersions. During these efforts, SODAR and other methods were developed. Year after year, new advancements were reported, demonstrating device and appliance technical versatility. With a new R&D concept and application potential, more companies have improved SODAR models.

Chapter 3. Methodology and SODAR System

This chapter highlights the methodology of SODAR operation, mechanism of SODAR echoes, nature of SODAR echoes, interpretation and information from SODAR data, parameters of importance in the development of SODAR. The preliminary studies were conducted for a monostatic SODAR system. Then Discuss the Study of Location and its Meteorological Condition and Method of Determining ABL Height using SODAR Echogram.

Chapter 4. Design of Acoustic Antenna

This chapter describes the design of the acoustic antenna. The first section describes the acoustic parabolic dish in detail; the second section describes the aluminium composite plate and its acoustic properties; and the third section describes how to build acoustic baffles.

Chapter 5. Computational Techniques based SODAR Structure Classification

In this chapter, the first part introduces the SODAR image classification model, which is based on machine learning, and the second part discusses the results and model. The structure classification model's data collection, statistical feature extraction, feature selection methods, and classifiers are also described.

Chapter 6. Temporal ABL Height Prediction using Deep Learning Model

This chapter deals with the LSTM prediction model for the future use of new SODAR data (December 2018 to February 2020) to calculate the ABL height value. The seasonal and annual variations in ABL height are investigated in this work. The presented work then proposed the ABL height data neural network prediction model. The model was evaluated for the ABL data height using the Delhi SODAR system. A time-series comparison of annual and seasonal changes in ABL height was also shown to evaluate model performance.

Chapter 7. ABL Height Estimation During Fireworks Emission

This chapter is divided into five sections: first, data were collected during the fireworks emission, i.e. Diwali festival, then ventilation coefficient was determined, ABL variation with meteorological parameters, ABL variation with pollutants, and finally, forward selection method was used to estimate the most dominant parameter to ABL height. Data analysis in this part gives an account of the occurrence characteristics of air pollution concerned meteorological aspects in terms of evolution characteristics of ABL height. Comparative analysis of occurrence characteristics was drawn for Pre-Diwali, Diwali and Post-Diwali conditions.

Chapter 8. Conclusion and Future Scope

This chapter summarizes the concluding remarks cum recommendation for future work. Conclusively, it is remarked that SODAR information on air pollution meteorological aspects contains useful guiding indicators (of ABL carrying capability) for planning strategies of emission control. To monitor air contamination levels, a unique combination of a motion-coil, a parabolic dish and an acoustic ACP sheet was developed. The system was used for a long time to collect data with a low probability of an electronic failure. The outcome of discussions recommends that the SODAR information be coupled with a prediction model for the future value of ABL height.

Chapter 2
Literature Survey

This chapter provides an exhaustive summary of the research work on sound and SODAR. It begins by providing an overview of the environmental sound origins, followed by a discussion of the application of the SODAR system to air pollution, identifying different types of ABL structures, and predicting ABL height.

2.1. Sound Effect on Atmosphere

Tyndall [11] was the first person to examine sound waves' dispersion under a variety of atmospheric circumstances. He traced the flocculent character of the atmosphere to the long-lasting echo of a siren heard on foggy days. While researching anomalous microwave transmission within the atmosphere, Gilman *et al.* [12] were the first to describe the observation of acoustic echoes of unexpectedly high strength from the lower atmosphere in 1946. To find proof for this unusual behaviour, they looked at the effects of dispersion, absorption, temperature, and humidity on travelling waves and concluded that the temperature changes in the earth's atmosphere governed the reflection mechanism of such high-intensity echoes. These experiments were designed for the aim of correlating observed atmospheric structure with microwave propagation characteristics. Cox [13] determined the temperature profiles of the upper atmosphere by using ground-based explosions while Crary [14] measured the stratospheric wind and temperature structure over Bermuda and Alaska. Rothwell [15] used an anti-aircraft gun to project explosive shells to controlled altitudes and measured both the range and angle of arrival of sound to derive the profiles of temperature and wind.

Thomas [16] realized the potential of acoustic sounding for remote detection of atmospheric thermal inversion layers. He used an *18 m* diameter parabolic dish with a transducer at its focus and worked at a frequency of *190 Hz*. The echoes from an altitude of *600 m* were received under low ground noise conditions. The received echoes were attributed to a temperature inversion, random atmospheric inhomogeneities, cloud layer boundaries, and temporary wind shear conditions. However, the echosounder / SODAR technique for remote sensing was used to study the index of refraction fluctuations within the atmosphere [17-19]. McAllister [17] developed an array of loudspeakers and parabolic dish with a horn-loaded transducer mounted at its focus to be used as an acoustic antenna. The frequency used was *950 Hz* and therefore the echoes from an

altitude of *1000 m* were detected. The increase in detection range compared to Thomas [16] could be ascribed to McAllister [19]'s use of a higher frequency, which increased the signal-to-noise ratio. The introduction of a facsimile recorder, which provided a 3-D display in terms of height, time, and intensity, improved the richness of the observations of atmospheric structure acquired by McAllister *et al.* [18]. The event of basic physical concepts of the influence of turbulent inhomogeneities on sound wave propagation and scattering within the atmosphere was surveyed by Kallistratova [20]. However, the most theoretical and experimental results were obtained and summarized the analysis of fundamental problems, requiring an answer for practical applications of sound waves within the atmospheric research was given.

Little [21] examined the possibility and limits of an acoustic radar and addressed several acoustic approaches for distant probing of the atmosphere. Fukushima *et al.* [22] used a concrete paraboloid dish having an aperture of *16 m* and this antenna was used as the acoustic sounder for studying the lower atmosphere. The interrogating waves had a frequency of *850 Hz* within the sort of pulses of *60* x 10^{-3} *s* duration repeated every *3.6* or *12 s* depending upon the detection range. They had recorded the meteorological structures of the lower troposphere and realized their usefulness within the effective monitoring of the troposphere. Hall [23] described an acoustic sonar for detecting the temperature and velocity structure of the Earth's physical phenomena. The specifics of the SODAR development and experiment work were documented by several experts [24-30]. Several studies [1-3, 31-35] provided outlines of the theory of SODAR research.

In late 1960s and early 1970s, scientists at the National Oceanic and Atmospheric Administration (NOAA) in the United States of America (USA) established the practical viability of using acoustic sounders to detect winds in the atmosphere and monitor the structure of temperature inversions by measuring Doppler shift in the received signal [17-19, 21]. Thereafter, numerous groups of researchers in the USA focused on the engineering design of SODAR in the 1970s, while the academic community began work on wind profiling utilising the Doppler shift in the signal return from a slightly titled SODAR.

Simultaneously, commercial SODAR interest arose in response to increased academic interest, technology development initiatives, and anticipated application potential. Bucket antennas were used in the commercial systems. The several commercial SODAR systems and their companies had below since 1970 [3, 36-50].

Table 2.1. Commercial SODAR and their company name with a country

S. No.	Country	Model and Company/ institute	Remarks
2.	USA	Model 300 AeroVironment Inc.	One of the first commercial devices, designed to measure turbulent structures up to a height of several 100 m.
3.	USA	Mark VII NOAA	The acoustic echo sounder is a portable system that provides an analogue record of backscatter data.
4.	Germany	Scientific Engineering System Inc. (SES)	By adding a microcomputer to the device, the first digital-based acoustic sounder was created.
5.	Germany and USA	SES and NOAA	A three-axis digital-based acoustic sounder is being developed. This device can calculate vertical and horizontal wind speed and direction by detecting both the Doppler shift and backscatter intensities in real-time.
6.	USA	Radian Corporation	SODAR system with three axes based on a microcomputer
7.	USA,	Xonder SODAR system Xonics Inc.	Wind profile and turbulence measurements are possible.
8.	USA	Invisible Tower (AVIT) Aero Vironment Inc.	Three neighboring parabolic dishes are operated consecutively with a three-axis arrangement.
9.	France	REMTECH	Up to 1000 m, a phased array SODAR system capable of sensing Doppler shifts and turbulence parameters, as well as being the first to use multiple-frequency coding.
10.	Germany	Doppler SODAR PCS.2000, Metek	Mobile stand-alone profiling at off-the-beaten-path locations
11.	Germany	Flat Array Sodar SFAS Scintec	The Scintec SFAS is a small acoustic profiler that can monitor wind and turbulence up to 500 m above ground level.
12.	Japan	Kaijo Corporation	The Doppler SODAR is developed.
13.	Australia	Atmospheric Research Pty Ltd	The Doppler SODAR is developed.
14.	USA	Model VT-1 Atmospheric Research & Technology	The Model VT-1 is a monostatic phased-array Doppler SODAR system with a monostatic antenna

These companies and their SODAR were mostly based on monostatic antenna setups and were primarily used for remote wind profile measurement. Signals from temperature fluctuations were captured by the monostatic configuration. As a result, determining wind speed (through Doppler shift measurement) was solely dependent on backscatter induced by linked temperature changes. During gloomy and strong wind circumstances, however, the atmosphere was primarily neutrally stratified, and signal intensity

frequently drops below essential levels for accurate wind speed detection. As a result, Mikkelsen *et al.* [51] created a new CW SODAR that was based on a Bi-static antenna design. A Bistatic SODAR configuration received and sound scatters from wind turbulence (C_v^2). Therefore, it continues to receive adequate backscatter signals even during high wind speed induced neutrally stratified conditions.

The integrated product of SODAR and RADAR termed RASS for measuring both wind and temperature profiles resulted from continuing R& D advances in technology as well as signal processing approaches [3]. The RASS operated at frequencies about 1 GHz, was rapidly becoming a common profiling tool for monitoring both temperature and wind profiles in the ABL [52]. SODAR technology had progressed quickly, and a variety of commercial versions are now available.

Singal and Pancholy [53] also experimented with sound waves to investigate the atmosphere in India. The classic monostatic SODAR was created at the Council of Scientific and Industrial Research - National Physical Laboratory (CSIR-NPL), New Delhi, which was one of India's top research institutions under the Department of Scientific and Industrial Research (DSIR) [54]. In addition, in 1997, a three-axis Doppler SODAR facility was developed [55]. The SODAR equipment and software were upgraded using the virtual LabVIEW platform as technological development tools improved [56-58]. In India, the SODAR system was used for ABL monitoring over the past five decades, with ongoing research and development efforts in SODAR technology application. During my Master of Engineering (M.E.) several tools and models were developed to analyse ABL height, structure, and stability class [58]. The technology and software were deployed in industrial and institutional areas to determine the carrying capacity of air pollution, as well as the stability class for dispersion modeling, as prescribed by the Central Pollution Control Board (CPCB) in New Delhi, for existing and new industries.

Aside from the summaries, there were many summaries of developments in acoustic remote sensing methods available, which represented both early ground-breaking efforts [21, 24] and later work [59-61]. SODAR is currently a globally recommended technology for a range of environmental and EIA applications [56].

2.2. SODAR Validation, Structure, and Application

SODAR is an important piece of equipment that measures ABL height in near real-time which has been used as a diagnostics tool in air quality management for environmental

monitoring in various hazardous conditions such as communication, aviation, wind energy sourcing evolution, meso-meteorology, and as a contemporary technique to other techniques. To achieve these aspirations and predictions, the most specialised ground-based distant sensing of the mean wind, temperature, and humidity within the troposphere is used to monitor and predict the weather. During that time, SODAR has been the favoured choice because of its integrated capacity to provide data on the dynamics of ABL thermal structures, the capacity to disperse the atmosphere, and wind profile measurements in real-time in a wide array of applications. However, the primary interest of researchers has been in data validation to make sure the standard of knowledge and gain confidence before its direct use as an alternative to standard data availability from existing conventional direct measurement technologies like an instrumented tower, radiosonde, *etc*.

Marshall *et al.* [62] conducted a theoretical examination of horizontal and vertical wind profiles using SODAR, while Beran *et al.* [63] and McAllister [19] conducted practical evaluations. Little [21], Beran *et al.* [65], and Wesely [66] investigated the viability of employing SODAR data to compute the vertical humidity profile. The ABL was precisely measured using a SODAR, a parameter used by Greenfield *et al.* [67] in the theoretical computation of temperature profiles inside the lower atmosphere under changing climatic conditions. Mahoney [68] conducted an experiment at Haswell including the use of 3-axis SODAR placed *240 m* apart at the corners of a triangle within which is a *150 m* instrumented tower capable of delivering information about temperature and wind at a rapid rate to correlate the information collected by the SODAR with meteorological factors. Although some of the SODAR data was understood in terms of the recorded turbulent heat flux and momentum, it was determined that the system required to be evolved into an independent quantitative instrument to unravel a large number of details seen. To ascertain the validity of SODAR records, dissimilar researchers had compared the SODAR observations with vertical temperature profiles obtained from radiosonde techniques, captive balloons, LIDAR, RADAR [69-80]. They showed that echoes on the SODAR echograms correspond to regions of enhanced temperature discontinuities.

The height of ABL during the inversion period was computed using the bulk-Richardson-number approach, diagnostic equations for the equilibrium ABL height, and a relaxation-type prognostic equation, and was explained in terms of their physical foundation and applicability of experimental data [81-83]. They concluded that the critical bulk Richardson number (R_{iBC})

of the ABL throughout the inversion period was not constant. They also stated that the Richardson number-based computation methodologies should only be used for rough ABL calculations.

Fukushima *et al.* [84] had deduced temperature fluctuation profiles from SODAR data obtained for two years. They had calculated monthly values of C_T^2 in different layers and brought out a profile of C_T^2. Also, the average profile of the refractive index structure constant C_n^2 were deduced. However, the profile C_n^2 in the clear night as summarized by Hafnagel [85] showed many small values than this. This discrepancy in the profiles of C_n^2 observed by Fukushima *et al.* [84] and Hafnagel [85] had been recognised as due to the difference of two techniques used.

Neff [86] had compared SODAR results with observations made on a *92 m* instrumented tower. SODAR derived values of temperature structure parameter C_T^2 were compared with values of C_T^2 obtained from the tower. An excellent agreement was seen between the two sets of C_T^2 values under statically unstable conditions. However, under stable settings, the values occasionally differed by a factor of 2-5. This was hypothesised to be attributable to sampling and averaging problems in in-situ sensors compared to finite volume echosounder readings due to quasi-horizontal spatial ordering of small-scale turbulence structures. Asimakopoulos *et al.* [87] had been also concluded from the SODAR test conducted under both stable and unstable conditions that the device was provided reliable estimates of C_T^2 but the apparent errors increased with increasing turbulence. Haugen and Kaimal [88] had also evaluated C_T^2 using SODAR and concluded that Excess attenuation owing to turbulence and beam bending had been factored into the RADAR equation. Emeis *et al.* [2] has done a comparative study of SODAR, RASS, and ceilometer for measurement of ABL structures. The RASS gave an instant measurement of the vertical temperature distribution within the ABL based on ceilometer data with the aerosol content of the air. The RASS and ceilometer provided further information on the moisture structure of the ABL that the SODAR had missed. On the other hand, this comparison supported the use of well-known approaches for mixing ABL height from SODAR data. The mixing layer had an important role in the transportation of air pollution since it was a crucial meteorological component. Between July 2009 and December 2012, Tang et al. [89] were also stated and their findings were compared. Between the above intervals, the ABL height (mixing layer height) was measured with a ceilometer and radiosonde. It was revealed that the ceilometer underestimates the ABL height when neutral stratification was caused by strong winds but overestimates it when sand-

dust was presented. They also identified a correlation coefficient of greater than 0.9 between ceilometer and radiosonde observations. They stated that ABL heights were low in the winter in Beijing, but high in the spring and summer. According to this study, when using visibility as an index for measuring the degree of air pollution, changes in the sensible heat and buoyancy term in turbulent kinetic energy were minor on somewhat cloudy days compared to clear days, but a reduction in the shear term was significant.

Internal fronts and atmospheric waves were investigated [90-96]. The formation of shear caused energy imbalances under steady settings was revealed to be one of the key drivers of wave formation in these studies. These waves were caused by pressure changes on the ground and interfere with microwave transmission by increasing fading. To investigate the phase speed and direction of propagation of these waves, a network of SODAR systems was necessary.

The structure and behaviour of maritime boundary layers had been investigated [97-103]. Under favourable weather circumstances, Ottersten *et al.* [97] found that a ship-borne SODAR system monitored temperature inversions up to *800 m* and thermal plumes up to *300-400 m*. Mandics and Hall [99] found that echograms displayed a mixed layer typified by thermal plumes under suppressed weather circumstances, whereas disturbed weather events resulted in significant ABL alteration. The ABL height might be as low as *100 m* at those times. At Miyakojima Island, Fukushima *et al.* [84, 104] conducted SODAR studies for the lower atmosphere. The occurrence of thermal plumes in the maritime ABL had been documented even at night. The SODAR technology was also used to examine the maritime boundary layer in San Diego [100-101]. They've demonstrated how this methodology might be used to track the dynamics of the marine layer. The presence of nocturnal convective plumes had also been documented in the San Francisco Bay area.

In the southern pole, SODAR was used by Neff and Hall [105] for the ABL. The climatology of the stable boundary layer covering the Antarctic ice dome was thoroughly investigated. Records from SODAR were correctly interpreted using in-site data.

SODAR echograms for unprecedented precision in research into ABL structure [106]. SODAR echogram is a new and exciting science that theorises the ABL structure can reveal vital information about the atmosphere, allowing for more accurate pollution research. Diverse ABL structure aspects were explored in terms of their prediction powers and reliability across various meteorological conditions in some research [107-110]. For the atmosphere and pollution investigations, some researches have shown a link between atmospheric structure and atmospheric stability [111]. Manual identification of various types

of atmospheric structures was a time-consuming process that requires skilled individuals. To automatically extract knowledge and discern patterns from these data, data mining and machine learning algorithms were developed. Machine learning was a type of computation that uses training data (experience data) to enhance performance or create a precise forecast [112-113]. These technologies could learn data and automating the prediction process to increase accuracy [114-115]. However, machine learning was used to identify SODAR echogram structures, and this was explored separately in Chapter 5.

Łobocki [116] looked at the variation of the logarithm of the Monin-Obukhov-scaled structural parameters (log C) of temperature and humidity. According to their observations, the difference in log C between upward (larger C) and downward (smaller C) motions increase as instability develops. As the average window size grows, the variances in log C become less. Due to discontinuity in the structure and a lack of data, the difference in variances between temperature and humidity profiles at different heights remained unexplained since they were explored. They only learned about the variability of temperature and humidity structural characteristics in the atmospheric surface layer at different stability conditions.

A three-axis monostatic Doppler SODAR was developed that measures the Doppler shift using a minicomputer-controlled processor FFT, and measurements utilising this SODAR were reported [117-121]. The wind speed and direction data from this system were compared to data collected from pilot balloons at heights of *30-500 m*, and the two values show a strong correlation [120].

Strauch and Sweezy [122] reported on the development of a Bistatic Doppler SODAR system, dubbed the "Simple Wind Shear Detector." For data analysis, they also used a microcomputer-controlled processor.

The development of a digital microprocessor-controlled Doppler SODAR for wind measurements was described [117, 123-124]. It was proven that a real covariance technique to spectral moment estimation was incredibly simple to implement out of all of the digital SODAR. The findings of Doppler estimates were demonstrated to agree well with FFT and adaptive filter techniques. The ability of the echosounder to measure the turbulent velocity structure functions *D(r)* and C_V^2 using the Doppler technique was demonstrated [125-126]. They compared time-averaged, acoustically derived C_V^2 values with acoustic facsimile records in both stable and unstable conditions. It was observed that temporal and spatial variations of C_V^2 were large and correlated well with SODAR detected structure.

In light of the growing range of SODAR applications, current standards, such as the ASTM standard on SODAR operation, the ISO standard, and several recent publications addressed difficulties affecting the concept of SODAR operation [127-136]. SODAR functioning was not subject to any international standards. The only standard was to verify the measurement's accuracy by comparing it to measurements taken using widely established standard methodologies. Several studies (described above) demonstrated the reliability of SODAR and established a solid foundation for using it as a standard instrument for air pollution meteorological data. Bradley *et al.* [137] published a paper on the calibration of SODAR systems for wind energy applications, with various proposals for increasing SODAR's use in such applications, including the creation of a self-calibration method.

Measurements of convection layer or mixing layer height, thickness and height of inversion layer and wind velocity, *etc*. were the important parameters in air pollution studies [78, 138-145]. SODAR might be utilised as a diagnostic tool in air quality management for air quality monitoring in a variety of hazardous circumstances that were directly linked to human health issues. SODAR had made Environmental Impact Assessment (EIA) mandatory, with suggestions for site-specific assessments of ABL dynamics (CPCB, 1992). SODAR was the only device that measures the ventilation coefficient to determine the region's pollutant loading capability. Wind speed and direction, turbulence temperature, lapse rate, and ABL height were all factors that influence the dilution, rise, and spread of pollutants [146-149]. Researchers need to know the ABL height and the different forms of ABL structure to comprehend local pollutants transfer and dispersion across a large area. SODAR's ability to map diverse forms of ABL structures were improved in recent years. The understanding of these structures was extremely useful in air pollution research [148].

SODAR is a low-cost, real-time remote sensing tool to use and assess any level of air pollution. Air quality measurements were directly related to the ABL [1, 146, 150-152] and showed significant correlations between air pollutant concentrations and continuously monitored ABL height [153-155]. The SODAR method contributed much to the meteorological studies of air pollution and the results were employed in prediction models of pollutant dispersion [146, 156]. It was gradually employed to provide quantitative and qualitative data on the temperature characteristic of the atmosphere. At the time a linkage between various atmospheric quantities and air quality patterns has been investigated and established particularly in metropolitan contexts [156]. The results showed that the pollutant concentration (O_3, NO_x, CO_2) is well correlated with ABL height and that the rate of height growth for ABL is highly dependent on the pollutant concentrations, especially during the

early morning-hours degrading period, and the ABL collapses in the afternoon. The concentration of $PM_{2.5}$, $PM_{1,}$ and PM_{10} was negatively correlated with ABL Height [154]. The dissipation of atmospheric particles was mainly dependent on the ABL Height. Mahalakshmi et al. [153] calculated the VC using ABL and wind speed in different seasons and found that VC played an important role in the dispersion of the pollutants.

During the late evening in Delhi, Singal et al. [111] analysed the case of serious saturation of air pollution and found the reported air pollution to be at a low ABL level. Singal et al. [151] have also investigated the association in SODAR-derived diurnal variance in carbon monoxide measured concentrations present near the earth's surface and the prevalent SODAR atmospheric stability class of Pasquill.

Gera *et al.* [157] studied diurnal, monthly, and seasonal variations in the ground/elevated inversion, thermally driven convection ABL, and fumigation characteristics, finding that poor atmospheric ventilation was associated with stable inversion conditions for about *10* hours (*1800-0600 IST*) while good ventilation was associated with convectively driven unstable ABL for about *8* hours (during *1000-1700 IST*). The duration of the fumigation varies from a few hours in the summer to more than *6-8* hours in the winter. This data was useful for planning and implementing environmental management initiatives.

Radioactive fog generation, according to Garratt [158] was a complicated phenomenon involving local physical and microphysical processes that occur when specific meteorological conditions occur. The regional weather model was built to anticipate fog, and it was found to detect *74 %* of the climatic circumstances leading to observed radiative fog and *48 %* two days ahead of time. The radiative fog was difficult to model and forecast, according to their research.

Murthy *et al.* [159] investigated the characteristics of ABL response during winter season about air pollution meteorological aspects and discovered that thermal structure characteristics relevant to air pollution, such as inversion/mixing height, fumigation, and lower-level raised inversion, experience significant deviations that were caused for concern for air quality and risk management strategy planning. The researchers established a link between ABL height and visibility, which was crucial for verifying ABL models and improving their performance in foggy settings.

Many authors considered soft computing and AI-based models to examine the impact of ABL on the climate and humans at the same time [160-162]. These models have used a variety of methodologies, including neural networks, fuzzy logic, deep learning, and the Adaptive Neuro-Fuzzy Inference System (ANFIS). To tackle real-world challenges, these strategies

were utilised to research, model, and analyse complicated situations and occurrences. The pollution control board, meteorological department, and atmospheric scientists all rely on accurate modeling of ABL height and the use of forecast tools to investigate the climatic conditions in local and remote places [163-164]. For example, ABL height was important in assessing a given area's pollutant bearing capacity, air quality assessments at the local or regional scale, emission control, air quality forecasts, and laws implementation. The meteorological data required for computing the transport, dispersion, and removal of pollutants was a major input to this model. The ABL height controls the volume available for pollutant dispersion and an important component in atmospheric flow models, such as the Wind Profile [165]. Using time-series prediction models, the instrument data was used to forecast ABL height. Linear and non-linear time series models were two types of time series models. Linear models include Auto-Regressive (AR), Auto-Regressive Moving-Average (ARMA), Auto-Regressive Integrated Moving-Average (ARIMA), and their variants. To fit a mathematical model to a univariate time series were used predetermined equations [166]. These models were unable to account for the data's latent dynamics. Artificial Neural Networks (ANN), Adaptive Network-based Fuzzy Inference (ANFIS), Genetic Algorithm, and Fuzzy Inference System were non-linear models that has been effectively applied to model of many factors such as ABL Height, pollution, temperature, and so on [167-170]. On the other hand, these models were less capable of detecting hidden patterns and underlying data dynamics. Through a self-learning process, deep learning algorithms were capable of finding hidden patterns and underlying dynamics in data [166, 171]. The data generated in the case of ABL height was massive and very non-linear [170]. Deep learning models, unlike other algorithms, successfully produced good predictions by analysing the relationships and hidden patterns within the data. A Recurrent Neural Network (RNN) with Long Short-Term Memory (LSTM) was a specific sort of RNN [172-173]. LSTM was a deep learning algorithm that operates on a gradient-based learning technique and is aimed to reduce error backflow.

Different input factors have been employed for predicting weather data in the area of meteorological parameters time series analysis utilising neural network models and deep learning algorithms. For heterogeneous weather information, time-series data were employed. In Colombia, Vivas *et al.* [170] used deep learning to detect ABL height from atmospheric LiDAR signals. Artificial neural networks were employed for the prediction of global solar radiation with air temperature and relative humidity for Saudi Arabia from 1998 to 2002, according to Rehman and Mohandes [169]. Zhao *et al.* [174] used the LSTM approach to

forecast RADAR sea clutter, and the results were shown to be superior to neural networks. However, the model's performance for long-term forecasting was not as good as it was for short-term forecasting.

2.3. Impact of Fireworks on Atmospheric Boundary Layer Height

Diwali is the most important and big festival, celebrated all over India. During the festival, fireworks create a lot of pollution in the environment resulting decrease in ABL height and cause negative effects on human health [154, 175]. Diwali is celebrated in the post-Monsoon season of October / November with the bursting of firecrackers, it was created a health hazard for human beings [176]. Uses of bulk firecrackers emit many pollutants into the atmosphere. The concentrations of SO_2 and NO_2, as well as particulate matter such as PM_{10} and $PM_{2.5}$, were found about *2-6 times* higher during Diwali day and next to Diwali day, when compared with the respective concentration of normal day [177-178]. The firecrackers were consisting of different types of chemicals (lead, magnesium, sodium, cadmium, zinc, nitrate, and nitrite), which was a harmful effect on the atmosphere and human beings. This high concentration of pollutants remained in the atmosphere for about *5-10 days* after the festival, having *8 - 9 times* more than that regulatory standard level [179]. Over Delhi, air pollution was reduced the life expectancy of people by six years and increased the number of cases of respiratory diseases, as well as pollution-related morbidity and mortality [180] due to an increase in vehicles, industries, and firecrackers pollutants [181]. Maji *et al.* [182] reported that in Delhi the mortality due to particulate matter increased to *2.25 %* in the year 2015 compared with the year 1995.

The pollutants' concentrations didn’t remain constant throughout the year, indicating that they were influenced not only by local sources but also by distant sources from other places [183-185]. Numerous studies [178, 186-189] confirmed that the burning of fireworks emits organic compounds, metals, sulphur dioxide, Ozone, and Nitrogen Oxides. Even when Ozone precursors and sunshine are missing, Attri *et al*. [186] found the synthesis of O_3 at the ground level at night. Short-term variations in air quality were documented with fireworks activities above Hisar city in Delhi-NCR, according to Ravindra *et al.* [190]. The effect of firecrackers on ambient air quality over Delhi was investigated by Singh et al. [191], who found that fireworks during the Diwali celebration harmed ambient air quality due to the emission and build-up of TSP, PM_{10}, SO_2, and NO_2. Mandal *et al.* [192] found a significant drop in particulate matter and sulphur dioxide concentrations in the air over the same city of Delhi on Diwali day. Yerramsetti *et al.* [177] investigated the impact of Diwali fireworks emissions on

air quality in a tropical site in Hyderabad over three years, observing air quality degradation due to firecrackers burning and validating their findings using the Cloud-Aerosol LiDAR and the Infrared Pathfinder Satellite Observation-derived aerosol sub-typing map. In the Valley city of North China, Song *et al.* [193] discovered a link between firecrackers and air pollution. Ghei and Sane [194] analysed long-term data from 2013 to 2017 to evaluate the Diwali influence on air quality, found that the festival results in a tiny but statistically significant increase in pollution. Zhang *et al.* [195] observed an unexpected and strong rise in air quality because of the use of firecrackers. Arora *et al.* [196] looked examined particle matter and chemical compounds before and after Diwali and discovered that fireworks had a substantial impact on air quality.

Apart from the burning of firecrackers, the activities of neighbouring states such as Haryana and Punjab, as well as meteorological circumstances in Delhi such as low temperature, low wind speed, and low relative humidity, were an impact on the air quality of the city. During the winter season, just after Diwali, dense fog, haze, and smog rose in Delhi, and these suitable conditions were also the cause of extremely high air pollution levels [185, 197]. It was discovered that the concentration and content of pollutants had altered over time because of Diwali fireworks. During the Diwali festival in Delhi and North Capital Region (NCR), firecracker activity was more prominent, to understand the variation of air quality and ABL height during the festival in-depth study and analysis in need.

The literary review provided a good understanding of the underlying idea that drives technological progress and various future applications for SODAR in the environment. SODAR has proven to be extremely useful in controlling air pollutants at a low cost for site-specific dispersions. In these efforts, SODAR and other approaches were now being developed. Year after year, new advances in devices and applications were reported, demonstrating technical versatility. More business enterprises have developed improvements of SODAR models with a new R&D concept and application potential.

Chapter 3
Methodology and SODAR System

SODAR is an important equipment that detected ABL height in real-time. It is used as a diagnostic tool in air quality management for air quality monitoring in a variety of hazardous circumstances, which are directly linked to human health issues. The objective scenario of the present work involved considerations of methods to understand ABL and SODAR system. The data generation, processing, and interpretation information was gathered to provide a better knowledge of the SODAR system to obtain the necessary data. This chapter began on the acoustic echo mechanism, various types of echoes received by the SODAR system, and how meaningful information can be interpreted. The next part is followed by a discussion on the design and preliminary measurements of SODAR hardware and software monostatic system.

3.1. Methodological Considerations

The present objective of SODAR studies of ABL and environmental applications call for 4-fold major steps of methodological considerations

1. Upgradation of SODAR system for different climate area
2. Understanding the role of ABL Height in air pollution applications
3. Study the ABL structure using SODAR echograms
4. Prediction of ABL height using SODAR data

Literature reviews have provided a solid grasp of ABL height, structure, usage of SODAR system in study of ABL, basic of SODAR system technology, data collecting and processing methodologies, which influenced air quality, and put forward the necessity for SODAR derived site-specific characterization for air quality management as a result of the above processes. The knowledge on air pollution, meteorological characteristics of the inversion or convection layer, stability, and the transitional phase of the ABL was abundant. In the interest of application, these data were analysed and used as specific information. New research and development findings support the identification of the scope of improvements in technology and data processing to detect new potential fields of use.

The purpose of the environmental application in the current work scenario was to investigate air pollution meteorological elements over Delhi. Thus, air pollution, meteorological parameters, and the ABL prediction for the height of the system development approach and

data processing technology. Fig. 3.1 depicted the essential technique for the study and development of SODAR systems, as well as their application in ABL research.

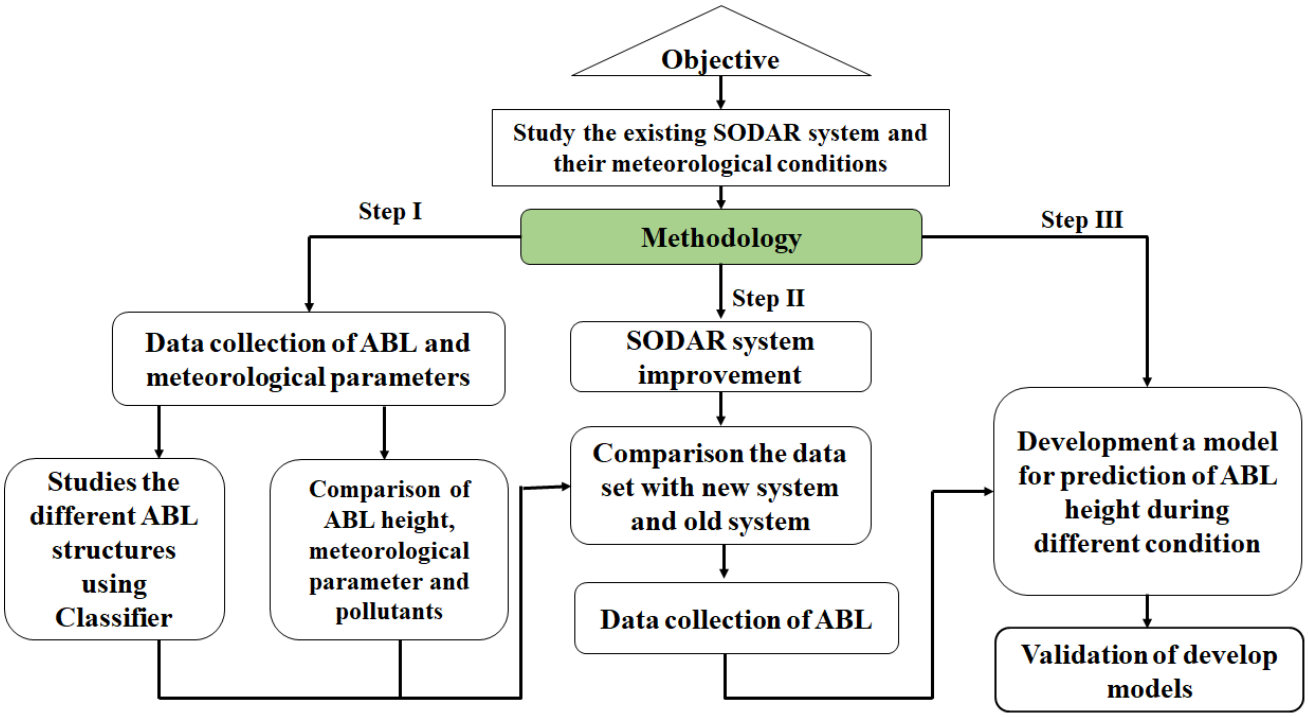

Figure 3.1. Flow chart of the methodology

The old monostatic SODAR system was in operation for the past two decades. The new monostatic SODAR system was developed for monitoring of ABL and their structure. The available old data, as well as new data, was used in this study, *i.e.*, years 2014-2020.

3.2. Mechanism of SODAR and Generation of Echogram

According to the literature, small-scale refractive index variations occur continuously in any volume of atmospheric air [1-3]. These variations provided tracers for the scattering of the acoustic beam. The fluctuations usually arise when turbulence occurred within a region of refractive index gradient associated either with temperature inversion or with convective activity. The energy was scattered from turbulent temperature fluctuations of half the acoustic wavelength. When wavelength was the lowest, the dispersion was highest. Temperature inversions alone (without turbulence) probably didn't have sufficiently strong temperature gradients to provide significant echoes directly. Turbulence fluctuations of proper scale accompanied with atmospheric stratification other than neutral were generally necessary to produce the scattering [1-3].

The mechanism of generation of turbulence due to temperature lapse rate other than dry adiabatic was discussed [20, 198-199]. Tatarski [198] obtained an expression for scattering cross-section $d\sigma$ as

$$d\sigma(\theta) = 2\pi k^4 v \left[\frac{1}{C^2} E_v(k) cos^2 \frac{\theta}{2} + \frac{1}{4T^2} \emptyset_T(k)\right] d\Omega \quad (3.1)$$

Kallistratova [20] and Monin [199] used a different approach to effects of wind speed and temperature to obtain the expression for *dσ*

$$d\sigma(\theta) = 2\pi k^4 v\, cos^2\theta \left[\frac{1}{C^2} E_v(k) cos^2 \frac{\theta}{2} + \frac{1}{4T^2} \emptyset_T(k)\right] d\Omega \quad (3.2)$$

This expression didn't consider the Doppler frequency shifts and scattering due to humidity fluctuations. However, such effects were normally quite small for sound waves. Furthermore, in the development of the expression for scattering cross-section, they assumed that the field of fluctuations within the scattering volume didn't vary significantly during the passage of sound waves. The refractive effects on the scattering volume, scattering angle, and Doppler bordering of frequency were investigated in detail [200-204]. They found that these effects were small for sounding up to a height of *1000 m*. The amplitude of the dispersed signal was proportional to the degree of turbulence, and the acoustic wave scattering occurred in all directions.

The estimation of received acoustic power in the case of a SODAR depends on the amount of atmospheric attenuation along its path in addition to various other parameters. In the case of hemispherical spreading of sound, the intensity I at a distance R from the source was expressed as

$$I = \frac{P}{2\pi R^2} e^{-\alpha R} \quad (3.3)$$

Harris [205-206] was published detailed results for sound absorption in the air as a function of humidity and temperature. However, this work was of significance for see-level investigations and was somewhat limited for use in the free atmosphere because it didn't include the less well-defined effects and results from scattering and refraction in the free atmosphere.

After the development of the SODAR system, receiving power was determined to be a finite value. The receiving power was depending on the number of parameters. These parameters were used to develop the system and affect the measuring of the ABL component.

$$Receiving\ Power, P_r = P_t \,.\sigma.\frac{c\tau}{2}\,\frac{A.L}{R^2} \quad (3.4)$$

$$C_T^2 = \frac{\sigma_{180} T^2}{4 * 10^{-3} k^{-1/3}} \quad (3.5)$$

where σ = scattering cross-section; c = speed of sound; τ = pulse width; R = range; A = antenna area; L = factor containing the equipment efficiencies, antenna gain, and the

atmospheric absorption; P_t = the transmitting power; C_T = temperature structure constant; k = angular wavenumber; T = temperature.

The monostatic SODAR power equation (3.4) and temperature structure equation (3.5) showed that backscattering was only due to temperature inhomogeneities. The monostatic SODAR system looked at these backscattered sound signals. So, the curvature area of dish, antenna gain, and atmospheric absorption were essential to transmitting and receiving the acoustic wave. Wind and humidity fluctuations cause temperature fluctuations and thus contribute by changing the temperature structure parameter. The received signal was processed to derive information on amplitude about the degree of prevalent turbulence while information about the current wind speed was contained in the frequency.

3.3. SODAR System Parameters

The preliminary review showed a highly directional acoustic antenna, recording system, background noise, and choice of frequency affected the operational efficiency of a SODAR system [3]. Fig. 3.2. shows the essential parameters used in the monostatic SODAR system.

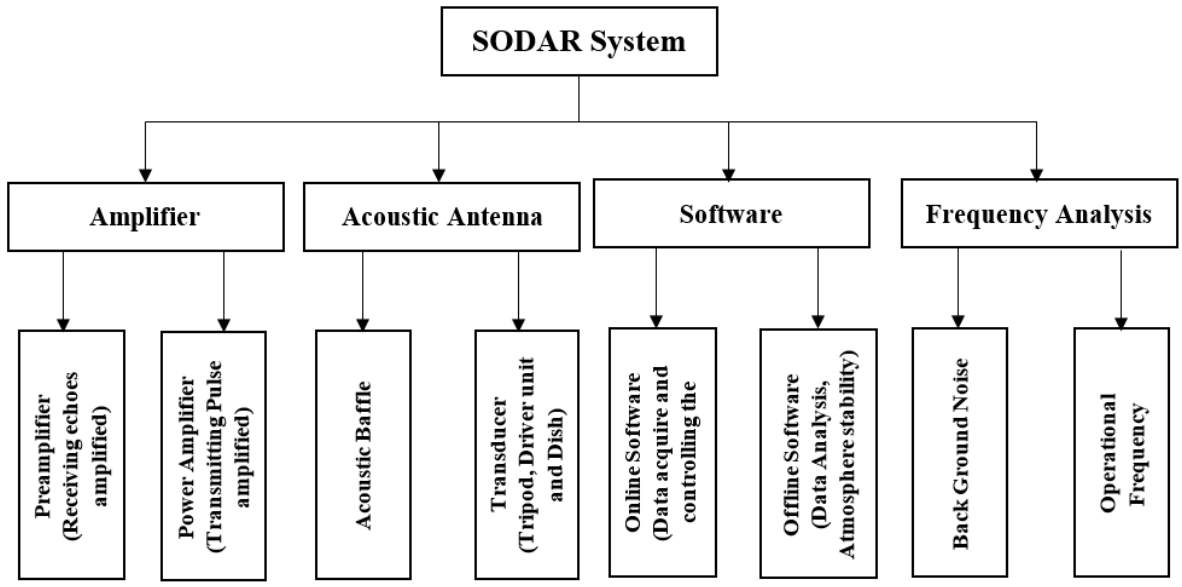

Figure 3.2. Preliminary experiment parameter

3.3.1. Amplifier

Most of the SODAR System hardware was scientific standard as shown in Figure 3.2. Every instrument specially designed or selected for the SODAR system was calibrated or tested. A power amplifier (Model- BR 250M, Ahuja Radios, New Delhi, India) was used in this system with a maximum output of *300 W*. The output regulation was less than or equal to *3 dB* from no load to full load at *1000 Hz*. This amplifier was used to boost the output power of the

sound wave to transmit the signal into the atmosphere. The transmitting sound pressure at the transducer was above *138 dB* SPL, as per requirement.

The preamplifiers were developed to provide the receiving signal with a gain of *70 dB* at *2250 Hz* with a *50 Hz* bandwidth and isolate the components for data acquisition of the transmitted pulse. Fig. 3.3. displayed a three-stage preamplifier block diagram. Additionally, the preamplifier provided the system with a security and switching mechanism. By physically incorporating it into the device, low noise characteristics of an OPA37 operational amp were evaluated and their acoustic and acoustic properties analysed with the standard secondary spectrum analyzer. The complete circuit of the preamplifier was calibrated in the Electrical and Electronics Metrology (PMM Division, CSIR-NPL), to calculate the standard uncertainty of the gain provided by the circuit at ± *2 dB.*

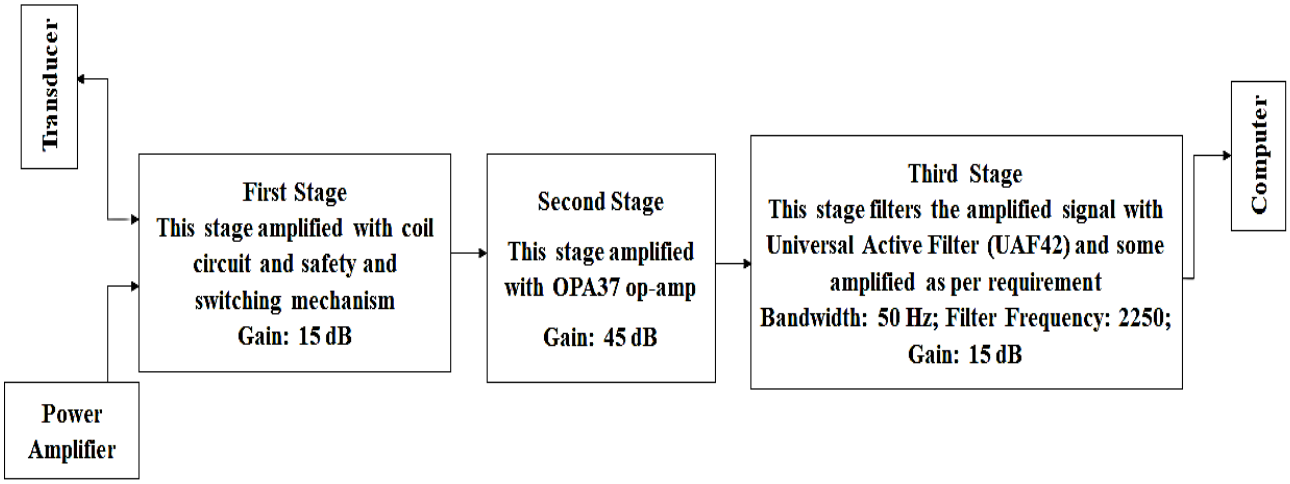

Figure 3.3. Block diagram of the preamplifier circuit

3.3.2. Acoustic antenna

It was essential to have a highly directional acoustic antenna. The directivity of the acoustic antenna determines the energy of a transducer projected into the scattered area as well as the amount of clutter and background noise received by its antenna in receiving mode. At a narrow angle, the antenna can transmit and received energy with the lowest possible sideload. The antenna's radiation pattern is shown in Fig. 3.4 [207]. The directional antennas were thought to be a parabolic dish in the centre, which was used to produce a monostatic configuration with a horn transducer. Details of the acoustic antenna have been described in Chapter 4.

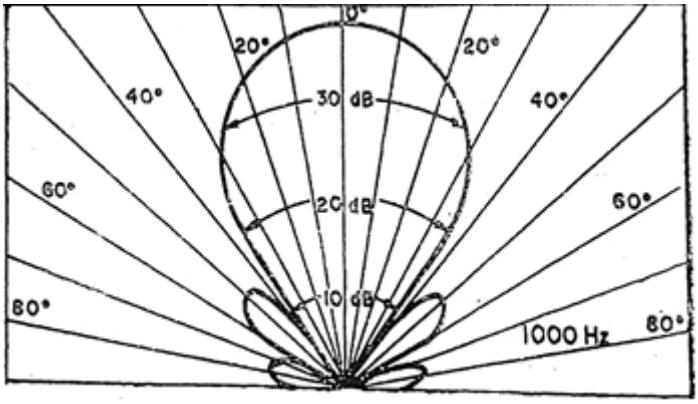

Figure 3.4. The radiation pattern of the parabolic dish

3.3.3. Software

A suitable recording system was required for the complete analysis of ABL. It featured a real-time display of the phenomena and was simple to operate. On the recorder, the noise was also easily distinguished. The LabVIEW software and computer were used for controlling and monitoring every operation of the hardware components. There are two parts to this software development. The first one is online software, which provided real-time data for observing the ABL and collecting data, and the second one is offline software, which was used to view previous data and the atmospheric stability class. Each software was developed in LabVIEW 2017 platform. Online or real-time software was provided with the turbulence intensity in pattern plots or picture forms in repetitive or sequential signals with a wealth of details and information content. This intensity plot was directly proportional to the received signal strength. The online and offline software quickly broke down into several blocks and subroutines which perform specific operations. Fig. 3.5. shows the overview of the developed software, each block is straightforward in its purpose, and the program design to be as helpful to the user interface. Fig. 3.6. represents the offline software, the time axis was represented in the horizontal axis and vertically found that ABL height in an upper block and subsequently below wind direction, wind speed, relative humidity, and temperature. This software showed the 24-hour data, this was helpful for diurnal and temporal analysis. This software also plotted the atmospheric stability class with ABL height. After the development of new software, the monostatic SODAR system was found more user-friendly than the last system. This software provided the FFT of the received signal, increased the resolution of echograms which provided up to 1-hour to 24-hours data in a single graph. Due to the increase in resolution, the microstructure of ABL like elevated layer, multi-layer, stratified layer, Kelvin-Helmholtz, *etc*. was studied easily.

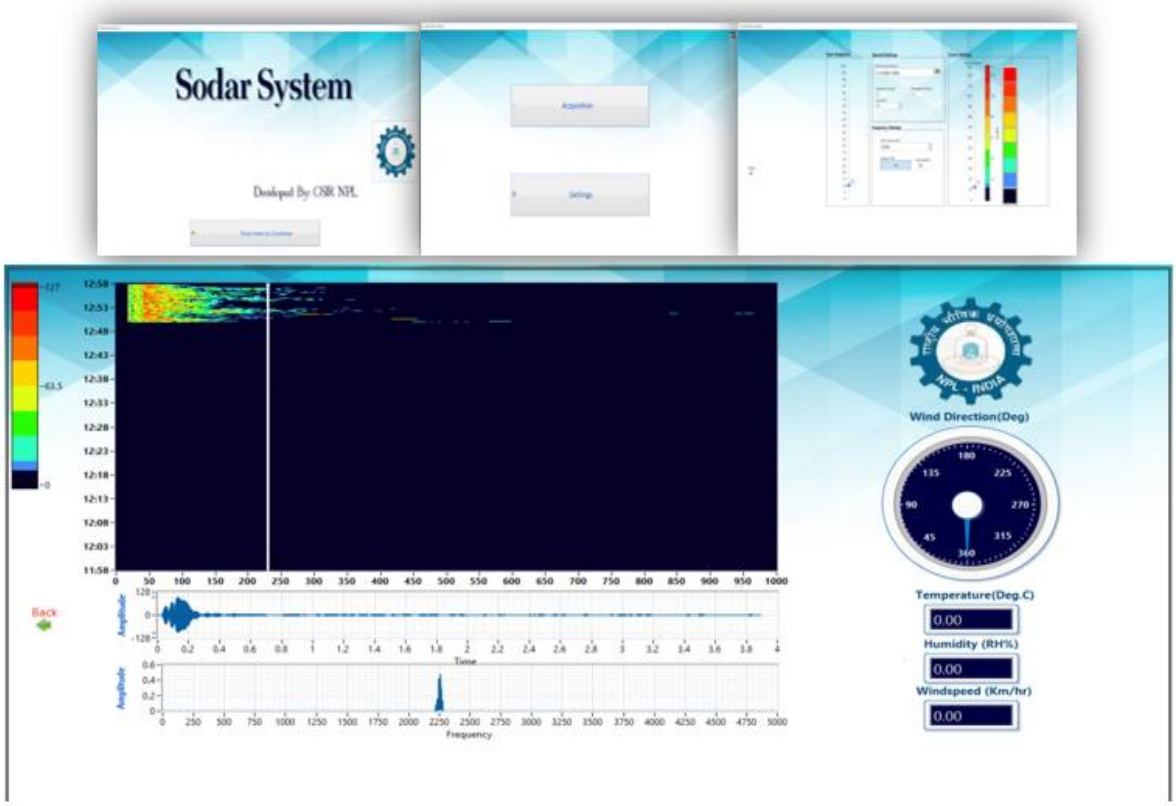

Figure 3.5. SODAR online software

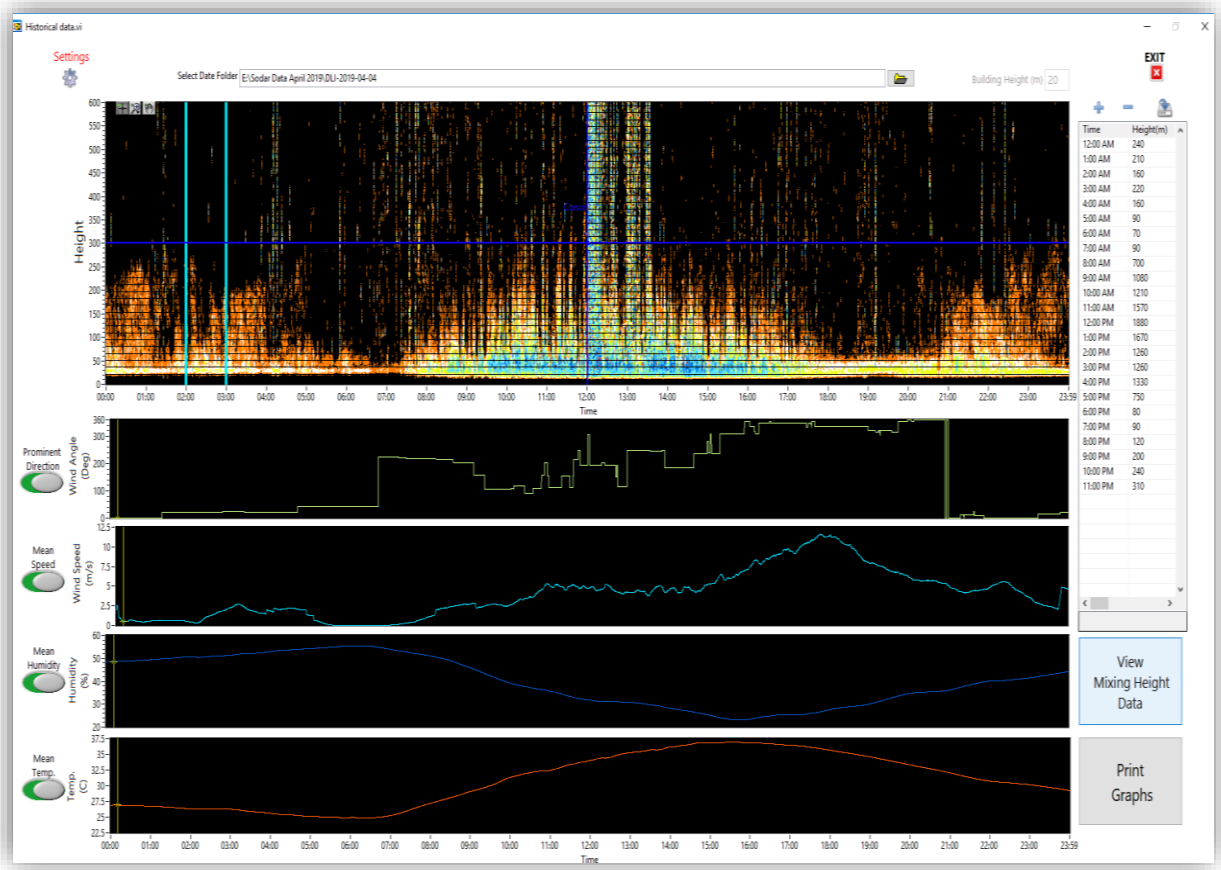

Figure 3.6. SODAR offline software

3.3.4. Frequency analysis

The SODAR system is an excellent tool to study ABL and ABL structures. It has a limited range that depends on the acoustic frequency used and atmospheric attenuation [208]. The SODAR estimated atmospheric structure and height by measuring the total acoustic energy scattered by the atmosphere. The transducer transmitting and receiving efficiencies measured the return power, which were an essential role in operating the SODAR system [18]. Apart from all other factors, the known ambient noise was a part of functioning the SODAR. The background noise at the antenna site was a major factor in the operation of SODAR and measures were taken to reduce the acoustics noise. Enclosing the antenna with an acoustic baffle was reduced the effective noise considerably. The choice of a narrow bandwidth receiver was further curtailing the noise and improved the signal to noise ratio.

The ratio of received signal power to received acoustic noise power (SNR) [3] was written as

$$SNR = A\frac{f_T^{1/3}e^{-2\propto z}}{f_T^{-q}} = Af_T^{q+1/3}e^{-2bf_T^2z} \tag{3.6}$$

So

$$\frac{dSNR}{df_T} = A\left[\frac{q+1/3}{f_T} - 4bzf_T\right]f_T^q e^{-2bf_T^2z} \tag{3.7}$$

and the optimal f_T for a fixed range z is

$$f_T = \sqrt{\frac{q+1/3}{4bz}} \tag{3.8}$$

where, A is amplitude, b is proportionality between absorption coefficient and f_T^2, f_T is transmitting frequency, q is atmospheric constant, and z is estimated height.

Bradley [3] calculated, the slope of the background noise spectrum for the daytime city is about $q = 2.8$ (taken from ISO standard) so for a range of $z = 1000\ m$, given $b = 0.003/10\log_{10} e = 7\ x\ 10^{-1}$ m^{-1}, the optimum $f_T = 1\ kHz$. In practice this is a little pessimistic, since good signal processing can extend the optimum frequency by about a factor of *2*.

The other parameter determining the successful operation of the SODAR was the choice of the operating frequency. The fraction of the incident power was scattered or reflected a strong function of frequency, scattering angle, and type of scattering targets. The increase in frequency was given to increase backscatter power, low noise level, and improve antenna gain but increased attenuation also [124-136]. Background noise depended on the power of f_T and absorption depending on the exponential of frequency-dependent absorption times range, a compromise was made while selecting the optimum frequency. So, the measurement of the

ambient sound pressure level was essential before installation of the SODAR system and was lower than *40 dBA*. The primary data of sound pressure level at octave frequencies were collected at the upper roof of the building. This site was chosen simply for convenience and available standard protocol. The operating frequency of the SODAR system was selected based on frequency response. Table 3.1 shows that a frequency range of *2000 - 2500 Hz* with a noise level of less than *40 dBA* were chosen. SODAR has selected a working frequency of *2250 Hz*, which yields good results.

Table 3.1. Frequency response of measured site

Frequency	Response (dB)
100	54.2
125	52
160	52.4
200	48.9
250	47.3
315	45.8
400	48.1
500	47.3
630	47.3
800	46.7
1000	44.9
1250	45.8
1600	39.4
2000	38.2
2500	37.9
3150	40.8
4000	40.6
5000	33.8

There were no obstacles in the vicinity of the SODAR system for transmitting and reflecting sound waves (buildings, reflecting surfaces, *etc*.). Fixed echoes or passive noise must be avoided when was installed SODAR.

3.4. Design Consideration of Monostatic SODAR System

Based on the foregoing considerations, the backscattering monostatic SODAR system was conceived and developed [56, 58, 151, 209]. Fig. 3.7. shows a schematic block diagram for the monostatic SODAR. The technique was used by transmitting a pulsed narrow sound beam into the atmosphere, where air inhomogeneity was contacted and partially reflected. It

received dispensed signals from the same transducer. With each echo scan, the time of delay and intensity were measured as intensity module on the PC, with visually displayed in either operational mode the height range (ordinate) versus the time (abscissa). The two main kinds of acoustic echoes seen in echograms were inversion echoes and thermal echoes. Thermal echoes appeared as vertical intermitted spikes, whereas inversion echoes were horizontal and continuous in time. An acoustic wave propagating through a turbulent medium getting scattered, refracted, and attenuated. The basic data was acquired through the monostatic SODAR system. The operation parameters are shown in Table 3.2.

Table 3.2 Specifications of monostatic SODAR system

Transmitted power (electrical)	90 Watts
Transmitted power (acoustical)	15 Watts
Pulse width	100 ms
Pulse repetition period	4 sec
Operational range	700 m
Receiver bandwidth	100 Hz
Frequency of operation	2250 Hz
Acoustic velocity	340 m/s (average)
Receiver Gain	66 dB
transmit-receive antenna	Parabolic reflector dish
Receiver area	2.5 sq. m
Preamplifier sensitivity	60 µV (theoretical Calculation)

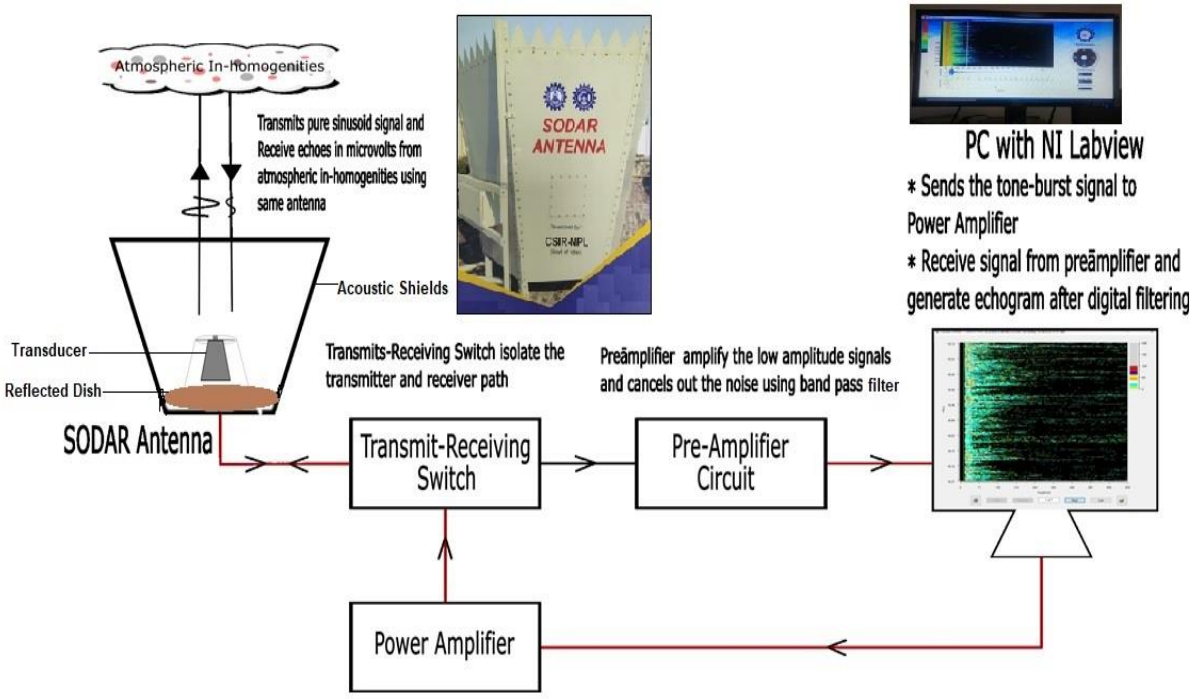

Figure 3.7. Block diagram of SODAR system

3.5. Study Location and its Meteorological Condition

The Capital Region of India, *i.e.*, Delhi (*28.70° N, 77.10° E*) in the homogeneous urban area is placed near the bank of the river Yamuna at *715 feet* above sea level [210]. It occupies a special position in the form of a gateway between the Thar desert to its southwest, Aravalli range in Northeast - Southwest Direction, and the Himalayas which lie to its north. Fig. 3.8 shows the climate of Delhi is mainly influenced by its remote inland position and prevalence air of continental character. Extreme dryness with intense summer and cold winter is the usual features of the climate of Delhi. This is modified by the air from the easterly or south-easterly direction and is responsible for the decrease in temperature, increase in humidity, cloudiness, and precipitation for some time of the year. The wind is an important climate feature for Delhi. The wind is moderate for most of the year. In June it is strongest and in November it is the lightest. During the summer months, hot and dust-living winds can lead to storms and storms. During the year, from September to May the prevailing wind direction to the north-west was dominated by the easterly monsoon component. In summer, the temperature increases gradually to 46^0 *C*, and in winter, to 2^0 *C* [211]. The meteorological and concentrations of pollutants data were taken from the Central Pollution Control Board (CPCB) *www.cpcb.nic.in*.

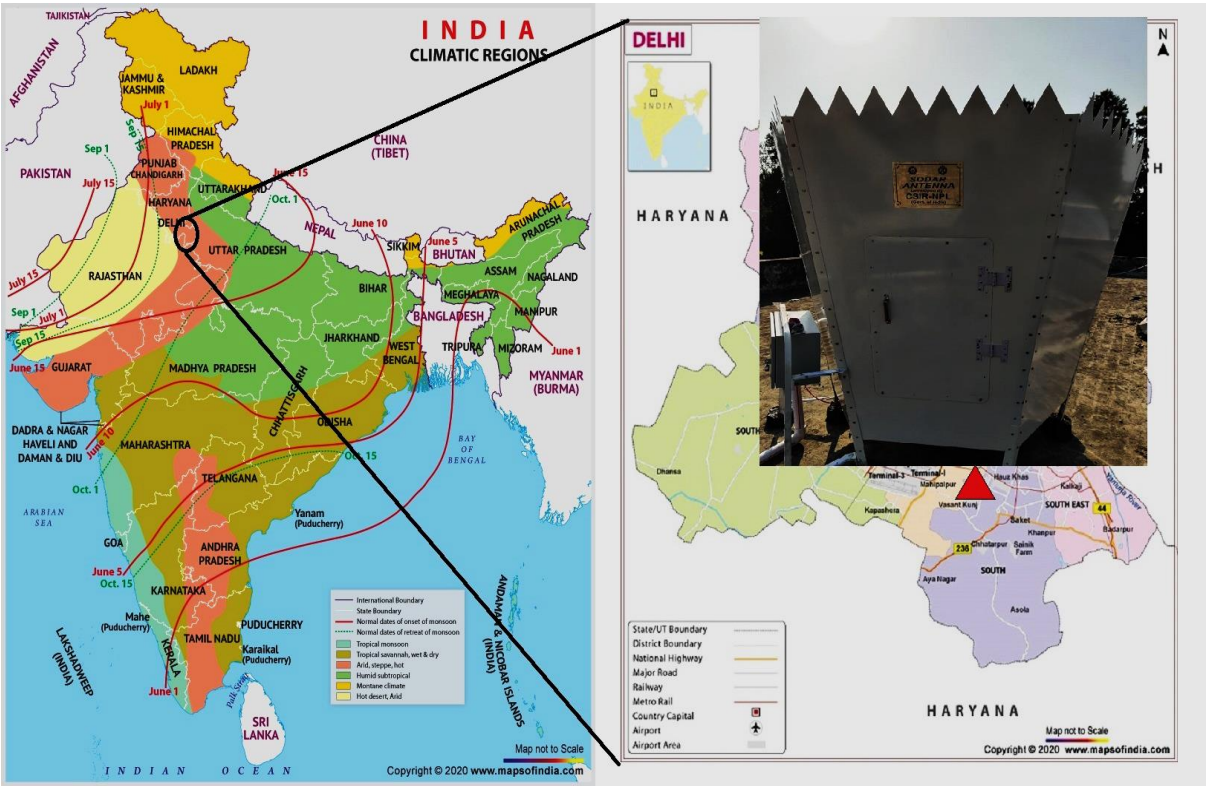

Figure 3.8. Monsoon map of India and installed SODAR system at Delhi
(Courtesy: www.mapindia.com)

3.6. Method of Determining ABL Height using SODAR Echogram

The SODAR is a cost-effective remote sensing system that uses sound waves. It allows *24*x*7* monitoring. This is a simple working principle. A SODAR emits sound pulses at various heights of the atmosphere and receives back dispersed pulse in temperature inhomogeneities. SODAR echograms provide lower climate turbulence pictures as well as contaminant distribution responsibilities. Based on the vertical profile of the acoustic refractive index shown in Fig. 3.9, the echogram, atmospheric conditions can be divided into two categories: convective period and non-convective(stable) period (output of SODAR). Bradley [3], Beyrich [27], and Singal et al. [111] have compiled methods and algorithms for calculating the ABL height using SODAR data. Being based on sonic principles, the range of SODARs is limited to a few hundred meters extending a maximum up to *1000 m* based on the power and frequency of the emitted pulse. The observer needs to broadly classify the data into two categories namely: inversion-time and convection-time. The other classifications of ABL structure are fog-layer, rising-layer, multi-layer, *etc*. and each classified structure demands a different approach for the ABL height estimation. The details of structures are mentioned in chapter 5. The ABL height has been directly picked up from the echogram by using visualization, apart from the convection period. During the convection period, when thermal plumes can be seen on the echogram, which gave an underestimated value unless. They were covered by a low-level elevated shear echo layer [2-3, 212]. So, the actual ABL height can be determined by using an empirical formula [212].

$$y = 4.24x + 95 \tag{3.9}$$

where y is the calculated ABL height and x is the observed thermal plumes height in the echogram. This formula was determined by comparing Sodar data with Radiosonde data [228].

Fig. 3.9. shows the stable and unstable conditions for the atmosphere on the echogram. These conditions were the manifestation of thermal inhomogeneities within the lower atmosphere caused by diverse meteorological phenomena.

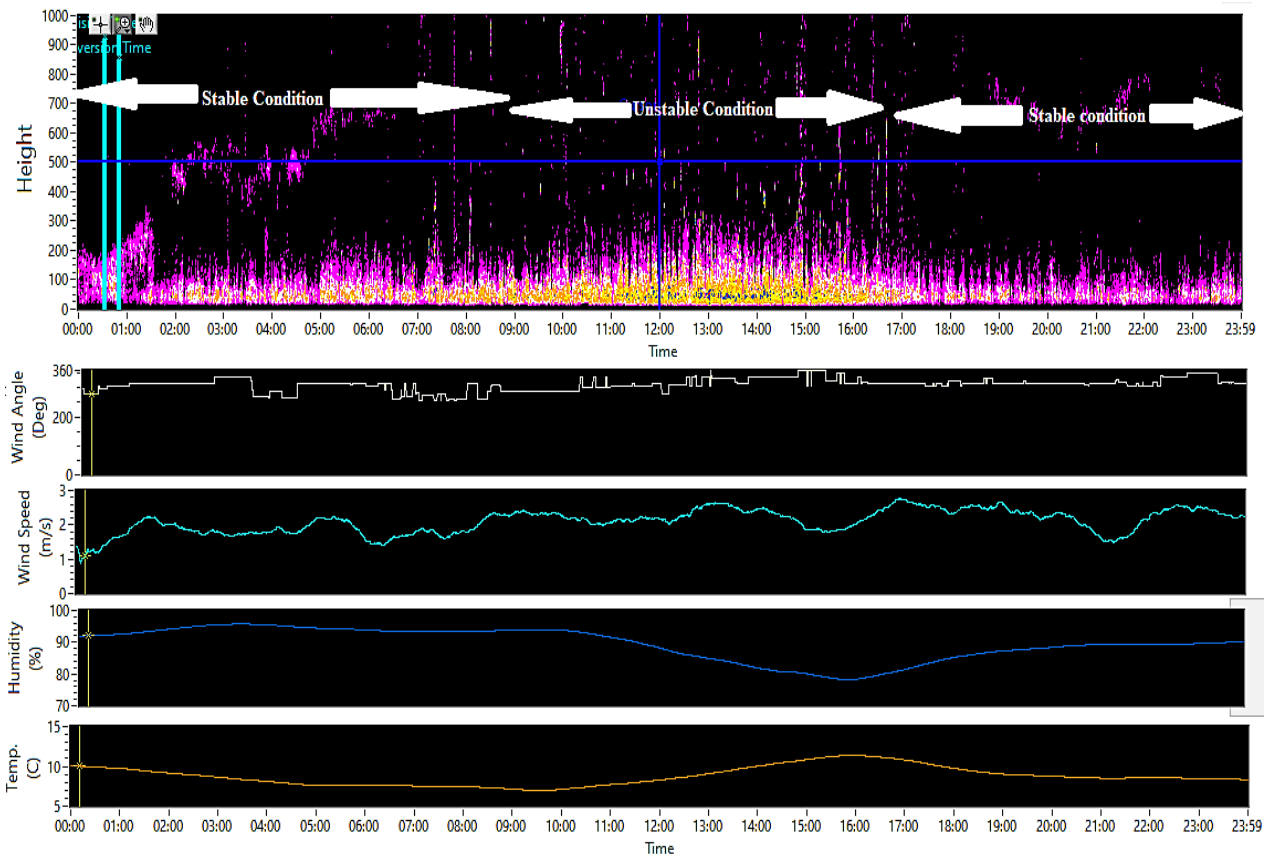

Figure 3.9. Stability conditions observation at Delhi

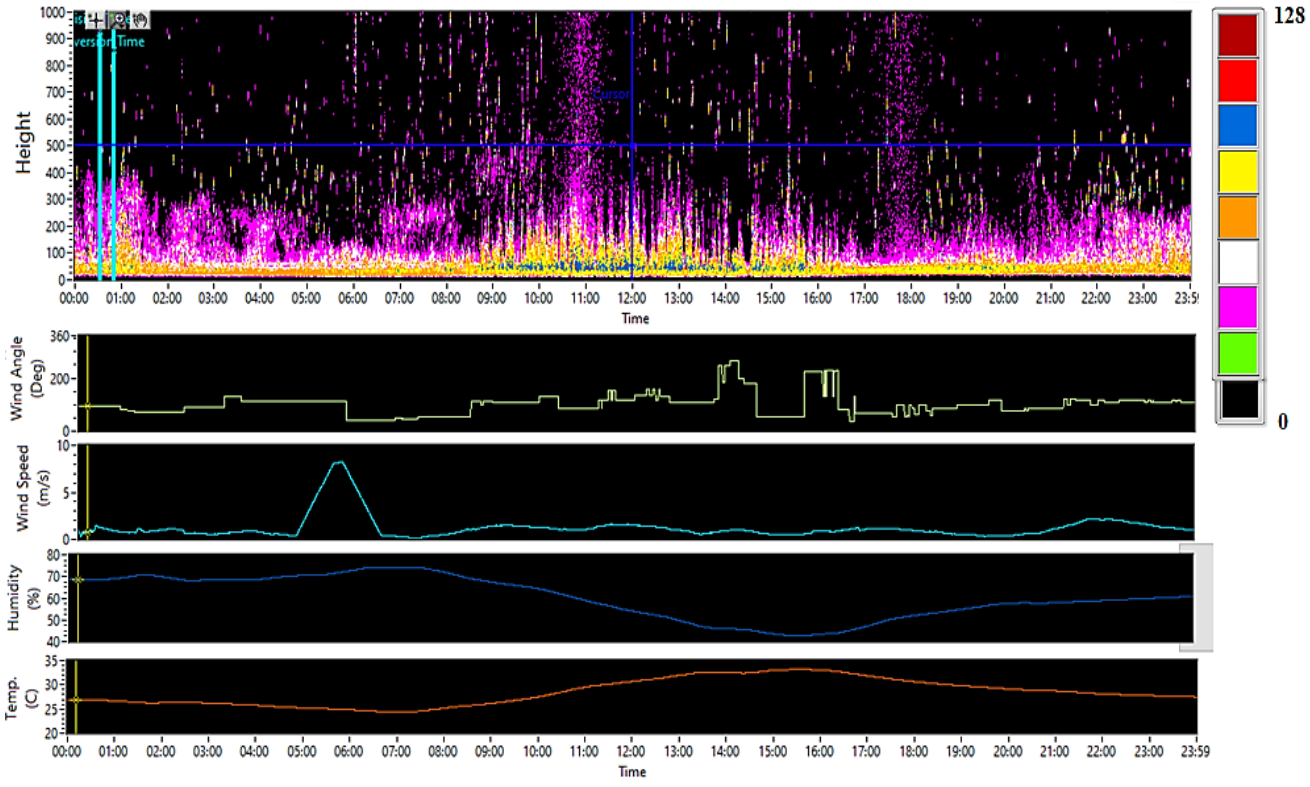

Figure 3.10. SODAR echogram observation at Delhi

Monostatic SODAR has operated in Delhi for a few months, during the day and at night, under different atmospheric conditions. It is seen that stable and unstable conditions can be easily determined and classified on the echograms, together with various types of perturbations and Kelvin-Helmholtz blows. The echograms have studied details with the application of software resolution. These structures are caused by various meteorological phenomena and are the appearance of thermal inhomogeneities within the low atmosphere. The diurnal variation and varied architectures of the ABL with variations in wind direction, wind speed, relative humidity, and temperature are shown in Fig. 3.10. SODAR echogram for the *17th October 2019*, from *0000 - 2359 IST*. The principal regime is a "classical" twenty-four-hour pattern with two transition phases of around *0700 – 1000 IST* and *1600 – 1800 IST*, alternating between stable (inversion in the evening and night, *1900 – 0900 IST*) and unstable (convection in the daytime, *0900 – 1700 IST*) stratification. Local circulation is unclear in this case; the wind pattern is described as a land breeze with a direction of *150 - 250 degrees*. Temperature and relative humidity diurnal patterns are typical of fair-weather circumstances. Wind speed increases monotonously with elevation in the inversion layer, reaching an extreme at the top of the inversion layer. Due to the disintegration of the stratified echo layer, the wind speed and direction change between *0430 - 0630 IST*. The ABL varied constantly throughout the day, as evidenced by these structures.

SODAR is a remote acoustic sensor system for ABL research. SODAR system is provided the result in real-time and spatial echograms and this echogram pictorial view of ABL dynamics. These are used to infer the weather conditions of ABL by visually examining and analysing Delhi's particular air pollution characteristics. The systematic development and improvement of the monostatic SODAR system with vertical points have been described. This development affects the data that have been observed and data will be more accurate with calibration and testing of equipment and material. The most important needs in any SODAR system are a transmission system to illuminate the highly directed signal in the turbulent area and a sensitive receiving signal to detect an air-scattered signal from the air.

Chapter 4
Design of Acoustic Antenna

This chapter details the acoustic antenna's design. The first section describes the details of the acoustic parabolic dish; the second section describes the aluminium composite plate and its acoustic features and the third section describes the construction of acoustic blasts. Parabolic acoustic dish, the calibration, and testing used for the monostatic SODAR were described in section 4.1. Sections 4.2 and 4.3 of the design and development of acoustic distortions were presented in the following section of the chapter.

4.1. Parabolic Acoustics Dish

A method using a theoretical antenna directivity pattern, together with measurements of transduction characteristics of the acoustic transducer was used for SODAR Antenna calibration. Theoretically (eq. 4.1) and experimentally determined directivities of the acoustic transducer, one from Russian Academy of Science, Moscow (LATAN-1) and other from CSIR- NPL, New Delhi have been compared. The output efficiency, the input efficiency and the directivity distribution for the transducer-horn assembly belonging to the LATAN-1 and CSIR - NPL SODAR were measured at working frequencies of *2·0 KHz* and *2·2 KHz* respectively in the anechoic chambers of the respective laboratories. The theoretical behaviour of directivity distribution was also computed and the two directivity behaviours were plotted. It may be seen from Fig. 4.1. that the two theoretical and experimental curves coincide rather satisfactorily within *20 %* of their values within the angles at which the paraboloids of the two SODARs are seen from their respective foci. With a view to illustrating the values of correction, the measured and corrected data were represented for the CSIR-NPL SODAR transducer in Table 4.1 [136].

Table 4.1. Measured and corrected data *for* directivity determination of the NPL SODAR source

Measured angle θ_m	0^0	10^0	20^0	30^0	40^0	50^0	60^0	70^0
Distance d from horn aperture to microphone (m)	0.80	0.80	0.81	0.83	0.86	0.88	0.92	0.95
Distance variation correction 20log(d/0.8)	0	0	0.1	0.32	0.65	0.87	1.30	1.65
Real angle θ_h	0^0	12.5^0	25^0	37^0	48^0	60^0	70^0	78^0
Measured level, dB	0	-0.3	-1.8	-4.0	-6.5	-10.5	-12.5	-16.0

$$D_h(\theta_h) = \frac{1+\cos(\theta_h)}{kR_h \sin(\theta_h)} J_1(kR_h \sin(\theta_h)) \quad (4.1)$$

where J_1 is the Bessel function, and R_h is horn aperture

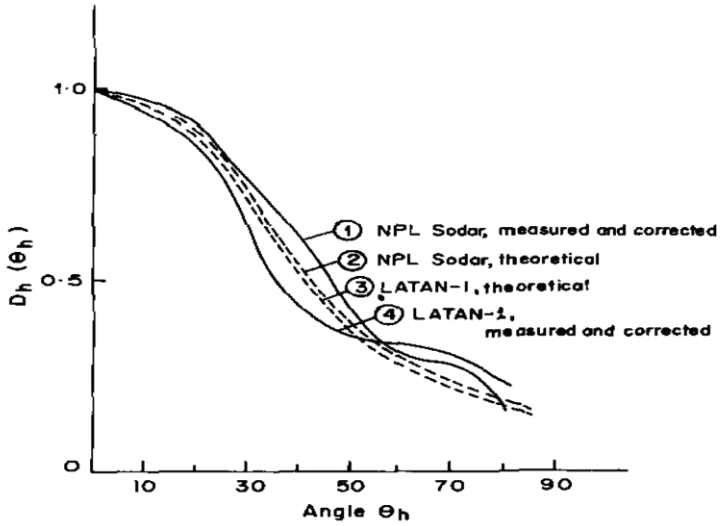

Figure 4.1. The comparison of the theoretical and the real directivity diagrams of loudspeaker units with horns [136]

Danilov *et al.* [136] computed the directivity behaviour, for the sodar LATAN-1 an exponential horn was used with $R_h = 0.085$ m which at a working frequency of 2 kHz gives $kR_h = 3.14$**.** The horn used for the NPL sodar is also exponential and has $R_h = 0.075$ *m*, which at a working frequency of *2.2 kHz* gives $kR_h = 3.04$**.** The angles at which the apertures of the reflecting paraboloids are seen from their respective foci are 61^0 for LATAN-1 and 67.5^0 for the NPL SODAR.

It may be noted that the output efficiencies and the parameters, kR_h and b, for the two sodars are more or less the same. It may also be noted that the numerical coefficient in eq. 4.2.:

$$K = 25\pi b^4 (kR)^2 (kR_b)^{-4} \quad (4.2)$$

is constant for a given device. For LATAN-I it has been computed and found to be $K = 10.7$.

The acoustic dish was designed and fabricated to study the lower atmosphere. The fibre parabolic dish was designed with an aperture diameter of *1.2 m*, depth of dish *0.22 m* for the acoustic antenna. A commercial driver unit *(60 watts RMS/90 watts maximum)* was fitted with a fibre exponential horn on a tripod stand at the focus of the dish with a height of *0.60 m* from its apex. Fig. 4.2 shows the whole combined dish, horn, and driver unit. The directional response of this antenna system at frequencies of *1000 Hz, 2000 Hz,* and *2500 Hz* was provided in Fig. 4.3 It represented that the ninety-degree side lobe suppression is around *15 dB, 20 dB, and 25 dB at 1000 Hz, 2000 Hz,* and *2500 Hz* respectively. The main lobe was a width of ± 12^0 at *1000 Hz*. The maximum impulse output was measured without the dish *110*

dB for an input of *60 W*, and with the dish, it increased to *136 dB* at *1000 Hz* using a standard sound source. The receiving sensitivity of the system was *12.5 mv/µbar* under free field conditions.

The characteristics of the parabolic dish shown in a receiving transducer with a *B&K* pre-polarized free-field ½" microphone *type 4189* of open-circuit sensitivity *-26.9 dB (1V/Pa)* with *0.2 dB* uncertainty (*95 % confidence level*) fixed at its focus. It was observed that the gain in the received signal due to the paraboloid reflecting surface is of the order of *25 dB* (approximate). The received signal was reduced by *10 dB* in case the sounding source moves by an angle of ± 20^0 on either side of the axial line of the paraboloid surface and *25 dB* side-lobe rejections at 90^0. Calculations were made [3] to determine the receiving and transmitting power efficiencies of the antenna transducer. It was found that receiving and transmitting efficiencies were determined as *21.3%* and *29%*, respectively.

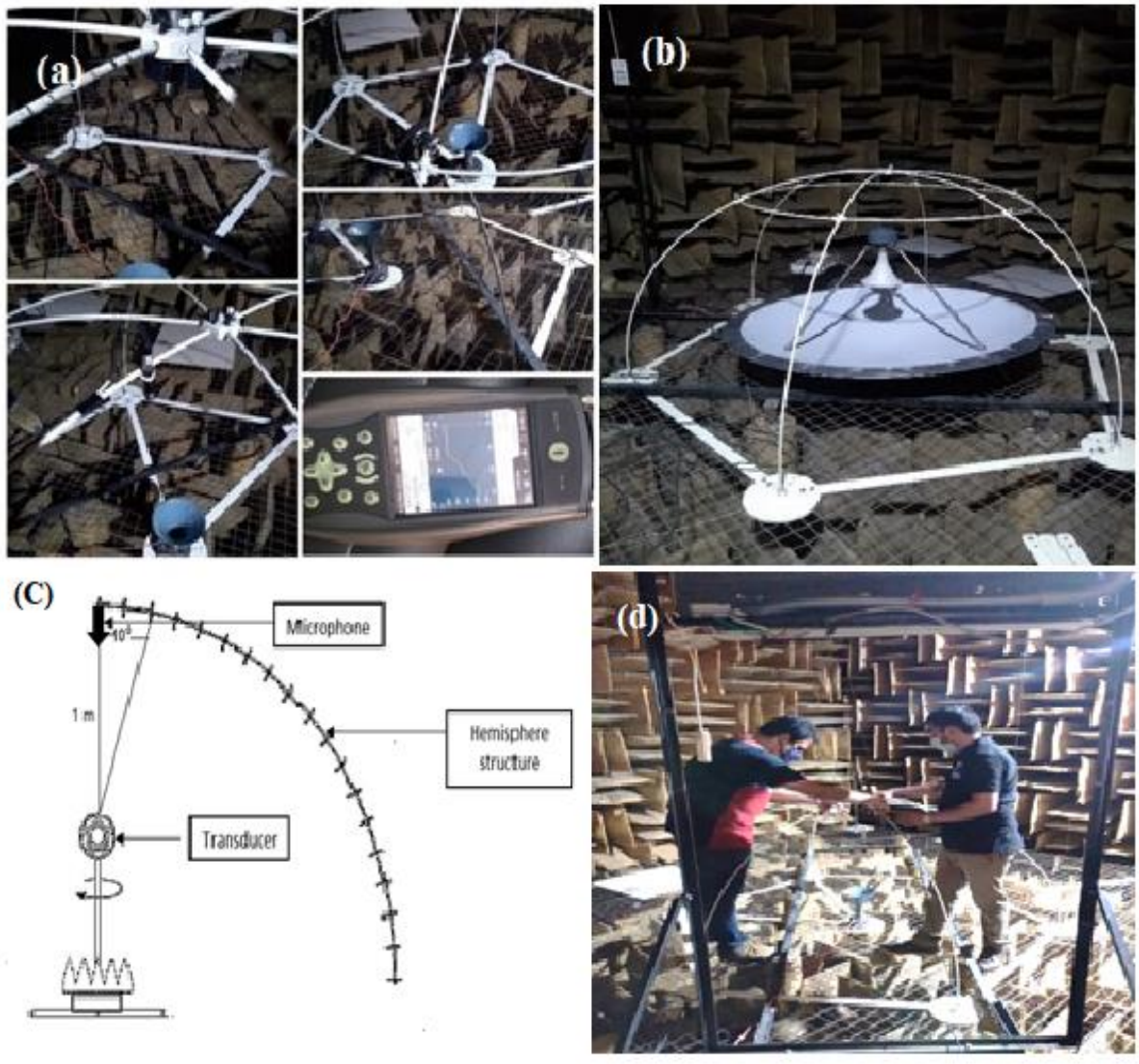

Figure 4.2. Transducer testing in anechoic chamber

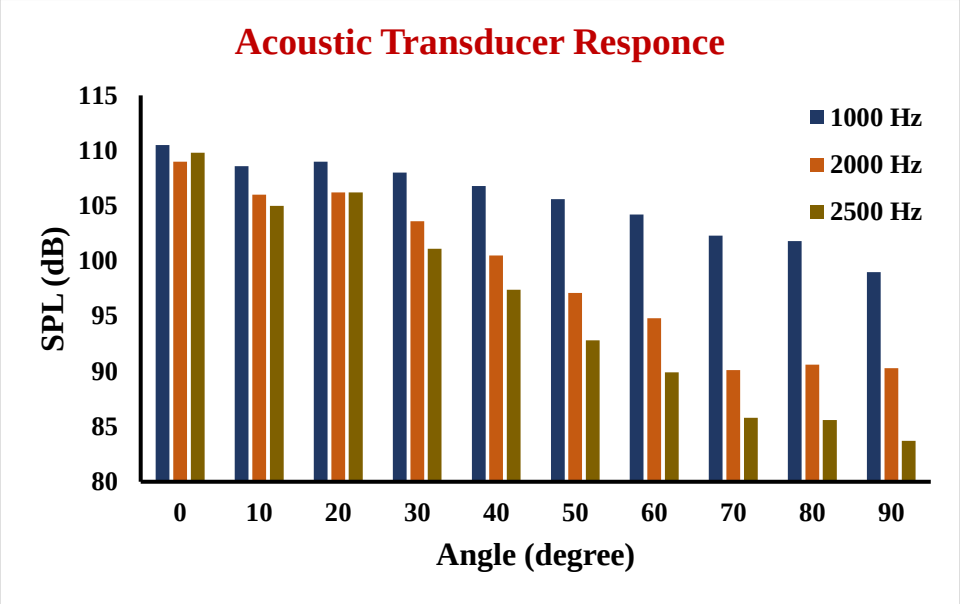

Figure 4.3. Transducer response in transmitting mode

4.2. Aluminium Composite Panel and their Acoustical Characteristics

The Aluminium Composite Panel (ACP) was a sandwich panel made up of two aluminium sheets connected to a core [213]. A low-density core was put between two rather thin skin layers of aluminium in Fig. 4.4. To display fire-retardant qualities, the core was generally made of polyethene (PE) or polyurethane (PU), or a combination of low-density polyethene and mineral material [214]. With this sandwich configuration, high mechanical performance was achieved while reducing weight. For all this type of panel, external cladding or façades, isolation, and board markings were common. It offers flexibility, low weight, and easy to form and manufacture qualities, which make new designs more rigid and durable. It also offered low cost, long life, and efficiency.

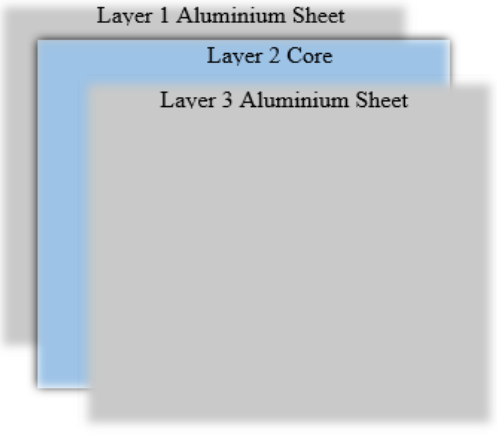

Figure 4.4. Aluminium composite panel

Two types of testing were performed for the selection of acoustic antenna baffles material, *i.e.*, sound transmission loss and sound absorption. During its first phase of the study, several types of ACP sheets in the reverberation chamber for the frequency range between *100* and *4000 Hz* were examined for their sound transmission loss properties. Sound transmission loss (eq. 4.3) was calculated for several ACP sheets by the Sound Transmission Coefficient (STC). STC [127] was a way for evaluating different wall, ceiling, floor, door, and window assemblies. It was calculated using transmission loss values measured at *16* standard frequencies ranging from *125 to 4000 Hz*. The sound transmission loss of sound-insulating material was determined in the laboratory by measuring the one-third octave band levels L_s and L_r at the source and receiver chambers, as well as the reverberation time T of the latter.

$$L = L_s - L_r + 10 \ln \frac{T*A}{0.161*V} \tag{4.3}$$

where, L is sound transmission loss *(dB)*, A is the area of the sample *(m^2)*, V is a volume of the receiver chamber *(m^3)*.

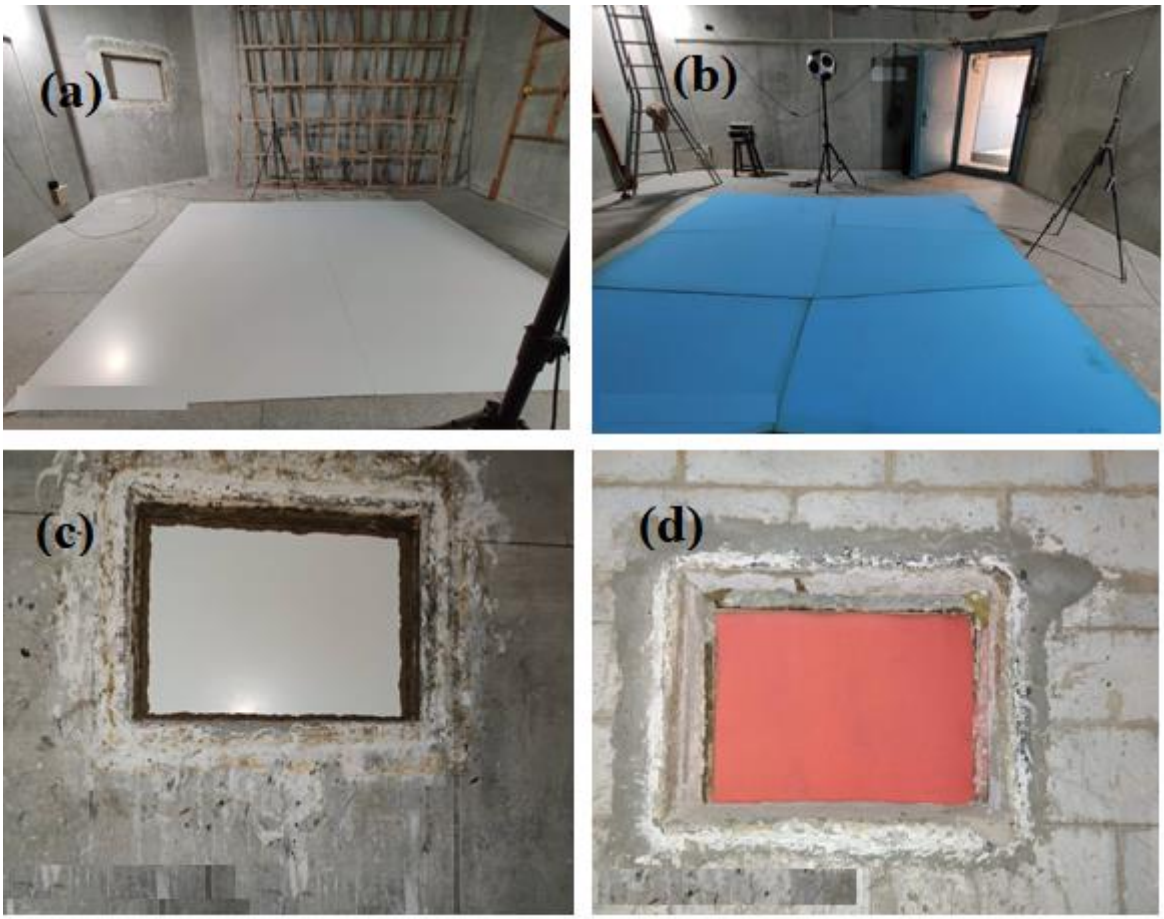

Figure 4.5. Testing in a reverberation chamber (a) NRC testing of ACP sheet, (b) NRC testing of combined ACP sheet and acoustic foam, (c) STC testing of ACP Sheet, and (d) STC testing of acoustic foam

To calculate STC (Fig.4.5), the sample size is *0.63 x 0.93 x 0.002* m^3, with a working standard microphone (associated uncertainty ± *0.2 dB*, traceable to national standards). As per requirement [127-133], the acoustical material was tested for its airborne sound insulation by using two reverberation chambers under existing environmental conditions. The sample was fixed in the standard opening window between the two chambers. The volume of the source room was *257* m^3, and that of the receiving room was *271* m^3. Adequate diffusion was excited in both chambers. The airborne sound insulation index was calculated by measuring the average sound pressure levels created in the source and receiver rooms using filtered noise in the *1/3 – octave band*, as shown in Table 4.2. The measured uncertainty was *1.0 dB*, which translates to a coverage probability of about *95%* for a normal distribution with a coverage factor of *2*.

Table 4.2. Transmission loss (Frequency response) of ACP sheet

Frequency	L_s	L_r	STL	
100	99.3	73.5	13	
125	104.4	78.1	15	
160	107.2	74.6	19	
200	107.4	74.2	20	
250	105.3	70.9	20	
315	103.6	65.7	24	
400	104.4	63.6	28	
500	103.4	57.8	33	
630	102.2	53.9	35	
800	101.3	49.3	39	
1000	99.7	46.9	40	
1250	100.8	44.5	43	
1600	101.3	42.5	45	
2000	99.2	37.5	47	
2500	100.1	35.6	50	
3150	96.6	30.3	51	
4000	94.2	28.6	50	

STC = 34

The sound absorption properties of the panel and acoustic foam were tested according to requirements in the second step. Noise Reduction Coefficient (NRC) was computed for the sound-absorbent medium (acoustic foam) using a specified ACP sheet for sound absorption (eq. 4.4). The NRC was a scalar representation of how much sound energy was absorbed when it hits a specific surface. Perfect reflection was indicated by an *NRC of 0*; great absorption was indicated by an *NRC of 1*. The absorption coefficients for a certain material and mounting situation were computed (eq. 4.5) for the one-octave band centre frequencies of *250, 500, 1000, and 2000 Hz* using the arithmetic average. In the reverberation rooms of

competent acoustical laboratory test facilities, absorption coefficients were employed to calculate NRC. The sound absorption of sound-absorbing materials was tested in the laboratory using one-octave band levels.

$$Sound\ Absorption, \alpha = \frac{55.3*V}{s*(331+0.6*t)}\left[\frac{1}{T_s} - \frac{1}{T_e}\right] \quad (4.4)$$

where V is the volume of the room (m^3), s is test sample area (m^2), t is Temperature of Room (^0C), T_s is Reverberation time with Sample (s), T_e is Reverberation Time without Sample *i.e.,* Empty Room (s),

$$NRC = \frac{\alpha_{250}+\alpha_{500}+\alpha_{1000}+\alpha_{2000}}{4} \quad (4.5)$$

To test the NRC (Fig. 4.5), acoustical material was tested in the reverberation chamber under existing environmental conditions [127-133]. The sample was fixed on the surface of the chamber with a rigid backing to get an exposed sample area of *12 m^2* and the chamber's volume was *257 m^3*. A loudspeaker with uniform spherical radiation was used as the source of sound suspended at a height of *2.5 m* above the floor in one corner and the microphone was kept at different locations near the other corners of the chamber at least *1 m* away from any surface. The measurements were made by using *1/3-octave bands* of random noise and several decay rates were measured. The sound absorption coefficient was calculated as shown in Table 4.3. The estimated measurement uncertainty was *5%*, which corresponds to a coverage probability of about 95% for a normal distribution with a coverage factor of *2*.

Table 4.3: Absorption of ACP sheet with acoustic foam

Frequency	T_e	T_s	Absorption	
100	7.2	4.47	0.32	
125	7.52	4.75	0.29	
160	7.78	3.41	0.63	
200	7.21	2.74	0.86	
250	6.17	2.48	0.92	
315	5.77	2.17	1.09	
400	5.88	2.2	1.08	
500	6.00	2.27	1.04	
630	6.04	2.24	1.07	
800	5.52	2.28	0.98	
1000	5.37	2.26	0.97	
1250	4.7	2.12	0.98	
1600	4.4	2.04	1.00	
2000	3.96	1.93	1.01	
2500	3.54	1.81	1.02	
3150	3.05	1.63	1.08	
4000	2.6	1.51	1.05	

NRC = 0.98

The NRC was used to grade acoustic ceilings for their overall acoustic qualities, banners, screens, and acoustic wall panels. Normally higher STC and NRC were preferable, although this was not always the case with a low-frequency problem. The material was used mostly at a higher frequency and the use of high STC and NRC values was necessary.

Table 4.4 shows STC and NRC of four different company's ACP sheets vary from *31- 34* and *0.04-0.07*, respectively. When the combination of ACP sheet and acoustic foam was tested for *STC (34)* and *NRC (0.98)*, it was found that by adding acoustic foam STC of the ACP sheet didn't change but NRC was improving. This combination was suitable for the SODAR antenna baffle.

Table 4.4. Different ACP sheet STC and NRC

Sample No.	STC	NRC
ACP 1	31	0.04
ACP 2	34	0.04
ACP 3	31	0.07
ACP 4	32	0.05
ACP 2 + Acoustic Foam	34	0.98

4.3. Design of Acoustic Baffles

The SODAR system was classified into three categories based on antenna design: monostatic, bistatic, and tri-axis [1-2]. For the reduction of atmospheric noise, all types of antennas required acoustic baffles or shields around the antenna [3-4]. Reflections of the sound pulse from non-atmospheric substances ("fixed echoes" or "clutter") and environmental noise from vehicles, birds, construction, animals, and other sources that reach the SODAR antenna were principal non-random noise sources for a SODAR. The noise sources were greatly reduced by installing an acoustic baffle to the SODAR dish and transducer. It is fascinating to consider how low the sound intensity should reflect a perfect mirror to ensure that the turbulence signal does not interfere. It did not prove useful, even though commercial SODARs were provided with no acoustic baffle. The baffle should be designed to absorb noise (at a minimum absorption/transmission of *30dB*) rather than soften it [26, 28]. The optimal baffle material should provide a non-reflective, absorbing, and non-transmitting shield [3]. The most frequent materials were fibreglass or marine plywood with acoustic foam on the interior. Some acoustic barriers were a thin lead sheet bonded to the fibreglass or wood base. This type of construction was usually enough to keep any major sound energy out of the acoustic baffle walls.

The SODAR dish's acoustic baffle was a hexagonal or cylindrical frustum [3]. Maximum baffles were straight edges, unlike some previous SODARs that featured horn-shaped baffles

with the highest softened away from the SODAR perpendicular axis. The employment of horns to send a few small speaker drivers into the environment was most likely the basis for this design. The application varied from speaker horns in that the scales were much greater than a wavelength and there was no acoustic impedance matching [7]. In monostatic SODAR, the acoustic baffle must have a larger range of departure to accommodate slanted beams that do not cross the baffle borders excessively. The topmost rim of the baffle was the nearby field of the SODAR beam. On the other hand, complete estimations were proven that far-field predictions were typically enough to improve a design [29]. The real issue with recording appropriate data at a lower altitude was the antenna and baffle shielding which can "ring" for a long period after the transmit pulse. It's not just the time it took for the sound to travel along with the baffle and back to the speakers, *e.g*, a typical speed in a complex wooden baffle might be around *103 m.s*$^{-1}$, but for a length of *2 m*, this would only give an arrival time of *4* x *10*$^{-3}$ *s* [2], which was the best configuration's attempt to dampen any reverberations. It was achieved with "soft" substances for the acoustic baffle. Furthermore, reverberation issues were likely to cause data from the previous *6 - 10* x *10*$^{-3}$ *s* to be skewed [15].

A hexagonal frustum shape baffle with *1.98 m* high walls and a *2.13 m* diameter was erected around the horn reflector antenna. Each plank of the hexagon used a plain ACP sheet (*1.21* x *2.13 m*^{2}) on the outer side and the inner side fixed with acoustic foam (density *40 kg m*$^{-3}$; thickness *0.10 m*). A hexagonal-shaped structure with its wall sloping slightly outwards (angle of the slope *9*^{0} with the vertical) was constructed to work as a baffle. The horn reflector antenna was placed at the centre of this baffle. It was an inside base diameter of *1.53 m* to fit the antenna and a *2.13 m* diameter at the top. The height of assembly was determined by the size of panels and the slope by diameter on the parabolic dish, which was *1.28 m*. However, it was found that this baffle was very useful and hardly raised any ringing effects. Fig. 4.6. shows the testing of acoustic baffles with a dish in the reverberation chamber. The whole combined system was tested in the reverberation chamber, and the noise level was found to be reduced by *32±2 dB*. The baffle was tested in an open atmosphere. In comparison to the measuring inside the baffle, an ambient noise level of *27±2 dB* was reduced.

Figure 4.6. SODAR baffle testing in a reverberation chamber

In the last 4 decades, monostatic SODAR was operating under varying atmospheric conditions for 24 hours [212-213], now a new SODAR system was developed using new acoustical baffles (with ACP sheet). Previously, it was found that SODAR operated on acoustic waves in the presence of high ambient noise from cars, birds, and other sources. This noise combined with poor SODAR signals created a major data processing issue. To insulate the antenna from ambient noise, effective acoustical fibre-based baffles (*STC - 35 with 13 mm* thickness) were traditionally utilised. Fibre-based baffles were bulky, less precise, heavier, more expensive, and so on. Nowadays, the SODAR antenna was installed on the building floor, therefore a lightweight acoustic baffle with high precision and cheaper were required. The ACP sheet-based baffles were more suited for the SODAR system. Its operation was carried out continuously for monitoring of ABL height with the new acoustical antenna.

The new design offered economic development of SODAR and a high-precision, lightweight acoustic baffle. In the reverberation chamber, acoustic characteristics (STC = 34 and NRC = 0.98) were calculated. The ACP foam sheet was the most appropriate acoustic baffles to design the acoustic antenna. Acoustic pressures of up to 138 dB can be radiated to a narrow atmospheric beam. The new acoustic disturbances remove the noise of 27±2 dB from open spaces. The merits of the new antenna are ideal for the mobile use of SODAR at various sites and field tests.

Chapter 5
Computational Techniques Based SODAR Structure Classification

The first part presents the SODAR image classification model using machine learning; the second part presents the results and model discussions. Section 5.1 describes the data collection, statistical extraction of features, selection methods of features, and classifiers for the structure classification model. Section 5.2 presents the results along with a discussion on the performance of the models.

5.1. SODAR Echograms Image Classification Model using Machine Learning

In Chapter 3, the presence of various structures, such as thermal plumes, inversion layers, gravity waves, fronts, etc., could be detected through a monostatic SODAR. These structures have been shown to have certain periodic variations with a particular phenomenon with each structure. Echogram obtained for 1 year to examine the various types of structure and associated phenomena from December 2013 to November 2014. It was systematically analysed in terms of their structural detail's diurnal and seasonal variations. The purpose of this section was to compare the different ABL structure recognition machine learning models using SODAR echograms and to remove noisy SODAR echograms data. The work involved algorithms that were based on fractal features, image processing, and pattern recognition techniques [214-215], or neural network-based real-time system classification was employed to classify SODAR structures [106]. Moreover, a wide range of machine-learning techniques was explored during the current work, based on their existence prediction for their predictive performance for the classification of the SODAR structure to define the various types of structures. This word helped to identify the appropriate machine learning algorithms for structural prediction studies based on SODAR echograms to enhance the cost and time efficiency of ABL studies.

5.1.1. Data collection and SODAR echogram

Five thousand eight hundred fifty (one-year dataset, the year *2014*) SODAR echograms were observed for various seasons and classified into different structures. Only clear structure echograms were considered for investigation (*1698 echograms*). They were divided into two classes, *i.e.,* convective boundary layer (basically present in the daytime) and stable boundary layer (mostly in the nighttime). Further, structures were divided into a different category (*12 Classes*) according to their structure and characteristics as shown in Table 5.1 [4, 35, 58, 106-110, 151, 214-216]. Fig. 5.1. shows a pie chart for different ABL structures under SODAR echograms.

Table 5.1. Description of SODAR structure and class numbers

Class	Description of SODAR Structure
1	Inversion with force convection
2	Inversion with a tall spike
3	Inversion with a single elevated layer
4	Inversion with two elevated layers
5	Inversion with wave motion
6	Inversion with one or two elevated layers in motion
7	Inversion with a small spike
8	Stratified layer
9	Diffuse thermal plumes
10	Thermal plumes with normal days
11	Thermal plumes with a foggy layer
12	Transition structure

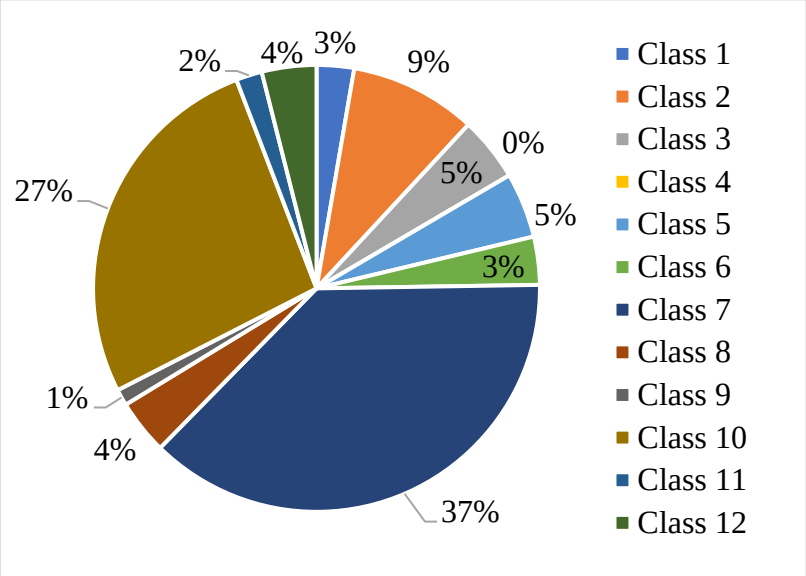

Figure 5.1. Percentage distribution of SODAR echograms into 12 classes

To study the relative occurrence for their distribution observations is provided in Fig. 5.1. It shows that in many ways these structures existed. Structures of investment seem to dominate other structures. 66% of the total time followed by convective feathers occurred 34% of the time. Further analysis of the structure of the layer shows that the structure is stable most of the time (55 %).

A unique convection layer structure or thermal plumes emphasised the unstable daytime conditions that change their form after the evening begins. [1, 158]. The plumes started forming early in the morning when the surface inversion dissipated. With more and more heat input to the ground, the intensity of the phenomena increased and was reflected on the SODAR echograms in the form of taller plumes. The height of plumes and the amount of

dispersion depended on the different weather conditions. The nature of the inversion layer in the night depends on the daytime rising layer and convection height [217].

The thermal plumes with the high spikes shown during the day are shown in Fig. 5.2 (a), The high temperatures (or solar radiation) in May were more common as high solar radiation revealed the height of thermal plumes in these structures (470-625 m). In this period, ABL height was increased because dispersion areas of pollutants were more [111, 146]. As a result, this condition was more favourable for the industry and human beings due to the high dispersion of pollutants [151]. Fig. 5.2. (b-d) displayed the thermal plume with spikes (less than *400 m*) which was observed during the daytime of the winter season and these types of structures were observed in December and January.

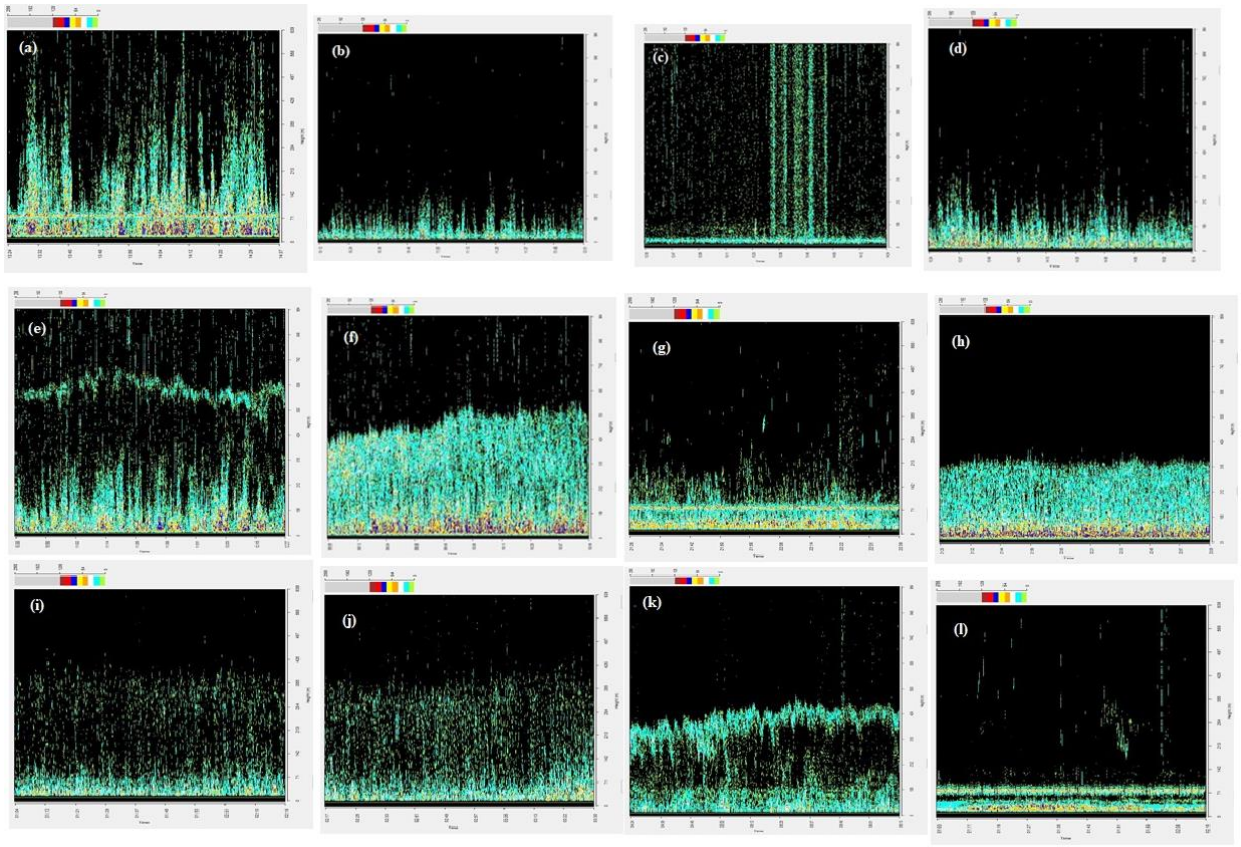

Figure 5.2. Different structure of ABL (a) Thermal plume long; (b) Thermal plume during Rainy Day; (c) Thermal plume during Before Rainy Day; (d) Thermal plume during winter; (e) Thermal plume with Foggy; (f) Rising layer during Winter Season; (g) Inversion with long Spikes; (h) Winter Inversion; (i) Inversion with one or two elevated layers in motion; (j) Inversion with wave motion; (k) Inversion with Fog; (l) Multilayer

A characteristic feature in the night-time stable conditions was the inversion layer structure. The morning after sunrise, it disintegrated due to the solar heating of the soil, and the

temperature profile was altered. After sunrise, the time needs to be split from day to day and season, depending on the cloud cover, the strength of the night-time inversion, the flow of the sun, and the high structure and fog layers. Fig. 5.2. (e-l) displayed the multilayer and inversion structures observed during the nighttime. Fig. 5.2. (g, l) commonly observed in May, due to more variation in temperature, wind speed, wind direction, and relative humidity [158]. This was a stable class and unfavourable condition for the industry and human beings [151]. The height of the inversion layer was generally in the range of *100-500 m*.

Fig. 5.2. (j) shows another wave structure of ABL, which was found and grouped specifically on the SODAR echograms. They were observed in the April, May, and June months, *i.e.*, in the pre-monsoon season. This kind of structure was essential to move waves and shapes because of the high wind speed and the change in direction [1].

The structure of the inversion layer was characterised by nighttime conditions stable, which spread after sunrise in the morning, and the temperature profile changes shape. The dispersion and formation of the rising layer depend on inversion height and structure. The night-time inversion showed its essence as the rising layer ranged to the most extreme height, which subsequently disappeared. The structure of this type was not seen daily in the morning, and the inversion layer changes to the structure of the feather. Also, during rainy spells and cloudy days, the inversion layer didn't change the rising layer, resulting in less rising layer formation in the monsoon season.

The image classification model of SODAR echograms was used for removing suitable features from different ABL structure types to extract the selected characteristics. For echograms in the current work image classification, the following measures were taken (Fig. 5.3.)

5.1.2. Statistical features extraction

In the investigation of different structures of ABL, a total of 133 SODAR structural properties were calculated. These features were divided into three groups: vertical direction, vertical transition calculation, and horizontal direction calculation [110]. The mean, maximum, and standard deviation from the SODAR echograms are included in those feature sets. Echogram's intensity-based features estimated the statistics of the intensity graph, whereas shape features (Table 5.2.) described the structure of the ABL [107, 109]. Considering a SODAR echograms image segment of size *640* x *560*, MATLAB 2017a was used for image analysis. SODAR structure features were automatically extracted by

developing structure image analysis software and MATLAB for the pre-processing of ABL images [108-109].

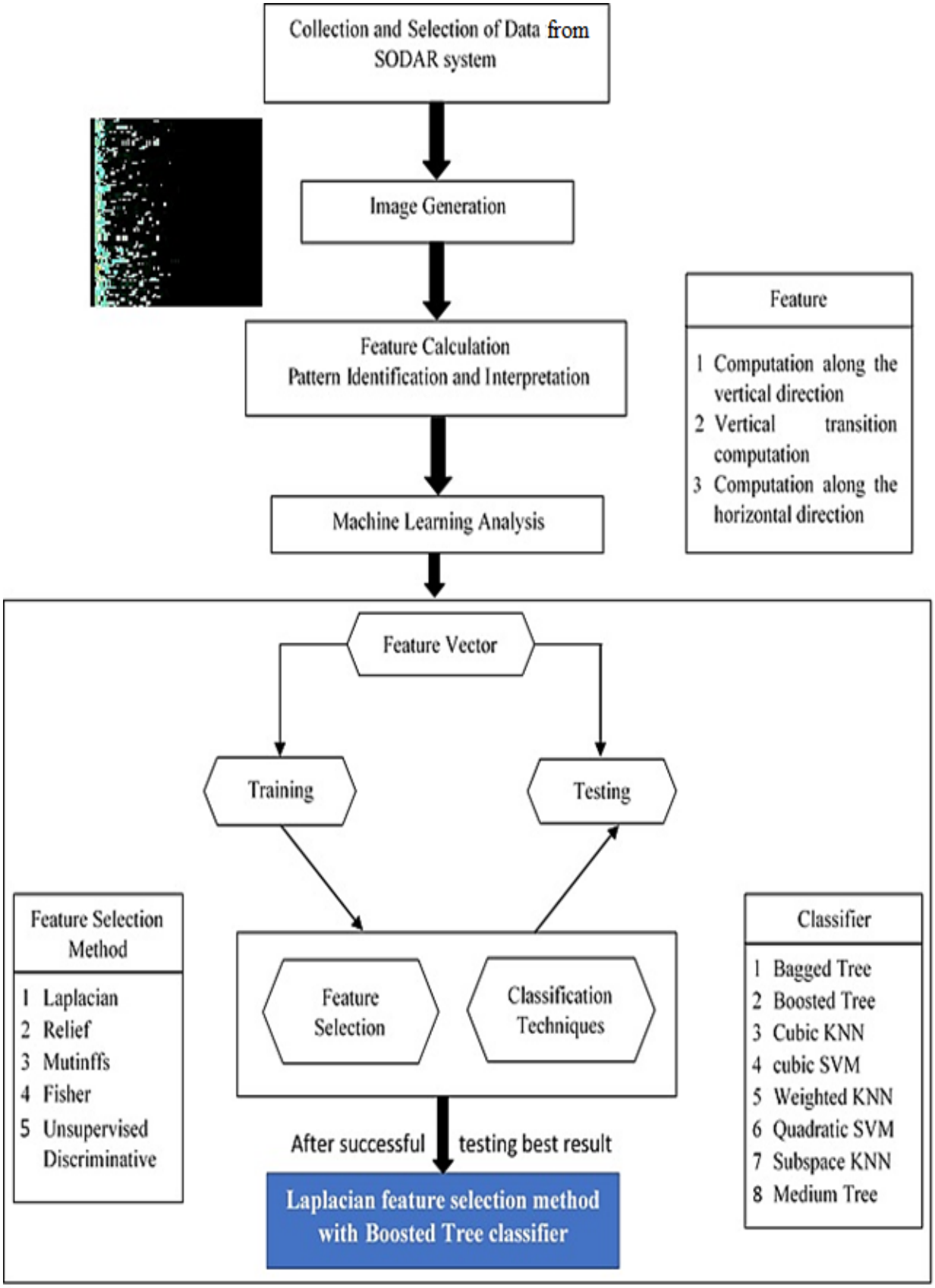

Figure 5.3. General flow chart of SODAR echogram-based classification model

Table 5.2. Statistical feature formula

Feature	Formula
Feature computation along a vertical direction	The average of the i^{th} row, $y_i = \frac{1}{640}\sum_{j=1}^{640} a_{ij}$ $i = 1,2, \ldots\ldots\ldots 550$ $mean, y_{mean} = \frac{1}{550}\sum_{i=1}^{550} y_i$ $Vertical\ maximum, y_{max} = Max_{i=1}^{550}\{y_i\}$ $\sigma_{ver} = \sqrt{\frac{1}{550}\sum_{i=1}^{640}(y_i - y_{mean})^2}$ k_{th} vertical average, $y_{avg_k} = \frac{1}{50}\sum_{i=1+50(k+1)}^{50k} y_i$ for k=1, 2, ……..,11
Vertical transition computation of r (in percentage)	$y_r = \sum_{i=1}^{10} h_i^{(r)}\left(1 - h_{i+1}^{(r)}\right) + \sum_{i=11}^{2} h_i^{(r)}\left(1 - h_{i-1}^{(r)}\right)$ $h_i^{(r)} = \begin{Bmatrix} 1, y_{avg} \geq \frac{r}{100} * y_{max} \\ 0, \quad otherwise \end{Bmatrix}$
Feature computation along a horizontal direction	The average of the j[th] column, $x_i = \frac{1}{550}\sum_{j=1}^{550} a_{ij}$ $j = 1,2, \ldots\ldots\ldots 640$ $mean, x_{mean} = \frac{1}{640}\sum_{i=1}^{640} x_i$ $Horizontal\ maximum, x_{max} = Max_{i=1}^{640}\{x_i\}$ $\sigma_{hor} = \sqrt{\frac{1}{640}\sum_{i=1}^{550}(x_i - x_{mean})^2}$ k_{th} horizontal average, $x_{avg_k} = \frac{1}{50}\sum_{i=1+50(k+1)}^{50k} x_i$ for k=1, 2, ……..,13

5.1.3. Feature selection methods

The analysis was carried out using five feature selection approaches, *i.e.*, Laplacian, Relief, Mutinffs, Fisher, and Unsupervised Discriminative feature selection (UDFS) [218-219]. These methods score the features using a scoring criterion, were chosen because of their prevalence in the literature, simplicity, and computing efficiency [220-221].

5.1.4. Classifiers

The classification was viewed as a supervised learning challenge of inferring a function from labelled training data in machine learning [218]. The classification algorithm (classifier) examined the training data and derives a hypothesis (function) that was used to predict the labels of yet-to-be-observed observations [222]. Machine learning classifiers utilised in this study include Bagged Tree, Boosted Tree, Cubic KNN (K-Nearest Neighbours), Cubic SVM (Support Vector Machine), Weighted KNN, Quadratic SVM, Subspace KNN, and Medium Tree [222-224]. The classification learner app in MATLAB 2017 was used to implement all of the classifiers, as it provided a great interface for accessing several machine-learning methods [224-225]. The repeated 10 folds cross-validation methodology was used to train, test, and validate classifiers. Percentage recognition scores were compared and evaluated to study and evaluate alternative feature selection and categorization approaches.

5.2. Results and Discussions

SODAR was utilised successfully for microclimate research and a comprehensive approach to the weather classification of contaminants concentration in the main metropolis. Convection and inversion heights were significant indicators for controlling and predicting air pollution [4]. The code for the SODAR echogram provides a wonderful possibility of gaining climate data and an image of the geographical distribution of ABL characteristics in real-time. Many research has been undertaken to predict ABL and categorization of structure [107, 109]. It was critical to assess and compare alternative feature selection approaches for classification analysis to successfully implement ABL prediction analysis based on the SODAR echogram. Five feature selection and eight classification methods were used. To minimise over-fitting, these strategies were chosen based on prior studies [109-110, 214-215, 218, 220-221, 224, 226-231].

For identifying the different forms of SODAR echograms, Chandara *et al.* [109] used a neural network design that combined multilayer perceptron and graph matching techniques. Choudhury and Mitra [106, 108] described a multilayer perceptron-based model for classifying various SODAR signals. This reduced the dependence on human professionals in the identifiable proof procedure. A new classifier was presented to compare classifiers from the same family while other classifier families were missing [222]. The proposed classifier will be favoured if the new classifier is used to compare different families and developed using simple tools for a limited parameter with a reference classifier. All (eight) of the classification were classified with the classification application (MATLAB 2018 Classifier

Learner App). The classifier parameter has been selected from the literature. Furthermore, the parameters of this study have only been changed by ten cross-validations of training data. The work has been developed to test several classifications and selections of features for the SODAR echogram.

To examine machine learning methodologies for SODAR echogram and to find out the distinct structures existing in the ABL, a total of *133* statistical features were derived from a distinct structure of the pre-treatment SODAR echogram images of the Delhi region. SODAR echogram pictures were used for feature selection, classification training, and testing (*10 - cross-validation*). The classification accuracies were used to evaluate the predicted performance of various feature selection and classification approaches.

Table 5.3. Classifier accuracy (in Percentage %)

		Bagged Tree	Boosted Tree	Cubic KNN	Cubic SVM	Weighted KNN	Quadratic SVM	Subspace KNN	Medium Tree
SODAR Structure Class Numbers	1	47.82	54.34	33.3	21	22.22	33.33	26.67	44.44
	2	49.35	66.02	36.53	46	33.97	67.3	39.74	37.17
	3	46.83	44.3	40.5	31	27.84	40.5	34.17	50.63
	5	43.75	51.25	23.75	38	28.75	30	28.75	42.5
	6	25	38.95	35.59	35	35.59	42.37	20.33	35.59
	7	32.91	84	45.61	68.96	77.27	76.33	61.28	77.42
	8	42.64	44.11	44.77	26.87	32.83	34.32	32.83	46.26
	9	50	25	25	25	35	25	40	40
	10	67.54	80.57	57.39	46.13	56.29	64.01	42.16	76.37
	11	40.62	37.5	25	21.87	21.87	37.5	34.37	40.62
	12	41.79	46.26	32.83	29.98	38.8	44.77	17.91	46.26
Over All		44.38	52.02	36.38	35.43	37.31	45.03	34.38	48.84

Table 5.3 showed the accuracy of the grading for the eight classifiers. In the overall boosted tree classification, the higher detection percentage (accuracy) was 52,02%. However, the accuracy of each classification ranged from 20% to 85%. In the increased tree classification, the results showed the highest prediction performance. Improved tree classification methods have been assessed for the prediction performance of several feature selection strategies.

The performance of feature selection and the boosted tree classification approach utilised *5, 10, 20, 30, and 50* features, which were the top-ranked features as a consequence of feature selection, is shown in Tables 5.4, 5.5, 5.6, and 5.7. Because the Mutinffs and Fisher procedures produced identical results, only the Fisher method was displayed above. With 30 (thirty) features, the Laplacian feature selection approach was the best predictive performance (*61.15 %*), while the UDFS approach was the least predictive performance (*46.04 %*).

Table 5.4. Classifier accuracy with Fisher selection method (In %)

		Number of features				
		5	10	20	30	50
SODAR Structure Class Numbers	1	62.22	66.66	51.11	44.44	42.64
	2	58.33	58.33	60.89	58.97	54.82
	3	49.36	45.56	48.1	44.3	43.1
	5	38.75	43.75	38.75	42.5	36.5
	6	35.59	38.98	50.84	44.06	40.1
	7	83.07	83.38	91.69	83.07	80.45
	8	43.28	34.32	47.76	38.8	36.67
	9	45	50	50	50	50
	10	78.14	83.88	84.54	84.32	81.78
	11	56.25	62.5	53.12	62.5	60.32
	12	44.77	55.22	44.77	49.25	45.2
Over all		54.06	56.59	56.50	54.74	54.74

Table 5.5. Classifier accuracy with Laplacian selection method (in %)

		Number of features				
		5	10	20	30	50
SODAR Structure Class Numbers	1	66.67	48.87	64.44	66.67	55.55
	2	57.68	64.1	60.89	60.89	62.17
	3	48.1	53.16	45.56	50.63	54.43
	5	37.5	48.75	51.25	48.75	43.75
	6	38.98	50.84	50.84	59.32	50.84
	7	88.08	88.08	89.96	87.46	85.1
	8	44.78	59.7	49.25	59.7	44.78
	9	50	50	50	50	50
	10	86.31	86.75	87.19	87.19	80.13
	11	31.25	59.37	59.37	46.87	34.37
	12	44.78	52.23	52.23	55.22	49.25
Overall		54.01	60.16	60.08	61.15	55.48

Table 5.6. Classifier accuracy with relief selection method (in %)

		Number of features				
		5	10	20	30	50
SODAR Structure Class Numbers	1	43.47	55.55	48.89	54.34	43.47
	2	58.33	58.97	63.46	62.82	58.97
	3	48.1	44.3	45.56	46.83	45.56
	5	50	45	48.75	45	46.25
	6	50.84	49.15	52.54	42.37	35.59
	7	85.57	88.08	88.75	82.75	80.4
	8	52.23	56.71	47.76	40.29	31.34
	9	40	45	50	50	40
	10	83.44	84.98	86.31	83.88	76.37
	11	62.5	62.5	59.37	46.87	50
	12	52.23	41.79	56.71	52.23	40.29
Overall		56.97	57.45	58.91	55.21	49.84

Table 5.7. Classifier accuracy with UDFS selection method (in %)

		Number of features				
		5	10	20	30	50
SODAR Structure Class Numbers	1	43.47	54.34	47.82	43.47	36.95
	2	53.84	57.65	52.56	54.48	53.2
	3	50.63	37.97	50.63	44.3	48.1
	5	32.5	31.25	37.5	38.75	38.75
	6	35.59	32.2	30.5	32.2	37.28
	7	81.97	82.13	81.5	78.36	78.52
	8	31.34	44.77	43.28	46.26	44.77
	9	35	35	40	35	35
	10	75.93	76.82	79.24	74.39	77.48
	11	40.62	43.75	34.37	25	34.37
	12	35.82	37.31	37.31	34.32	35.82
Overall		46.97	48.47	48.61	46.04	47.29

The primary objective of experimenting with different approaches to select and classify features was to select the best method for selecting features and classifying them for the given data set. Based on the precision of each function selection method, the top 50 features were chosen. These functions are used for the preparation and prediction of classes with test data, as shown in Table 5.4, 5.5, 5.6, and 5.7. Accuracy was measured to assess the performance of the classifiers. The classifier performance was generalised with a 10-fold cross-validation methodology. Detailed feature selection comparisons and analysis (number of features five, ten, twenty, thirty, and fifty) revealed that the number of features increases above twenty, and therefore the model has taken a long time, giving less precision. This time was exponentially growing, which meant that the iteration had to be completed and a full model was executed. Accuracy and iteration time was critical metrics in the performance evaluation of each classification.

Table 5.8. Monthly predictive performance

		Months											
		January	February	March	April	May	June	July	August	September	October	November	December
SODAR Structure Class Numbers	1	62.5	33.33	NA	25	0	23	66.67	25	25	NA	33.33	0
	2	45.45	0	12.5	33.33	21.05	10.25	0	0	58.33	NA	40	51.72
	3	66.67	NA	50	NA	0	28.57	40	33.33	50	50	38.89	58.82
	5	50	38.46	NA	25	40.74	40	33.3	11.11	0	NA	33.33	33.33
	6	66.67	0	0	46.67	37.5	46.15	0	50	33.3	NA	33.33	57.14
	7	76.62	71.42	80.95	48.78	42.85	48.07	81.18	57.3	65.38	88.63	63.63	59.03
	8	40	40	50	37.5	33.33	50	40	40	33.33	NA	100	0
	9	33.33	50	50	NA	100	33.33	NA	0	0	NA	NA	NA
	10	45.16	39.02	20	72.97	71.25	53.12	73.43	66.19	50	78.26	55.55	66.67
	11	52.38	NA	NA	40	0	NA	NA	NA	0	NA	NA	55.55
	12	25.92	27.27	NA	NA	100	40	0	33.33	33.33	NA	0	33.33
Overall		51.34	33.28	37.64	41.16	40.61	37.25	37.17	31.63	31.7	72.3	44.23	41.559

Monthly predictive performance was calculated using 20 selected features, which are 20 top-ranked features after the best classifier and feature selection method was chosen. Table 5.8 represents monthly predictive performance. The month of October had the highest overall accuracy (72.29 %), while August had the lowest (31.62 %). The ability to identify and observed air structures formed by a SODAR system was entirely dependent on the system's knowledge, experience, and competence. The data collected by SODAR technology were useful to a selected group of individuals with previous field experience. Consequently, a computer-based SODAR identification system that includes human know-how and expertise requires the development of a suitable SODAR information utility and potential SODAR monitoring. An analysis and comparison of various classification approaches for effective implementation of functional classification analysis was a major goal of the analysis. The highest prediction presentation was obtained using the Laplacian approach for feature selection and a boosted tree classification with an overall performance of 61.15 % with 20 ABL structure classification features.

In this chapter, the techniques adopted provided an automated tool with machine learning techniques to access the various ABL structures. The boosted tree classifier method was the highest predictive performance in SODAR echogram / ABL structure identification, which is 52 percent of eight classifications (totaling 133 features) and the highest predictive exactness along with the Laplacian function selection method. The monthly prediction was used as the best predictive accuracy in October (72% with a total of 20 functions) and the lowest predictive accuracy in August (overall preformation 31 percent with 20 features).

Chapter 6
Temporal ABL Height Prediction using Deep Learning Model

This chapter discussed the LSTM prediction model for the future use of new SODAR data to reach the ABL height value. This work explores the seasonal and annual variations in the ABL height. The presented work then proposed the ABL height data neural network prediction model. For the ABL data height, the model was evaluated using the Delhi SODAR system. A time-series comparison of annual and seasonal changes in ABL height was also shown to measure model performance.

6.1. Data Collection and Deep Learning Model using SODAR Data

A New SODAR system was developed and installed in CSIR-NPL, New Delhi to study the ABL height. Based on the methodologies (section 3.6) to determine ABL height of stable and unstable conditions and collected hourly averaged SODAR data from *1st Dec 2018 – 29 Feb 2020*. In this study, the data set has a temporal value (*1 hour = one value*).

A Long Short-Term Memory (LSTM) network predicted the next moment state based on data from the previous moment state [174]. Fig. 6.1 shows, the hidden unit was the most significant difference between regular RNN and LSTM. Self-loops, which can be thought of as several copies of the same neural network, were the hidden layer of an LSTM network, and each neural network module transferred information to the next level. It also compensated for RNN's inability to predict long-distance collaborations [172]. It was used to tackle the time-series prediction problem because it was a well-known component of current deep learning research. One input layer, one output layer, and many intermediate layers, together known as the hidden layer, made a neural network [232]. The input of each subsequent hidden layer was made up of the output of the input layer appearances, the input of the first hidden layer, and the output of each hidden layer [213]. LSTM was a form of RNN in which the normally concealed layers were replaced by LSTM cells, which were made up of different gates that govern the input flow [166, 174]. An LSTM cell consisted of an input gate, a cell state (which flows across the entire network and can add or remove information using gates), a forget gate (which controls the level of cell state reset/forget), and an output gate (control level of cell state added to hidden state). Hochreiter and Schmidhuber [172] and Kawakami [173] had explained the architecture of the LSTM network in detail.

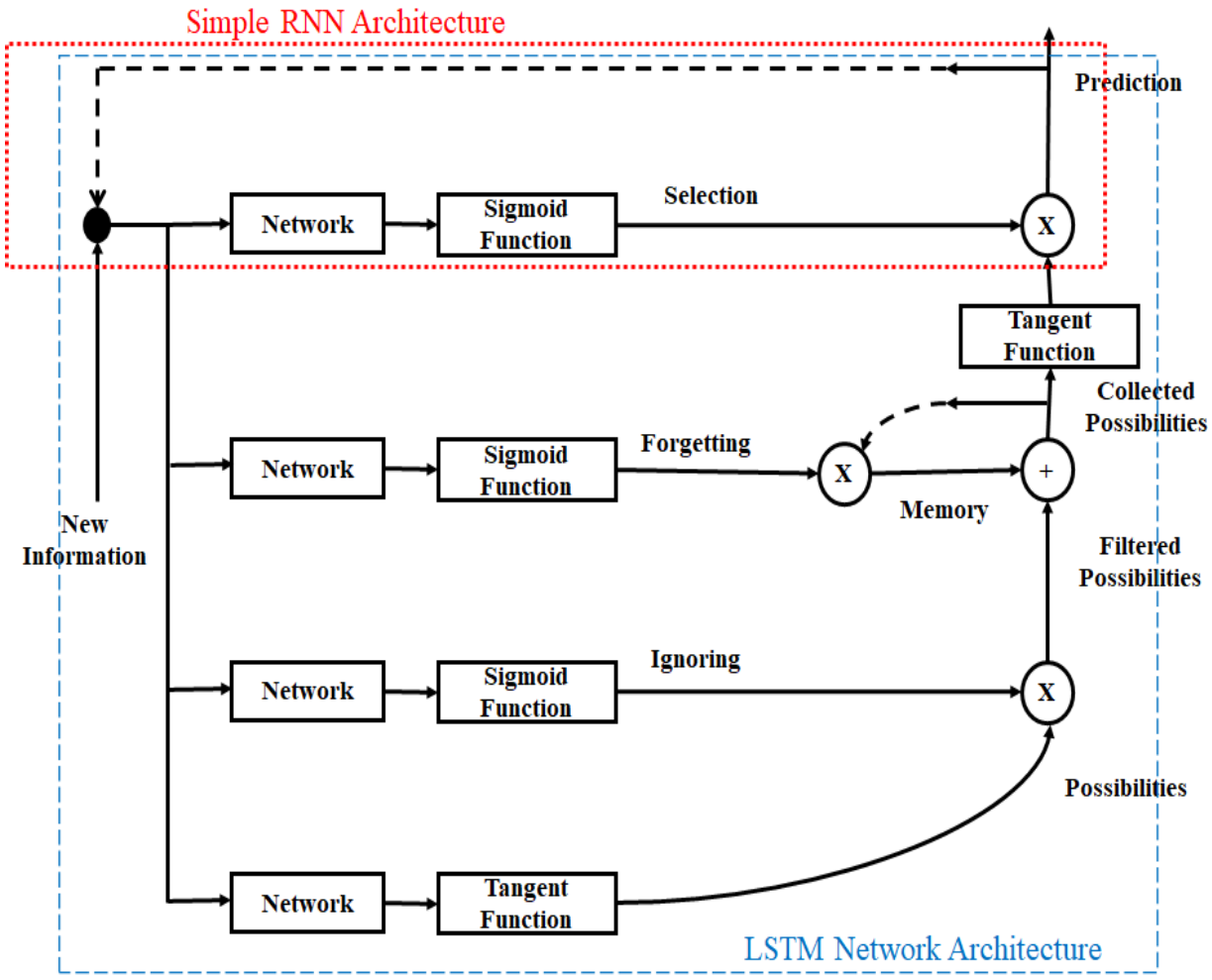

Figure 6.1. Network architecture

Figure 6.2 shows a block diagram of the ABL height LSTM network prediction model's development for training and testing. The LSTM prediction network could pass the ABL height characteristics indefinitely, *i.e.*, from one step to the next, and forecast the future point from the previous point. As a result, it was able to predict the height of the ABL over time. A series of temporal ABL heights recorded by the SODAR system served as the input data for the LSTM prediction model.

A set of ABL height temporal series was used as the input data for the ABL height prediction problem. As the series progresses, the hidden layer of the previous point will influence the hidden layer of the next point. This was particularly useful for the ABL height, which had a nonlinear link between the previous and following data. As a result, the LSTM network was trained using Back Propagation Through Time (BPTT) and configured as a sequence-to-sequence regression. The values changed with a particular time interval as time passed, and there was some periodic volatility. The LSTM neural network model was found to be suitable for the nonlinear parameter based on the preceding.

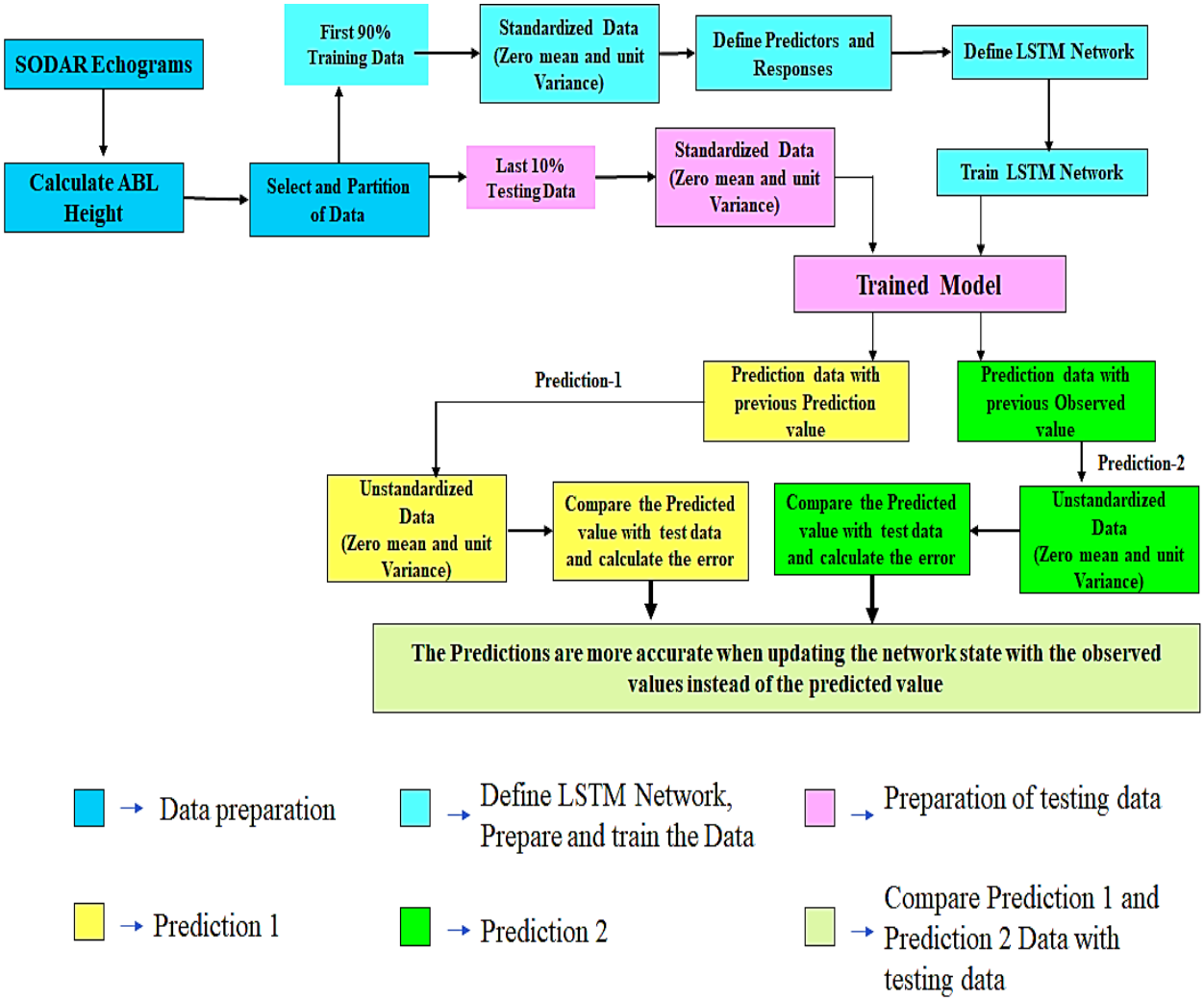

Figure 6.2. Block diagram of the LSTM ABL height model

The first 90% of the input data was chosen as the training set, and the last 10% was chosen as the test set, based on checking the pattern of convection and inversion period of ABL on a temporal basis, and the following functions were chosen as performance measures of the prediction model:

$$Root\ Mean\ Square\ Error, RMSE = \sqrt{\frac{1}{n}\sum_{i=1}^{n}(Predicated_i - Measured_i)^2} \quad (6.1)$$

$$Relative\ Root\ Mean\ Square\ Error, rRMSE = \sqrt{\frac{1}{n}\sum_{i=1}^{n}\left(\frac{Predicated_i - Measured_i}{Measured_i}\right)^2} \quad (6.2)$$

$$Mean\ Absolute\ Error, MAE = \frac{1}{n}\sum_{i=1}^{n}|Predicated_i - Measured_i| \quad (6.3)$$

$$Mean\ Absolute\ Percentage\ Error, MAPE = \frac{100}{n}\sum_{i=1}^{n}\left|\frac{Predicated_i - Measured_i}{Measured_i}\right| \quad (6.4)$$

In this research work, deep learning training was carried out using the pre-defined Deep Learning Models included in the MATLAB R2019a software's Deep Learning toolbox. These pre-defined networks were retrained and fine-tuned using expanded training and validation sets with SODAR ABL height data. For a better fit and to prevent training and testing from diverging, the data were standardised with zero mean and unit variance [233]. The "adam" function [234] was used to optimise the networks. The architectural parameters of the LSTM network are listed in Table 6.1.

Table 6.1. LSTM architecture parameters

Network Parameters	Value
Gradient Decay Factor	0.9
Squared Gradient Decay Factor	0.9990
Initial Learn Rate	0.005
Learn rate schedule	Piecewise
Learn rate drop factor	0.20
Learn rate drop period	125
Gradient Threshold Method	I2norm
Gradient Threshold	1
Verbose Frequency	50
Validation Frequency	50
Shuffle	once
Sequence Length	Longest
State Activation Function	tanh
Gate Activation Function	sigmoid
Input weight initializer	glorot
Recurrent weight learn initializer	orthogonal
Bias Initializer	Unit-forget-gate
Bias learns rate factor	1

* drop the learning rate after 125 epochs by a factor of 0.2

The performance of the prediction model was measured for the test set and used to calculate the RMSE, rRMSE, MAE, and MAPE. The calculated error was lower than what was needed to improve the accuracy of the prediction model [235].

The data set included approximately one year of data value. It cannot adjust the gradient and when the whole set of data was used at every training run the network cannot converge to optimum globally. The mini-batch sizes were chosen carefully to ensure that every training season the entire dataset was fed through the network without losing data. The experiment for ABL height prediction models was carried out using 3 months of data (1 April 2019 to 30 June 2019). The data available at the time was more dynamic and continuous. In addition, the greatest change in ABL height occurred in May. This work included two types of forecasts. Prediction-1 was used to update the network using previously predicted values as input to the function, and Prediction-2 was used to update the network using observed values rather than

anticipated values. When the LSTM network completed one loop, i.e. when the input ABL height data set travelled through the network once and returned once, the process was called an epoch.

6.2. Results

Performance evaluation of the experiment for the ABL height LSTM model was obtained for the optimal parameters. The testing was done for two parameters, *i.e.*, hidden neurons and epochs with constant data set (*2160 data points*). To avoid overfitting, the networks were trained using different hidden layers varying in the range (*2, 5, 10, 20, 30, 50, 100, 35, 28, 32,* respectively) with different epochs (*250, 500, 750*). The network (*32 hidden layer and 500 epoches*) training progress is shown in Fig. 6.3., which provided the best result among the combinations tried.

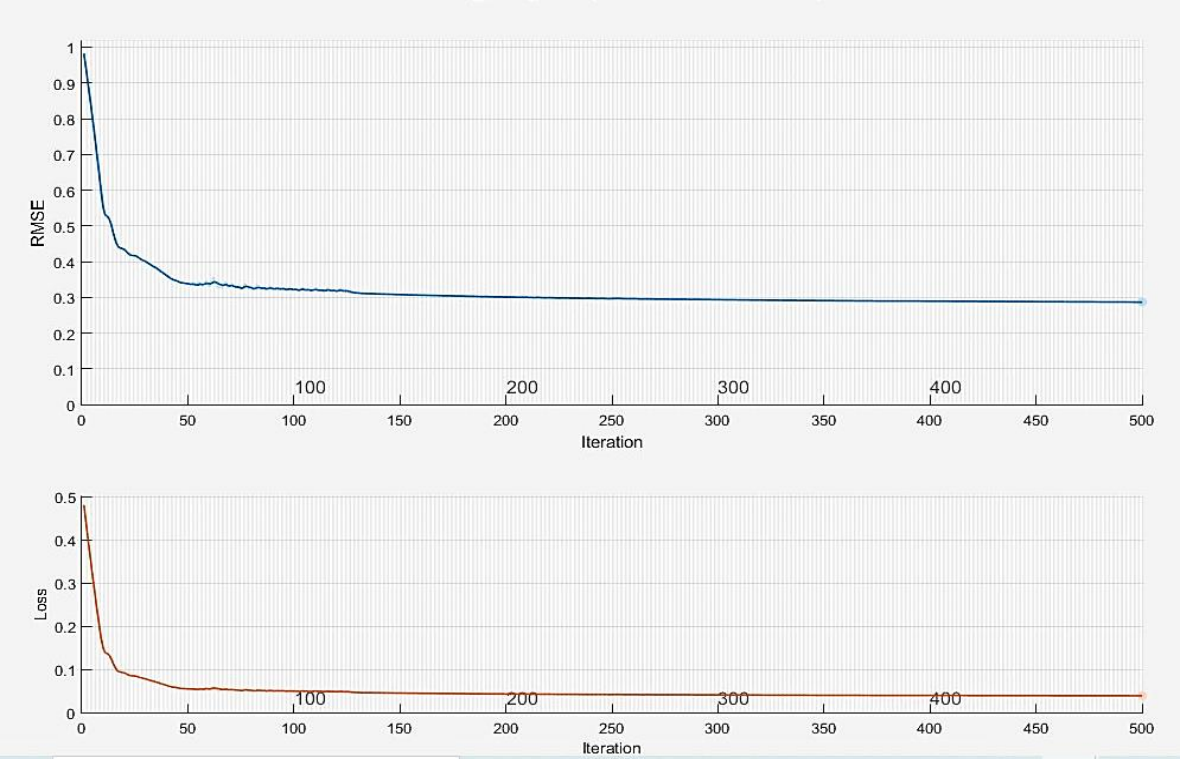

Figure 6.3. Training progress with hidden layer 32 and epoch 500

The test results are shown in Tables 6.2 and 6.4. The error value in the test set and training set decreases both with the number of ages and the hidden (neuron) layer increasing. Table 6.2. shows the number of hidden layers and the error value increased as time passed, which indicated that the accuracy of prediction improved.

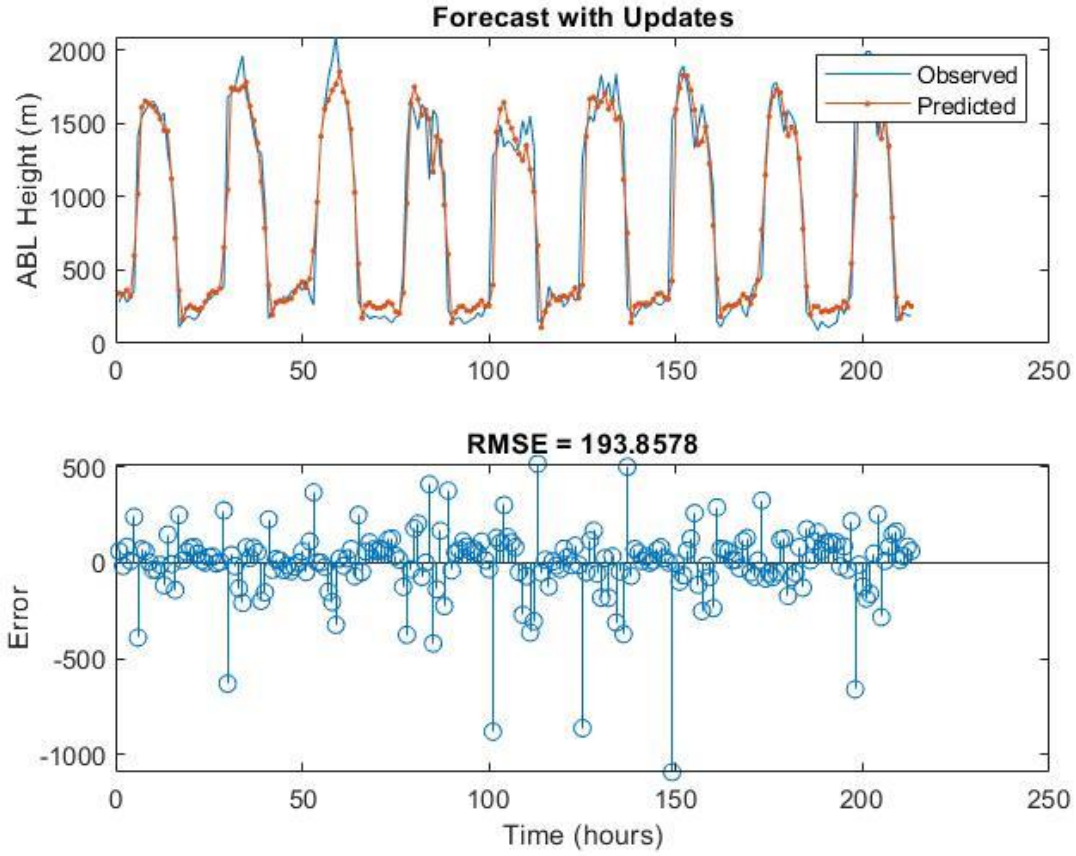

Figure 6.4. Prediction result LSTM network update with observed values (Prediction-2), hidden layer 32 and maximum epochs 500

To check the uncertainties in the LSTM model, different parameters were calculated and represented in Table 6.3. and Fig. 6.5. It was observed that the testing values and predicted values had followed the same pattern. Fig. 6.4 and 6.5 show the line plot of the temporal average of testing ABL height data and predicted ABL height data. In the LSTM model, Prediction-1 represented the updated network with predicted value (*1650 m maximum*) and Prediction-2 represented the updated network with observed values (*1700 m maximum*), for the highest value of ABL height from SODAR *1775 m.*

In addition, using the preconfigured model of MATLAB 2019a, the Non-linear Auto-Regressive (NAR) model was employed to forecast the ABL height. Table 6.4. shows the highest value of errors obtained for each model. The Prediction-2 model values were more accurate than the NAR model. However, the NAR model was used to anticipate future instances using data from earlier lags. For the day-to-day atmosphere, the ABL height was very dynamic. This generated a learning problem in the NAR design, which failed to accurately record dynamical changes.

Table 6.2. Comparison of accuracy of LSTM model

Hidden Layer	Prediction-1				Prediction-2			
	RMSE1	rRMSE1	MAE1	MAPE1	RMSE2	rRMSE2	MAE2	MAPE2
Max epochs – 500								
2	790.3	24.69	617.5	72.37	315.69	9.86	197.41	17.11
5	317.83	9.93	199.61	20.22	212.48	6.64	133.99	12.74
10	270.58	8.45	181	20.1	214.71	6.7	130.24	12.29
20	250.93	7.84	175.36	18.27	202.13	6.31	121.86	11.43
25	289.34	9.04	197.85	20.47	204.76	6.39	120.59	11.43
28	290.05	9.06	198.89	22.33	205.31	6.41	118.31	11.25
30	235.4	7.35	166.91	17.31	192.01	6	114.01	10.96
32	220.31	7.33	167.12	17.3	193.85	5.95	113.72	10.62
35	272.51	8.51	194.47	19.56	197.15	6.16	117.52	10.87
50	264.61	8.26	186.84	19.27	192.48	6.01	112.21	10.54
100	291.14	9.09	205.52	21.92	198.86	6.21	116.06	11.11
Max epochs – 250								
32	373.89	11.68	250.20	24.37	193.66	6.05	115.99	10.90
Max epochs – 750								
32	271.66	8.48	189.62	20.68	193.35	6.04	112.08	10.77

*Red colour row shows best prediction result

Table 6.3. Statistical analysis of LSTM model with hidden layer 32 and epoch 500

Parameter	Training Data	Test Data	Prediction-1 Data	Prediction-2 Data
Mean	737	837	849	852
Median	430	551	547	400
Kurtosis	-1.22	-1.67	-1.66	-1.71
Skewness	0.56	0.35	0.32	0.26
Coefficient of Variation	0.80	0.68	0.72	0.78

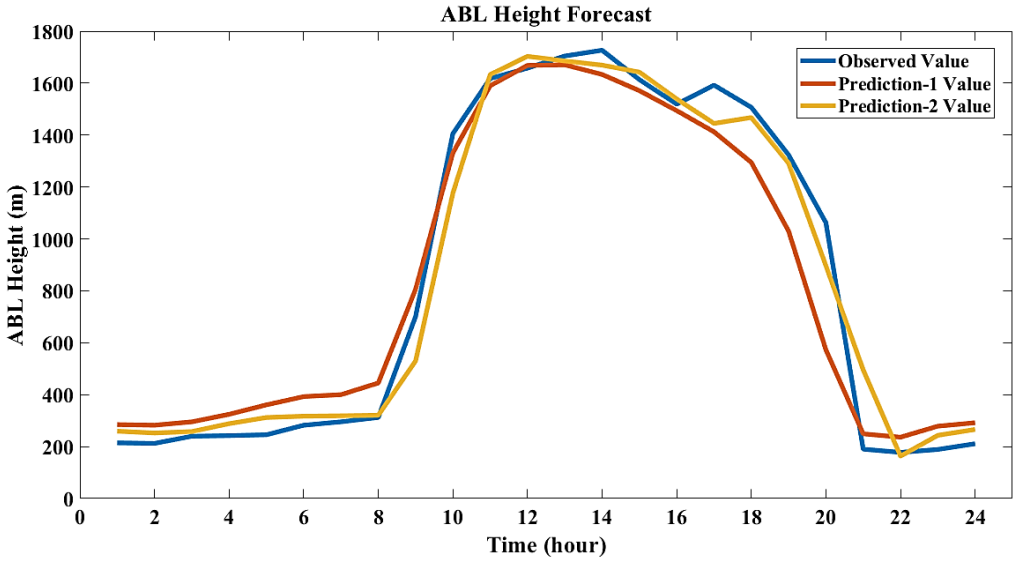

Figure 6.5. Comparison of observed ABL height and predicated ABL height

Table 6.4. Comparison between NAR and LSTM model

	NAR	Prediction-1	Prediction-2
RMSE	259.65	220.31	193.85
MAE	164.97	167.12	113.72

6.2.1. Analysis and prediction of annual ABL height

The ABL is a zone with an almost constant potential temperature and a particular relative high humidity. ABL height determines the volume available and describes the structure of the lower atmosphere for the dispersion of the pollutants. The higher the mixing value, the higher the dispersion rate. The ABL height changes constantly based on the observation of the SODAR echograms. So, the box plot was used to interpret the data [236-237] The box plot used the median, the approximate quartiles, and the lowest and highest data points to convey the level, spread, and symmetry of a distribution of data values. Every box was a central mark, which indicated median value and whereas the bottom-line represented the 25th percentiles, and the top-line indicates 75th percentiles of the data. The whiskers covered the most extreme data points and the outliers were plotted individually using the '+' symbol. Fig. 6.6. represents the annual variation of temporal ABL height and Month average. The vertical bars denoted the $\pm\ \sigma$ standard deviation from the temporal average. Fig. 6.6 and Table 6.5., present the temporal average SODAR data for about one year.

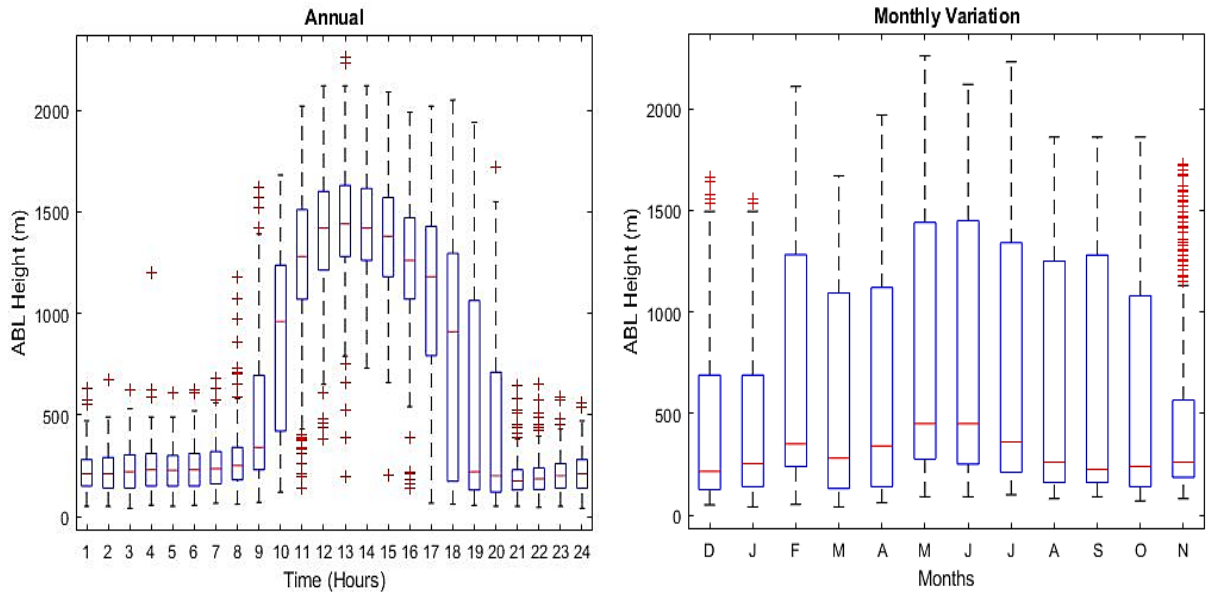

Fig. 6.6. Annual ABL height temporal and monthly variation

Table 6.5. Monthly ABL height variation during different hours

Month	Maximum ABL Height (m)	Corresponding Hour of Maximum ABL Height (hour)	Average ABL Height (m) during		
			Day Time (09:00-18:00 hour)	Remaining Hours (19:00 - 08:00 hour)	Diurnal Average (m)
December	1255	13:00	795	170	435
January	1120	13:00	710	200	415
February	1565	13:00	1125	265	620
March	1360	12:00	1035	185	545
April	1435	13:00	1145	225	615
May	1745	12:00	1480	350	810
June	1635	13:00	1475	325	795
July	1520	12:00	1380	325	760
August	1410	12:00	1305	260	690
September	1485	14:00	1280	190	645
October	1445	12:00	995	225	550
November	1405	11:00	850	230	490

The annual ABL height data was used to retained the LSTM model to predict the annual temporal ABL height. The Prediction-2 model was the smallest RMSE, according to the

results (187.71 m). Figure 6.7 shows that the Prediction-1 model produced a good result for 30 days with an RSME value of 0. (329.55 m). During the convention period, the predicted ABL height was lower than observed, which increased the error. In addition, the annual data set was used in the NAR model, which yielded a higher RSME value (261.80 m) than the Prediction-2 model.

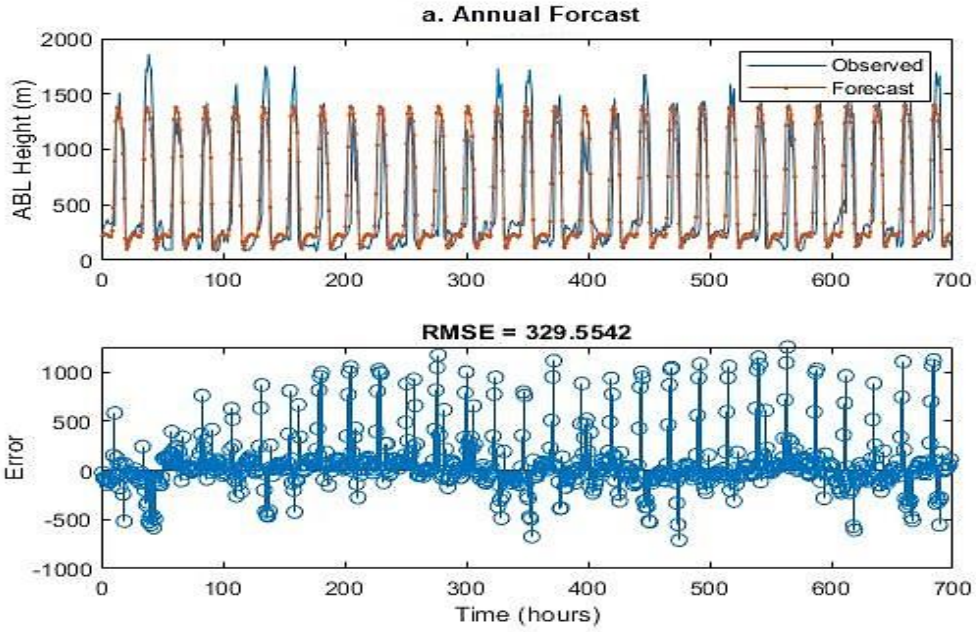

Figure 6.7. Prediction result LSTM network update with predicted values (Prediction-1), hidden layer 32, and maximum epochs 500

6.2.2. Comparison and prediction of seasonal ABL height

For the analysis of seasonal ABL height, the total data set was divided into four seasons based on meteorology over northern India, namely winter (December - January - February), pre-monsoon (March - April - May), monsoon (June - July - August - September), and post-monsoon (October - November) [58, 210, 238]. Fig. 6.8 depicts the temporal seasonal variation of mixing height over the entire year of observation. The convection period was found to be the longest during the monsoon and the shortest during the post-monsoon. The maximum mixing height (approximately 1510 m) was observed during the pre-monsoon season, while the minimum mixing height (approximately 1315 m) was discovered during the winter season. Table 6.5 shows the monthly average ABL Height hours. It was discovered that ABL height was highest in May (pre-monsoon season) and lowest in January (winter season).

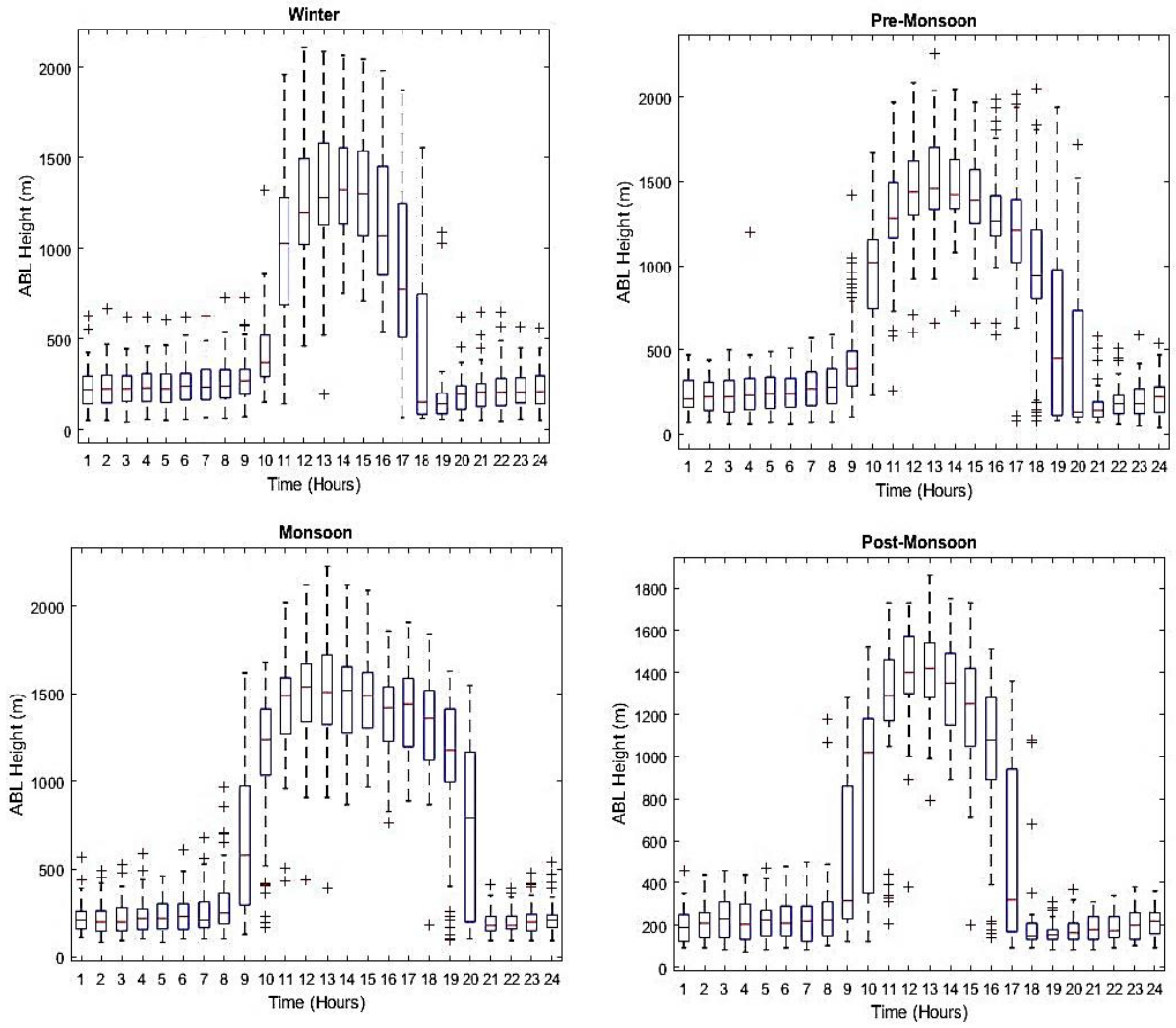

Figure 6.8. Temporal variation of seasonal ABL height

ABL height was a positive correlation with temperature and wind speed, whereas a negative relationship with relative humidity [58]. Temperature and wind speed influenced positively to the ABL, while relative humidity influences negatively to the ABL heights, during all the seasons due to an increase or decrease in solar heating. The convective boundary layer height increased and decreased during the daytime due to the change in surface temperature. The variation in surface temperature controlled the existence of atmospheric convection. Therefore, it strongly affected the height. It was high between *1100 to 1400 IST* during all seasons. ABL height started decreasing due to the decrease in solar heat during the evening. The ABL height during the convection period was found at *1510 m, 1485 m, 1395 m, and 1315 m* in pre-monsoon, monsoon, post-monsoon, and winter seasons, respectively.

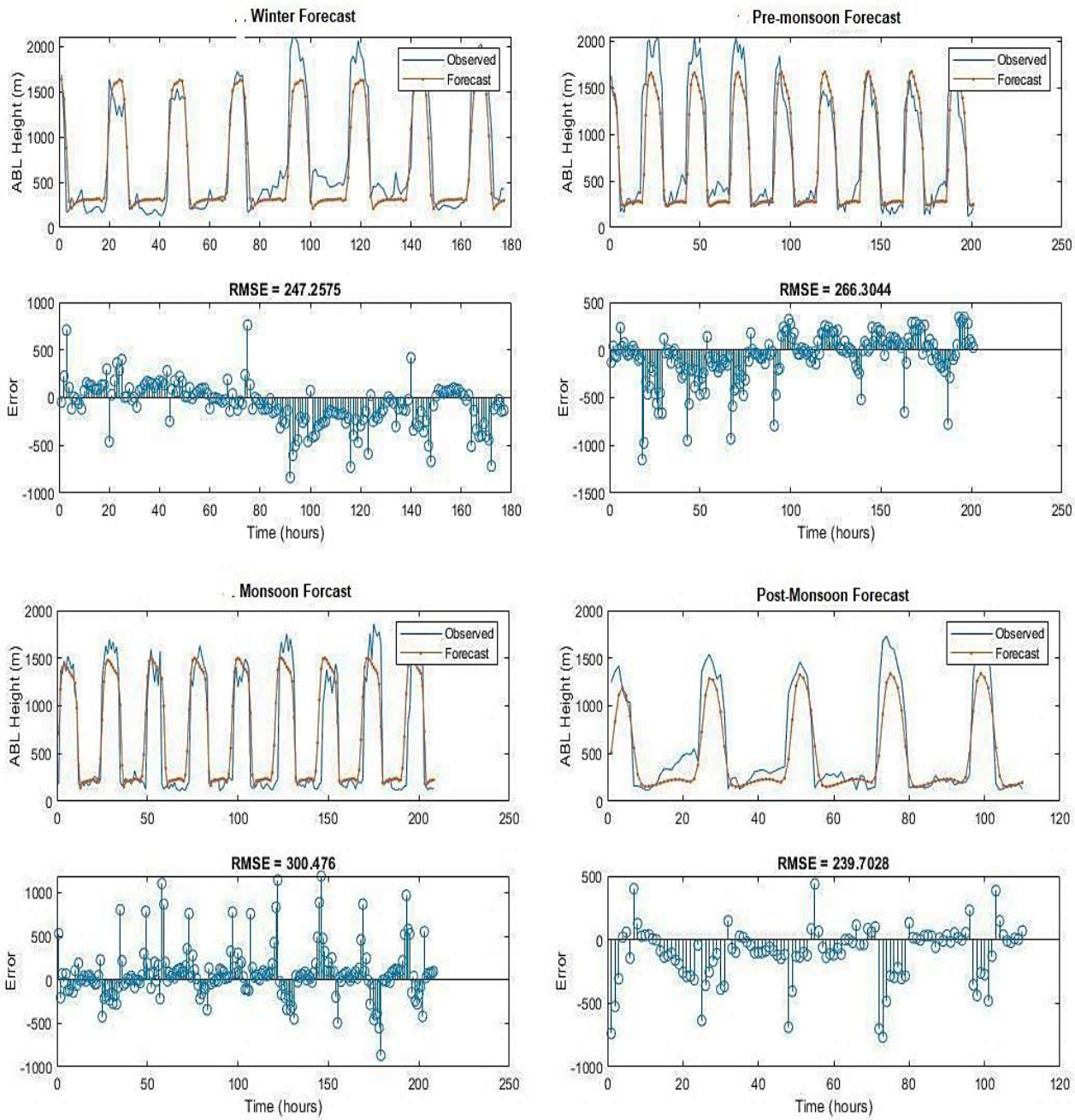

Figure 6.9. Seasonal ABL height prediction result from the update network state with predicted values (Prediction-1)

The prediction of seasonal ABL height was based on all of the season data. Both LSTM models were retrained and tested with seasonal data to get a result for seasonal ABL height prediction. The seasonal ABL height prediction result from the Prediction-1 model was represented in Figure 6.9. The Prediction-1 model's accuracy decreased as the prediction days grew longer. To retrain and test the NAR model, we used seasonal data. The NAR model was found to have a higher RMSE value than the other two models (Table 6.6.).

6.3. Discussion

The LSTM model was trained using data from four seasons of ABL height in various atmospheric conditions. Then, to compare with the annual prediction, the trained prediction model was used to predict the ABL height for each season (Fig. 6.7. & 6.9.). The ABL height predictions shows a comparable result with the SODAR data, especially over the transition period (from inversion to convection or vice versa). Table 6.6. shows the error of ABL height prediction using the LSTM network, which was relatively lower in the winter season and higher in annual data. Whereas error in all conditions of Prediction-2 was lower as compared to Prediction-1 and NAR model. But the related error generated by Prediction-1 was not much higher compared to Prediction-2. The LSTM network model provided high accuracy compared to the NAR model. The LSTM models simulated the seasonal ABL height reasonably well, *i.e.*, inferred from the periodicity in the ABL height time series. It also provided reliable ABL height simulations and predictions at any sites where the yearly ABL height pattern remains somewhat similar. The highest ABL height was observed during the convection period (daytime), which did not follow any periodicity and had the highest errors. These LSTM models were useful to the pollution regulatory body to control atmospheric pollution.

Table 6.6. Comparison of seasonal prediction of ABL height

	Data Point	Hidden Layers – 32; Max Epochs – 500								NAR Models
		Prediction-1				Prediction-2				
		RMSE1	rRMSE1	MAE1	MAPE1	RMSE2	rRMSE2	MAE2	MAPE2	RMSE
Annual	6984	329.55	10.29	200.13	23.35	187.71	5.86	118.78	17.04	261.80
Winter	1776	247.25	7.72	181.83	19.59	187.77	5.86	125.81	13.19	307.33
Pre-Monsoon	2016	266.30	8.32	182.99	20.02	181.18	5.66	116.24	11.04	245.91
Monsoon	2088	300.47	9.38	187.14	15.62	255.45	7.98	151.71	12.74	281.25
Post-Monsoon	1104	239.70	7.49	163.73	25.15	178.92	5.59	118.57	15.17	250.94

The LSTM neural network architecture was found to capture the dynamics of temporal ABL height and also for seasonal and annual ABL height prediction. In short training periods, the number of neurons and epochs were 32 and 500 respectively, which provided a precise result to achieve a long-term prediction. This work presented a neural network-based temporal ABL prediction.

Chapter 7
ABL Height Estimation During Fireworks Emission

This chapter is divided into five sections: first, data was collected during the fireworks, *i.e.,* Diwali period, then ventilation coefficient was determined, ABL variation with meteorological parameters, ABL variation with pollutants, and finally, forward selection method was used to estimate the most dominant parameter to ABL height during the Diwali periods.

7.1. Data Collection during the Fireworks Emission

Based on the methodologies (section 3.6) for determining ABL height of stable and unstable conditions, and collected hourly averaged SODAR data, meteorological parameters (*i.e.*, temperature, wind speed, and relative humidity), and pollutants (*i.e*, SO_2, CO, NO_2, $PM_{2.5}$) during the Diwali periods (2014-2017).

7.2. Determination of Ventilation Coefficient

The Ventilation Coefficient (VC) is an atmospheric dispersion parameter that indicates air quality and pollution potential, *i.e.*, the atmosphere's ability to dilute and distribute pollutants across a certain area [239]. The product of the ABL height (mixing height) and the average wind speed was used to calculate it. The VC was greater, the better the atmospheric qualities, *i.e.,* the more pollutants were removed from the atmosphere. On the other hand, lower VC, resulted in poor pollutant dispersal, stagnation, and poor air quality, which could lead to pollution-related health problems. A change in the VC was caused by changes in the ABL height and average wind speed [113]. The VC was less than $6000\ m^2.s^{-1}$ indicates high pollution potential in the afternoon hours, but ABL height was less than *500 m* in the morning hours, indicating the conditions for the occurrence of high pollution potential. The VC was used to calculate the assimilative capacity of the atmosphere. The pollutant loading capacity of the region was measured.

Fig. 7.1. represents the temporal variation of VC during Diwali days for the years from 2014 to 2017. However, the overall average value of VC was much lower than the 6000 m2.s-1 for all four years, i.e., the occurrence of high pollution potential over the region [240-241]. Due to strong prevailing winds and rain in 2015, the highest VC value was found for the years. In 2017, the lowest VC value was recorded. Sujatha et al. [239] stated that the dispersion of pollutants is dependent on several meteorological parameters, the wind, and ABL height being the most important to define air mixing. A higher value of VC was therefore observed

during the day and decreases at night, i.e. the atmospheric loading capacity was good during daytime and in the nighttime poor.

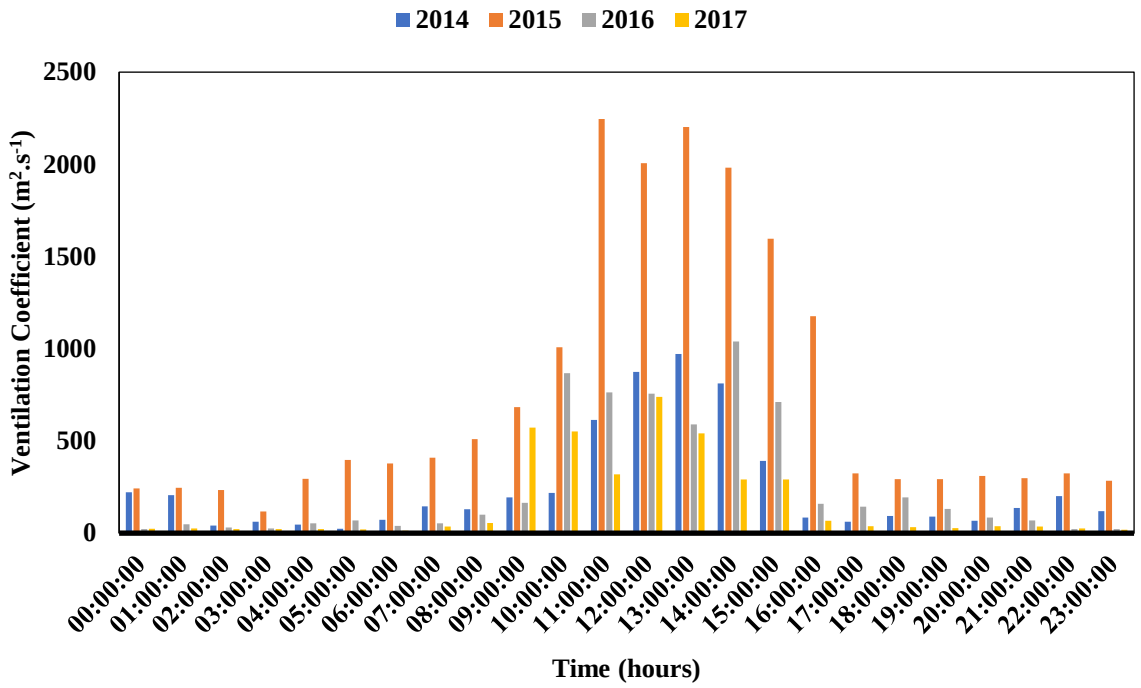

Figure 7.1. Ventilation coefficient during Diwali day

7.3.Variation of ABL with Meteorological Parameters

The ABL was influenced positively by temperature and wind speed [58]. During the day, the height of the convective boundary layer raised and failed in response to changes in surface temperature caused by solar heating of the ground. The presence of atmospheric convection was controlled by surface temperature variations that had an important effect on the ABL height. Relative humidity adversely affected the ABL height. During the Diwali period, Table 7.1 shows the average daily weather with ABL records. ABL values were lowest during post-Diwali in 2017 (*191 m* on *20-Oct-17*) and higher mean ABL values during Post-Diwali in 2015 (*663 m* on *12-Nov-15*). The purpose of the day before, after and Diwali day comparison was to identify the contribution of fireworks burning on air quality.

Table 7.1 depicts the wind speed years from 2014 to 2017; it was highest in the year 2015 while the lowest in the year 2017. The low wind speed was associated with elevated pollution levels [1]. If the wind direction remained constant throughout the year, the area will be exposed to high pollution levels. Pollutants are disseminated across a vast area as the wind direction changes. Humidity played a significant role in determining the ABL height [58, 151]. In 2016, the humidity was at its greatest, and in 2015, it was at its lowest.

Table 7.1. The daily average of meteorological parameters

Year	Day	ABL (m)	Temperature (^{0}C)	Wind Speed (m/s)	Relative Humidity (%)
2014	22-Oct-14	300	27.79	0.9	61.78
	23-Oct-14	297	28.09	0.74	61.37
	24-Oct-14	327	27.99	0.76	61.7
2015	10-Nov-15	495	25.14	0.89	61.06
	11-Nov-15	660	24.98	1.06	43.49
	12-Nov-15	663	24.52	0.92	46.03
2016	29-Oct-16	286	26.0	0.58	48.04
	30-Oct-16	307	25.45	0.68	62.56
	31-Oct-16	310	24.57	0.63	71.79
2017	18-Oct-17	258	---	0.75	42.42
	19-Oct-17	263	16.06	0.53	46.36
	20-Oct-17	191	----	0.54	50.07

7.4.Variation of ABL with Pollutants

To analyse the variation of ABL with a concentration of air pollutants during the Diwali festival period, the SODAR data for ABL and concentration of pollutants data were collected for the years 2014 (18 October to 28 October), 2015 (6 November to 16 November), 2016 (25 October to 04 November) and 2017 (14 October to 24 October). Round-the-year SODAR measurements were carried out in New Delhi. An hourly average of ABL during Diwali day is shown in Fig. 7.2.

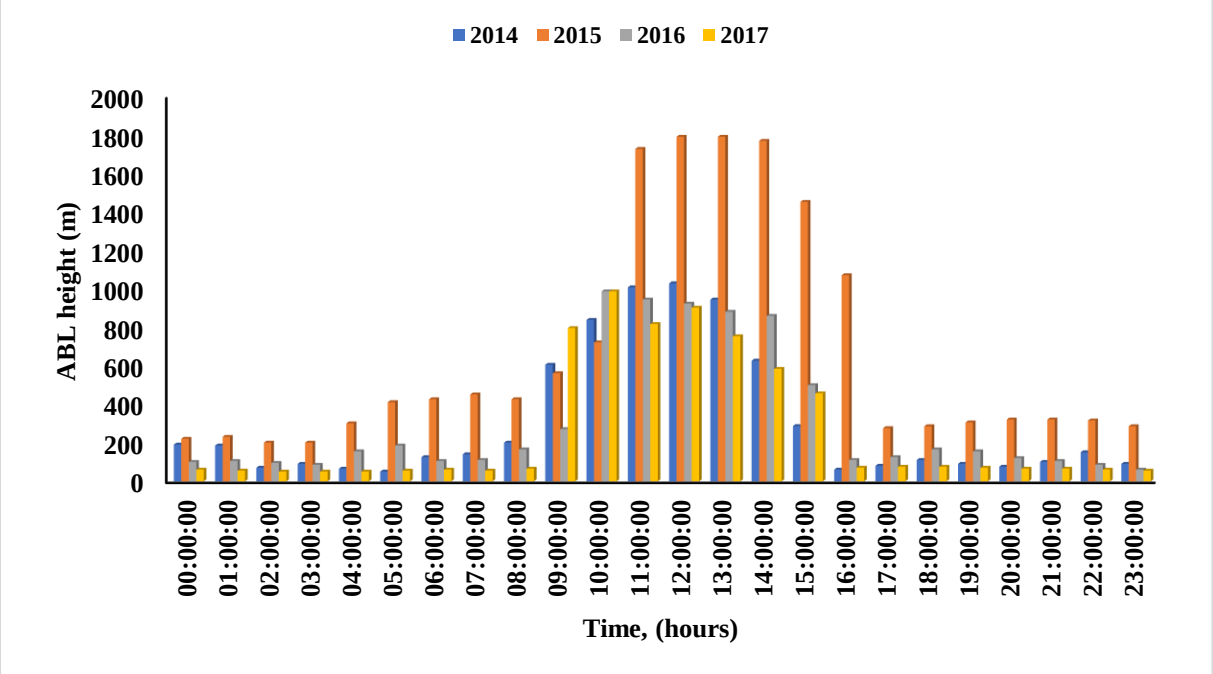

Figure 7.2. Hourly average of ABL height during Diwali day

During the Diwali process, a variety of other materials that are found in the fireworks polluted air with sulphur nitrates, magnesium, aluminium, and paper. The complete structure and relative concentrations of the various gaseous vapours and released particulate pollutants remain unknown. The cause of particular concern, however, were sulphur oxide, nitrogen oxide, and particulate matter, as they are linked to respiratory and other health problems [242]. In addition, existing industries, control plant utilization of vast scale vehicular exercises, and habitually tidy tempest essentially contributed to high air contamination [176, 181, 243]. Air contamination has caused eye irritation, cough, headache, and respiratory problem [182-183]. The daily average of ABL height, concentrations of $PM_{2.5}$, SO_2, CO, and NO_2 were calculated for Pre-Diwali Episodes (before five days of Diwali), Diwali day, and Post-Diwali Episodes (After five days of Diwali) during the year 2014, 2015, 2016 and 2017. The maximum variation of ABL was observed during the year 2015 and the minimum variation was observed during the year 2017. On Diwali 2017, a daily average value of CO, NO_2, and SO_2 recorded *1330* $\mu g.m^{-3}$, *58.24* $\mu g.m^{-3}$ and *66* $\mu g.m^{-3}$ respectively, which were also compared to other years and observed that CO was nearly *1.05, 1.94, and 0.73*; NO_2 nearly *1.09, 1.13* and *0.52*; and SO_2 nearly *1.43, 3.16* and *1.13* times higher in 2014, 2015 and 2016 respectively. The concentration of $PM_{2.5}$ was noted *260* $\mu g.m^{-3}$ in 2017, nearly above 2.55 from 2015 and 0.45 times below from 2016 respectively. Also, the same trend was observed in the case of Pre-Diwali and Post-Diwali. Variety of pollutant concentration was not consistent during Diwali periods, its segment varieties demonstrated that these contaminations were influenced by the nearby source, as well as remote sources in different areas. It established a link between ABL height and air pollution concentration, laying the groundwork for studies to monitor and forecast the urban environment. Pollution levels were found to be higher at night when ABL levels were low and lower during the day when ABL levels were higher. The ABL was affected by temperature, sensible and latent heat fluxes, wind speed and direction, cloud cover, and relative humidity [1, 3].

Wagner and Schafer et al. [244] proposed that the influence of ABL height on pollutants was analysed by grouping ABL height data into periods and correlating classified ABL with concentrations of pollutants. The 8-hourly average (*00:00 - 08:00, 08:00 - 16:00, 16:00 - 24:00*) value of ABL and concentration of pollutants (SO_2, NO_2, CO, $PM_{2.5}$) are presented in Table 7.2 to further analyse their relation. It was found that ABL height and concentrations of pollutants were inversely correlation between them. Concentrations of pollutants (SO_2, CO, and $PM_{2.5}$) were increased, whereas concentrations of NO_2 were decreased from the Pre-Diwali period to the Post-Diwali period, and reached maximum value during next to Diwali

day. Variation of ABL was an opposite correlation with the concentrations of pollutants which decrease gradually from Pre-Diwali to Post-Diwali. Table 7.2. (a, b and c), showed that the pollutants were dispersed in the atmosphere during the daytime (*08:00 – 16:00*), whereas accumulated during mid-night time and early morning time (*00:00 – 08:00*). The maximum value (*1375 m*) of ABL height was found during daytime in the year 2015, whereas the minimum value (*54 m*) during night-time in the year 2017. The minimum value of pollutants SO_2 ($\mu g.m^{-3}$), NO_2 ($\mu g.m^{-3}$), CO ($\mu g.m^{-3}$), and $PM_{2.5}$ ($\mu g.m^{-3}$) were observed *2.67, 1.24, 250,* and *73* during daytime and a maximum value *171, 145, 3090* and *980.25* during midnight time respectively.

Table 7.2. 8-hourly average of ABL and pollutants concentrations

00 AM-8 AM						
Year	**Period**	**ABL (m)**	**SO_2 ($\mu g.m^{-3}$)**	**NO_2 ($\mu g.m^{-3}$)**	**CO ($\mu g.m^{-3}$)**	**$PM_{2.5}$ ($\mu g.m^{-3}$)**
2014	22-Oct-14	114	47.79	120	656	-
	23-Oct-14	101	67.46	25.39	486	-
	24-Oct-14	98	181.89	5.95	158	-
2015	10-Nov-15	88	8.62	81	560	134
	11-Nov-15	304	5.9	54	590	102
	12-Nov-15	343	17.89	42	1190	151
2016	29-Oct-16	115	25.73	88.85	3090	466
	30-Oct-16	117	20.85	91.92	2440	581
	31-Oct-16	70	146.43	65	1530	731
2017	18-Oct-17	86	50.94	34.27	1390	180.1
	19-Oct-17	54	99.45	41.65	1320	270.19
	20-Oct-17	58	171	75.65	2510	980.25

8 AM- 4 PM						
Year	**Period**	**ABL (m)**	**SO_2 ($\mu g.m^{-3}$)**	**NO_2 ($\mu g.m^{-3}$)**	**CO ($\mu g.m^{-3}$)**	**$PM_{2.5}$ ($\mu g.m^{-3}$)**
2014	22-Oct-14	691	46.47	70.3	530	-
	23-Oct-14	718	41.91	4.81	461	-
	24-Oct-14	785	57.17	11.05	219	-
2015	10-Nov-15	1117	11	77	280	128
	11-Nov-15	1279	3.35	31	740	73
	12-Nov-15	1375	2.67	31	250	110
2016	29-Oct-16	611	11.75	150.5	1520	398
	30-Oct-16	690	10.45	113.86	1170	378
	31-Oct-16	757	50.48	93.75	1110	232
2017	18-Oct-17	617	9.1	34.39	560	140.36
	19-Oct-17	668	21.75	64.23	550	139.58
	20-Oct-17	444	24.78	64.64	250	311.5

4 PM - 12 AM						
Year	**Period**	**ABL (m)**	**SO_2 ($\mu g.m^{-3}$)**	**NO_2 ($\mu g.m^{-3}$)**	**CO ($\mu g.m^{-3}$)**	**$PM_{2.5}$ ($\mu g.m^{-3}$)**
2014	22-Oct-14	94	52.63	29.94	790	-
	23-Oct-14	73	187.24	3.46	907	-
	24-Oct-14	100	46.75	18.46	642	-
2015	10-Nov-15	279	9	111	1010	172
	11-Nov-15	397	53.31	68	720	137
	12-Nov-15	272	7.73	94.74	880	143
2016	29-Oct-16	133	39.22	165.99	2730	568
	30-Oct-16	115	137.61	123.97	1810	441
	31-Oct-16	104	35.59	123.7	750	160
2017	18-Oct-17	73	100.35	38.7	2460	233.73
	19-Oct-17	66	76.84	68.86	2100	368.73
	20-Oct-17	70	98.91	45.66	1380	281.88

7.5. Forward Selection Method

Section 7.3 and 7.4 concluded that the ABL height was dependent on different parameters. Many authors [3, 58, 151, 244] also mentioned the correlation between ABL height, meteorological parameters, and pollutants concentration. Stull [1] said that the diurnal cycle of changes in temperature, humidity, pollutants concentrations, and winds are governed by ABL height physics and dynamics. In this section, the most dominant correlation between ABL height, meteorological parameters, and pollutants concentration was determined using a Forward Selection (FS) method/technique.

FS method was successfully used to develop various accurate prediction models [245-247]. It was based on a linear regression model. For a small number of sample covariates (N), a prediction model was selected by which certain measure such as CVE (Cross Validation Error), RMSE (Root Mean Square Error) was computed for given subgroups of predictors [248]. For a large sample size, the computational content was increased very rapidly. Therefore, to overcome this problem, one method was the FS method, which was a well-defined step-by-step algorithm [249-251]. The following algorithm was used to find the best subsets for the relationship between ABL height and seven input parameters in this study (meteorological and pollutants data).

Step 1: Choose independent and dependent variables and make a correlation with the independent variable and dependent variable

$$R = \frac{n(\sum xy) - (\sum x)(\sum y)}{\sqrt{[n(\sum x^2) - (\sum x)^2]}\sqrt{[n(\sum y^2) - (\sum y)^2]}} \quad (7.1)$$

Step 2: Find the independent variable with the highest squared correlation with the dependent variable and arrange it in decreasing order

Step 3: Fit k-1 different regressions using each of the remaining variables separately

Step 4: Record the incremental changes in R^2 and select the variable with the highest R^2 meeting this criterion (R^2 increment is less than 5 %)

Step 5: Stop when no variable satisfies this criterion

Table 7.3. Result of forward selection method

2017 Sub-Table – 7.3. (a)							
Temp.							0.472
Temp.	RH						0.494
Temp.	RH	CO					0.529
Temp.	RH	CO	SO_2				0.534
Temp.	**RH**	**CO**	**SO_2**	**WS**			**0.561***
Temp.	RH	CO	SO_2	WS	$PM_{2.5}$		0.561
Temp.	RH	CO	SO_2	WS	$PM_{2.5}$	NO_2	0.591

2016 Sub-Table – 7.3.(b)							
Temp.							0.384
Temp.	CO						0.448
Temp.	CO	RH					0.486
Temp.	CO	RH	WS				0.517
Temp.	CO	RH	WS	SO_2			0.561
Temp.	**CO**	**RH**	**WS**	**SO_2**	**NO_2**		**0.576***
Temp.	CO	RH	WS	SO_2	NO_2	$PM_{2.5}$	0.574

2015 Sub-Table – 7.3. (c)							
Temp							0.522
Temp	RH						0.528
Temp	**RH**	**NO_2**					**0.653***
Temp	RH	NO_2	$PM_{2.5}$				0.654
Temp	RH	NO_2	$PM_{2.5}$	CO			0.652
Temp	RH	NO_2	$PM_{2.5}$	CO	WS		0.653
Temp	RH	NO_2	$PM_{2.5}$	CO	WS	SO_2	0.653

2014 Sub-Table – 7.3. (d)						
Temp						0.349
Temp	RH					0.35
Temp	RH	CO				0.427
Temp	RH	CO	NO_2			0.403
Temp	**RH**	**CO**	**NO_2**	**WS**		**0.464***
Temp	RH	CO	NO_2	WS	SO_2	0.466

*and **_ denotes** After this value, a variation of R^2 is negligible change (less than 5 %) and thus, inputs related to this value are selected

The best-correlated subset of inputs was used to create a linear model. According to the algorithm, the input candidates were implemented one by one into the technique. The correlation coefficient (R^2) was used to assess the modeling quality. Finally, the input variables with the greatest impact on output were chosen, and other variables were eliminated. Table 7.3. shows the results of the FS technique, with 5, 6, 3 and 5 input variables chosen according to their importance in the years 2017, 2016, 2015, and 2014, respectively. It increased the forecast capability of models by taking into account the importance of daily ABL height in the Delhi atmosphere. Because there were fewer input variables, it minimised output error and calculation time. According to Noori *et al.* [247], FS method-based models were more accurate than gamma test-based models. During the Diwali period, the significant increase in pollutants (CO, NO_2, SO_2, and $PM_{2.5}$) indicated that the burning of fireworks was the main source of pollutants, whereas Table 7.3 observed the pollutants concentration and meteorological parameters were correlated with ABL height. It was also observed that temperature was one of the most dominant parameters for the ABL height as in every year FS technique result, the temperature was present.

It was obvious from Table 7.3. (a to d) that during the year 2017 highly dominating subset was (Temp, RH, CO, SO_2, and WS), in the year 2016 (Temp, CO, RH, WS, SO_2 and NO_2), in the year 2015 (Temp, RH and NO_2), and in the year 2014 was (Temp, RH, CO, NO_2, and WS).

Findings show firecracker emissions and deposition of particulates harm ambient air quality during the burning of fireworks, i.e, Diwali Festival. Concentrations in air pollutants were 1,14, 2,52 and 1,16 times higher in 2017 compared to the years 2014, 2015 and 2016. The importance of a thorough assessment of ABL for air contaminants in the Indian cities and the need for a denser monitoring station network was emphasised. The FS technique was successfully used to select the highly influential ABL height parameter. The excessive loading of ABL pollutants with this methodology was also determined by this parameter.

Chapter 8
Conclusion and Future Scope

8.1. Conclusion

SODAR is a well-known and widely accepted meteorological tool for supplying continuous real-time and critical ABL data. SODAR assists in city planning, industrial zoning, and other methods planned for air quality control. Data is critical for evaluating environmental impact assessments and city-specific carrying capacity for pollutants. In light of Delhi's air quality concerns, air pollution meteorological features in terms of ABL characterizations were investigated from 2014 to 2020.

Existing SODAR technology was improved, which included, acoustic antenna advancements, virtual instrumentation, and improved data processing approaches. It has previously been difficult for these instruments to work well in densely populated metropolitan areas due to echoes from buildings and repercussions on people, but this is improving as the instruments' acoustic design improves. A vertically pointed monostatic SODAR system was developed through a deliberate development and improvement process. This advancement will affect the observed data, and data will be more accurate as a result of calibration and testing of equipment and materials. To achieve the goal, the work focuses mainly on four areas, *i.e.*, developing a SODAR system with a new acoustics antenna design, developing a new model of ABL structure identification using feature selection and classifier method, developing an LSTM model for ABL height prediction using SODAR data, and analysing ABL height, atmospheric pollutants, and meteorological data during fireworks (Diwali).

A new SODAR system for monitoring has been built using a unique combination of a moving-coil transducer, parabolic dish, and acoustic ACP sheet baffle. It is the first time in history that an acoustical parabolic antenna has been used to transmit acoustics into the turbulent zone.

The novel design enables the development of a low-cost SODAR system as well as a lightweight, high-precision acoustic baffle. The acoustical parameters of baffles were calculated in the reverberation chamber (STC = 34 and NRC = 0.98). An ACP sheet with foam was the suitable acoustic baffle for an acoustic antenna design. It can generate up to 138 dB of acoustic pressure in a narrow beam in the atmosphere. The new open-air acoustical barriers reduce environmental noise by 272 decibels. The benefits of a novel antenna make it ideal for transportable SODAR applications and field tests in a variety of locations. The system can be used for long-term continuous collection of data with a low probability of an

electronic failure. Data on ABL height and structure in the current study were successfully collected using the created technique.

The methodologies for machine learning were used for the identification of various ABL structures in the SODAR echogram. The ABL structures were identified by feature selection and classification of functions. The Boosting Tree classification method was the highest predicated accuracy in SODAR echograms / ABL structure recognition, combined with the selecting of the Laplacian feature (overall performance 61% with 30 features) from 8 classification devices (overall preformation 52 percent with a total 133 feature). These models were used as a monthly predictive model with the highest predictive precision in October and with the lowest prediction in August (72 % with 20 features in total) (overall preformation 31 % with 20 features).

The neural architecture of the LSTM network was used to capture the hidden dynamics and provide predictions of temporal ABL. A fundamental component of this technique was the division of time into seasonal and annual ABL predictions from December 2018 to March 2020. With LSTM the accuracy of the seasonal forecasts, and consequently of aggregating the year data, in place of a standard neural network was improved to test the recommended model. The investigation showed that in a short training time the best results were obtained if the numbers of neurons were equal to 32 and the epoch 500. Therefore, the prediction results are precise even for long-term forecasts. The innovative method provides the basis for a reliable ABL prediction for the next step. The LSTM network provides the information to determine the atmospheric condition using a separate environmental parameter. The LSTM neural network model for the nonlinear parameter was found appropriate.

During pre-Diwali, Diwali, and post-Diwali, between 2014 and 2017, the fluctuation of ABL, meteorological conditions, and pollutant concentrations were studied. To compare the days before, after, and on Diwali day, the impact of cracker burn on air quality was determined. During the period of Post-Diwali in 2017 (191 m) the lowest ABL values were found; in 2015 (663 m), the highest ABL values in Post-Diwali were found. The concentrations of pollutants in the atmosphere were 1,14, 2,52, and 1,16 times greater for 2017 from 2014, 2015, and 2016, respectively. The pollution levels were found higher at night when the ABL height was low, and lower during the day when the ABL height was higher. Due to the emission and deposition of particulate matter and gas pollutants, firecrackers had a significant influence on ambient air quality during the Diwali festival. The most dominant relationship between ABL height and weather parameters, as well as pollutants concentration, was

determined using the forward selection technique. The highly influencing parameter for ABL height was successfully selected.

In a nutshell, a new SODAR system for monitoring was built using a unique combination of a moving-coil transducer, parabolic dish, and acoustic ACP sheet baffle. An acoustical parabolic antenna was used to transmit acoustics into the turbulent zone. The system was used for the long-term continuous collection of data with a low probability of an electronic failure. Machine learning was used for the identification of various ABL structures in the SODAR echogram. The LSTM network was used to capture the hidden dynamics and provide predictions of temporal ABL from December 2018 to March 2020. During foreworks (pre-Diwali, Diwali, and post-Diwali) between 2014 and 2017, the fluctuation of ABL, meteorological conditions, and pollutant concentrations were studied and analysed. Air pollution levels were found higher at night when the ABL height was low, and lower during the day when it was higher.

8.2. Future Scope

The following suggestions for improving the performance and use of the SODAR system are made in future work:

A high acoustics material and high-density foam combination antenna baffle may provide better atmospheric noise cancellation for low-strength backscatter signals from crucial atmospheric structure information in the spatial domain. The hardware-based machine learning system composed of an electronic representation of the output of the pre-amplifier in real-time mode can be designed for better ABL structure identification and atmospheric noise reduction. The acoustic antenna structure can be fabricated using a 3D printing technique using low-weight fibre material.

A unique combination of a moving-coil transducer, parabolic dish, and an acoustic ACP sheet was developed for monitoring the levels of contamination in the air. The system was used to collect data for a long time with a low likelihood of an electronic failure. Machine learning was used in the SODAR echogram to identify different ABL systems. The LSTM network captured hidden dynamics and temporal ABL predictions from December 2018 to March 2020. During fireworks between 2014 and 2017, the fluctuation of ABL, meteorological conditions, and pollutant concentrations were studied and analysed.

List of Publication

Journal Publication

1. Nishant Kumar, Kirti Soni, Ravinder Agarwal, Naveen Garg, D. Saha, and Gurbir Singh SODAR pattern classification and its dependence on meteorological parameters over semi-arid region. ***International Journal of Remote Sensing***. 38 (11), 3466–3482, 2017.
2. Nishant Kumar, Kirti Soni and Ravinder Agarwal. Predication of temporal atmospheric boundary layer height using Long Short-Term Memory network. ***Tellus A: Dynamics Meteorology and Oceanography***. 73(1), 1-14, 2021.
3. Nishant Kumar, Kirti Soni and Ravinder Agarwal. Design and development of SODAR antenna structure. ***MAPAN***. 2021. (Accepted)
4. Nishant Kumar, Kirti Soni and Ravinder Agarwal. Detection of Kelvin-Helmholtz Billows over the capital region of India using SODAR. ***Annales Geophysicae*** (Preprint Published and Under Discussion)
5. Nishant Kumar, K. S. Parmar, Kirti Soni, Naveen Garg, and Ravinder Agarwal. Prediction of ventilation coefficient using a conjunction model of Wavelet-Neuro-Fuzzy Model: A Case Study Delhi, India. ***Academia Journal of Scientific Research***. 3(12), 184-191, 2015.
6. Nishant Kumar, Kirti Soni, Ravinder Agarwal and Mahavir Singh. SODAR as a diagnostics tool for urban air-quality and health care system. ***The Journal of Acoustical Society of India***. 44 (4), 213–222, 2017.
7. Nishant Kumar, Kirti Soni and Ravinder Agarwal. A comprehensive study of different feature selection methods and machine-learning techniques for SODAR structure classification. ***Modeling Earth Systems and Environment***. 7(1), 1-12, 2021.

Book Chapter

Nishant Kumar, Kirti Soni, Ravinder Agarwal, and Mahavir Singh. Studies Different Structure of Atmospheric Boundary Layer Using Monostatic SODAR. ***Recent Developments in Acoustics, Lecture Notes in Mechanical Engineering***. Springer Nature Singapore Pte Ltd., 2021.

Conference

1. Nishant Kumar, Ravinder Agarwal, Kirti Soni, and Gurbir Singh. (2015). Development on LabVIEW based program for the Classification of Stability Class in SODAR Observations. ***National Symposium on Acoustics "Acoustics for Ocean Environment"*** *7-9 October 2015*, CSIR-NIO Goa.
2. Nishant Kumar, Kirti Soni, Ravinder Agarwal, Naveen Garg, and Gurbir Singh. (2016). Development of Mixing Height based Fog Predications Models using Artificial Neural Network and Fuzzy Logic. ***9th International Conference on "AdMet-2016"*** *24-26 February 2016*, CSIR-NPL, New Delhi
3. Nishant Kumar, Ravinder Agarwal, and Kirti Soni. (2017). The Impact Assessment of Diwali Firecrackers Emissions on the Air Quality of the Capital Region of India. ***"URSI-RCRS 2017"*** *1-4 March 2017*. NARL-Tirupati.
4. Nishant Kumar, Kirti Soni, Ravinder Agarwal, and Mahavir Singh. (2017). Studies Different Structure of Atmospheric Boundary Layer using Monostatic SODAR. ***"National Symposium on Acoustics-2017"***, *October 28-30, 2017*, AMU-Aligarh.

5. Nishant Kumar, Kirti Soni, Ravinder Agarwal. (2017). Linear Support Vector Machine methods for quantitative SODAR Structure. ***"National Symposium on Ultrasonic-2017", November 8-10, 2017,*** CUHP-Dharamshala. (Dr. M. Pancholy Memorial Award-2017)
6. Nishant Kumar, Kirti Soni, Ravinder Agarwal, and Mahavir Singh. (2018). Validation of Mono-Static SODAR data for Atmospheric Boundary Layer Height to MERRA-2 model data. ***"WESPAC-2018"****, 11-15 November 2018*, CSIR-NPL, New Delhi.
7. Nishant Kumar, Kirti Soni, and Mahavir Singh. (2018). Measurement Uncertainty of the Sound Transmission Loss with Different Thickness Materials. ***"WESPAC-2018"****, 11-15 November 2018*, CSIR-NPL, New Delhi.
8. Nishant Kumar, Y. K. Yadav, Kirti Soni, and Mahavir Singh. (2018). Ultrasonic transducer selection for Non-Destructive Testing of materials. ***"WESPAC-2018"****, 11-15 November 2018,* CSIR-NPL, New Delhi. (WESPAC Best Poster Award-2018)
9. Nishant Kumar, Yudhisther K. Yadav, Kirti Soni, Mahavir Singh and Ravinder Agarwal. (2019) Material Characterization by Acoustics Attenuation Measurements in Solids. ***"AdMet 2019",*** *20-22 February 2019,* New Delhi.
10. Nishant Kumar, Kirti Soni, Ravinder Agarwal and Mahavir Singh. (2019). Performance of Acoustic Sounder and analysis of various features of Atmospheric Boundary Layer height during extreme weather conditions. ***"AP-RASC-2019",*** *9-15 March 2019*, New Delhi.
11. Nishant Kumar, Kirti Soni, Ravinder Agarwal, Mahavir Singh and Yudhister K. Yadav. (2019). Detection of Kelvin-Helmholtz billows in the rising layer over Delhi region using SODAR. ***"National Symposium on Acoustics -2019",*** *17-19 October 2019,* Cuttack.
12. **Nishant Kumar,** Kirti Soni, Ravinder Agarwal and Mahavir Singh. (2019). Preliminary analysis of operating conditions of Acoustic Sounder (SODAR) before the installation ***178th Meeting of the Acoustical Society of America (ASA),*** *2-6 December 2019,* San Diego USA.
13. Nishant Kumar, Parag Chourey, Rohan Kamra, Priyanka Singh, Anjali S. Nair, Mamta Devi, Kirti Soni and Mahavir Singh. (2020). Design Considerations and Ambient Noise Problem in SODAR System. ***6th National Conference on "Advances in Metrology – 2020****,* CSIR-NPL, New Delhi.
14. Nishant Kumar, Kirti Soni, Ravinder Agarwal. (2021). Calibration of indigenously developed SODAR Antenna structure acoustic baffle and parabolic dish assembly. ***7th National Conference on "AdMet-2021"*** *05-06 March 2021,* MSIT, New Delhi.

Reference

[1] Stull, Roland B. *An introduction to boundary layer meteorology*. Vol. 13. Springer Science & Business Media, 1988. eBook ISBN 978-94-009-3027-8 DOI 10.1007/978-94-009-3027-8

[2] Emeis, Stefan. *Surface-based remote sensing of the atmospheric boundary layer*. Vol. 40. Springer Science & Business Media, 2010.

[3] Bradley, Stuart. *Atmospheric acoustic remote sensing: principles and applications*. CRC press, 2007.

[4] Singal, Sagar Pal, ed. *Acoustic remote sensing applications*. Vol. 69. Springer, 2006.

[5] Emeis, Stefan, Klaus Schafer, and C. H. R. I. S. T. O. P. H. Munkel. "Surface-based remote sensing of the mixing-layer height-a review." *Meteorologische Zeitschrift* 17, no. 5 (2008): 621.

[6] Seibert, Petra, Frank Beyrich, Sven-Erik Gryning, Sylvain Joffre, Alix Rasmussen, and Philippe Tercier. "Review and intercomparison of operational methods for the determination of the mixing height." *Atmospheric environment* 34, no. 7 (2000): 1001-1027.

[7] Rossing, Thomas D. "Introduction to acoustics." In *Springer handbook of acoustics*, pp. 1-7. Springer, New York, NY, 2014.

[8] Müller, Gerhard, and Michael Möser, eds. *Handbook of engineering acoustics*. Springer Science & Business Media, 2012.

[9] Lo, Yuen T., and S. W. Lee. *Antenna Handbook: theory, applications, and design*. Springer Science & Business Media, 2013.

[10] Coulter, R. L., and M. A. Kallistratova. "Two decades of progress in SODAR techniques: a review of 11 ISARS proceedings." *Meteorology and Atmospheric Physics* 85, no. 1 (2004): 3-19.

[11] Tyndall, John. "VII. On the atmosphere as a vehicle of sound." *Philosophical Transactions of the Royal Society of London* 164 (1874): 183-244.

[12] Gilman, G. W., H. B. Coxhead, and F. H. Willis. "Reflection of sound signals in the troposphere." *The Journal of the Acoustical Society of America* 18, no. 2 (1946): 274-283.

[13] Cox, Everett F. "Upper atmosphere temperatures from remote sound measurements." *American Journal of Physics* 16, no. 9 (1948): 465-474.

[14] Crary, Albert Paddock. *Investigation of stratosphere winds and temperatures from acoustical propagation studies*. Air force cambridge research labs lg hanscom field mass, 1950. Investigation of stratosphere winds and temperatures from acoustical propagation studies. (dtics.mil)

[15] Rothwell, P. "Sound propagation in the lower atmosphere." *The Journal of the Acoustical Society of America* 28, no. 4 (1956): 656-665.

[16] Thomas Jr, Alex Roscoe. *Sonic Investigation of Thermal Inversion Layers of the Atmosphere*. The University of Texas at Austin, 1968.

[17] McAllister, L. G. "Acoustic sounding of the lower troposphere." *Journal of Atmospheric and Terrestrial Physics* 30, no. 7 (1968): 1439-1440.

[18] McAllister, Linday G., John R. Pollard, Allan R. Mahoney, and P. J. R. Shaw. "Acoustic sounding—A new approach to the study of atmospheric structure." *Proceedings of the IEEE* 57, no. 4 (1969): 579-587.

[19] McAllister, L. G. *Wind velocity measurements in the lower atmosphere using acoustic sounding techniques*. WRE, 1971.

[20] Kallistratova, M. A. *Experimental investigation of sound wave scattering in the atmosphere*. Foreign technology div wright-patterson AFB OHIO, 1963.
[21] Little, C. Gordon. "Acoustic methods for the remote probing of the lower atmosphere." *Proceedings of the IEEE* 57, no. 4 (1969): 571-578.
[22] Fukushima, Madoka, Kin-ichiro Akita, and Hiroshi Tanaka. "Sodar probing of small-scale ordered motions appeared in the atmospheric planetary boundary layer." *Journal of the Meteorological Society of Japan. Ser. II* 52, no. 5 (1974): 428-439.
[23] Hall Jr, Freeman F. "Temperature and wind structure studies by acoustic echo-sounding." *Remote sensing of the troposphere* (1972): 18-1.
[24] Brown, Edmund H., and Freeman F. Hall Jr. "Advances in atmospheric acoustics." *Reviews of Geophysics* 16, no. 1 (1978): 47-110.
[25] Mastrantonio, G., F. Einaudi, D. Fua, and D. P. Lalas. "Generation of gravity waves by jet streams in the atmosphere." *Journal of Atmospheric Sciences* 33, no. 9 (1976): 1730-1738.
[26] Ito, Yoshiki, Yasuhiro Kobori, Mitsuaki Horiguchi, Masato Takehisa, and Yasushi Mitsuta. "Development of wind profiling sodar." *Journal of Atmospheric and oceanic technology* 6, no. 5 (1989): 779-784.
[27] Beyrich, F. "Mixing height estimation from sodar data—a critical discussion." *Atmospheric Environment* 31, no. 23 (1997): 3941-3953.
[28] Crescenti, Gennaro H. "The degradation of Doppler sodar performance due to noise: A review." *Atmospheric Environment* 32, no. 9 (1998): 1499-1509.
[29] Ito, Yoshiki. "Design and performance of an acoustic antenna for a phased array Doppler sodar." *Meteorological Applications: A journal of forecasting, practical applications, training techniques and modelling* 5, no. 2 (1998): 149-156.
[30] Sgouros, G., C. G. Helmis, and J. Degleris. "Development and application of an algorithm for the estimation of mixing height with the use of a SODAR-RASS remote sensing system." *International journal of remote sensing* 32, no. 22 (2011): 7297-7313.
[31] Melas, D. "Similarity methods to derive turbulence quantities and mixed-layer depth from sodar measurements in the convective boundary layer: A review." *Applied Physics B Photophysics and Laser Chemistry* 57, no. 1 (1993): 11-17.
[32] Antoniou, Ioannis, Hans E. Jørgensen, Frank Ormel, Stuart Bradley, Sabine von Hünerbein, Stefan Emeis, and Günter Warmbier. "On the theory of SODAR measurement techniques." *Risø National Laboratory, Roskilde, Denmark* (2003).
[33] Bradley, Stuart, and Torben Mikkelsen. "A Review of Sodar Accuracy." In *16th International Symposium for the Advancement of Boundary-Layer Remote Sensing*, pp. 9-14. Steering Committee of the 16th International Symposium for the Advancement of Boundary-Layer Remote Sensing, 2012.
[34] Zlomušica, Elvir. "Particular review on SODAR and LIDAR measurements of Bora wind in Mostar, Bosnia and Herzegovina." *Int. J. Eng. Technol. IJET-IJENS* 13, no. 06 (2013): 53-61.
[35] Kallistratova, M. A., I. V. Petenko, R. D. Kouznetsov, S. N. Kulichkov, O. G. Chkhetiani, I. P. Chunchusov, V. S. Lyulyukin et al. "Sodar sounding of the atmospheric boundary layer: Review of studies at the Obukhov Institute of Atmospheric Physics, Russian Academy of Sciences." *Izvestiya, Atmospheric and Oceanic Physics* 54, no. 3 (2018): 242-256.
[36] Thomson, D. W., and J. P. Scheib. "Improved display techniques for sodar measurements." *Bulletin of the American Meteorological Society* 59, no. 2 (1978): 147-152.
[37] MacCready, Paul. "12. Doppler acoustic system for wind profiling (avit)." *The Boulder Low-level Intercomparison Experiment* 2 (1980): 70.

[38] Maughan, R. A., A. M. Spanton, and M. L. Williams. "An analysis of the frequency distribution of sodar derived mixing heights classified by atmospheric stability." *Atmospheric Environment (1967)* 16, no. 5 (1982): 1209-1218.
[39] Kaimal, J. C. *An evaluation of wind measurements by four Doppler sodars*. Vol. 55. Wave Propagation Laboratory, Environmental Research Laboratory, US Department of Commerce, 1984.
[40] Finkelstein, P. L., J. C. Kaimal, J. E. Gaynor, M. E. Graves, and T. J. Lockhart. "Comparison of wind monitoring systems. Pad II: Doppley. Sodars." *Journal of Atmospheric and Oceanic Technology* 3, no. 4 (1986): 594-604.
[41] Kleppe, John A. "An overview of the technological development of atmospheric echosounders (SODARS)." *Acoustic Remote Sensing Applications* (1997): 35-84.
[42] Crescenti, Gennaro H. "A look back on two decades of Doppler sodar comparison studies." *Bulletin of the American Meteorological society* 78, no. 4 (1997): 651-674.
[43] Seibert, Petra. *Long-time comparison of Remtech PA2 sodar wind and turbulence measurements with Cabauw tower data*. na, 1998.
[44] Keder, J. "Detection of inversions and mixing height by REMTECH PA2 sodar in comparison with collocated radiosonde measurements." *Meteorology and Atmospheric Physics* 71, no. 1 (1999): 133-138.
[45] Amano, T., H. Fukushima, T. Ohkuma, A. Kawaguchi, and S. Goto. "The observation of typhoon winds in Okinawa by Doppler sodar." *Journal of Wind Engineering and Industrial Aerodynamics* 83, no. 1-3 (1999): 11-20.
[46] Antoniou, Ioannis, Hans E. Jørgensen, S. von Hünerbein, Stuart G. Bradley, and Detlef Kindler. "Inter-comparison of commercially available SODARs for wind energy applications." In *Proceedings of the 12th International Symposium on Acoustic Remote Sensing and Associated Techniques of the Atmosphere and Oceans*. 2004.
[47] Kleppe, John A. "Echosounders (SODARS)." *Acoustic Remote Sensing Applications* 69 (2006): 35.
[48] Piper, B., and S. von Hünerbein. "The development of a transponder-based technique for the acoustic calibration of SODARs." In *IOP Conference Series: Earth and Environmental Science*, vol. 1, no. 1, p. 012044. IOP Publishing, 2008.
[49] Urlea, Ana-Denisa, and Mirela Pietrisi. "Study of the Low Level Wind Shear using AMDAR reports." In *EGU General Assembly Conference Abstracts*, p. 2185. 2015.
[50] Zak, J. Allen, and David Rutishauser. "Atmospheric Boundary layer sensors for application in a wake vortex advisory system." (2003).
[51] Mikkelsen, T., L. Kristensen, and H. E. Jørgensen. "Performance test of a new CW bi-static Sodar designed for wind speed measurement during near neutral atmospheric stratifications." In *EGS-AGU-EUG Joint Assembly*, p. 2899. 2003.
[52] Engelbart, D. A. M., and J. Bange. "Determination of boundary-layer parameters using wind profiler/RASS and sodar/RASS in the frame of the LITFASS project." *Theoretical and applied climatology* 73, no. 1 (2002): 53-65.
[53] Singal, S. P., and M. Pancholy. "Acoustic sounder for probing of the lower atmosphere." (1972). 1, 202-204.
[54] Singal, S. P., B. S. Gera, S. K. Aggarwal, and Mrs M. Saxena. "Use of monostatic sodar in probing the lower atmosphere." (1975).4 146-156.
[55] Gera, B. S., and Neeraj Saxena. "Sodar data—A useful input for dispersion modeling." *Atmospheric environment* 30, no. 21 (1996): 3623-3631.
[56] Gera, B. S., T. Raghavendra, G. Singh, V. K. Ojha, Joginder Malik, Neha Gera, and N. C. Gupta. "Instrumentation and computer capabilities for improving sodar data acquisition." *International journal of remote sensing* 32, no. 17 (2011): 4807-4817.

[57] Kumar, Nishant "Atmospheric boundary layer characteristics using monostatic SODAR." M.E. diss., 2015, Published by Thapar University, Patiala.
[58] Kumar, Nishant, Kirti Soni, Naveen Garg, Ravinder Agarwal, D. Saha, Mahavir Singh, and Gurbir Singh. "SODAR pattern classification and its dependence on meteorological parameters over a semiarid region of India." *International Journal of Remote Sensing* 38, no. 11 (2017): 3466-3482.
[59] Neff, W. D., and R. L. Coulter. "Acoustic remote sensing." In *Probing the Atmospheric Boundary Layer*, pp. 201-239. American Meteorological Society, Boston, MA, 1986.
[60] Weill, A., C. Klapisz, and F. Baudin. "The CRPE minisodar: Applications in micrometeorology and in physics of precipitations." *Atmospheric Research* 20, no. 2 (1986): 317-333.
[61] Asimakopoulos, D. N. "High frequency acoustic sounding and its applications." In *Acoustic Remote Sensing: Proc. 5th Int. Symp. on Acoustic Remote Sensing of the Atmosphere and Oceans*, pp. 75-87. 1990.
[62] Marshall, J. M., A. M. Peterson, and A. A. Barnes. "Combined radar-acoustic sounding system." *Applied Optics* 11, no. 1 (1972): 108-112.
[63] Beran, D. W., B. C. Willmarth, F. C. Carsey, and F. F. Hall Jr. "An acoustic Doppler wind measuring system." *The Journal of the Acoustical Society of America* 55, no. 2 (1974): 334-338.
[64] McAllister, L. G. *Wind velocity measurements in the lower atmosphere using acoustic sounding techniques*. WRE, 1971.
[65] Beran, D. W., W. H. Hooke, and S. F. Clifford. "Acoustic echo-sounding techniques and their application to gravity-wave, turbulence, and stability studies." *Boundary-Layer Meteorology* 4, no. 1 (1973): 133-153.
[66] Wesely, Marvin L. "The combined effect of temperature and humidity fluctuations on refractive index." *Journal of Applied Meteorology* 15, no. 1 (1976): 43-49.
[67] Greenfield, R. J., M. Teufel, D. W. Thomson, and R. L. Coulter. "A method for measurement of temperature profiles in inversions from refractive transmission of sound." *Journal of Geophysical Research* 79, no. 36 (1974): 5551-5554.
[68] Mahoney, A. R., L. G. McAllister, and J. R. Pollard. "The remote sensing of wind velocity in the lower troposphere using an acoustic sounder." *Boundary-Layer Meteorology* 4, no. 1 (1973): 155-167.
[69] Lokoshchenko, Mikhail A. "Long-term sodar observations in Moscow and a new approach to potential mixing determination by radiosonde data." *Journal of Atmospheric and oceanic Technology* 19, no. 8 (2002): 1151-1162.
[70] Neff, W., D. Helmig, A. Grachev, and D. Davis. "A study of boundary layer behavior associated with high NO concentrations at the South Pole using a minisodar, tethered balloon, and sonic anemometer." *Atmospheric Environment* 42, no. 12 (2008): 2762-2779.
[71] Emeis, Stefan, Klaus Schäfer, and Christoph Münkel. "Long-term observations of the urban mixing-layer height with ceilometers." In *IOP Conference Series: Earth and Environmental Science*, vol. 1, no. 1, p. 012027. IOP Publishing, 2008.
[72] Sarma, TV Chandrasekhar, D. Narayana Rao, J. Furumoto, and T. Tsuda. "Development of radio acoustic sounding system (RASS) with Gadanki MST radar–first results." *Ann. Geophys* 26 (2008): 2531-2542.
[73] Basha, Ghouse, and M. Venkat Ratnam. "Identification of atmospheric boundary layer height over a tropical station using high-resolution radiosonde refractivity profiles: Comparison with GPS radio occultation measurements." *Journal of Geophysical Research: Atmospheres* 114, no. D16 (2009).

[74] Argentini, S., I. Pietroni, C. Gariazzo, A. Amicarelli, G. Mastrantonio, A. Pelliccioni, I. Petenko, and A. Viola. "Boundary layer temperature profiles by a RASS and a microwave radiometer: Differences, limits and advantages." *Il Nuovo Cimento della Società Italiana di Fisica-B: General Physics, Relativity, Astronomy and Mathematical Physics and Methods* 124, no. 5 (2009): 549.

[75] Legain, Dominique, Olivier Bousquet, Thierry Douffet, Diane Tzanos, Eric Moulin, Joël Barrié, and J-B. Renard. "High-frequency boundary layer profiling with reusable radiosondes." *Atmospheric Measurement Techniques* 6, no. 8 (2013): 2195-2205.

[76] Bonin, Timothy A., David C. Goines, Aaron K. Scott, Charlotte E. Wainwright, Jeremy A. Gibbs, and Phillip B. Chilson. "Measurements of the temperature structure-function parameters with a small unmanned aerial system compared with a sodar." *Boundary-Layer Meteorology* 155, no. 3 (2015): 417-434.

[77] Finn, Anthony, Kevin Rogers, Feng Rice, Joshua Meade, Greg Holland, and Peter May. "A comparison of vertical atmospheric wind profiles obtained from monostatic sodar and unmanned aerial vehicle–based acoustic tomography." *Journal of Atmospheric and Oceanic Technology* 34, no. 10 (2017): 2311-2328.

[78] Dang, Ruijun, Yi Yang, Xiao-Ming Hu, Zhiting Wang, and Shuwen Zhang. "A review of techniques for diagnosing the atmospheric boundary layer height (ABLH) using aerosol lidar data." *Remote Sensing* 11, no. 13 (2019): 1590.

[79] Nambiar, Manoj K., R. Byerlay, Amir Nazem, M. Rafsan Nahian, Mohsen Moradi, and Amir A. Aliabadi. "A Tethered And Navigated Air Blimp (TANAB) for observing the microclimate over a complex terrain." *Geosci. Instrum. Method. Data Syst. Discuss* (2019).

[80] Lyulyukin, Vasily, Margarita Kallistratova, Daria Zaitseva, Dmitry Kuznetsov, Arseniy Artamonov, Irina Repina, Igor Petenko, Rostislav Kouznetsov, and Artem Pashkin. "Sodar observation of the ABL structure and waves over the Black Sea offshore site." *Atmosphere* 10, no. 12 (2019): 811.

[81] Jeričević, Amela, and Branko Grisogono. "The critical bulk Richardson number in urban areas: verification and application in a numerical weather prediction model." *Tellus A: Dynamic Meteorology and Oceanography* 58, no. 1 (2006): 19-27.

[82] Richardson, H., S. Basu, and A. A. M. Holtslag. "Improving stable boundary-layer height estimation using a stability-dependent critical bulk Richardson number." *Boundary-layer meteorology* 148, no. 1 (2013): 93-109.

[83] Upadhyay, Shikhar, Sarit K. Das, and C. S. P. Ojha. "Probabilistic comparison between turbulence closure model and Bulk Richardson Number approach for ABL height estimation using copula." *Dynamics of Atmospheres and Oceans* 87 (2019): 101094.

[84] Fukushima, Madoka. "SODAR probing of small-scale temperature structure in the clear troposphere." (1976).

[85] Hufnagel, Robert E. "An improved model turbulent atmosphere." In *Restoration of Atmospherically Degraded Images*, vol. 2, pp. 14-18. National Academy of Sciences, 1966.

[86] Neff, William D. *Quantitative evaluation of acoustic echoes from the planetary boundary layer*. Vol. 55. Environmental Research Laboratories, 1975.

[87] Asimakopoulos, D. N., R. S. Cole, S. J. Caughey, and B. A. Crease. "A quantitative comparison between acoustic sounder returns and the direct measurement of atmospheric temperature fluctuations." *Boundary-Layer Meteorology* 10, no. 2 (1976): 137-147.

[88] Haugen, Duane A., and J. Chandran Kaimal. "Measuring temperature structure parameter profiles with an acoustic sounder." *Journal of Applied Meteorology and Climatology* 17, no. 6 (1978): 895-899.

[89] Tang, Guiqian, Jinqiang Zhang, Xiaowan Zhu, Tao Song, Christoph Münkel, Bo Hu, Klaus Schäfer et al. "Mixing layer height and its implications for air pollution over Beijing, China." *Atmospheric Chemistry and Physics* 16, no. 4 (2016): 2459-2475.
[90] Gossard, E. E., and J. H. Richter. "The shape of internal waves of finite amplitude from high-resolution radar sounding of the lower atmosphere." *Journal of the Atmospheric Sciences* 27, no. 6 (1970): 971-973.
[91] Beran, D. W., F. F. Hall Jr, J. W. Wescott, and W. D. Neff. "Application of an acoustic sounder to air pollution monitoring." *Collected Reprints* (1974): 75.
[92] Prakash, J. Winston Jeeva, Radhika Ramachandran, K. Narayanan Nair, K. Sen Gupta, and P. K. Kunhikrishnan. "On the structure of sea-breeze fronts observed near the coastline of Thumba, India." *Boundary-layer meteorology* 59, no. 1 (1992): 111-124.
[93] Rees, J. M., J. C. W. Denholm-Price, J. C. King, and P. S. Anderson. "A climatological study of internal gravity waves in the atmospheric boundary layer overlying the Brunt Ice Shelf, Antarctica." *Journal of the atmospheric sciences* 57, no. 4 (2000): 511-526.
[94] Fritts, David C., and M. Joan Alexander. "Gravity wave dynamics and effects in the middle atmosphere." *Reviews of geophysics* 41, no. 1 (2003).
[95] Banakh, Viktor A., and Igor N. Smalikho. "Lidar observations of atmospheric internal waves in the boundary layer of the atmosphere on the coast of Lake Baikal." *Atmospheric Measurement Techniques* 9, no. 10 (2016): 5239-5248.
[96] Kulichkov, S. N., N. D. Tsybulskaya, I. P. Chunchuzov, V. A. Gordin, Ph L. Bykov, A. I. Chulichkov, V. G. Perepelkin, G. A. Bush, and E. V. Golikova. "Studying internal gravity waves generated by atmospheric fronts over the Moscow region." *Izvestiya, Atmospheric and Oceanic Physics* 53, no. 4 (2017): 402-412.
[97] Ottersten, H., M. Hurtig, G. Stilke, B. Brümmer, and G. Peters. "Shipborne sodar measurements during Jonswap 2." *Journal of Geophysical Research* 79, no. 36 (1974): 5573-5584.
[98] Carstensen, Stefan, B. Mutlu Sumer, and Jørgen Fredsøe. "Coherent structures in wave boundary layers. Part 1. Oscillatory motion." *Journal of Fluid Mechanics* 646 (2010): 169.
[99] Mandics, P. A., and F. F. Hall Jr. "Preliminary results from the GATE acoustic echo sounder." *Bulletin of the American Meteorological Society* 57, no. 9 (1976): 1142-1149.
[100] von Glasow, Roland, Rolf Sander, Andreas Bott, and Paul J. Crutzen. "Modeling halogen chemistry in the marine boundary layer 1. Cloud-free MBL." *Journal of Geophysical Research: Atmospheres* 107, no. D17 (2002): ACH-9.
[101] von Glasow, Roland, Rolf Sander, Andreas Bott, and Paul J. Crutzen. "Modeling halogen chemistry in the marine boundary layer 2. Interactions with sulfur and the cloud-covered MBL." *Journal of Geophysical Research: Atmospheres* 107, no. D17 (2002): ACH-2.
[102] Caughey, S. J., and M. Kitchen. "Simultaneous measurements of the turbulent and microphysical structure of nocturnal stratocumulus cloud." *Quarterly Journal of the Royal Meteorological Society* 110, no. 463 (1984): 13-34.
[103] Welti, André, Konrad Müller, Zoë L. Fleming, and Frank Stratmann. "Concentration and variability of ice nuclei in the subtropical maritime boundary layer." *Atmospheric Chemistry and Physics* 18, no. 8 (2018): 5307-5320.
[104] Fukushima, M. "Features of SODAR echoes observed at miyakoma island during the amtex 75." (1976).
[105] Neff, W. D. "Acoustic sounder measurements of the south pole boundary layer." (1976).
[106] Choudhury, Swati, and Sushmita Mitra. "A connectionist approach to SODAR pattern classification." *IEEE Geoscience and Remote Sensing Letters* 1, no. 2 (2004): 42-46.

[107] De, Anindya K., D. P. Mukherjee, P. Pal, and J. Das. "SODAPRETER: a novel approach towards automatic SODAR data interpretation." *International Journal of Remote Sensing* 19, no. 15 (1998): 2987-3002.
[108] Choudhury, Swati, and Sushmita Mitra. "Feature extraction and connectionist classification of SODAR echograms." *IEEE Geoscience and Remote Sensing Letters* 3, no. 1 (2006): 19-22.
[109] Chandara Deb, Narayan, Srimanta Pal, Dipak Chandra Patranabis, and H. N. Dutta. "A neurocomputing model for SODAR structure classification." *International Journal of Remote Sensing* 31, no. 11 (2010): 2995-3018.
[110] Deb, Narayan Chandra, Kumar S. Ray, and Hirday N. Dutta. "SODAR pattern classification by graph matching." *IEEE Geoscience and Remote Sensing Letters* 8, no. 3 (2010): 483-487.
[111] Singal, S. P., B. S. Gera, and Neeraj Saxena. "Sodar: A tool to characterize hazardous situations in air pollution and communication." In *Acoustic remote sensing applications*, pp. 325-384. Springer, Berlin, Heidelberg, 1997.
[112] Parmar, Kulwinder Singh, Sidhu Jitendra Singh Makkhan, and Sachin Kaushal. "Neuro-fuzzy-wavelet hybrid approach to estimate the future trends of river water quality." *Neural Computing and Applications* 31, no. 12 (2019): 8463-8473.
[113] Nair, Hema C., Ammini Joseph, and Vinod Padmakumari Gopinathan. "GIS Based landform classification using digital elevation model: a case study from two river basins of Southern Western Ghats, Kerala, India." *Modeling Earth Systems and Environment* 4, no. 4 (2018): 1355-1363.
[114] Martins, Sarah, Nariane Bernardo, Igor Ogashawara, and Enner Alcantara. "Support vector machine algorithm optimal parameterization for change detection mapping in Funil Hydroelectric Reservoir (Rio de Janeiro State, Brazil)." *Modeling Earth Systems and Environment* 2, no. 3 (2016): 1-10.
[115] Sulma, Sayidah, Fajar Yulianto, Jalu Tejo Nugroho, and Parwati Sofan. "A support vector machine object-based image analysis approach on urban green space extraction using Pleiades-1A imagery." *Modeling Earth Systems and Environment* 2, no. 2 (2016): 54.
[116] Łobocki, Lech. "Relationship between the Monin–Obukhov Stability Parameter and the Bulk Richardson Number at Sea under Unstable Conditions, Derived from a Turbulence-Closure Model." *Journal of Applied Meteorology* 42, no. 5 (2003): 661-666.
[117] Elisei, G., M. Maini, A. Marzorati, M. G. Morselli, G. Fiocco, S. Cantarano, and G. Mastrantonio. "Implementation of a multiaxial Doppler sodar system with advanced data processing." *Atmospheric Research* 20, no. 2-4 (1986): 109-118.
[118] Takehisa, Masato, Yoshiki Ito, Tsuyoshi Kataoka, and Yasushi Mitsuta. "Precision and relative accuracy of a phased array Doppler sodar." *Bulletin of the Disaster Prevention Research Institute* 42, no. 2 (1992): 65-70.
[119] Ito, Yoshiki. "Design of a tri-monostatic doppler sodar system." In *Acoustic Remote Sensing Applications*, pp. 85-104. Springer, Berlin, Heidelberg, 1997.
[120] Engelbart, D., H. Steinhagen, U. Görsdorf, J. Neisser, H. J. Kirtzel, and G. Peters. "First results of measurements with a newly-designed phased-array sodar with RASS." *Meteorology and Atmospheric Physics* 71, no. 1 (1999): 61-68.
[121] Anandan, V. K., M. Shravan Kumar, and I. Srinivasa Rao. "First results of experimental tests of the newly developed NARL phased-array Doppler Sodar." *Journal of Atmospheric and Oceanic Technology* 25, no. 10 (2008): 1778-1784.

[122] Strauch, R. G., and W. B. Sweezy. *Wind Shear Detection with Pulse Doppler Radar*. National Oceanic and Atmospheric Administration Boulder Co Wave Propagation Lab, 1980.
[123] Owens, Edward J. *Microcomputer-controlled acoustic echo sounder*. Vol. 21. Department of Commerce, National Oceanic and Atmospheric Administration, Environmental Research Laboratories, Wave Propagation Laboratory, 1977.
[124] Argentini, Stefania, Giangiuseppe Mastrantonio, Igor Petenko, Ilaria Pietroni, and Angelo Viola. "Use of a high-resolution sodar to study surface-layer turbulence at night." *Boundary-layer meteorology* 143, no. 1 (2012): 177-188.
[125] Gaynor, J. E. "Acoustic Doppler measurement of atmospheric boundary layer velocity structure functions and energy dissipation rates." *Journal of Applied Meteorology and Climatology* 16, no. 2 (1977): 148-155.
[126] Coulter, R. L. "A case study of turbulence in the stable nocturnal boundary layer." *Boundary-Layer Meteorology* 52, no. 1 (1990): 75-91.
[127] L E. Kinsler, A. R. Frey, A. B. Coppens and J. V. Sanders, Fundamentals of acoustics, 4th Edition, Wiley-VCH, (1999). ISBN 0-471-84789-5
[128] ISO 6926:2016(en) Acoustics — Requirements for the performance and calibration of reference sound sources used for the determination of sound power levels.
[129] ANSI/ASA S1.13-2005 (R2010) Measurement of Sound Pressure Levels in Air.
[130] ANSI S1.22-1992 (R2007) American National Standard Scales and Sizes for Frequency Characteristics and Polar Diagrams in Acoustics.
[131] ANSI/ASA S1.26-2014 Methods for Calculation of The Absorption of Sound by The Atmosphere.
[132] ISO 26101:2012 Acoustics — Test methods for the qualification of free-field environments.
[133] Chiariotti, Paolo, Milena Martarelli, and Paolo Castellini. "Acoustic beamforming for noise source localization–Reviews, methodology and applications." *Mechanical Systems and Signal Processing* 120 (2019): 422-448.
[134] Gaynor, J. E. "Accuracy of sodar wind variance measurements." *Remote Sensing* 15, no. 2 (1994): 313-324.
[135] Travouillon, T. "SODAR calibration for turbulence profiling in TMT site testing." In *Ground-based and Airborne Telescopes*, vol. 6267, p. 626720. International Society for Optics and Photonics, 2006.
[136] Danilov, S. D., A. E. Gur'Yanov, M. A. Kallistratova, I. V. Petenko, S. P. Singal, D. R. Pahwa, and B. S. Gera. "Acoustic calibration of sodars." *Measurement Science and Technology* 3, no. 10 (1992): 1001.
[137] Bradley, Stuart, Ioannis Antoniou, and S. Von Hunerbein. "Sodar calibration procedure." *Final Reporting on WP3, EU WISE Project NNE5-2001* 297 (2005).
[138] Simmons, W. R., J. W. Wescott, and Freeman F. Hall. *Acoustic echo sounding as related to air pollution in urban environments*. Vol. 2. Environmental Research Laboratories, 1971.
[139] Beran, D. W., and F. F. Hall Jr. "Remote sensing for air pollution meteorology." *Bulletin of the American Meteorological Society* 55, no. 9 (1974): 1097-1106.
[140] Hicks, R. B., and T. Mathews. "Impact of chinooks on Calgary's air quality: Acoustic sounder observations of atmospheric stability." *Water, Air, and Soil Pollution* 11, no. 2 (1979): 159-172.

[141] Jensen, Niels Otto, and Erik L. Petersen. "The box model and the acoustic sounder, a case study." *Atmospheric Environment (1967)* 13, no. 5 (1979): 717-720.
[142] Asimakopoulos, D. N. "Application of sodar and lidar techniques in air pollution monitoring: A report on the EURASAP 90 international meeting." *Atmospheric Environment. Part A. General Topics* 25, no. 9 (1991): 2057-2060.
[143] Singal, S. P. "Monitoring air pollution related meteorology using sodar." *Applied Physics B Photophysics and Laser Chemistry* 57, no. 1 (1993): 65-82.
[144] Walczewski, Jacek. "Application of sodar in urban air-quality monitoring systems." In *Acoustic Remote Sensing Applications*, pp. 385-394. Springer, Berlin, Heidelberg, 1997.
[145] Li, Xiaolan, Xiao-Ming Hu, Yanjun Ma, Yangfeng Wang, Liguang Li, and Ziqi Zhao. "Impact of planetary boundary layer structure on the formation and evolution of air-pollution episodes in Shenyang, Northeast China." *Atmospheric Environment* 214 (2019): 116850.
[146] Singal, S. P., B. S. Gera, and D. R. Pahwa. "Application of sodar to air pollution meteorology." *Remote Sensing* 15, no. 2 (1994): 427-441.
[147] Soni, Kirti, Kulwinder Singh Parmar, and Sanjeev Agrawal. "Modeling of air pollution in residential and industrial sites by integrating statistical and Daubechies wavelet (level 5) analysis." *Modeling Earth Systems and Environment* 3, no. 3 (2017): 1187-1198.
[148] Makkhan, Sidhu Jitendra Singh, Kulwinder Singh Parmar, Sachin Kaushal, and Kirti Soni. "Correlation and time-series analysis of black carbon in the coal mine regions of India: a case study." *Modeling Earth Systems and Environment* 6, no. 2 (2020): 659-669.
[149] Kisi, Ozgur, Kulwinder Singh Parmar, Kirti Soni, and Vahdettin Demir. "Modeling of air pollutants using least square support vector regression, multivariate adaptive regression spline, and M5 model tree models." *Air Quality, Atmosphere & Health* 10, no. 7 (2017): 873-883.
[150] Moulsley, T. J., D. N. Asimakopoulos, R. S. Cole, B. A. Crease, and S. J. Caughey. "Measurement of boundary layer structure parameter profiles by acoustic sounding and comparison with direct measurements." *Quarterly Journal of the Royal Meteorological Society* 107, no. 451 (1981): 203-230.
[151] Singal, S. P., S. K. Aggarwal, D. R. Pahwa, and B. S. Gera. "Stability studies with the help of acoustic sounding." *Atmospheric Environment (1967)* 19, no. 2 (1985): 221-228.
[152] Helmis, C. G., G. Sgouros, M. Tombrou, K. Schäfer, C. Münkel, E. Bossioli, and A. Dandou. "A comparative study and evaluation of mixing-height estimation based on sodar-RASS, ceilometer data and numerical model simulations." *Boundary-layer meteorology* 145, no. 3 (2012): 507-526.
[153] Mahalakshmi, D. V., K. V. S. Badarinath, and C. V. Naidu. "Influence of boundary layer dynamics on pollutant concentrations over urban region–A study using ground-based measurements." IJRSP 40 no. 3 (2011): 147-152.
[154] Du, Chuanli, Shuyan Liu, Xing Yu, Xingmin Li, Chuang Chen, Yang Peng, Yan Dong, Zipeng Dong, and Fanqiang Wang. "Urban boundary layer height characteristics and relationship with particulate matter mass concentrations in Xi'an, central China." *Aerosol and Air Quality Research* 13, no. 5 (2013): 1598-1607.
[155] Saha, D., Kirti Soni, M. N. Mohanan, and Mahavir Singh. "Long-term trend of ventilation coefficient over Delhi and its potential impacts on air quality." *Remote Sensing Applications: Society and Environment* 15 (2019): 100234.

[156] Kumar, M., K. S. Parmar, D. B. Kumar, A. Mhawish, D. M. Broday, R. K. Mall, and T. Banerjee. "Long-term aerosol climatology over Indo-Gangetic Plain: Trend, prediction and potential source fields." *Atmospheric environment* 180 (2018): 37-50.
[157] Gera, N., N. C. Gupta, V. Mohanan, and B. S. Gera. "Sodar studies of air pollution meteorology over Delhi." *International Journal of Scientific and Engineering Research* 4, no. 8 (2013): 1805-1811.
[158] Garratt, John Roy. "The atmospheric boundary layers." *Earth-Science Reviews* 37, no. 1-2 (1994): 89-134.
[159] Murthy, B. S., R. Latha, Arpit Tiwari, Aditi Rathod, Siddhartha Singh, and G. Beig. "Impact of mixing layer height on air quality in winter." *Journal of Atmospheric and Solar-Terrestrial Physics* 197 (2020): 105157.
[160] Terradellas, E., M. R. Soler, E. Ferreres, and M. Bravo. "Analysis of oscillations in the stable atmospheric boundary layer using wavelet methods." *Boundary-layer meteorology* 114, no. 3 (2005): 489-518.
[161] Niska, Harri, Teri Hiltunen, Ari Karppinen, Juhani Ruuskanen, and Mikko Kolehmainen. "Evolving the neural network model for forecasting air pollution time series." *Engineering Applications of Artificial Intelligence* 17, no. 2 (2004): 159-167.
[162] Freeman, Brian S., Graham Taylor, Bahram Gharabaghi, and Jesse Thé. "Forecasting air quality time series using deep learning." *Journal of the Air & Waste Management Association* 68, no. 8 (2018): 866-886.
[163] Levi, Yoav, Uri Dayan, Ilan Levy, and David M. Broday. "On the association between characteristics of the atmospheric boundary layer and air pollution concentrations." *Atmospheric Research* 231 (2020): 104675.
[164] Liu, Cheng, Jianping Huang, Yongwei Wang, Xinyu Tao, Cheng Hu, Lichen Deng, Jiaping Xu et al. "Vertical distribution of PM2. 5 and interactions with the atmospheric boundary layer during the development stage of a heavy haze pollution event." *Science of the Total Environment* 704 (2020): 135329.
[165] Koffi, E. N., P. Bergamaschi, Ute Karstens, M. Krol, A. Segers, M. Schmidt, I. Levin et al. "Evaluation of the boundary layer dynamics of the TM5 model over Europe." *Geoscientific Model Development* 9, no. 9 (2016): 3137-3160.
[166] Selvin, Sreelekshmy, R. Vinayakumar, E. A. Gopalakrishnan, Vijay Krishna Menon, and K. P. Soman. "Stock price prediction using LSTM, RNN and CNN-sliding window model." In *2017 international conference on advances in computing, communications and informatics (icacci)*, pp. 1643-1647. IEEE, 2017.
[167] Ettouney, Reem S., Farouq S. Mjalli, John G. Zaki, Mahmoud A. El-Rifai, and Hisham M. Ettouney. "Forecasting of ozone pollution using artificial neural networks." *Management of Environmental Quality: An International Journal* (2009).
[168] Chelani, A. B. "Predicting chaotic time series of PM10 concentration using artificial neural network." *International journal of environmental studies* 62, no. 2 (2005): 181-191.
[169] Rehman, Shafiqur, and Mohamed Mohandes. "Artificial neural network estimation of global solar radiation using air temperature and relative humidity." *Energy Policy* 36, no. 2 (2008): 571-576.
[170] Vivas, David R., Estiven Sánchez, and John H. Reina. "Deep learning the atmospheric boundary layer height." *arXiv preprint arXiv:2004.04353* (2020).
[171] Zaidi, Sheheryar, Arber Zela, Thomas Elsken, Chris Holmes, Frank Hutter, and Yee Whye Teh. "Neural ensemble search for performant and calibrated predictions." *arXiv preprint arXiv:2006.08573* (2020).
[172] Hochreiter, Sepp, and Jürgen Schmidhuber. "Long short-term memory." *Neural computation* 9, no. 8 (1997): 1735-1780.

[173] Kawakami, Kazuya. "Supervised sequence labelling with recurrent neural networks." *Ph. D. thesis* (2008).
[174] Zhao, Jun, Jiaji Wu, Xiaowei Guo, Jie Han, Kai Yang, and Hongguang Wang. "Prediction of radar sea clutter based on LSTM." *Journal of Ambient Intelligence and Humanized Computing* (2019): 1-8.
[175] Peshin, Sunil Kumar, Priyanka Sinha, and A. M. I. T. Bisht. "Impact of Diwali firework emissions on air quality of New Delhi, India during 2013-2015." *Mausam* 68, no. 1 (2017): 111-118.
[176] Tiwari, Suresh, Dilip M. Chate, Manoj K. Srivastava, P. D. Safai, A. K. Srivastava, D. S. Bisht, and B. Padmanabhamurty. "Statistical evaluation of PM 10 and distribution of PM 1, PM 2.5, and PM 10 in ambient air due to extreme fireworks episodes (Deepawali festivals) in megacity Delhi." *Natural hazards* 61, no. 2 (2012): 521-531.
[177] Yerramsetti, Venkata Swamy, Anu Rani Sharma, Nikhil Gauravarapu Navlur, Venkanna Rapolu, NSK Chitanya Dhulipala, and P. R. Sinha. "The impact assessment of Diwali fireworks emissions on the air quality of a tropical urban site, Hyderabad, India, during three consecutive years." *Environmental monitoring and assessment* 185, no. 9 (2013): 7309-7325.
[178] Barman, S. C., Ramesh Singh, M. P. S. Negi, and S. K. Bhargava. "Ambient air quality of Lucknow City (India) during use of fireworks on Diwali Festival." *Environmental monitoring and assessment* 137, no. 1 (2008): 495-504.
[179] National Ambient Air Quality Standards (NAAQS), Notification 18th Nov. 2009, Central Pollution Control Board. SO 384(E) and SO 935(E). *http://cpcb.nic.in/cpcbold/upload/Publications/Publication_514_airqualitystatus2009.pdf*
[180] Khafaie, Morteza Abdullatif, Chittaranjan S. Yajnik, Sundeep S. Salvi, and Ajay Ojha. "Critical review of air pollution health effects with special concern on respiratory health." *Journal of air pollution and health* 1, no. 2 (2016): 123-136.
[181] Rizwan, S. A., Baridalyne Nongkynrih, and Sanjeev Kumar Gupta. "Air pollution in Delhi: its magnitude and effects on health." *Indian journal of community medicine: official publication of Indian Association of Preventive & Social Medicine* 38, no. 1 (2013): 4.
[182] Maji, Kamal Jyoti, Anil Kumar Dikshit, and Ashok Deshpande. "Disability-adjusted life years and economic cost assessment of the health effects related to PM 2.5 and PM 10 pollution in Mumbai and Delhi, in India from 1991 to 2015." *Environmental Science and Pollution Research* 24, no. 5 (2017): 4709-4730.
[183] Nasir, U. P., and D. Brahmaiah. "Impact of fireworks on ambient air quality: a case study." *International journal of environmental science and technology* 12, no. 4 (2015): 1379-1386.
[184] SENGUPTA, B. "Epidemiological study on effect of air pollution on human health (adults) in Delhi." (2008): 229-235.
[185] Kumar, G. "Epidemiological study on effect of air pollution on human health (adults) in Delhi." *Central pollution control board, Ministry of environment and forests, Delhi, India, (Jan. 2012)*.
[186] Attri, Arun K., Ujjwal Kumar, and V. K. Jain. "Formation of ozone by fireworks." *Nature* 411, no. 6841 (2001): 1015-1015.
[187] Kulshrestha, U. C., T. Nageswara Rao, S. Azhaguvel, and M. J. Kulshrestha. "Emissions and accumulation of metals in the atmosphere due to crackers and sparkles during Diwali festival in India." *Atmospheric Environment* 38, no. 27 (2004): 4421-4425.

[188] Wang, Ying, Guoshun Zhuang, Chang Xu, and Zhisheng An. "The air pollution caused by the burning of fireworks during the lantern festival in Beijing." *Atmospheric Environment* 41, no. 2 (2007): 417-431.
[189] Vecchi, Roberta, Vera Bernardoni, Diana Cricchio, Alessandra D'Alessandro, Paola Fermo, Franco Lucarelli, Silvia Nava, Andrea Piazzalunga, and Gianluigi Valli. "The impact of fireworks on airborne particles." *Atmospheric Environment* 42, no. 6 (2008): 1121-1132.
[190] Ravindra, Khaiwal, Suman Mor, and C. P. Kaushik. "Short-term variation in air quality associated with firework events: a case study." *Journal of Environmental Monitoring* 5, no. 2 (2003): 260-264.
[191] Singh, D. P., Ranu Gadi, T. K. Mandal, C. K. Dixit, Khem Singh, T. Saud, Nahar Singh, and Prabhat K. Gupta. "Study of temporal variation in ambient air quality during Diwali festival in India." *Environmental monitoring and assessment* 169, no. 1 (2010): 1-13.
[192] Mandal, Papiya, Mamta Prakash, and J. K. Bassin. "Impact of Diwali celebrations on urban air and noise quality in Delhi City, India." *Environmental monitoring and assessment* 184, no. 1 (2012): 209-215.
[193] Song, Yang, Xiaoming Wan, Shuoxin Bai, Dong Guo, Ci Ren, Yu Zeng, Yirui Li, and Xuewen Li. "The characteristics of air pollutants during two distinct episodes of fireworks burning in a Valley City of North China." *PloS one* 12, no. 1 (2017): e0168297.
[194] Ghei, Dhananjay, and Renuka Sane. "Estimates of air pollution in Delhi from the burning of firecrackers during the festival of Diwali." *PloS one* 13, no. 8 (2018): e0200371.
[195] Zhang, Min, Xuemei Wang, Jianmin Chen, Tiantao Cheng, Tao Wang, Xin Yang, Youguo Gong, Fuhai Geng, and Changhong Chen. "Physical characterization of aerosol particles during the Chinese New Year's firework events." *Atmospheric Environment* 44, no. 39 (2010): 5191-5198.
[196] Arora, Anu, Anita Kumari, and Umesh Kulshrestha. "Respirable mercury particulates and other chemical constituents in festival aerosols in Delhi." *Current World Environment* 13, no. 1 (2018): 3.
[197] Sharma, Disha, and U. C. Kulshrestha. "Spatial and temporal patterns of air pollutants in rural and urban areas of India." *Environmental pollution* 195 (2014): 276-281.
[198] Tatarskii, Valerian Ilich. "Wave Propagation in Turbulent Medium." *Wave Propagation in Turbulent Medium* (1961).
[199] Monin, A. S. "Characteristics of the scattering of sound in a turbulent atmosphere." *Sov. Phys. Acoust* 7, no. 4 (1962): 370-373.
[200] Parry, H. Dean, and Melvin J. Sanders. "The design and operation of an acoustic radar." *IEEE Transactions on Geoscience Electronics* 10, no. 1 (1972): 58-64.
[201] Georges, T. M., and S. F. Clifford. "Acoustic sounding in a refracting atmosphere." *The Journal of the Acoustical Society of America* 52, no. 5B (1972): 1397-1405.
[202] Georges, T. M., & Clifford, S. F. (1974). Estimating refractive effects in acoustic sounding. *The Journal of the Acoustical Society of America*, *55*(5), 934-936.
[203] Nalbandian, O. G. "The signal frequency spectrum in radioacoustic sounding of the atmosphere." *Akademiia Nauk SSSR Fizika Atmosfery i Okeana* 12 (1977): 772-774.
[204] Fortuna, J., and E. Kozaczka. "Review of acoustical methods of probing the atmoshperic boundary layer." *Archives of Acoustics* 17, no. 4 (2014): 453-510.
[205] Harris, Cyril M. "Absorption of Sound in Air in the Audio-Frequency Range." *The Journal of the Acoustical Society of America* 35, no. 1 (1963): 11-17.

[206] Harris, Cyril M. "Absorption of sound in air versus humidity and temperature." *The Journal of the Acoustical Society of America* 40, no. 1 (1966): 148-159.
[207] Singal, S. P., J. R. Anand, B. S. Gera, and S. K. Agarwal. "Design, Fabrication & Studifs of the Directional Acoustic Antennas for Use in the Acoustic Sounding Technique." (1975).
[208] Bass, H. E., L. C. Sutherland, and A. J. Zuckerwar. "Atmospheric absorption of sound: Update." *The Journal of the Acoustical Society of America* 88, no. 4 (1990): 2019-2021.
[209] Aggarwal, S. K., S. P. Singal, Ramesh K. Kapoor, and B. B. Adiga. "A study of atmospheric structures using sodar in relation to land and sea breezes." *Boundary-Layer Meteorology* 18, no. 4 (1980): 361-371.
[210] Ramachandran, S., Sumita Kedia, and Rohit Srivastava. "Aerosol optical depth trends over different regions of India." *Atmospheric Environment* 49 (2012): 338-347.
[211] Roy, Shouraseni Sen, R. B. Singh, and Manoj Kumar. "An analysis of local spatial temperature patterns in the Delhi Metropolitan Area." *Physical Geography* 32, no. 2 (2011): 114-138.
[212] Singal, S. P., and S. K. Aggarwal. "Sodar & radiosonde studies of thermal structure of the lower atmosphere at Delhi." 8 (1979): 76-81.
[213] Kumar, N., K. S. Parmar, K. Soni, N. Garg, and R. Agarwal. "Prediction of ventilation coefficient, using a conjunction model of wavelet-Neuro-fuzzy Model: A Case Study Delhi, India." *Academia Journal of Scientific Research* 3 (2015): 184-191.
[214] Paktiawal, Ajmal, and Mehtab Alam. "An experimental study on effect of aluminum composite panel waste on performance of cement concrete." *Ain Shams Engineering Journal* 12, no. 1 (2021): 83-98.
[215] Kalogiros, J. A., C. G. Helmis, D. N. Asimakopoulos, P. G. Papageorgas, and A. T. Soilemes. "A layer detection and classification algorithm for sodar facsimile records." *Remote Sensing* 16, no. 15 (1995): 2939-2954.
[216] Mukherjee, Abhik, Pinakpani Pal, and J. Das. "Classification of Sodar Data Using Fractal Features." In *ICVGIP*. 2002.
[217] Chaudhuri, B. B., A. Ganguli, A. K. De, and J. Das. "Algorithm development for the machine recognition of sodar structure." *Acoustic Remote Sensing* (1990): 155-160.
[218] Tang, Jiliang, Salem Alelyani, and Huan Liu. "Feature selection for classification: A review." *Data classification: Algorithms and applications* (2014): 37.
[219] Zaffalon, Marco, and Marcus Hutter. "Robust feature selection by mutual information distributions." *arXiv preprint cs/0206006* (2002).
[220] Biesiada, Jacek, Włodzisław Duch, Adam Kachel, Krystian Maczka, and Sebastian Palucha. "Feature ranking methods based on information entropy with parzen windows." In *International Conference on Research in Electrotechnology and Applied Informatics*, vol. 1, p. 1. 2005.
[221] Wang, Jun, Jin-Mao Wei, Zhenglu Yang, and Shu-Qin Wang. "Feature selection by maximizing independent classification information." *IEEE transactions on knowledge and data engineering* 29, no. 4 (2017): 828-841.
[222] Parmar, Chintan, Patrick Grossmann, Johan Bussink, Philippe Lambin, and Hugo JWL Aerts. "Machine learning methods for quantitative radiomic biomarkers." *Scientific reports* 5, no. 1 (2015): 1-11.
[223] Kriti, J. Virmani and R.Agarwal. "Characterization of breast tumors using selected laws' mask texture features." In *2017 Fourth International Conference on Image Information Processing (ICIIP)*, pp. 1-6. IEEE, 2017.
[224] Samant, Piyush, and Ravinder Agarwal. "Machine learning techniques for medical diagnosis of diabetes using iris images." *Computer methods and programs in biomedicine* 157 (2018): 121-128.

[225] CLA, Classification Learner App 2018. https://in.mathworks.com/help/stats/classification-learner-app.html
[226] Bonacich, Phillip. "Power and centrality: A family of measures." *American journal of sociology* 92, no. 5 (1987): 1170-1182.
[227] Guyon, Isabelle, Jason Weston, Stephen Barnhill, and Vladimir Vapnik. "Gene selection for cancer classification using support vector machines." *Machine learning* 46, no. 1 (2002): 389-422.
[228] He, Xiaofei, Deng Cai, and Partha Niyogi. "Laplacian score for feature selection." *Advances in neural information processing systems* 18 (2005): 507-514.
[229] Gu, Quanquan, Zhenhui Li, and Jiawei Han. "Generalized fisher score for feature selection." *arXiv preprint arXiv:1202.3725* (2012).
[230] Borah, Pallabi, Hasin A. Ahmed, and Dhruba K. Bhattacharyya. "A statistical feature selection technique." *Network Modeling Analysis in Health Informatics and Bioinformatics* 3, no. 1 (2014): 1-13.
[231] Roffo, G., and S. Melzi. "Ranking to learn: Feature ranking and selection via eigenvector centrality. New Frontiers in Mining Complex Patterns." In *Fifth International workshop, nfMCP2016*. 2017.
[232] Soni, Kirti, and Kulwinder Singh Parmar. "Soft computing applications in air pollution meteorology." *Intelligent Data Analytics for Decision-Support Systems in Hazard Mitigation* (2021): 441-469.
[233] Unal, Yurdanur, Tayfun Kindap, and Mehmet Karaca. "Redefining the climate zones of Turkey using cluster analysis." *International Journal of Climatology: A Journal of the Royal Meteorological Society* 23, no. 9 (2003): 1045-1055.
[234] Kingma, Diederik P., and Jimmy Ba. "Adam: A method for stochastic optimization." *arXiv preprint arXiv:1412.6980* (2014).
[235] Adnan, Rana Muhammad, Zhongmin Liang, Kulwinder Singh Parmar, Kirti Soni, and Ozgur Kisi. "Modeling monthly streamflow in mountainous basin by MARS, GMDH-NN and DENFIS using hydroclimatic data." *Neural Computing and Applications* 33, no. 7 (2021): 2853-2871.
[236] Frigge, Michael, David C. Hoaglin, and Boris Iglewicz. "Some implementations of the boxplot." *The American Statistician* 43, no. 1 (1989): 50-54.
[237] Williamson, David F., Robert A. Parker, and Juliette S. Kendrick. "The box plot: a simple visual method to interpret data." *Annals of internal medicine* 110, no. 11 (1989): 916-921.
[238] Soni, Kirti, Sachchidanand Singh, Tarannum Bano, R. S. Tanwar, and Shambhu Nath. "Wavelength dependence of the aerosol Angstrom exponent and its implications over Delhi, India." *Aerosol Science and Technology* 45, no. 12 (2011): 1488-1498.
[239] Sujatha, P., D. V. Mahalakshmi, A. Ramiz, P. V. N. Rao, and C. V. Naidu. "Ventilation coefficient and boundary layer height impact on urban air quality." *Cogent Environmental Science* 2, no. 1 (2016): 1125284.
[240] Stackpole, John D. "Numerical analysis of atmospheric soundings." *Journal of Applied Meteorology* 6, no. 3 (1967): 464-467.
[241] Gross, Edward. *The national air pollution potential forecast program*. National Meteorological Center Washington DC, 1970.
[242] Kaul, Nivedita, A. B. Gupta, Sumit Khandelwal, Gaurav Singh, and Virendra Singh. "Impact of exposure to cooking-generated air pollution on human respiratory health: A case study of different microenvironments of India." *Human and Ecological Risk Assessment: An International Journal* 23, no. 8 (2017): 1989-2001.
[243] Kathuria, Vinish. "Vehicular pollution control in Delhi." *Transportation Research Part D: Transport and Environment* 7, no. 5 (2002): 373-387.

[244] Wagner, Patrick, and Klaus Schäfer. "Influence of mixing layer height on air pollutant concentrations in an urban street canyon." *Urban Climate* 22 (2017): 64-79.
[245] Chen, Sheng, Xia Hong, Chris J. Harris, and Paul M. Sharkey. "Sparse modeling using orthogonal forward regression with PRESS statistic and regularization." *IEEE Transactions on Systems, Man, and Cybernetics, Part B (Cybernetics)* 34, no. 2 (2004): 898-911.
[246] Noori, Roohollah, Gholamali Hoshyaripour, Khosro Ashrafi, and Babak Nadjar Araabi. "Uncertainty analysis of developed ANN and ANFIS models in prediction of carbon monoxide daily concentration." *Atmospheric Environment* 44, no. 4 (2010): 476-482.
[247] Noori, R., A. R. Karbassi, A. Moghaddamnia, D. Han, M. H. Zokaei-Ashtiani, A. Farokhnia, and M. Ghafari Gousheh. "Assessment of input variables determination on the SVM model performance using PCA, Gamma test, and forward selection techniques for monthly stream flow prediction." *Journal of hydrology* 401, no. 3-4 (2011): 177-189.
[248] Eksioglu, Burak, Riza Demirer, and Ismail Capar. "Subset selection in multiple linear regression: a new mathematical programming approach." *Computers & Industrial Engineering* 49, no. 1 (2005): 155-167.
[249] Chen, Sheng, Stephen A. Billings, and Wan Luo. "Orthogonal least squares methods and their application to non-linear system identification." *International Journal of control* 50, no. 5 (1989): 1873-1896.
[250] Wang, X. X., Sheng Chen, David Lowe, and Chris J. Harris. "Sparse support vector regression based on orthogonal forward selection for the generalised kernel model." *Neurocomputing* 70, no. 1-3 (2006): 462-474.
[251] Moazami, Saber, Roohollah Noori, Bahman Jabbarian Amiri, Bijan Yeganeh, Sadegh Partani, and Salman Safavi. "Reliable prediction of carbon monoxide using developed support vector machine." *Atmospheric Pollution Research* 7, no. 3 (2016): 412-418.

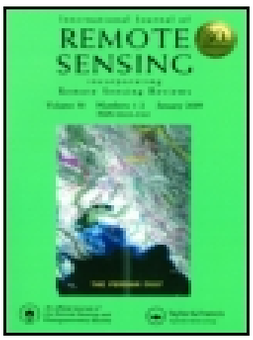

International Journal of Remote Sensing

ISSN: 0143-1161 (Print) 1366-5901 (Online) Journal homepage: http://www.tandfonline.com/loi/tres20

SODAR pattern classification and its dependence on meteorological parameters over a semiarid region of India

Nishant Kumar, Kirti Soni, Naveen Garg, Ravinder Agarwal, D. Saha, Mahavir Singh & Gurbir Singh

To cite this article: Nishant Kumar, Kirti Soni, Naveen Garg, Ravinder Agarwal, D. Saha, Mahavir Singh & Gurbir Singh (2017) SODAR pattern classification and its dependence on meteorological parameters over a semiarid region of India, International Journal of Remote Sensing, 38:11, 3466-3482, DOI: 10.1080/01431161.2017.1294774

To link to this article: http://dx.doi.org/10.1080/01431161.2017.1294774

INTERNATIONAL JOURNAL OF REMOTE SENSING, 2017
VOL. 38, NO. 11, 3466–3482
http://dx.doi.org/10.1080/01431161.2017.1294774

Taylor & Francis
Taylor & Francis Group

SODAR pattern classification and its dependence on meteorological parameters over a semiarid region of India

Nishant Kumar[a], Kirti Soni[b], Naveen Garg[b], Ravinder Agarwal[a], D. Saha[c], Mahavir Singh[b] and Gurbir Singh[b]

[a]Electrical and Instrumentation Engineering Department, Thapar University, Patiala, India; [b]Physico Mechanical Standards (PMS) Division, CSIR-National Physical Laboratory, New Delhi, India; [c]I/c-Air Laboratory Division, Parivesh Bhawan, East Arjun Nagar, New Delhi, India

ABSTRACT

The variability of the atmospheric boundary layer together with meteorological parameters has been investigated over the semiarid region Delhi. Two sources of the dataset have been used: sound detection and ranging (SODAR) and automatic weather station during the period from December 2013 to November 2014. A Laboratory Virtual Instrument Engineering Workbench (LabVIEW)-based programme has been developed to plot the stability class from A to F directly from the mixing height dataset. Based on the SODAR echograms and mixing height, temporal and seasonal variability of stability classes has been estimated. It is observed that the convective boundary layer height advances and decreases during the daytime depending on the increase and decrease of surface temperature due to solar heating of the ground. From seasonal classification of the stability class, it is observed that the class A and class E are dominated in convection and nocturnal periods in all seasons, whereas class F is not found during the winter and pre-monsoon seasons. Impact of meteorological parameters, that is, wind speed, temperature, and relative humidity on mixing height during different seasons has also been studied.

ARTICLE HISTORY
Received 14 July 2015
Accepted 30 January 2017

1. Introduction

The lower atmospheric boundary layer (ABL) is the part of the troposphere where human beings live. In this layer, air pollutants are transported and dispersed and therefore atmospheric stability plays the important role. The extent of stability near the ground is dependent mainly upon the net radiation and wind speed. Instability usually occurs with high positive net radiation and high wind speed; stability usually occurs with high negative net radiation and low winds; and neutral conditions are produced by cloudy skies and/or high wind speeds. The stability conditions can occur only during the night and unstable conditions during the day, night being taken as the period from 1 h before sunset to 1 h after sunrise (Zoras, Triantafyllou, and Deligiorgi 2006; Ashrafi and Hoshyaripour 2008). ABL height totally depends on meteorological parameters. The degree of stability of the atmosphere should be

CONTACT Kirti Soni soniks@nplindia.org CSIR-National Physical Laboratory, Delhi, India

known to estimate the ability of it to disperse air pollutants (Wark, Warner, and Davis 1998; Ashrafi and Hoshyaripour 2008). To estimate the atmospheric stability and mixing height different methods are used, for example, Pasquill–Gifford stability classification, Pasquill–Turner stability classification, among others and for the calculation of the mixing height radiosonde, sound detection and ranging (SODAR), lidar, radio acoustic sounding systems (RASS), among others are used (Singal 1989). These methods define different ways to estimate atmospheric stability and mixing height when convection and mechanical turbulence are considered. The information on the 'open' structure (associated with unstable mixing height) of the ABL is of great importance since it has an impact on future weather prediction methods. In addition to this, the knowledge of the 'close' structure (associated with the stable mixing height) case assists in predicting the strength and the duration of air pollution events. SODAR and its capabilities provide a direct pictorial view of the prevailing meteorological processes such as onset/dissipation of free convection, inversion, fumigation (the phase of breaking inversion, Gera et al. 2013a), and is considered a useful aid for air quality assessment studies. Consequently, the continuous monitoring of ABL is essential for the air pollution loading study and it is possible only using the SODAR remote-sensing technique (Singal, Gera, and Aggarwal 1984; Singal, Gera, and Saxena 1997; Singal 1988, 1989).

At any given location or region the value of the mixing height may be greatly affected by the meteorological parameters and their variation during different seasons (Singal, Gera, and Pahwa 1994; Singal 1988; Roy et al. 2011; Roy, Gupta, and Singh 2012). Delhi is a highly polluted metropolitan city; most of the air-pollutants are either locally produced by extensive urbanization, industrialization, construction activities, increased vehicular pollution and biomass burning, or transported from northeastern India.

On the basis of previous research (Singal and Aggarwal 1979; Singal 1988; Singal, Gera, and Saxena 1997), SODAR echograms register a characteristic repeatable structure in a cyclic order on daily scale, which is in accordance with solar heating and nocturnal cooling of the ground. The height and structural details of ABL keep on changing depending upon the progress and meteorological conditions of the day. An unstable convective boundary layer is developed during daytime whereas a stable boundary layer appear during night-time. The nocturnal stable boundary layer on a clear day begins to establish soon after sunset, continues to grow till early morning and dissipates after sunrise when a thermally convective atmosphere starts developing on the ground. The unstable state is an indicator of good ventilation and stable states are indicators of poor ventilation. Due to low winds speed and temperature the pollutants are not dispersed and they get trapped below the stability layer which acts as capping to mixed layer, which leads to higher ground level concentration of pollutants. In the morning, the stable state is converted into the unstable state with rising temperature, this means shifting from poor ventilation to good ventilation of pollutants (Singal, Gera, and Pahwa 1994; Singal, Gera, and Saxena 1997; Singal 1988; Gera et al. 2013a, 2013b).

The mixing height and the associated stability class have been estimated and plotted from SODAR echograms at Delhi for December 2013 to November 2014. Thereafter, the relationship between mixing height and atmospheric parameters (temperature, wind speed, and relative humidity) have been studied. The behaviour

of the stability classes during different weather conditions (clear, cloudy, and foggy) have also been discussed.

2. Data and meteorology

The meteorological parameters data such as wind speed, temperature, and relative humidity were measured at the observation site (New Delhi) using an automated weather station. The whole system has been installed by Campbell Scientific, Canada, USA. The meteorological tower is a combination of atmospheric pressure sensor, temperature sensor, wind profile sensor, humidity sensor, solar radiation, etc. This tower is used for continuous monitoring of meteorology condition. The total data set has been classified into four seasons, namely winter (December–January–February), pre-monsoon (March–April–May), monsoon (June–July–August–September) and post-monsoon (October–November) on the basis of meteorology over northern India (Ramachandran, Kedia, and Srivastava 2012).

SODAR is a well-recognized acoustic remote-sensing technique (Singal, Gera, and Aggarwal 1984; Singal, Gera, and Pahwa 1994; Singal, Gera, and Saxena 1997; Operational Manual 2008) that continuously monitors ABL thermal structures up to heights in the range of 340–3400 m. Mixing height has been measured using monostatic SODAR system, which was designed, developed and fabricated at Council of Scientific and Industrial Research (CSIR)-National Physical Laboratory (NPL) and operated in various frequencies according to its specific requirements. The SODAR was operated at a frequency of 2.25 kHz with 50–350 ms (selectable) pulse duration, a cycle time of 2–20 s (selectable) and electrical transmitting power of 50 W and an acoustic power 10 W. The SODAR antenna is a parabolic dish 1.22 m in diameter and the beam width is 15°. The antenna is enclosed in an acoustic shield so as to attenuate the outside noise and has been characterized at anechoic chambers at CSIR-NPL for the transmitting and receiving efficiency and directional characteristics(Garg and Maji 2013). The transducer output efficiency is measured to be 1.32 Pa V^{-1} in the anechoic chamber using a sound level analyser and is thus traceable to the national standards of sound pressure realized at CSIR-NPL, India (Garg and Sharma 2012). Highly directional short bursts of sound energy are radiated into the atmosphere, which after scattering from atmospheric fluctuations of eddy sizes within the inertial sub range of 0.1–10 m are being received back by the receiving antenna, conditioned through a premplifier and fed as analogue input signal at the microphone input terminal of the computer. Each acquired data is read with an 8 bit resolution and stored in the data file with a pre-assigned file name depending upon the date and time at the beginning of the data acquisition. The data points are allocated different colour codes depending upon the signal intensity. The dynamic range of the acquired signal 0–5 V is divided into eight steps and each step is pre-assigned a special colour code. Depending upon the time lapsed t after transmission of tone burst and digitalization of individual data points, the acquired data point is assigned a height value of

$$h = \frac{ct}{2}, \tag{1}$$

where c is the speed of sound in the air and t is time lapsed measured in seconds. Each data point with assigned colour is displayed as a two-dimensional image in time *versus* height graphics, on the computer monitor in real time. Depending on the chosen data sampling rate and the repetition rate of tone burst, the number of data points acquired per scan are displayed as marking one horizontal line of coloured dots on the monitor. Line by line integration of different scans produces a pictorial view of the SODAR echograms. A narrow band filter is used in the hardware, electronics, so as to suppress the noise at unwanted frequencies and improve the signal to noise ratio (Gera et al. 2011). The signals are processed to produce an online facsimile display of the dynamics of ABL thermal structures. The SODAR system has been calibrated using a simple methodology reported by Danilov et al. (1992) in anechoic chambers at CSIR-NPL.

SODAR echograms are reflex images of the turbulence in the lower atmosphere. This turbulence is accountable for the dispersion of pollutants. Thus, a measure of the height of thermals plumes in daytime and of shear echoes for the duration of night-time can be used to give a measure of the mixing height for pollutants. Though SODAR sensitivity becomes poor in daytime compared to the night-time, due to prevailing ambient noise, which decreases its probing range, the height of the thermal plumes by SODAR during daytime will always give an underestimated value unless they are capped by a low-level elevated shear echo layer. A technique to determine mixing height during the daytime, when the plumes are not capped by a stable layer, has been established on the basis of a Holzworth model using radiosonde data for Delhi (Singal, Gera, and Aggarwal 1984; Singal, Gera, and Pahwa 1994; Singal, Gera, and Saxena 1997; Operational Manual 2008; Roy et al. 2011; Gera et al. 2013a, 2013b). The following empirical relation has been found:

$$y = 4.24\,x + 95, \tag{2}$$

where y is the mixing height (m) for unstable ABL, x is the depth of the SODAR measured thermal plumes (m)

Equation (2) has been found to be valid in the plains of India and have also been used to determine the daytime mixing height at Tarapur, Nagothane, and Bombay (Maharashtra), at Chittorgarh and Jodhpur (Rajasthan), and Jamshedpur (Bihar). Walczewski (1989) has also reported this relation to estimate the mixing height under free convective conditions while comparing it with lidar measured dust layer depths. In consequence, the earlier empirical relation is true only in the plains of India. Somewhat different values of the constants may occur in places which have complex terrain, or in different geographical locations.

In several previous observations, the SODAR mixing height, has been found to be equal to the height measured using radiosonde, tethered balloon sensors, and instrumented tower and aircraft (Goroch 1976; Hicks et al. 1977; Wyckoff, Beran, and Hall 1973; Singal and Aggarwal 1979; Evers, Neiseer, and Weiss 1987; Gogh, Von, and Zib 1978; Fitzharris, Turner, and McKinley 1983; Walczewski 1989; Russell and Uthe 1978).

Atmospheric stability is a measure of the prevailing turbulence strength, which ranges over a broad spectrum. It ranges from vigorous turbulence (highly unstable ABL) to nearly no turbulence (highly stable ABL) conditions. Pasquill (1962) divided the ABL into six categories of stability from A to F, which can be classified on the basis of data of surface wind speed, wind direction, daytime insulation, night-time sky

conditions, and temperature lapse rate. Singal, Gera, and Aggarwal (1983, 1984, 1985) and Singal (1989) developed a method based on SODAR echo patterns to classify Pasquill stability categories. Singal (1989) classified stability into six classes based on the Pasquill (1962) classification.

The stability classes can be determined based on mixing height and SODAR echograms (Gera and Saxena 1996; Singal, Gera, and Saxena 1997). SODAR-based stability classification information given in Table 1. In this article, the following algorithm based on Laboratory Virtual Instrument Engineering Workbench (LabVIEW) has been developed to plot the stability class from A to F directly from the mixing height data.

Step 1: The acquired data of whole month is converted into array (column represents day and row represents hour ('00:00–23:00')

Step 2: Average temporal data is calculated

For t ('00:00–23:00')

$$D_{\text{at}} = \frac{\sum_{d=1}^{d_{\max}} h_d(t)}{d_{\max}}, \tag{3}$$

where D_{at} is the average temporal data, $d_{\max}$ is the maximum number of days in particular month,

h_d (t) is the ABL height at particular day (d = 1: $d_{\max}$) at time hour.

Step 3: Check weather temporal height is according to Table 2 or not

(i) If not generate an error signal and end programme

Table 1. Sound detection and ranging (SODAR)-based stability classification scheme.

Local time	Sodar structure	Stability class
05:00–10:00	Stable layer (>150 m)	E
	Stable layer (<150 m)	F
	Rising layer	C
	Elevated layer/or multi-layer/or waves	F
	(200 m) ≥ convection plumes ≥ (125 m)	B
	Convection plumes (<125 m)	C
	No structure	D
10:00–18:00	Rising layer	C
	Convection plumes ≥ (200 m)	A
	(200 m) ≥ convection plumes ≥ (125 m)	B
	Convection plumes (<125 m)	C
	No structure	D
	Stable layer(>150 m)	E
	Stable layer (<150 m) with elevated layer/waves	F
	Elevated layer with plumes below	C
18:00–21:00	No structure	D
	Stable layer (>150 m) with flat top/short spikes	E
	Stable layer with tall spikes (≥300 m)	D
	Stable layer with wavy top	F
	Elevated layer/waves	F
21:00–05:00	No structure	D
	Stable layer (<125 m) with flat top	F
	Stable layer (≥125 m) with flat top	E
	Stable layer with spikes (≥300 m)	D
	Stable layer with wavy top	F
	Elevated layer	E

Table 2. Average values of mixing height and meteorological parameters during different seasons.

Parameters	Winter	Pre-monsoon	Monsoon	Post-monsoon
Mixing height (m)	555 ± 115	650 ± 145	535 ± 145	365 ± 50
Temperature (°C)	15 ± 3.0	27 ± 3.5	31 ± 2.0	24 ± 3.0
Wind speed (ms^{-1})	1.52 ± 0.44	1.77 ± 0.41	1.67 ± 0.48	1.18 ± 0.34
Humidity (%RH)	71 ± 13	39 ± 10	60 ± 8.0	45 ± 12

(ii) If yes then store the value temporal height in an array

Step 4: Repeat step no. 3 till total no. of elements in the array reaches maximum

Step 5: Display the data and plot the graph

Six thousand five hundred twenty-two SODAR echograms have been observed at the study location for different seasons and were analysed and classified into different categories. Figure 1(a–e) show the multilayer, rising layer, thermal plume, waves and perturbations, and stratified layer echograms

Figure 1(a) exhibits the multilayer types of echograms, which were observed during night-time. They are more frequent in the month of May i.e. pre-monsoon months (Singal and Gera 1982) and not common in the post-monsoon months, that is, October and November. Figure 1(a) reveals that the height of multilayer is 318 m and can goes up to 600 m.

The inversion layer structure, that is, characteristic feature of the night-time stable conditions, dissipates in the morning after sunrise due to solar heating of the ground and the temperature profile changes its shape. The time taken for an inversion layer to dissipate after sunrise varies from day to day and season to season depending upon the presence of cloud cover, the strength of the inversion layer formed during the night, influx of solar heat, and the presence of elevated layer or fog layer. In rising layer (Figure 1(b)), rising rate is faster in the pre-monsoon season than in the winter and post-monsoon season due to the change in the temperature profile.

The nocturnal inversion while dissipation shows its presence in the form of a rising layer, which reaches to a certain maximum height and then disappears. This type of structure is not seen daily in the morning time. However, sometimes a direct transition of the inversion layer changes to the plume structure. During rainy spell and cloud cover days, the inversion layer does not show a rising layer (Singal 1989). As a result of which, less rising layer is formed during the monsoon season.

Thermal plume structure (Figure 1(c)) is a daytime structure and is associated with solar heating of the ground. The plume starts forming early in the morning after dissipation of the surface inversion. The height of thermal plumes increase with increase in temperature. The duration of thermal plumes is maximum in the pre-monsoon or summer and minimum in the winter and post-monsoon seasons.

Waves and perturbations (Figure 1(d)) are another class of thermal plume structures, which have been observed and classified directly on the SODAR echograms. The wave structure mostly observed in the April, May and June months, that is, in the pre-monsoon season. This type of structure is important in the study of wave motion (Singal 1988).

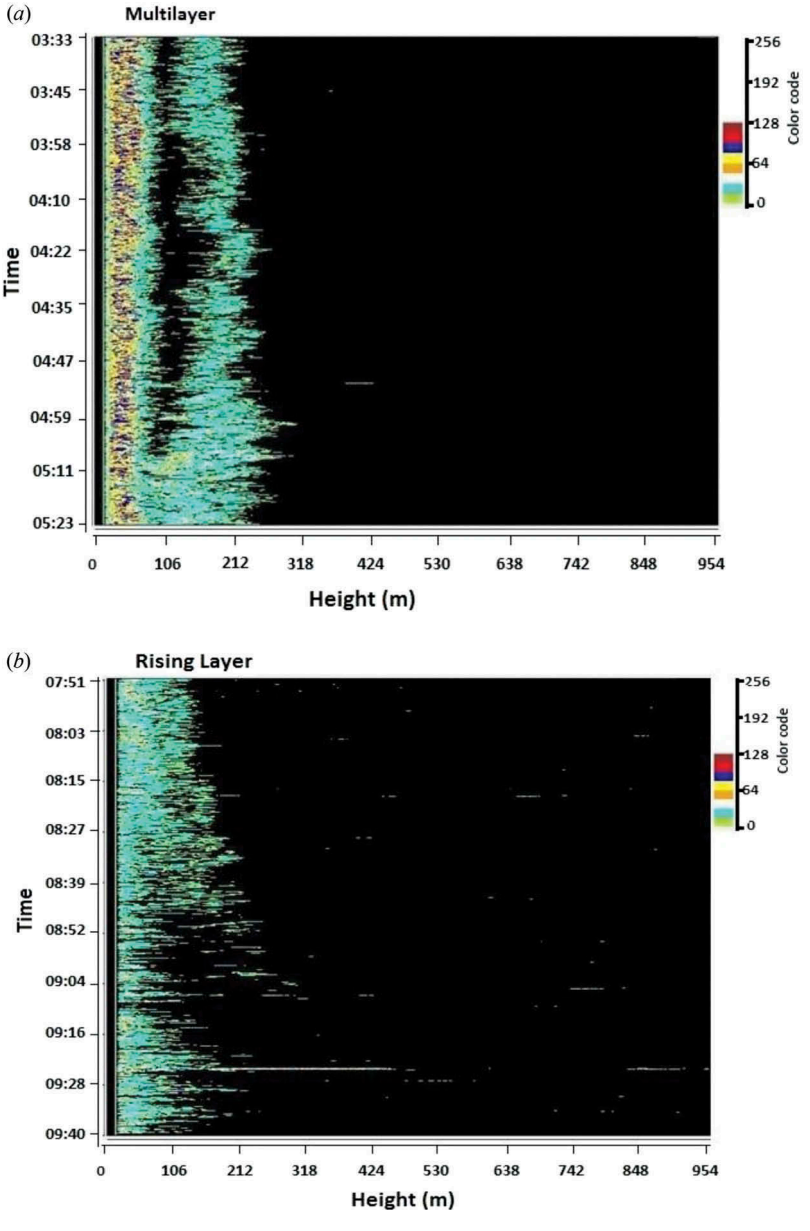

Figure 1. Different layers in sound detection and ranging (SODAR) echograms. (a) Multilayer '4 June 2014', (b) rising layer '23 April 2014', (c) thermal plume '3 May 2014', (d) wave structure '13 August 2014', (e) stratified layer '19 October 2014'.

Figure 1(e) represents the stratified layers in the lower atmosphere under statically stable conditions on the land. Stratification represents turbulent interface between two layers of stable layer and the variations in the structure with time give information on the thermally induced changes occurring in the nocturnal ABL.

Atmospheric stability is one of the essential parameter for air quality studies. Pasquill categorized atmospheric stability from A to F in terms of increasing stability order from

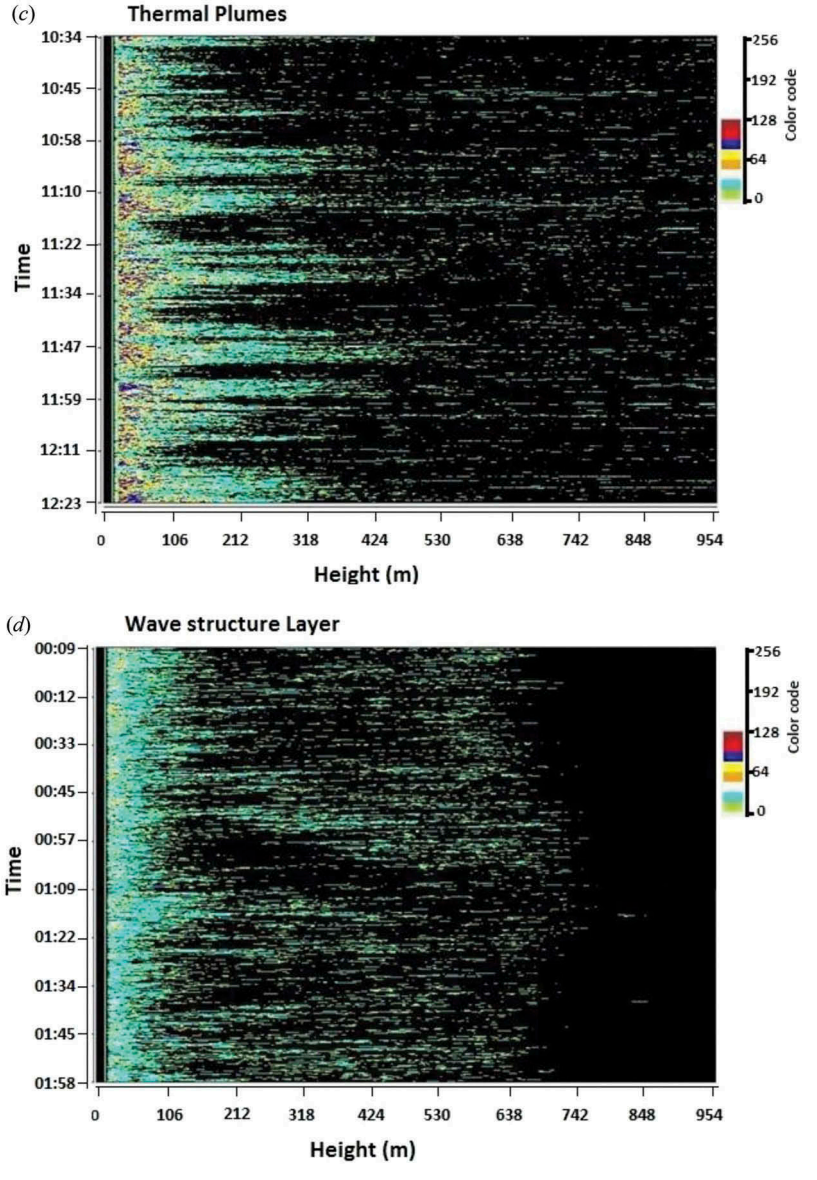

Figure 1. Continued.

very unstable (A), moderately unstable (B), slightly unstable (C), neutral (D), slightly stable (E) to moderately stable (F) conditions, respectively. Figure 2(a–c) and Table 3 represent stability class in different weather conditions (i.e. clear day, cloudy day, and foggy day). Figure 2(a) represents stability class for clear day. All stability classes are observed in Figure 2(a). Unstable category (A, B, C) exists during the daytime when SODAR records thermal plumes and showing variation in height in accordance with solar heating of the ground and related lapse rate profile. During the whole day the class A is dominant. The stable categories (E and F) of the ABL exist mostly during night-time when SODAR maps a ground based layer with flat/spiky top. Figure 2(b) represents

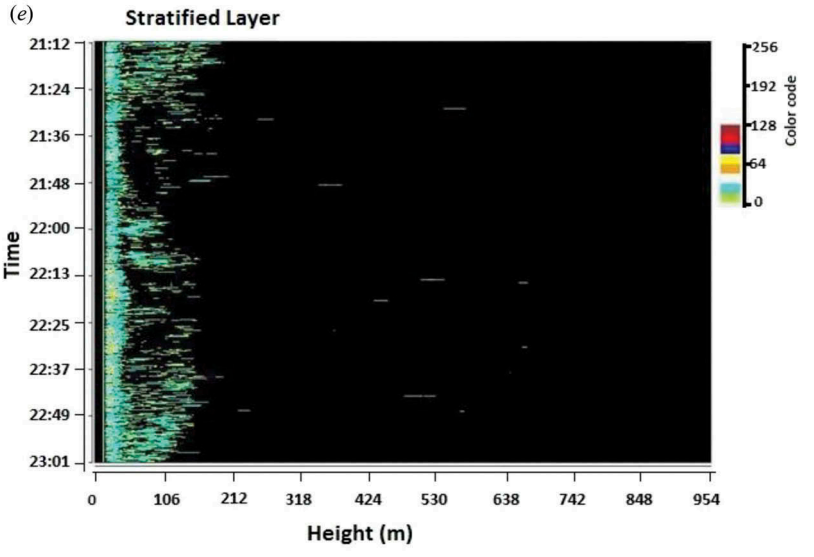

Figure 1. Continued.

stability class of cloudy days, stability A is seen to occur mainly during '08:00–12:00' h and stability B and C has mainly occurred during morning transitional phase ('07:00–08:00' h) or prior to evening transitional phase around '17:00' h. In this figure during midday the class B is dominant and during night-time class E is dominant due to cloud. Similarly, Figure 2(c) represents stability class of foggy days. Stability F occurs relatively more during the evening to midnight ('16:00–23:00' h). It indicates that night of foggy days are relatively more critical stable periods for dispersion of pollutants. Further, sub-divisional hourly stability distribution analysis for the clear, cloudy, and foggy days shows that on a clear day the stability A has occurred in 29.16%, B and C for 4.17%, D for 18.75%, E for 35.42%, and F for 8.33% of the total observational hours. Similarly for cloudy day stability A and B has found in 20.83%, C for 4.17%, E for 45.83%, and F for 8.33%. For foggy day the stability A has occurred in 16.67%, B for 4.17%, C and D for 12.5%, E for 29.17%, and F for 25% of the total observational period.

3. Results and discussion

Daily average SODAR data of a particular year throughout the months have been analysed to derive the mixing height. The daily average seasonal variation of mixing height during the whole year of observation shown in Figure 3(a–d). Figure 3(a–d) show the variation of mixing height during different seasons. The daily average values of mixing height during the four seasons, winter, pre-monsoon, monsoon, and post-monsoon have been found to be 555 ± 115, 650 ± 145, 535 ± 145, 365 ± 50 m, respectively. The vertical bars denote the $\pm\sigma$ standard deviations from the daily mean values. The minimum values of mixing (365 ± 50 m) during post-monsoon were caused by high concentration of pollutants, due to low winds speed and temperature the pollutants are not dispersed and they get trapped below the stability layer which acts as a capping to

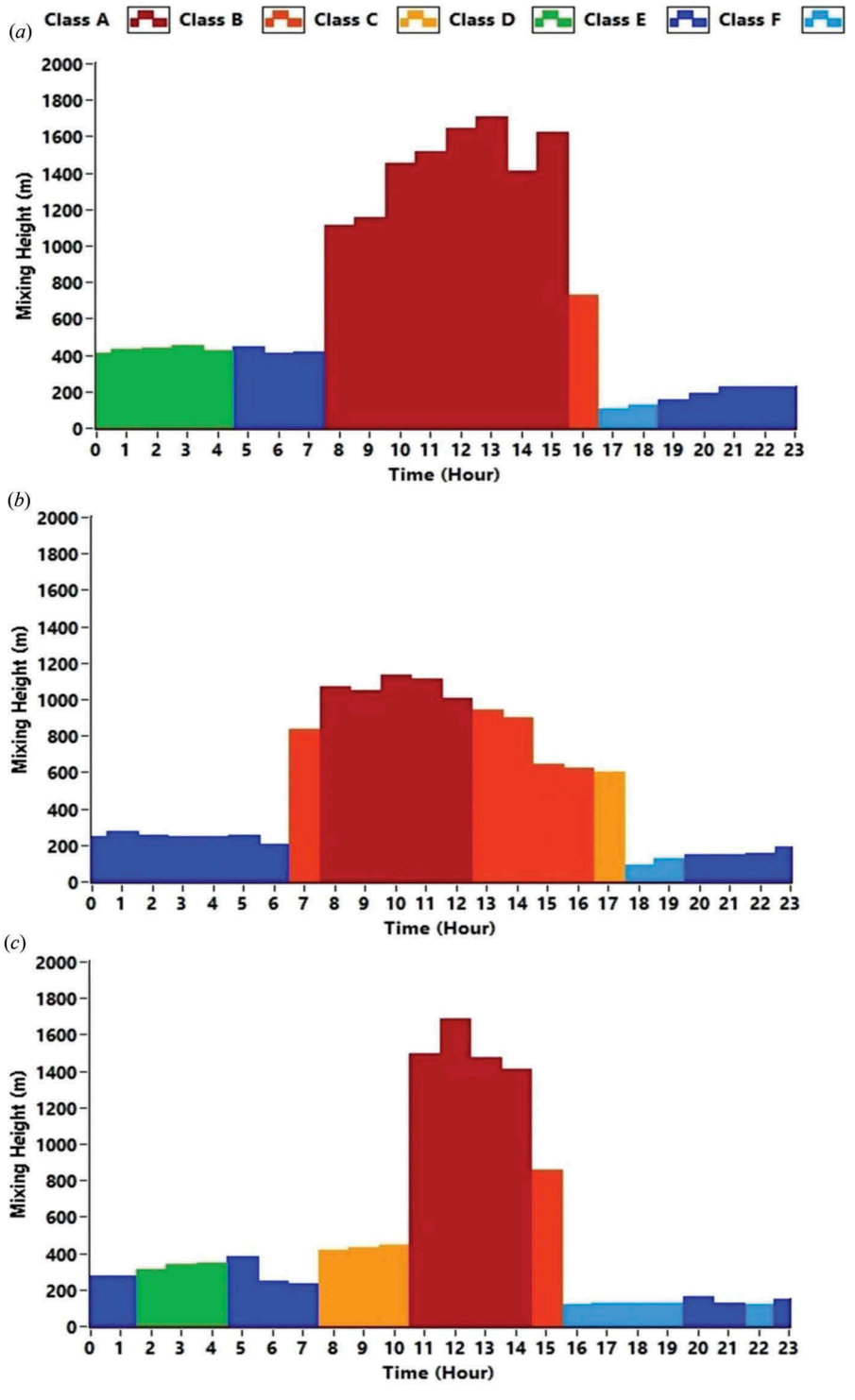

Figure 2. Stability class study during different weather conditions. (a) Clear day '7 June 2014', (b) cloudy day '15 August 2014', (c) foggy day '18 December 2014'.

Table 3. Stability class during different weather conditions at New Delhi.

Hours	Sodar structure Clear day (7 June 2014)	Class
00:00–05:00	Tall spiky stable layer	D
05:00–08:00	Stable layer	E
08:00–09:00	Rising layer	C
09:00–16:00	200 m > thermal plumes	A
16:00–17:00	200 m < thermal plume	B
17:00–19:00	Unstable to stable state condition	F
19:00–23:59	Stable layer	E
	Cloudy day (15 August 2014)	
00:00–07:00	Small spiky stable layer	E
07:00–08:00	Breaking of inversion	B
08:00–13:00	Wave thermal plumes	A
13:00–17:00	Cloud thermal plumes	B
17:00–18:00	During sunset	C
18:00–20:00	Extreme stable condition	F
20:00–00:00	Stable layer	E
	Foggy day (18 December 2014)	
00:00–02:00	Stable layer	E
02:00–05:00	Neutral condition	D
05:00–08:00	Stable and foggy layer	E
08:00–11:00	Fog and unstable layer	C
11:00–15:00	Thermal Plumes	A
15:00–16:00	Moderate unstable	B
16:00–20:00	Stable layer	F
20:00–00:00	Stable layer	E

mixed layer, leads to higher ground level concentration of pollutants (Soni et al. 2010, 2011; Bano et al. 2011; Iyer and Raj, 2013). On the other hand, the mixing height in the pre monsoon were much higher than the other seasons. This was due to the higher ambient air temperature and wind speed.

The temporal variation of mixing height and meteorological parameters during different seasons is shown in Figure 4(a–d). The daily average values of mixing height, temperature, wind speed and relative humidity were found to be 530 ± 155 m, 25 ± 7°C, 1.53 ± 0.70 ms^{-1}, 53 ± 18% RH, respectively. Maximum value (about 1700 m) of mixing height was observed in pre-monsoon months, while the minimum value of mixing height (around 950 m) found in post-monsoon months. Generally, mixing height is high in between '11:00' A.M. to '14:00' P.M. in all seasons. The variation in surface temperature controls the existence of atmospheric convection, which strongly affects the mixing height (Singal 1997).

The temporal average values of the mixing height during the different seasons and the corresponding value of meteorological parameters are given in Table 3. The highest mixing height during convection period was approximately 1550, 1495, 1280, and 1050 m during pre-monsoon, winter, monsoon, and post-monsoon seasons, respectively. The results observed from this present study agree with those reported by Roy et al. (2011), Singal, Gera, and Saxena (1997), and Zhou et al. (2009).

Based on the observation of SODAR echograms, the mixing height of ABL is changing continuously. Figure 5(a–d) represent the time series of daily average values of mixing height and meteorological parameters (temperature, relative humidity, and wind speed). The vertical bars denote the $\pm\sigma$ standard deviation from the daily mean. The positive

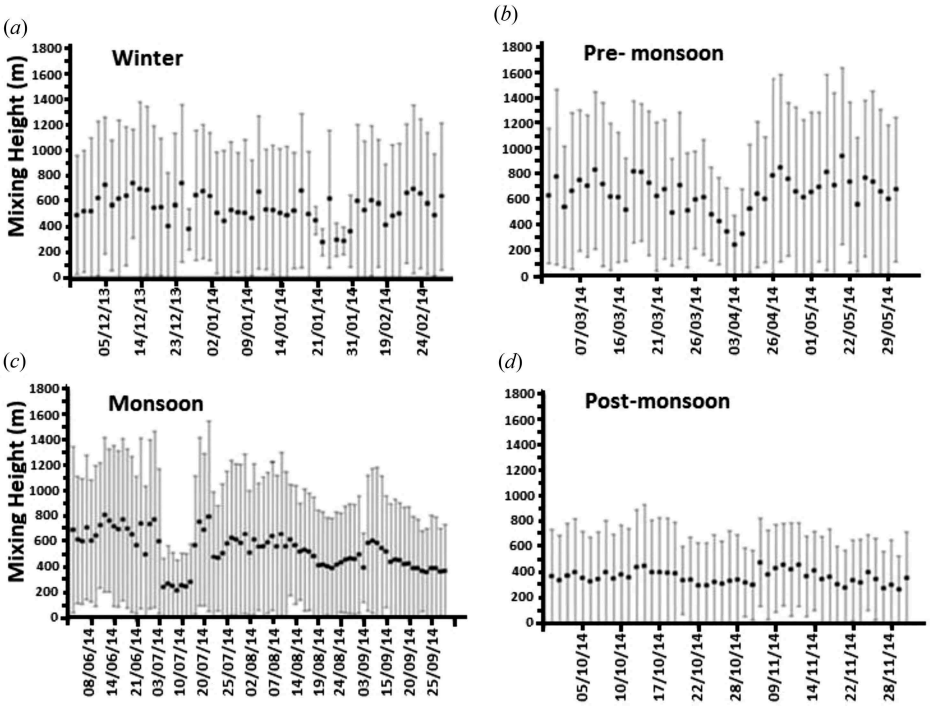

Figure 3. Daily average seasonal variation of mixing height from December 2013 to November 2014 during different seasons. (a) Winter, (b) pre-monsoon, (c) monsoon, (d) post-monsoon.

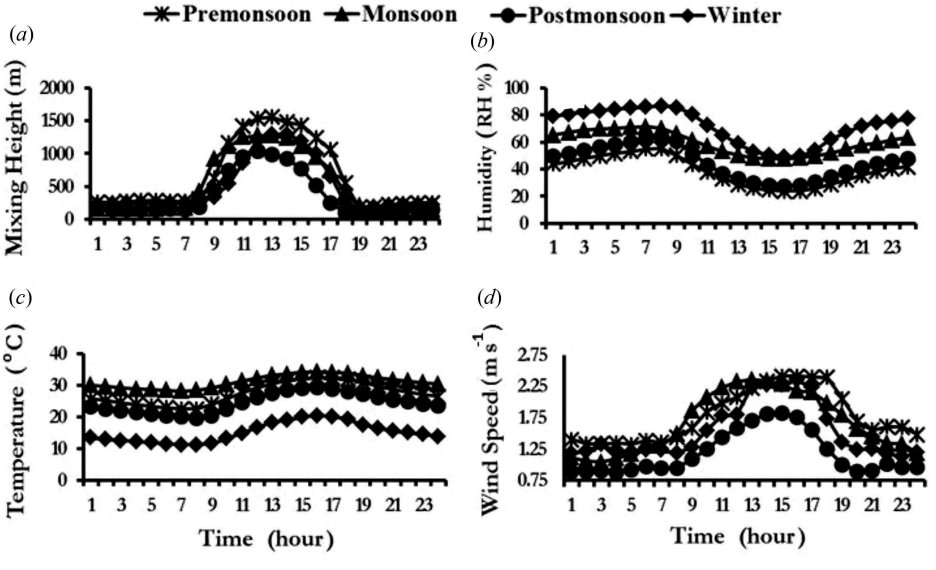

Figure 4. Temporal variation of mixing height and meteorological parameters during different seasons. (a) Mixing height, (b) humidity, (c) temperature, (d) wind speed.

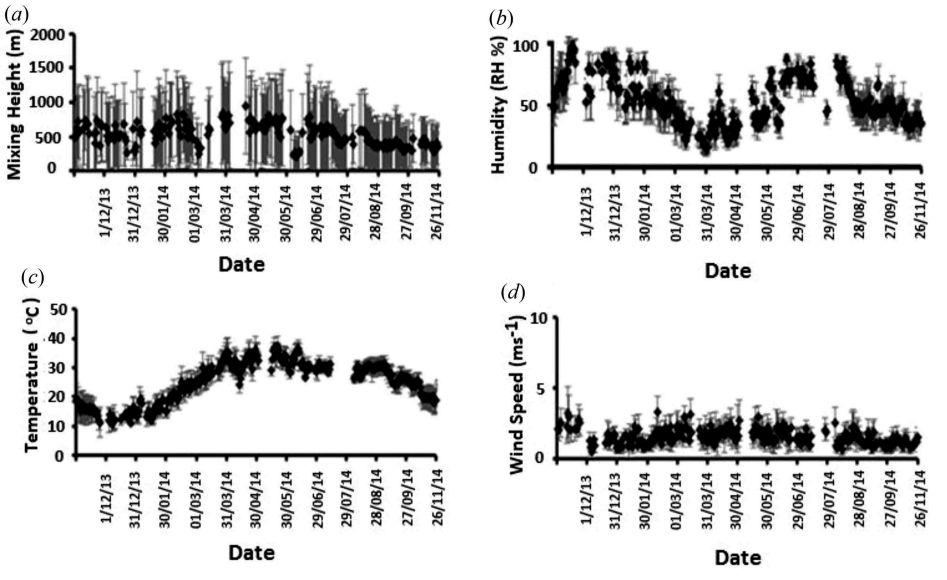

Figure 5. Daily average variation of mixing height and meteorological parameters from December 2013 to November 2014. (a) Mixing height, (b) humidity, (c) temperature, (d) wind speed.

correlation has been observed between mixing height with temperature and wind speed during all seasons, whereas negative correlation has been observed between mixing height and relative humidity. The positive correlation between mixing height and wind speed during four seasons, winter, post-monsoon, monsoon and pre-monsoon were found to be 0.41, 0.24, 0.21, and 0.31, respectively. Statistically significant correlation is observed only for winter and pre-monsoon season.

Higher correlation (0.41) has been observed during the winters between mixing height and wind speed. Similarly, positive correlation between mixing height and temperature were also found to be 0.08, 0.3, 0.31, and 0.14 during different seasons namely winter, post-monsoon, monsoon, and pre-monsoon, respectively, without being statistically significant. In contrast, negative correlation between mixing height and humidity during different seasons winter, post-monsoon, monsoon, and pre-monsoon were found to be −0.18, −0.17, −0.16, and −0.06, respectively. Almost equal negative and statistically insignificant correlation has been observed between mixing height and humidity during all seasons, indicates that as the relative humidity increases mixing height decreases. The results are in agreement with those reported by Roy et al. (2011) and Myrick et al. (1994).

Figure 6(a–d) show the temporal variation of stability class in different seasons and SODAR based stability classification information given in Table 1. From Figure 6(a–d), it is observed that, class A was predominant in pre-monsoon (33.33%) months, followed by monsoon (29.17%), winter (20.83%), and post-monsoon(12.5%) months during the convection period. In the winter months the stability class E (66.67%) occurs relatively more during '17:00–09:00' h from evening to early morning. It indicates that nights of the winter months are relatively more critical stable periods for dispersion of pollutants.

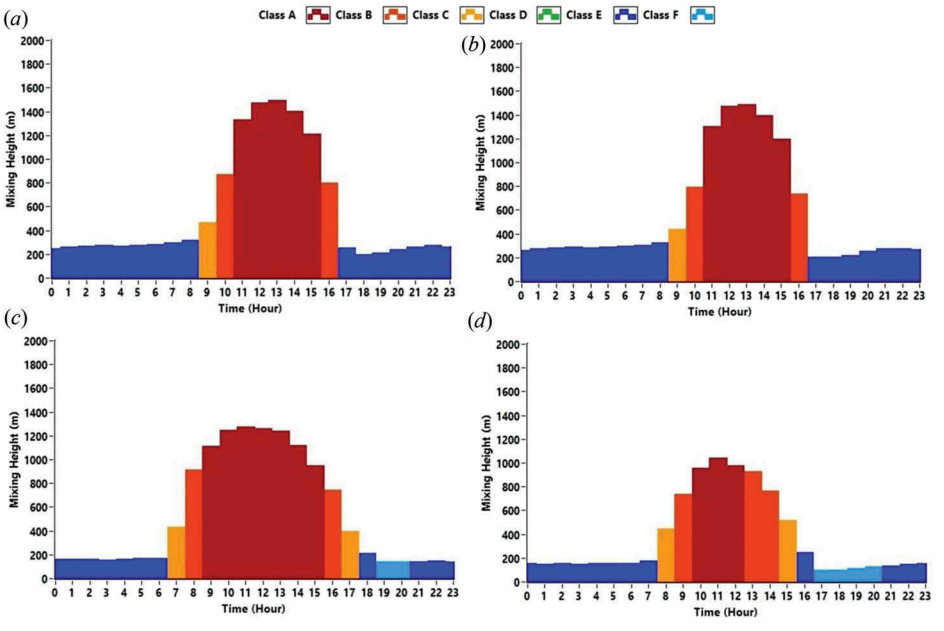

Figure 6. Stability class and its seasonal and temporal variability. (a) Winter, (b) pre-monsoon, (c) monsoon, (d) post-monsoon.

The stability class A persists in general up to '16:00' h and is seen to quickly recede to stability class B and turning through a transitional phase to stability class E within an hour. During pre-monsoon months class A was predominant from '09:00–17:00'. These periods fall under strong convection period of the day while class E (50.7%) was predominant during 18:00–08:00 h. The wind was highest in pre-monsoon and monsoon months while the lowest in the post-monsoon and winter months. The low wind speeds are associated with elevated pollution levels (Papanastasiou, Melas, and Kioutsioukis 2007). If the wind direction is constant the area remains exposed to high pollutant levels during winter and post-monsoon. As the wind direction changes, pollutants disperse over a large area. Humidity also plays an important role in affecting the mixing height (Beyrich 1997; Zhou et al. 2009). The humidity was highest in monsoon and the lowest in pre-monsoon months. Higher temperature during pre-monsoon period might be due to the lower humidity. Similarly rainfall might be the reason for higher humidity in monsoon period.

The stability class predominance during different seasons observed at Delhi is different from the study reported by Roy et al. (2011); Roy, Gupta, and Singh (2012) over coal mine and the gold mine may be due to the difference in synoptic-dynamic meteorology and regional topography along with local emissions, boundary layer dynamics, dust transport, monsoon and rainfall, over the observation sites. Gera et al. (2013a) also reported ABL stability distribution for a decade from 2001 to 2010 over the same site but for a foggy ABL. The lower latitudes receive more solar energy because of higher solar zenith angle as compared to higher altitude. The high latitude (28° 38′, 77° 10′) at Delhi might be the reasons for the lower mixing height as compared to Kolar Gold Field (12° 56′, 17° 93′) in the different seasons.

4. Conclusion

The variability of the ABL along with meteorological parameters have been studied in Delhi area. A LabVIEW-based programme has been successfully developed to plot the stability class from A to F directly from the mixing height dataset. The LabVIEW-based programme for stability class analysis has the advantage of increased efficiency and time management as compared with the existing manual analysis method. From the seasonal classification of stability class it is observed that, the stability class A has occurred predominantly for 33.33%, 29.17%, 20.83%, and 12.5% in pre-monsoon, monsoon, winter, and post-monsoon months, respectively, during the convection period, whereas class E has found predominantly in winter (66.67%) months followed by pre-monsoon (58.33%), monsoon (45.83%), and post-monsoon (50.7%) months during night-time. The wind speed was highest in pre-monsoon and monsoon months whereas lowest in the post-monsoon and winter months. The low wind speeds are associated with elevated pollution levels. Stability class along with air pollutants and meteorological data can be used for the air pollution prediction model using artificial intelligence techniques such as neural networks, Adaptive Neuro-Fuzzy Inference System (ANFIS), and fuzzy logic, etc.

Acknowledgements

We are thankful to the anonymous reviewers for their valuable suggestions and comments in improving the manuscript.

Disclosure statement

No potential conflict of interest was reported by the authors.

Reference

Ashrafi, K. H., and G. H. A. Hoshyaripour. 2008. "A Model to Determine Atmospheric Stability and Its Correlation with CO Concentration." *World Academy of Science, Engineering and Technology* 2: 2008–2021.

Bano, T., S. Singh, N. C. Gupta, K. Soni, R. S. Tanwar, S. Nath, B. C. Arya, and B. S. Gera. 2011. "Variation in Aerosol Black Carbon Concentration and Its Emission Estimates at the Mega-City Delhi." *International Journal of Remote Sensing* 1–16. doi:10.1080/01431161.2010.512943.

Beyrich, F. 1997. "Mixing Height Estimation from SODAR Data- A Critical Discussion." *Atmospheric Environment* 31 (23): 3941–3953. doi:10.1016/S1352-2310(97)00231-8.

Danilov, S. D., A. E. Gur'yanov, M. A. Kallistratova, I. V. Petenko, S. P. Singal, D. R. Pahwa, and B. S. Gera. 1992. "Acoustic Calibration of Sodars." *Meas.Sci. Technol* 3: 1001. doi:10.1088/0957-0233/3/10/012.

Evers, K., J. Neiseer, and E. Weiss. 1987. "Acoustic Sounding of the Urban Boundary Layer over Berlin-Adlershof in Summer." *Zeitschrift Fur Meteorologie* 37: 241–252.

Fitzharris, B. B., A. Turner, and W. McKinley. 1983. "Cold Season Inversion Frequencies as Measured by Acoustic Sounder in the Cromwell Basin." *New Zealand Journal of Science* 26: 307–313.

Garg, N., and S. Maji. 2013. "Vibration Induced Due to Acoustic Excitation in Diffuse Field Conditions." *Acoustics Australia* 41: 219–224.

Garg, N., and O. Sharma. 2012. "Measurement Accuracy of Secondary Standards of Sound Pressure in Comparison to Primary Standards." *MAPAN-J of Metrology Society of India* 27 (4): 219–229.

Gera, B. S., T. Raghavendra, G. Singh, V. K. Ojha, J. Malik, N. Gera, and N. C. Gupta. 2011. "Instrumentation and Computer Capabilities for Improving SODAR Data Acquisition." *International Journal of Remote Sensing* 32 (17): 4807–4817. doi:10.1080/01431161.2010.489072.

Gera, B. S., and N. Saxena. 1996. "SODAR Data- A Useful Input for Dispersion Modeling." *Atmospheric Enivironment* 30 (21): 3623–3631. doi:10.1016/1352-2310(96)00062-3.

Gera, N., N. C. Gupta, V. Mohanan, and B. S. Gera. 2013a. "SODAR Studies of Foggy Atmospheric Boundary Layer over Delhi." *International Journal of Scientific and Engineering Research* 4: 1634–1639.

Gera, N., N. C. Gupta, V. Mohanan, and B. S. Gera. 2013b. "SODAR Studies of Air Pollution Meteorology over Delhi." *International Journal of Scientific and Engineering Research* 4: 1805–1811.

Gogh, R., G. Von, and P. Zib. 1978. "Comparision of Simultaneous Tethered Ballon and Monostatic Acoustic Sounder Records of the Statically Stable Lower Atmosphere." *Journal of Apllied Meteorology* 17: 34–39. doi:10.1175/1520-0450(1978)017<0034:COSTBA>2.0.CO;2.

Goroch, A. K. 1976. "Comparision of Radiosonde and Acoustic Echo Sounder Measurements of Atmospheric Thermal Strata." *Journal of Applied Meteorology* 15: 520–521. doi:10.1175/1520-0450(1976)015<0520:CORAAE>2.0.CO;2.

Hicks, R. B., D. Smith, P. J. Irwin, and T. Mathews. 1977. "Preliminary Results of Atmospheric Acoustic Sounding at Calgary." *Boundary-Layer Meteorology* 12: 201–212. doi:10.1007/BF00121973.

Iyer, U., and P. Raj. 2013. "Ventilation Coefficients Trends In Recent Decades Over Four Major Indian Metropolitan Cities." *Journal Of Earth System Science* 122 (2): 53.

Myrick, R. H., S. K. Sakiyama, R. P. Angle, and H. S. Sandhu. 1994. "Seasonal Mixing Heights and Inversions at Edmonton, Alberta." *Atmospheric Environment* 28 (4): 723–729. doi:10.1016/1352-2310(94)90049-3.

Operational Manual. 2008. Sodar. In: *Global Environmental Technologies*. New Delhi, India: Global Environmental Technologies.

Papanastasiou, D. K., D. Melas, and I. Kioutsioukis. 2007. "Development and Assessment of Neural Network and Multiple Regression Models in order to Predict PM10 Levels in a Medium–Sized Mediterranean City." *Water Air and Soil Poll* 182: 325–334. doi:10.1007/s11270-007-9341-0.

Pasquill, F. 1962. *Atmospheric Diffusion*. London: D. Van Nostrand Co. Ltd.

Ramachandran, S., S. Kedia, and R. Srivastava. 2012. "Aerosol Optical Depth Trends over Different Regions of India." *Atmospheric Environment* 49: 338–347. doi:10.1016/j.atmosenv.2011.11.017.

Roy, S., G. R. Adhikari, T. A. Renaldy, and T. N. Singh. 2011. "Assessment of Atmospheric and Meteorological Parameters for Control of Blasting Dust at an Indian Large Surface Coal Mine Research." *Journal of Environmental and Earth Sciences* 3 (3): 234–248.

Roy, S., P. Gupta, and T. N. Singh. 2012. "Studies on Meteorological Parameters and Mixing Height in Gold Mining Area." *Resources and Environment* 2 (5): 228–239. doi:10.5923/j.re.20120205.06.

Russell, P. B., and E. E. Uthe. 1978. "Acoustic and Direct Measurements of Atmospheric Mixing at Three Sites during an Air Pollution Incident." *Atmospheric Environment* 12: 1061–1074. doi:10.1016/0004-6981(78)90351-7.

Singal, S. P. 1988. "The Use of an Acoustic Sounder in Air Quality Studies." *Journal Scient Indres* 47: 520–533.

Singal, S. P. 1989. "Acoustic Sounding Stability Studies." In *Encyclopedia of Environment Control Technology,Chere*, edited by P. N. Cheremisinoff, 1003–1062. U.S.A.: Golf Publishing.

Singal, S. P. 1997. *Acoustic Remote Sensing Applications*. New Delhi, India: Narosa Publishing House, ISBN 81-7319-110-7.

Singal, S. P., and S. K. Aggarwal. 1979. "SODAR and Radiosonde Studies of Thermal Structure of the Lower Atmosphere at Delhi." *Indian Journal of Radio Space Physics* 8: 76–81.

Singal, S. P., and B. S. Gera. 1982. "Acoustic Remote Sensing of the Boundary Layer." *Proceedings Indian Academic Sciences (Engg Section)* 5: 65–82.

Singal, S. P., B. S. Gera, and S. K. Aggarwal. 1983. "Studies of the Boundary Layer at Delhi Using SODAR." In: Proc. second Int. Symp. on *acoustic remote sensing of the atmosphere and oceans*, Rome, Italy.

Singal, S. P., B. S. Gera, and S. K. Aggarwal. 1984. "Nowcasting by Acoustic Remote Sensing: Experience with the Systems Established at the National Physical Laboratory, New Delhi." *Journal Sciences Industrial Researcher* 4: 469–488.

Singal, S. P., B. S. Gera, and S. K. Aggarwal. 1985. "Studies of SODAR-Observed Dot Echostructures." *Atmospheric Ocean* 23 (3): 304–312. doi:10.1080/07055900.1985.9649230.

Singal, S. P., B. S. Gera, and D. R. Pahwa. 1994. "Application of SODAR to Air Pollution Meteorology." *International Journal Remote Sensing* 15: 427–441. doi:10.1080/01431169408954084.

Singal, S. P., B. S. Gera, and N. Saxena. 1997. "SODAR: A Tool to Characterize Hazardous Situations in Air Pollution and Communication." In *Acoustic Remote Sensing Applications*, Ed. S. P. Singal, 326–384. New Delhi, India: Narosa Publishing House.

Soni, K., S. Singh, T. Bano, R. S. Tanwar, and S. Nath. 2011. "Wavelength Dependence of the Aerosol Angstrom Exponent and Its Implications over Delhi, India." *Aerosol Sciences Technological* 45: 1488–1498. doi:10.1080/02786826.2011.601774.

Soni, K., S. Singh, T. Bano, R. S. Tanwar, S. Nath, and B. C. Arya. 2010. "Variations in Single Scattering Albsinghedo and Angstrom Absorption Exponent during Different Seasons at Delhi India." *Atmospheric Environment* 44: 4355–4363. doi:10.1016/j.atmosenv.2010.07.058.

Walczewski, J. 1989. "Development of SODAR and Acoustic Sounding of the Atmosphere in Poland." *Zeitschrift Fur Meterologie* 39: 119–131.

Wark, K., C. F. Warner, and W. T. Davis. 1998. *Air Pollution: Its Origin and Control 3rd edition* . Addison Wesley.

Wyckoff, R. J., D. W. Beran, and F. F. Hall Jr. 1973. "A Comparison of the Low Level Radiosonde and the Acoustic Echo Sounder for Monitoring Atmospheric Stability." *Journal of Applied Meteorology* 12: 1196–1204. doi:10.1175/1520-0450(1973)012<1196:ACOTLL>2.0.CO;2.

Zhou, B., S. N. Yang, S. S. Wang, and T. Wagner. 2009. "Determination of an Effective Trace Gas Mixing Height by Differential Optical Absorption Spectroscopy (DOAS)." *Atmos. Meas. Techn.* 2: 1663–1692. doi:10.5194/amtd-2-1663-2009.

Zoras, S., A. G. Triantafyllou, and D. Deligiorgi. 2006. "Atmospheric Stability and PM_{10} Concentrations at Far Distance from Elevated Point Sources in Complex Terrain: Worst Case Episode Study." *J. of Environmental Management* 80: 295–302. doi:10.1016/j.jenvman.2005.09.010.

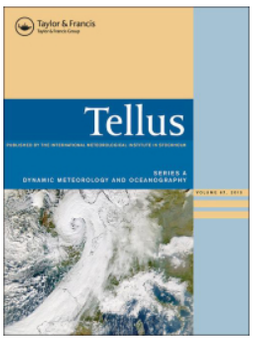

Tellus A: Dynamic Meteorology and Oceanography

ISSN: (Print) (Online) Journal homepage: https://www.tandfonline.com/loi/zela20

Prediction of temporal atmospheric boundary layer height using long short-term memory network

Nishant Kumar, Kirti Soni & Ravinder Agarwal

To cite this article: Nishant Kumar, Kirti Soni & Ravinder Agarwal (2021) Prediction of temporal atmospheric boundary layer height using long short-term memory network, Tellus A: Dynamic Meteorology and Oceanography, 73:1, 1-14, DOI: 10.1080/16000870.2021.1926132

To link to this article: https://doi.org/10.1080/16000870.2021.1926132

Tellus SERIES A DYANAMIC METEOROLOGY AND OCEANOGRAPHY
PUBLISHED BY THE INTERNATIONAL METEOROLOGICAL INSTITUTE IN STOCKHOLM

Prediction of temporal atmospheric boundary layer height using long short-term memory network

By NISHANT KUMAR[1], KIRTI SONI[2]*, and RAVINDER AGARWAL[1], [1]*Thapar Institute of Engineering and Technology, Patiala, India;* [2]*CSIR-National Physical Laboratory, New Delhi, India*

(Manuscript Received 29 November 2020; in final form 2 May 2021)

ABSTRACT

Nowadays, the city's rapid growth of industrialisation, population, human activities, vehicular traffic density, unplanned urbanisation with poor ventilation contributes to increasing large amount of pollutants concentration. Atmospheric Boundary Layer (ABL) height is a basic parameter to define the pollution carrying capacity of any area in a big city. In the time series analysis and prediction of ABL height, the existing models use linear (AR, ARMA, ARIMA etc.) and non-linear (ANN, ANFIS etc) algorithms, but these models less capable of identifying the hidden pattern and underlying dynamics of ABL patterns. This paper presents a Long Short-Term Memory (LSTM) model using deep learning-based algorithms for temporal/seasonal and annual ABL height prediction and identified the latent dynamics of the ABL height pattern. The results of the model have been compared with the measurements made by SOnic Detection And Ranging (SODAR) system. LSTM model is used for prediction and to analyse their performance affected by the model. The observed ABL height data and model data are used to predict the ABL height by applying the neural network of LSTM. It is observed from the analysis that the optimal results can be achieved when the number of neurons is equal to 32, an epoch is equal to 500. To obtain the acceptable accuracy of prediction, various error-based performance indices have been calculated. Mean Absolute Percentage Error (MAPE) and relative Root Mean Square Error (rRMSE) have been calculated for the updated network with predicted values 17.3% and 7.33%, and, for the updated network with observed values 10.62% and 5.95%, respectively. Also, the performance of the proposed model has been estimated for the annual and seasonal prediction of ABL height. The results depict rRMSE values (7.49% and 5.59%) as lowest during post-monsoon for seasonal prediction and (10.29% and 5.86%) highest for annual prediction.

Keywords: atmospheric boundary layer height, LSTM network, SODAR, deep learning

1. Introduction

Atmospheric Boundary Layer (ABL) is a base of life on the Earth. The ABL includes a fair-weather cloud related to thermals and a stratocumulus cloud that fills the upper portion of the well-mixed moist boundary layer (Garratt, 1994). Fog is a form of stratocumulus cloud that touches the ground, also reported as a special feature of ABL (Stull, 2012). Continuously increasing atmospheric pollution and its long-term exposure pose many challenges for global public health which includes cardiovascular and cardio-respiratory diseases. It has become a latent need to accurately monitor the atmospheric variables that allow for the prediction of air pollution behaviour, to issue early alarms for the protection of the population. One of the variables of greatest interest is the dynamical height of the ABL, the lowest layer of the troposphere is directly influenced by the Earth surface by means of both natural and anthropogenic emissions (Koffi et al., 2016).

Many authors discussed soft computing and artificial intelligence-based model to study the effect of ABL on the atmosphere and human beings simultaneously (Terradellas et al., 2005). These models utilised different techniques i.e. Neural Network, Fuzzy Logic Technique, Deep Learning, Adaptive Neuro-Fuzzy Inference System (ANFIS), etc. (Niska et al., 2004; Freeman et al., 2018). These techniques are used to investigate, simulate, and analyse complex issues and phenomena in an attempt to solve real-world problems. The accurate modelling of ABL height and the realisation of prediction techniques are of great significance to the pollution control board, meteorological department, atmospheric scientists to study the climatic condition for local or remote areas

*Corresponding author. e-mail: 2006.kirti@gmail.com

Citation: Tellus A: 2021, **73**, 1926132, https://doi.org/10.1080/16000870.2021.1926132

(Caughey, 1984; Singal et al., 1994; Levi et al., 2020; Liu et al., 2020). For example, ABL height is significant in calculating the pollution carrying capacity in a specific area. Air quality assessments at the local or regional scale require for a variety of purposes such as emission control, air quality forecasts, and implementation of legislation. A key input to this model is the meteorological data that require computing the transport, dispersion, and removal of pollutants. ABL height determines the volume available for the diffusion of contaminants and also an essential parameter, i.e. Wind Profile in atmospheric flow models (Koffi et al., 2016). Besides, ABL height is vital to air-space study, wind structure of the area, atmospheric stability class, etc. To calculate/measure the ABL height, there are two methods, viz. in-situ or direct method (such as tethered balloons, masts, rawinsonde etc.) and remote sensing method (such as LIDAR, SODAR, wind profilers) (Bradley, 2007; Lee and Pal, 2017). SOnic Detection And Ranging (SODAR) is one of the remote sensing instruments (Beyrich, 1997; Emeis et al., 2008). This instrument works with the acoustic wave, where the acoustic wave is transmitted into the atmosphere and gets reflected on to the antenna due to the inhomogeneous structure in the atmosphere (Gilman et al., 1946). The output of the SODAR data is plotted in the form of an echogram, which represents the reflection of the signal from the atmosphere. This data has been used for the prediction of ABL height using time series prediction models. The time series models can be classified as Linear and Non-linear models. Auto Regressive (AR), Auto Regressive Moving-Average (ARMA), Auto Regressive Integrated Moving-Average (ARIMA) and its variation are linear models. They work on predefined equations to fit a mathematical model to a univariate time series (Selvin et al., 2017). These models fail to cope up with latent dynamics in the data. The advanced soft computing techniques such as Artificial Neural Network (ANN), Adaptive Network-based Fuzzy Inference (ANFIS) system, Genetic Algorithm, and Fuzzy Inference System, are non-linear models and being successfully applied for modelling of different parameters such as ABL Height, pollutant, temperature, etc. (Chelani, 2005; Rehman and Mohandes, 2008; Ettouney et al., 2009; Paoli et al., 2010; Kumar and Jha, 2013; Vivas et al., 2020). However, these models are less capable of identifying the hidden pattern and underlying dynamics of data. Deep learning algorithms are capable of identifying the hidden patterns and underlying dynamics in the data through a self-learning process (Selvin et al., 2017; Zaidi et al., 2020). In the case of ABL height, the data generated is enormous and is highly non-linear (Vivas et al., 2020). Unlike other algorithms, deep learning models can provide effectively good predictions by analysing the interactions and hidden patterns within the data. Long Short-Term Memory (LSTM) is the special type of a Recurrent Neural Network (RNN) (Hochreiter and Schmidhuber, 1997; Kawakami, 2008). LSTM is used in the deep learning methods, that works on the gradient-based learning algorithm and designed to minimise the backflow of the error.

In the area of meteorological parameters, time series analysis using neural network models and deep learning algorithms have used different input variables for predicting the weather data. The data for time series has been used for heterogeneous weather information. Vivas et al. (2020) has applied deep learning for the detection of ABL height from atmospheric LiDAR signals in Colombia. Rehman and Mohandes (2008) reported that an Artificial neural network has used for the prediction of global solar radiation with air temperature and relative humidity for Saudi Arabia from 1998 to 2002. Zhao et al. (2019) has applied the LSTM method to predict RADAR sea clutter and the performance of a particular method has found superior over neural network. However, for long term prediction, the performance of model is not as good as short-term prediction.

In the present work, the LSTM model has been implemented to obtain the future value of ABL height using SODAR data. The seasonal and annual variability have been studied for significant difference in ABL height. This model incorporates the factor and principle, which affect performance. Also, the performance of the model has been quantified for the data of ABL height using the SODAR system. Further, to estimate the performance of the model in picture, a time-series comparison of annual and seasonal ABL height variations is presented. This work will help to air quality study, seasonal variability for the Delhi region. Section 2 briefly describes the Delhi region, SODAR ABL height data. This section also describes the ABL height LSTM model and architecture. Section 3 begins with the general result of LSTM network then describes the annual and seasonal ABL height analysis and prediction. Section 4 and 5 discuss and conclusions of annual and seasonal ABL height prediction.

2. Data and methodology

Delhi is a site in the northern region of India at 715 feet above sea level, where it has a semi-arid or steppe climate, with scorching summers, heavy rainfalls in the monsoon months, and cold winter (Ramachandran et al., 2012; Kumar et al., 2017b). There are dust storms in summer and foggy mornings in winter. The temperature gradually rises to 46^0C in the summer and falls to 2^0C in winter (Roy et al., 2011). In the winter months, temperature inversion and low wind speed are the leading causes

Table 1. Designing specifications of CSIR-NPL monostatic SODAR.

Transmitted power (electrcical)	90 Watts
Transmitted power (acoustical)	15 Watts
Pulse width	100 ms
Pulse repetition period	4 sec
Operational range	1000 m
Receiver bandwidth	50 Hz
Frequency of operation	2250 Hz
Acoustic velocity	340 m/s (average)
Receiver Gain	80 dB
Transmit-receive antenna	Parabolic reflector dish surrounded by conical acoustic cuff
Receiver area	2.5 sq. m
Preamplifier sensitivity	The fraction of a micro-Volt

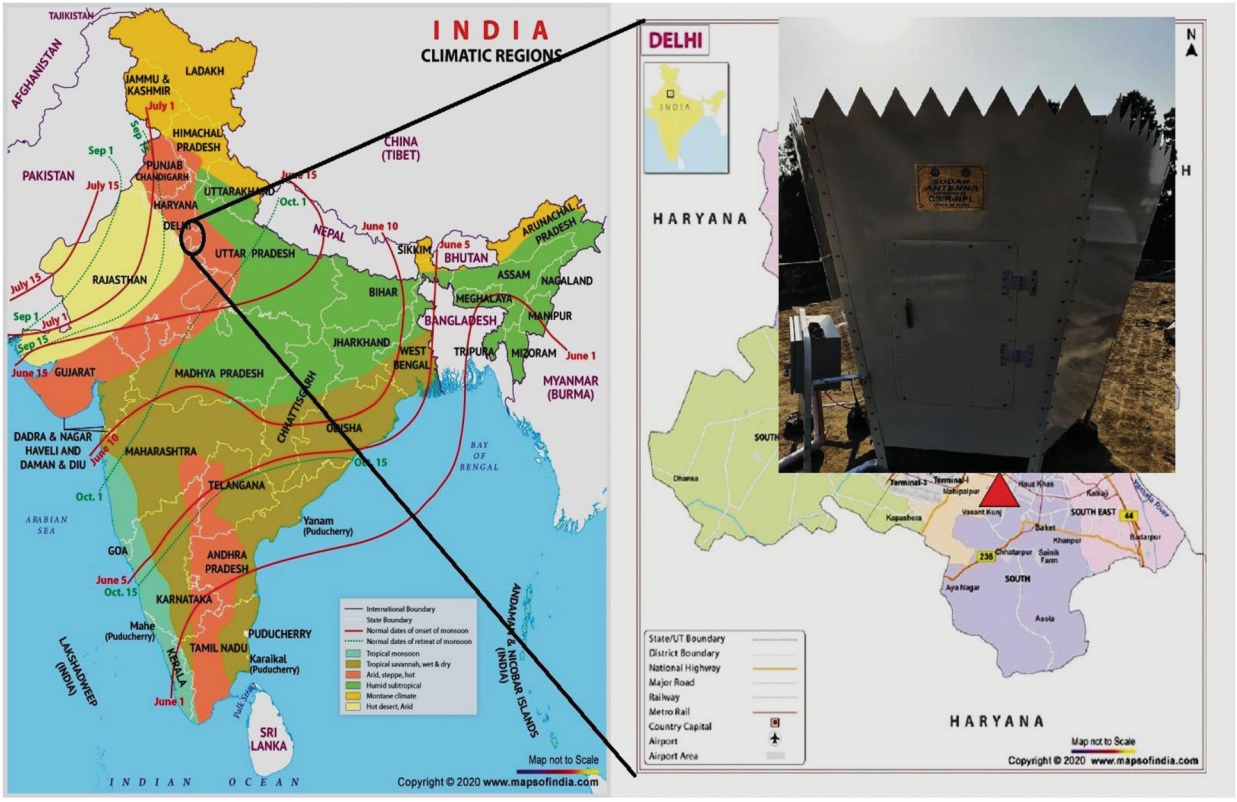

Fig. 1. Monsoon Map of India and SODAR system installed at Delhi (Courtesy: www.mapindia.com).

of the accumulation of airborne pollutants in Delhi. Delhi, being the capital of India has been chosen as the site for the installation of the SODAR as it faces extensive change in the atmosphere (Figure 1).

SODAR system was developed at CSIR-NPL in 1973 and modified from time to time. The system is installed on the roof of the main building, CSIR-NPL, New Delhi. Table 1 shown the design specifications of SODAR system which are used for measurement of ABL height (Gera et al., 2011; Kumar et al., 2019). The data of ABL height is obtained in the echogram, which is shown in Fig. 2 and measured by visualisation (Kumar et al., 2017a, 2017b). In this study, the data set has a temporal value (1 hour = one value) for one year (1 Dec 2018–30 Nov 2019).

2.1. Basic of LSTM network

LSTM network predicts the next moment state based on the data at the previous moment state (Zhao et al., 2019). From Fig. 3, it has been observed that the most

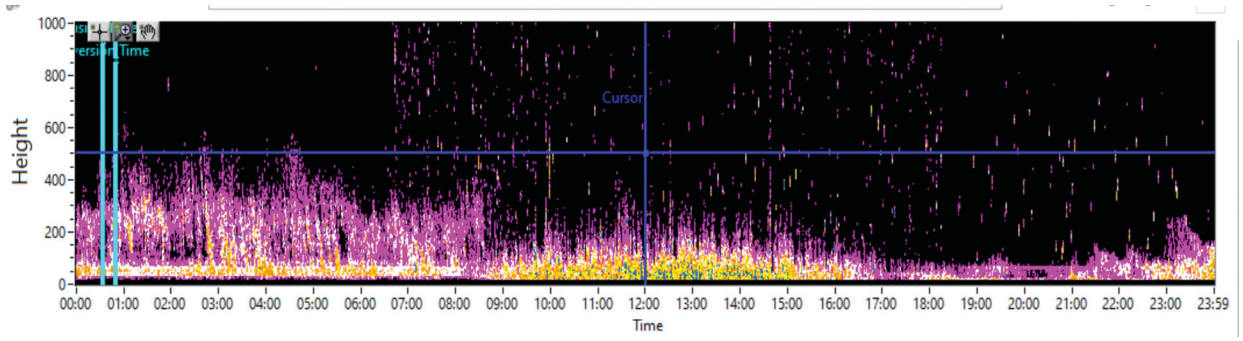

Fig. 2. 24 hours echogram of SODAR system.

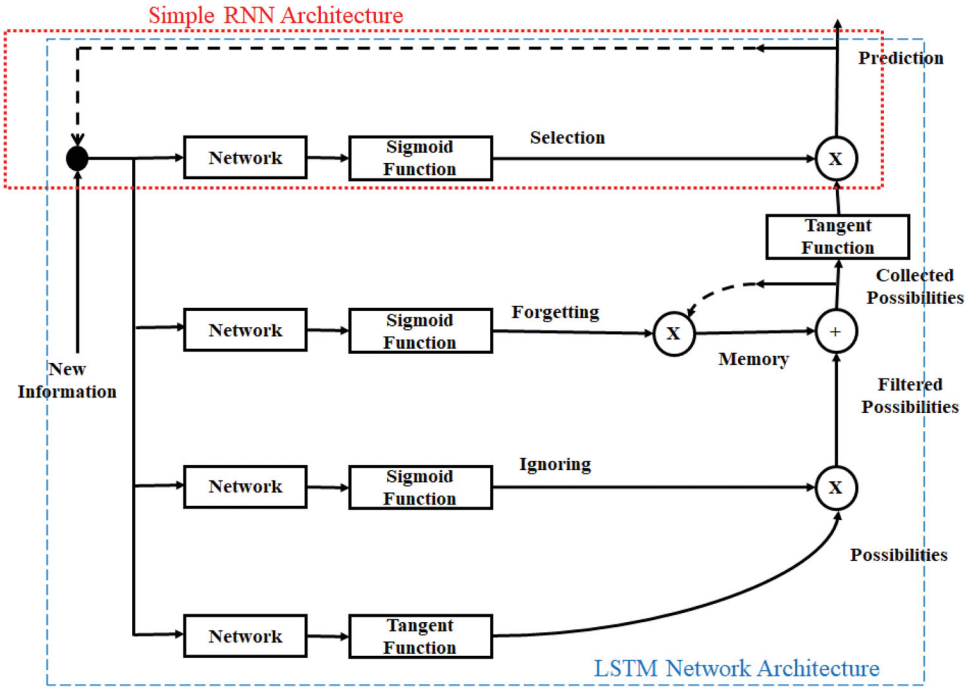

Fig. 3. Network architecture.

significant difference between ordinary RNN and LSTM is the hidden unit. In LSTM network, the hidden layer does self-looping, which can be seen as multiple copies of the same neural network, and each neural network module passes the information to the next level. It is also recompensed for the incapability of RNN to predict long-distance relationships (Hochreiter and Schmidhuber, 1997). It is used due to the famous part of the current deep learning field to solve the time-series prediction problem. A neural network contains one input layer, one output layer, and many intermediate layers, which are called the hidden layer (Soni and Parmar, 2020). The output of the input layer appearances, the input of the first hidden layer, and the output of each hidden layer constitutes the input of each subsequent hidden layer (Kumar et al., 2015). LSTM is a type of RNN but the usually hidden layers are replaced with LSTM cells and these cells are composed of various gates that control the input flow (Selvin et al., 2017; Zhao et al., 2019). An LSTM cell consists of input gate (consist of input), cell state (runs through the entire network and has the ability to add or remove information with help of gates), forget gate (control level of cell state reset/forget), and output gate (control level of cell state added to hidden state). The details of architecture of LSTM network have been described in Hochreiter and Schmidhuber (1997) and Kawakami (2008).

2.2. Sodar ABL height prediction model

Figure 4 represents the block diagram of development of the ABL height LSTM network prediction model for the

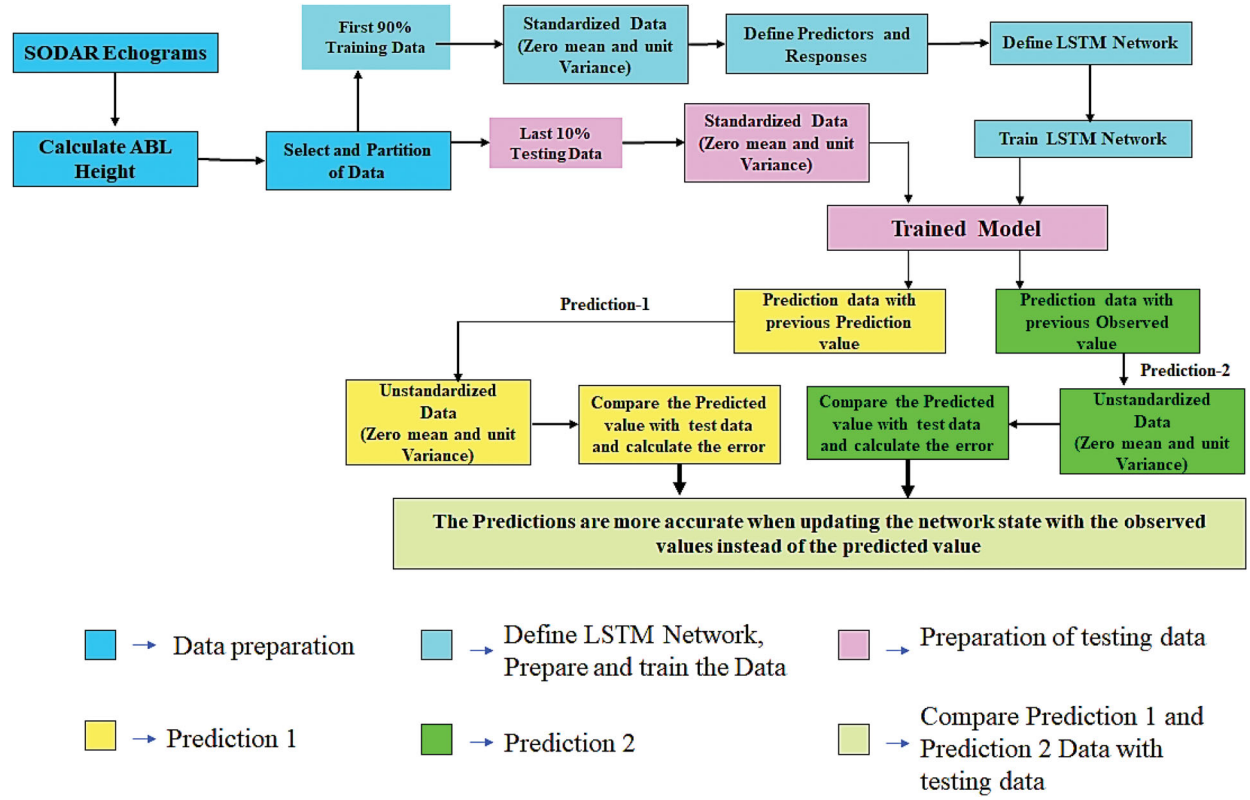

Fig. 4. Block diagram of the LSTM ABL height model.

training and testing of the network. Block diagram depicts that the LSTM prediction network could uninterruptedly pass the ABL height characteristics, i.e. from the current step to the next step, and predicate the next point from the previous point. Thus, it predicts the temporal ABL height. While creating the LSTM prediction model, the input data are a set of temporal ABL height, that is measured by the SODAR system.

For the solving of ABL height prediction problematic, the input data are a set of ABL height temporal series. As the series progresses, the hidden layer of the previous point will affect the hidden layer of the next point. This feature is of great help to the ABL height that has a specific nonlinear relationship between the previous data and the last data. Therefore, the configuration of LSTM network was a sequence-to-sequence regression and trained from Back Propagation Through Time (BPTT). It is observed that as time increases, the values are also changing with a specific time, and there is some periodic change. From the above observation, LSTM neural network model is good for nonlinear parameter.

To check the generalised capacity and accuracy of model, first 90% of the input data are selected as the training set, and the last 10% as the test set, due to checking the pattern of convection and inversion period of ABL on temporal basis and below functions are selected as performance measures of prediction model:

$$\textit{Root Mean Square Error, RMSE} = \sqrt{\frac{1}{n}\sum_{i=1}^{n}(Predicated_i - Measured_i)^2}$$

$$\textit{Relative Root Mean Square Error, rRMSE} = \sqrt{\frac{1}{n}\sum_{i=1}^{n}\left(\frac{Predicated_i - Measured_i}{Measured_i}\right)^2}$$

$$\textit{Mean Absolute Error, MAE} = \frac{1}{n}\sum_{i=1}^{n}|Predicated_i - Measured_i|$$

$$\textit{Mean Absolute Percentage Error, MAPE} = \frac{100}{n}\sum_{i=1}^{n}\left|\frac{Predicated_i - Measured_i}{Measured_i}\right|$$

In this paper, the pre-defined Deep Learning Models available in the Deep Learning toolbox of MATLAB R2019a software is used for deep learning training. These pre-defined networks are retrained and fine-tuned on augmented training and validation sets with SODAR ABL height data. For the better fit, to prevent the training and testing from diverging, the data are standardised with

zero mean and unit variance (Unal et al., 2003). The networks are trained using 'adam' function as an optimiser (Kingma and Ba, 2014). LSTM network architecture parameters are defined in Table 2.

Table 2. LSTM architecture parameters.

Network parameters	Value
Gradient decay factor	0.9
Squared gradient decay factor	0.9990
Initial learn rate	0.005
Learn rate schedule	Piecewise
Learn rate drop factor	0.20
Learn rate drop period	125[a]
Gradient threshold method	I2 norm
Gradient threshold	1
Verbose frequency	50
Validation frequency	50
Shuffle	once
Sequence length	Longest
State activation function	tanh
Gate activation function	sigmoid
Input weight initializer	glorot
Recurrent weight learn initializer	orthogonal
Bias initializer	Unit-forget-gate
Bias learns rate factor	1

[a]Drop the learning rate after 125 epochs by a factor of 0.2.

The performance of the prediction model is quantified for the test set and used for estimating the RMSE, rRMSE, MAE, and MAPE. The calculated error is lower than to gets a higher accuracy of the prediction model (Adnan et al., 2020; Kumar et al., 2021).

The input data set has a nearly one-year data point. When the complete data set is used in each training process, the gradient cannot be corrected, and the network cannot converge to the global optimum. The size of the mini-batch is selected with care such that the whole dataset is to be passed through the network every epoch during training and no data is discarded. The experiment is done for ABL height prediction models using the 3 months data (1 April 2019 to 30 June 2019). During this period, available data is continuous and more dynamic in nature. Also, the change in ABL height is maximum during May month. In this paper, two types of predictions are presented. Firstly, the network is updated with previously predicted values as input to the function, which is called Prediction-1 and secondly, the network is updated with observed values instead of the predicted values, this is called Prediction-2. When the LSTM network completes the one loop, i.e. the input ABL height data set passes through the network once and returns once, the process is called an epoch.

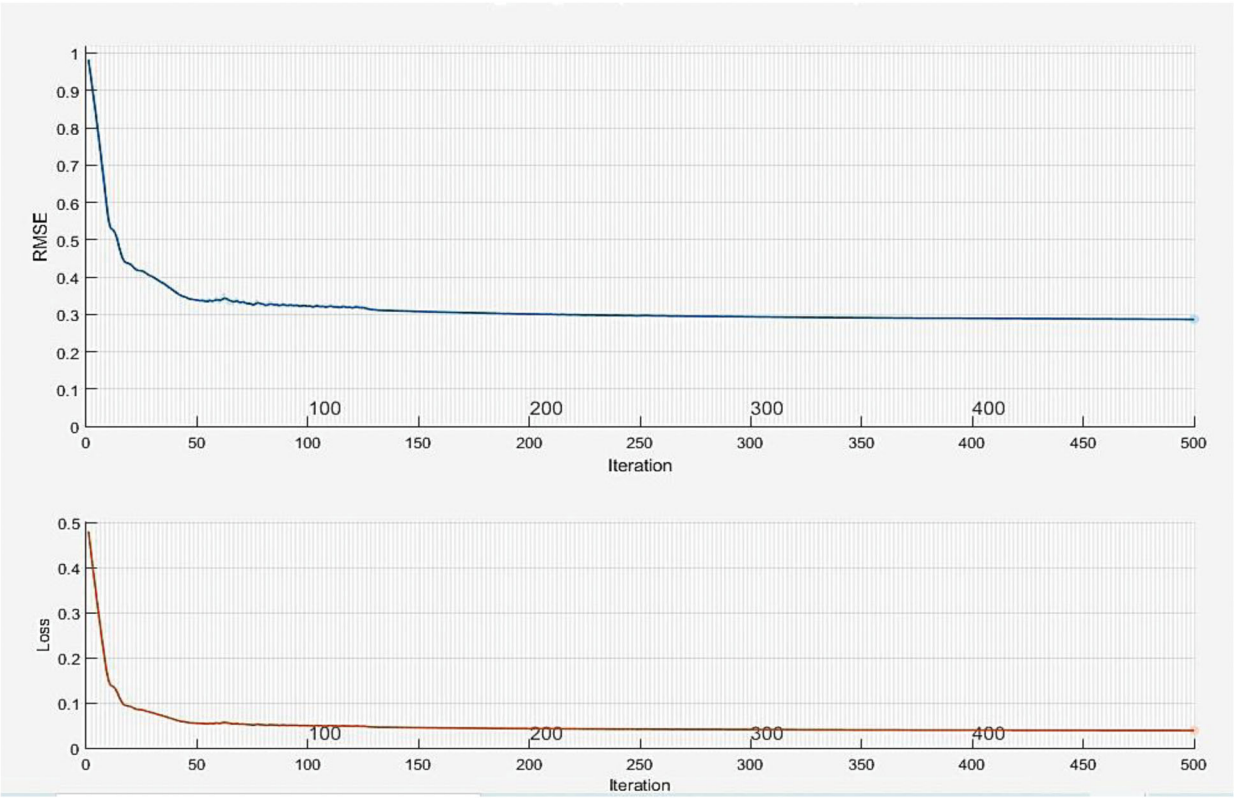

Fig. 5. Training progress with hidden layer 32 and Epoch 500.

Table 3. Comparison of accuracy of LSTM model.

	Prediction-1				Prediction-2			
Hidden layer	RMSE1	rRMSE1	MAE1	MAPE1	RMSE2	rRMSE2	MAE2	MAPE2
Max epochs – 500								
2	790.3	24.69	617.5	72.37	315.69	9.86	197.41	17.11
5	317.83	9.93	199.61	20.22	212.48	6.64	133.99	12.74
10	270.58	8.45	181	20.1	214.71	6.7	130.24	12.29
20	250.93	7.84	175.36	18.27	202.13	6.31	121.86	11.43
25	289.34	9.04	197.85	20.47	204.76	6.39	120.59	11.43
28	290.05	9.06	198.89	22.33	205.31	6.41	118.31	11.25
30	235.4	7.35	166.91	17.31	192.01	6	114.01	10.96
32	220.31	7.33	167.12	17.3	193.81	5.95	113.72	10.62
35	272.51	8.51	194.47	19.56	197.15	6.16	117.52	10.87
50	264.61	8.26	186.84	19.27	192.48	6.01	112.21	10.54
100	291.14	9.09	205.52	21.92	198.86	6.21	116.06	11.11
Max epochs – 250								
32	373.89	11.68	250.20	24.37	193.66	6.05	115.99	10.90
Max epochs – 750								
32	271.66	8.48	189.62	20.68	193.35	6.04	112.08	10.77

[a]Red colour row shows best prediction result.

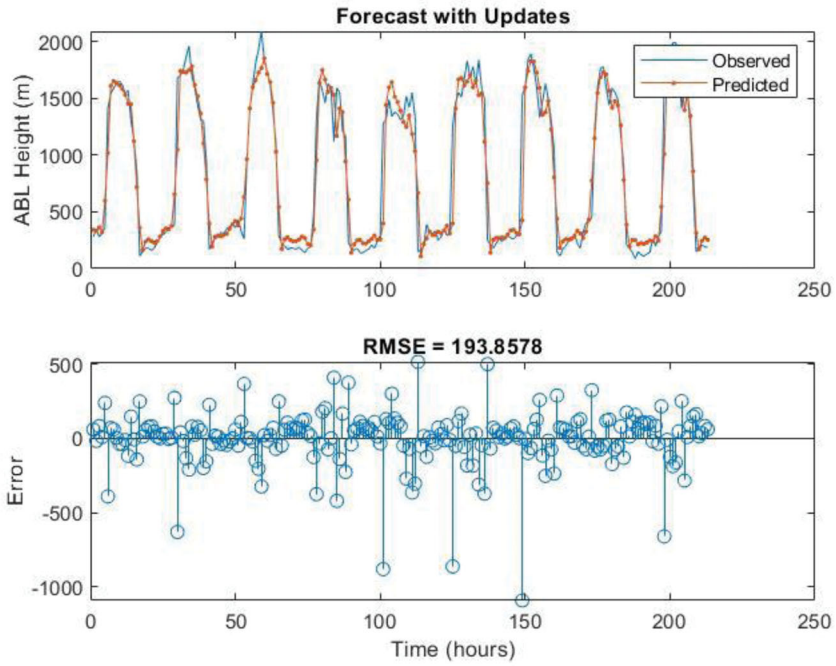

Fig. 6. Prediction result LSTM Network update with observed values (Prediction-2), hidden layer 32 and maximum epochs 500.

Table 4. Statistical analysis of LSTM model with hidden layer 32 and epoch 500.

Parameter	Training data	Test data	Prediction-1 data	Prediction-2 data
Mean	737	837	849	852
Median	430	551	547	400
Kurtosis	–1.22	–1.67	–1.66	–1.71
Skewness	0.56	0.35	0.32	0.26
Coefficient of variation	0.80	0.68	0.72	0.78

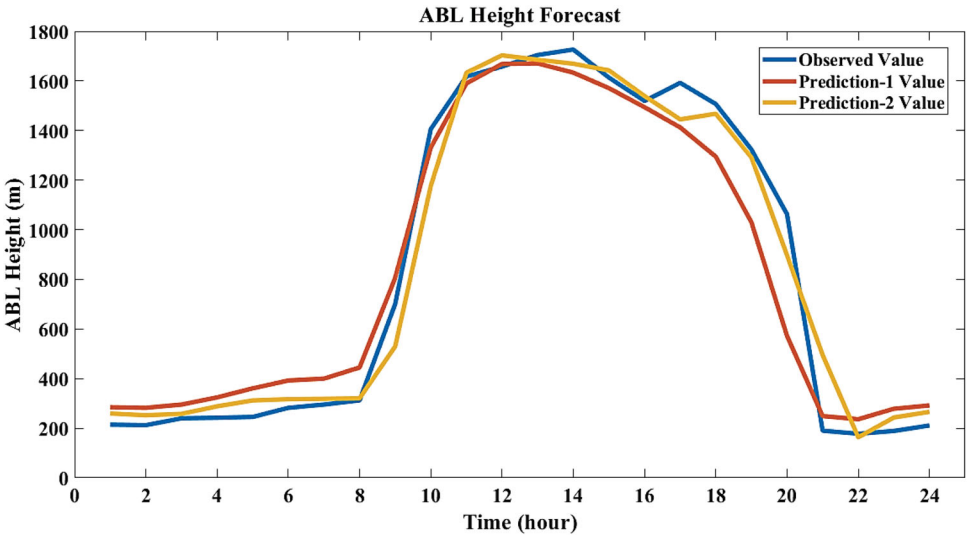

Fig. 7. Comparison of Line Plot of Observed ABL Height and Predication ABL Height.

Table 5. Comparison between NAR and LSTM Model.

	NAR	Prediction-1	Prediction-2
RMSE	259.65	220.31	193.85
MAE	164.97	167.12	113.72

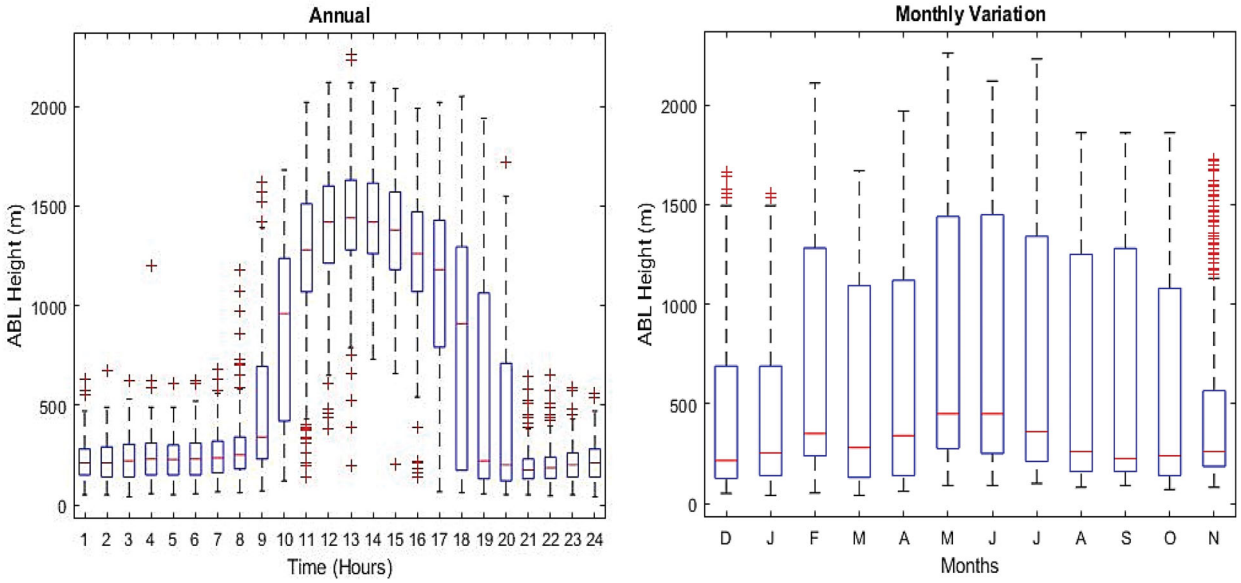

Fig. 8. Annual ABL height Temporal and Monthly variation.

3. Results

Performance evaluation of the experiment for ABL height LSTM model has been obtained for the optimal parameters. The testing is done for two parameters, i.e. hidden neuron and epochs with constant data set (2160 data point). To avoid overfitting, the networks are trained using different hidden layer varying in the range (2, 5, 10, 20, 30, 50, 100, 35, 28, 32, respectively) with different epochs (250, 500, 750). The network (32 hidden layer and 500 epochs) training progress is shown in Fig. 5, which provide the best result from among other combination.

Table 6. Monthly ABL height variation during different hours.

Month	Maximum ABL height (m)	Corresponding hour of maximum ABL height (hrs)	Average ABL height (m) during Day time (09:00–18:00 hr)	Average ABL height (m) during Remaining hours (19:00–08:00 hr)	Diurnal average (m)
December	1255	13:00	795	170	435
January	1120	13:00	710	200	415
February	1565	13:00	1125	265	620
March	1360	12:00	1035	185	545
April	1435	13:00	1145	225	615
May	1745	12:00	1480	350	810
June	1635	13:00	1475	325	795
July	1520	12:00	1380	325	760
August	1410	12:00	1305	260	690
September	1485	14:00	1280	190	645
October	1445	12:00	995	225	550
November	1405	11:00	850	230	490

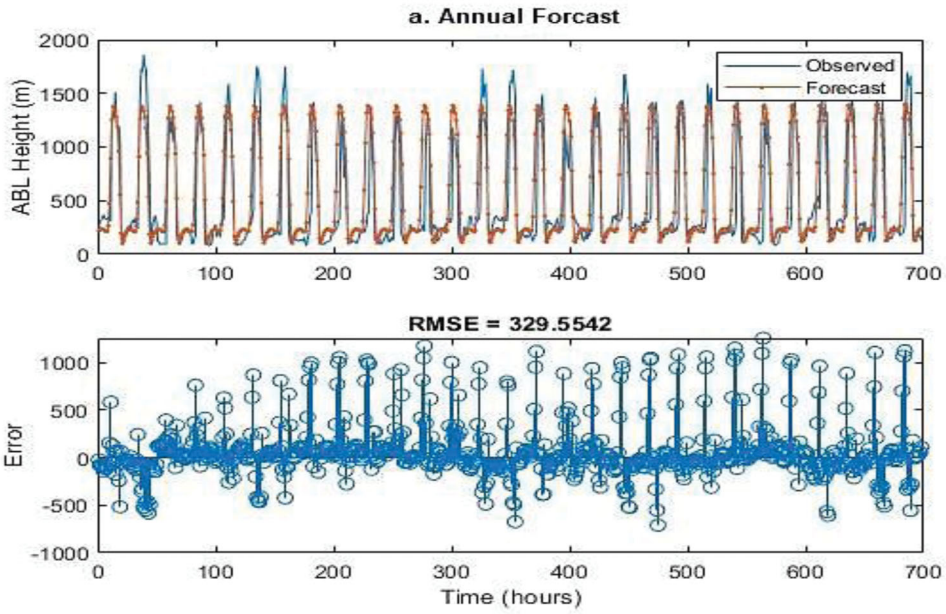

Fig. 9. Prediction result LSTM Network update with predicted values (Prediction-1), hidden layer 32 and maximum epochs 500.

Results obtained after testing is shown in Table 3 and Fig. 6. It has been observed that as the epochs and hidden layer (neuron) increases, the error value on the test set and training set both decreases. Table 3 shows that after certain epochs and the number of hidden layers and the error value increases, i.e. the prediction accuracy is improving.

To check the uncertainties in the LSTM model, different parameters have been calculated and represented in Table 4 and Fig. 7. It has been observed that the testing values and predicted values have followed the same pattern. Figure 7 shows the line plot of temporal average of testing ABL height data and prediction ABL height data. In the LSTM model, Prediction-1 represents the updated network with predicted value (1650 m maximum) and Prediction-2 represents the updated network with observed values (1700 m maximum), with respect to the highest value of ABL height from SODAR 1775 m.

Also, Non-linear Auto Regressive (NAR) model is used to predict the ABL height using the predefined model of MATLAB 2019a. The maximum value of errors is obtained for each model is shown in Table 5. It has

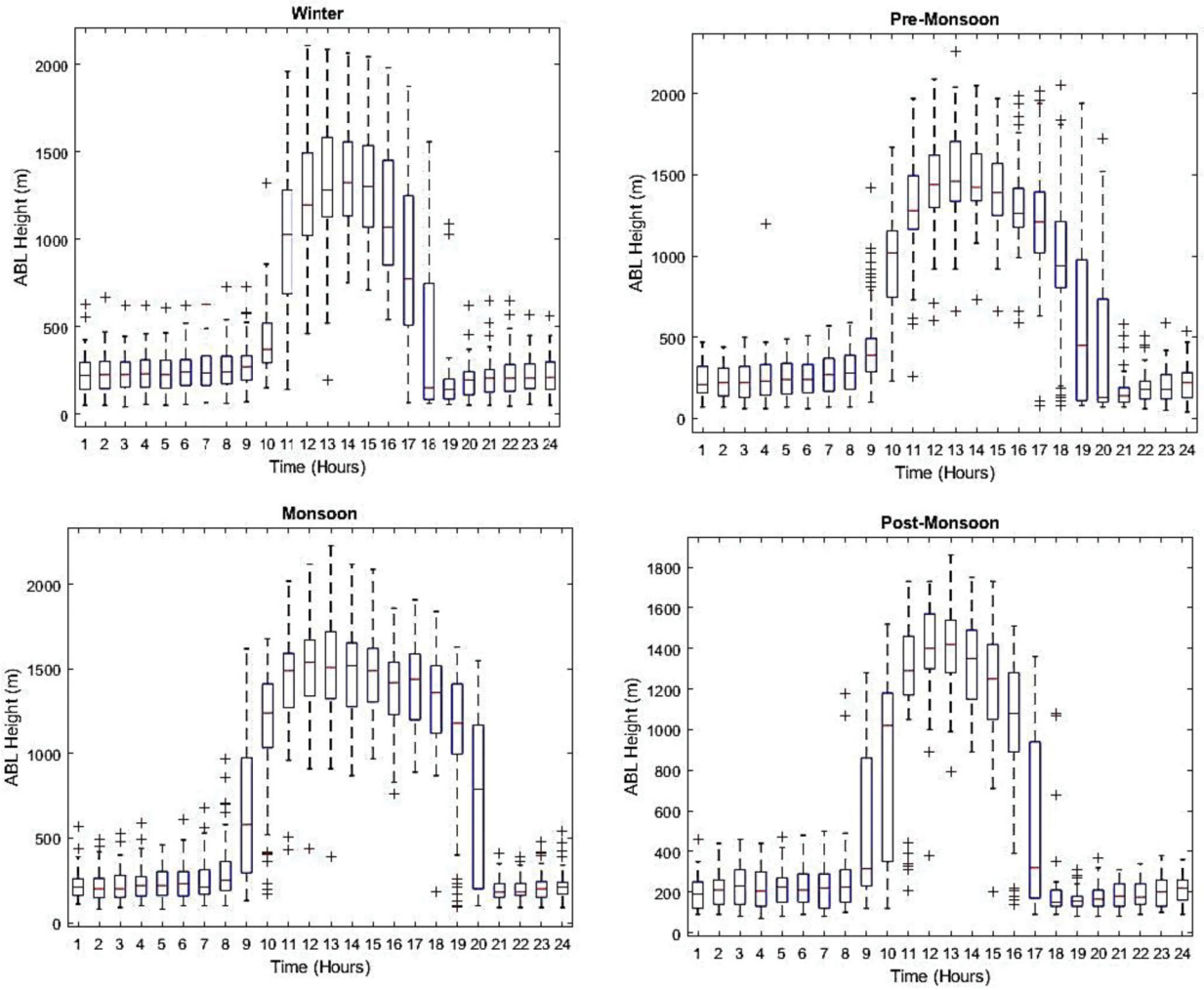

Fig. 10. Box plot of temporal seasonal ABL height.

been observed that Prediction-2 model values are more accurate than the NAR model. However, NAR model is used for the information from previous lags to predict future instances. The ABL height is highly dynamical in nature for day-to-day atmosphere. This causes a learning problem to NAR architecture and fails to capture the dynamical changes accurately.

3.1. Analysis and prediction of annual ABL height

The ABL is a zone having nearly constant potential temperature and specific relative humidity with height. ABL height determines the volume available for dispersion of pollutants and characterises the structure of the lower atmosphere. Higher the value of mixing height, the greater is dispersion rate and vice versa. Based on the observation of SODAR echograms, the ABL height is changing continuously. So, the box plot is used to interpret the data (Frigge et al., 1989; Williamson et al., 1989). The box plot uses the median, the approximate quartiles, and the lowest and highest data points to convey the level, spread, and symmetry of a distribution of data values. Every box has a central mark, which indicates median value and whereas the bottom-line represents the 25th percentiles, and top-line indicates 75th percentiles of the data. The whiskers cover the most extreme data points and the outliers have plotted individually using the '+' symbol. Figure 8 represents the annual variation of temporal ABL height and Month average. The vertical bars denote the ± σ standard deviation from the temporal average. Figure 8 and Table 6, presents the temporal average SODAR data for about one year (December 2018 to November 2019).

The annual ABL height data have been used to retained LSTM model to predict the annual temporal ABL height. The result obtained shows the Prediction-2 model has the lowest RSME (187.71 m). Figure 9, Prediction-1 model provides a good result for 30 days

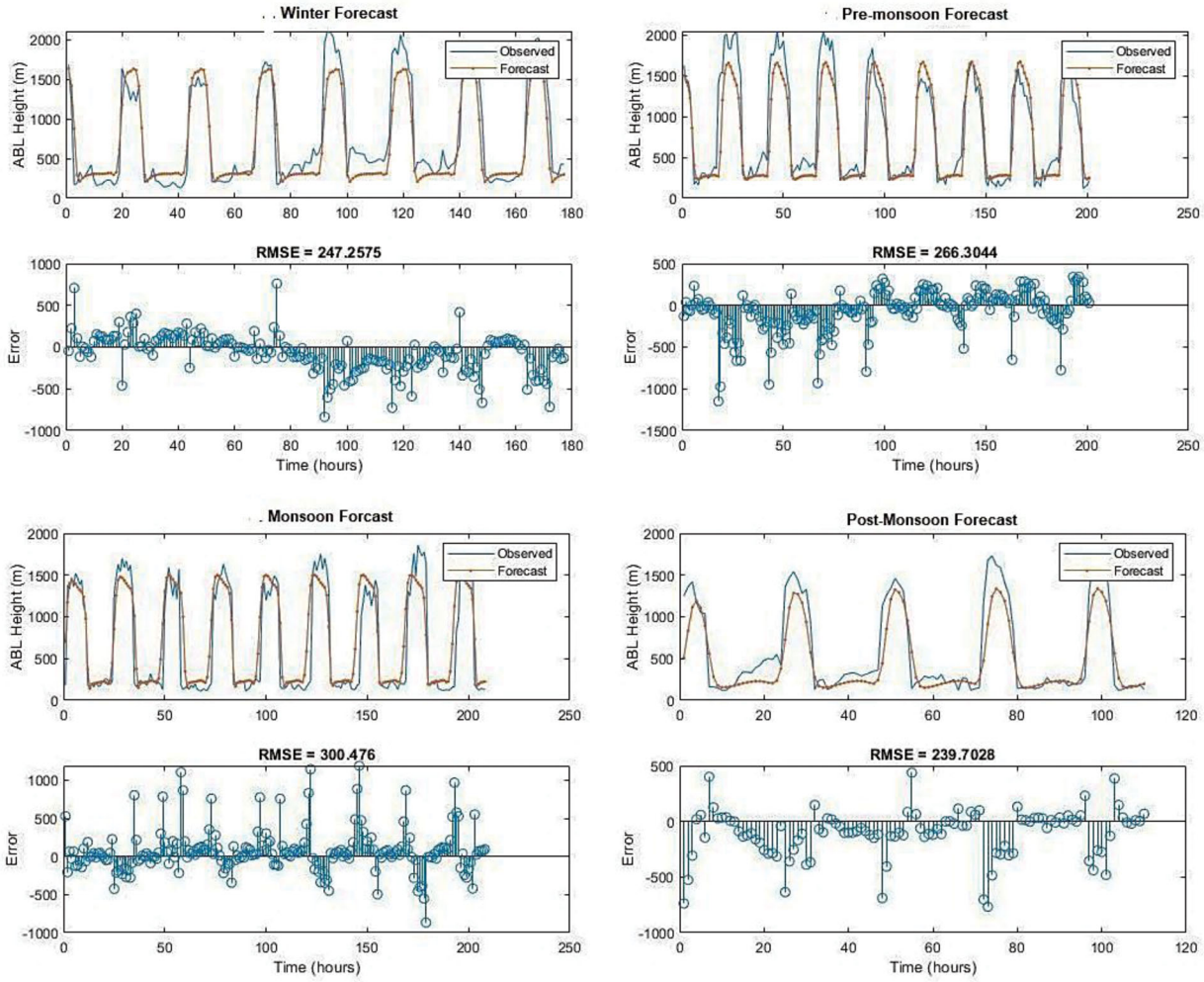

Fig. 11. Seasonal ABL height Prediction result from the update network state with predicted values (Prediction-1).

with RSME value (329.55 m). During convention period, the predicted ABL height is lower than observed, which increases the error. Also, the annual data set has been applied on NAR model and obtained a higher RSME value (261.80 m) compared to Prediction-2 model.

3.2. Comparison and prediction of seasonal ABL height

Total data set has been classified into four seasons based on meteorology over northern India (Soni et al., 2011; Ramachandran et al., 2012; Kumar et al., 2017b) namely, winter (December-January-February), Pre-monsoon (March-April-May), Monsoon (June-July-August-September) and Post-monsoon (October-November) for the analysis of seasonal ABL height. The temporal seasonal variation of mixing height during the whole year of observation is shown in Fig. 10. It is observed that the convection period is most extended during monsoon and lowest during the post-monsoon. The maximum value (about 1510 m) of mixing height has been observed in the pre-monsoon season, while the minimum value of mixing height (around 1315 m) is found during the winter season. The monthly average ABL Height during different hours has been represented in Table 6 and found that in May month (Pre-Monsoon season), ABL height is the highest and lowest in January (winter season).

ABL height has a positive correlation with temperature and wind speed, whereas a negative relationship with relative humidity (Kumar et al., 2017b). Temperature and wind speed influences positively to the ABL, while relative humidity influences negatively to the ABL heights, during all the seasons due to an increase or decrease in solar heating. The convective boundary layer height increases and decreases during the day time due to the change in surface temperature. The variation in surface temperature carbon monoxide mixing ratio the existence of atmospheric convection; therefore, it strongly affects

Table 7. Comparison of seasonal prediction of ABL height.

		Hidden layers – 32; Max Epochs – 500								
		Prediction-1				Prediction-2				NAR models
	Data point	RMSE1	rRMSE1	MAE1	MAPE1	RMSE2	rRMSE2	MAE2	MAPE2	RMSE
Annual	6984	329.55	10.29	200.13	23.35	187.71	5.86	118.78	17.04	261.80
Winter	1776	247.25	7.72	181.83	19.59	187.77	5.86	125.81	13.19	307.33
Pre-Monsoon	2016	266.30	8.32	182.99	20.02	181.18	5.66	116.24	11.04	245.91
Monsoon	2088	300.47	9.38	187.14	15.62	255.45	7.98	151.71	12.74	281.25
Post-Monsoon	1104	239.70	7.49	163.73	25.15	178.92	5.59	118.57	15.17	250.94

the height. Generally, it is high between 11:00 to 14:00 during all seasons. Mixing height starts decreasing due to the decrease in solar heat during the evening. The ABL height during the convection period is found 1510 m, 1485 m, 1395 m, and 1315 m in pre-monsoon, monsoon, post-monsoon, and winter seasons, respectively.

All the season data is used for the prediction of seasonal ABL height. Both LSTM models are retrained and tested with seasonal data and to obtain the result for the prediction of seasonal ABL height. Figure 11 represents the seasonal ABL height prediction result from the Prediction-1 model. It is observed that when the prediction days increases the accuracy of Prediction-1 model decrease. Seasonal data is used to retrain and test the NAR model. It has been observed that the NAR model gives a higher RSME value.

4. Discussion

The four season's data sets of the ABL height in different atmospheric conditions are selected to train the LSTM model. Then, the trained prediction model is used to predict the ABL height of each season to compare with the annual prediction (Figures 9 and 11). The predictions ABL height shows a comparable result with the SODAR data, especially over transition period (from inversion to convection or vice versa). Table 7 shows the error of ABL height prediction using the LSTM network, which is lower in winter season and higher in annual data. Whereas error in all conditions of Prediction-2 is lower as compare to Prediction-1 and NAR model. But the related error generated by Prediction-1 is not much higher as compared to Prediction-2. The LSTM network model is providing high prediction accuracy as compared to NAR model. The LSTM models simulate the seasonal ABL height reasonably well, i.e. inferred from the periodicity in the ABL height time series. It also provides reliable ABL height simulations and predictions at any sites where the yearly ABL height pattern remains somewhat similar. It is observed that ABL height is highest in the convection period (daytime), do not follow any periodicity and somewhat errors are highest during this period. These LSTM models are useful to the pollution regulatory body to control atmospheric pollution.

5. Conclusion

A neural network based temporal ABL height prediction is presented in this paper. It has been observed that LSTM neural network architecture is capable of capturing the hidden dynamics of temporal ABL and able to make predictions. The critical point of this approach is the decomposition of the temporal data into seasonal and the annual prediction of ABL height. Application of LSTM instead of classical neural network has enabled to obtain better accuracy of the seasonal prediction and, aggregate annual data. The proposed model is applied to ABL height data measurement using the SODAR system situated at CSIR-NPL, Delhi. The obtained results of prediction are in good agreement with the actual measurements. It is found that the optimal results achieved in short training time, when the number of neurons is equal to 32 and epoch are equal to 500, which provide accurate prediction result to obtain a long-term prediction. The LSTM model has foundation for the next step of accurate prediction of ABL height. Two types of prediction LSTM model have been applied for prediction of annual and seasonal ABL height. Both the models have provided good accuracy as compared to NAR model. These LSTM networks will apply to a different environmental parameter to find out the atmospheric condition in future.

Disclosure statement

No potential conflict of interest was reported by the authors.

References

Adnan, R. M., Liang, Z., Parmar, K. S., Soni, K. and Kisi, O. 2021 . Modeling monthly streamflow in mountainous basin

by MARS, GMDH-NN and DENFIS using hydroclimatic data. *Neural Comput. Appl.* 33(7), 2853–2871.

Beyrich, F. 1997. Mixing height estimation from SODAR data—a critical discussion. *Atmos. Environ.* 31, 3941–3953. doi:10.1016/S1352-2310(97)00231-8

Bradley, S. 2007. *Atmospheric Acoustic Remote Sensing: Principles and Applications*. Taylor & Francis Group, USA: CRC Press.

Caughey, S. J. 1984. Observed characteristics of the atmospheric boundary layer. In: *Atmospheric Turbulence and Air Pollution Modelling*. Springer, Dordrecht, pp. 107–158.

Chelani, A. B. 2005. Predicting chaotic time series of PM10 concentration using artificial neural network. *Int. J. Environ. Stud.* 62, 181–191. doi:10.1080/0020723042000285906

Emeis, S., Schäfer, K. and Münkel, C. 2008. Surface-based remote sensing of the mixing-layer height–a review. *Metz.* 17, 621–630. doi:10.1127/0941-2948/2008/0312

Ettouney, R. S., Farouq, S. M., John, G. Z., Mahmoud, A. E. and Hisham, M. E. 2009. Forecasting of ozone pollution using artificial neural networks. *Manag. Environ. Qual.* 20, 668–683. doi:10.1108/14777830910990843

Freeman, B. S., Taylor, G., Gharabaghi, B. and Thé, J. 2018. Forecasting air quality time series using deep learning. *J. Air Waste Manag. Assoc.* 68, 866–886. doi:10.1080/10962247.2018.1459956

Frigge, M., Hoaglin, D. C. and Iglewicz, B. 1989. Some implementations of the boxplot. *Am. Statist.* 43, 50–54.

Garratt, J. R. 1994. The atmospheric boundary layers. *Earth. Sci. Rev.* 37, 89–134. doi:10.1016/0012-8252(94)90026-4

Gera, B. S., Raghavendra, T., Singh, G., Ojha, V. K., Malik, J. and co-authors. 2011. Instrumentation and computer capabilities for improving SODAR data acquisition. *Int. J. Remote Sens.* 32, 4807–4817. doi:10.1080/01431161.2010.489072

Gilman, G. W., Coxhead, W. B. and Willis, F. H. 1946. Reflection of sound signals in the troposphere. *J. Acoust. Soc. Am.* 18, 274–283. doi:10.1121/1.1916364

Hochreiter, S. and Schmidhuber, J. 1997. Long short-term memory. *Neural Comput.* 9, 1735–1780. doi:10.1162/neco.1997.9.8.1735

Kawakami, K. 2008. Supervised sequence labelling with recurrent neural networks. Ph.D. dissertation.

Kingma, D. P. and Ba, J. 2014. Adam: A method for stochastic optimization. *arXiv preprint arXiv:1412.6980*.

Koffi, E. N., Bergamaschi, P., Karstens, U., Krol, M., Segers, A. and co-authors. 2016. Evaluation of the boundary layer dynamics of the TM5 model over Europe. *Geosci. Model Dev. 9*, 3137–3160. doi:10.5194/gmd-9-3137-2016

Kumar, N. and Jha, G. K. 2013. A time series ANN approach for weather forecasting. *Int. J. Control Theory Comput. Model* 3, 19–25. doi:10.5121/ijctcm.2013.3102

Kumar, N., Parmar, K. S., Soni, K., Garg, N. and Agarwal, R. 2015. Prediction of ventilation coefficient, using a conjunction model of wavelet-neuro-fuzzy model: A case study Delhi, India. *Acad. J. Sci. Res.* 3, 184–191.

Kumar, N., Soni, K. and Agarwal, R. 2021. A comprehensive study of different feature selection methods and machine-learning techniques for SODAR structure classification. *Model. Earth Syst. Environ.* 7, 209–212. doi:10.1007/s40808-020-00872-0

Kumar, N., Soni, K., Agarwal, R. and Singh, M. 2017a. SODAR as a diagnostics tool for urban air-quality and health care system. *J. Acoust. Soc. India* 44, 213–222.

Kumar, N., Soni, K., Agarwal, R. and Singh, M. 2019. Preliminary analysis of operating conditions of acoustic sounder (SODAR) before the installation. *J. Acoust. Soc. Am.* 146, 2997–2998. doi:10.1121/1.5137378

Kumar, N., Soni, K., Garg, N., Agarwal, R., Saha, D. and co-authors. 2017b. SODAR pattern classification and its dependence on meteorological parameters over a semiarid region of India. *Int. J. Remote Sens.* 38, 3466–3482. doi:10.1080/01431161.2017.1294774

Lee, T. R. and Pal, S. 2017. On the potential of 25 years (1991–2015) of rawinsonde measurements for elucidating climatological and spatiotemporal patterns of afternoon boundary layer depths over the contiguous US. *Adv. Meteorol.* 2017, 1–20.

Levi, Y., Dayan, U., Levy, I. and Broday, D. M. 2020. On the association between characteristics of the atmospheric boundary layer and air pollution concentrations. *Atmos. Res.* 231, 1–16.

Liu, C., Huang, J., Wang, Y., Tao, X., Hu, C. and co-authors. 2020. Vertical distribution of PM2.5 and interactions with the atmospheric boundary layer during the development stage of a heavy haze pollution event. *Sci. Total Environ.* 704, 135329–135348. doi:10.1016/j.scitotenv.2019.135329

Niska, H., Hiltunen, T., Karppinen, A., Ruuskanen, J. and Kolehmainen, M. 2004. Evolving the neural network model for forecasting air pollution time series. *Eng. Appl. Artif. Intell.* 17, 159–167. doi:10.1016/j.engappai.2004.02.002

Paoli, C., Cyril, V., Marc, M. and Marie-Laure, N. 2010. Forecasting of preprocessed daily solar radiation time series using neural networks. *Sol. Energy* 84, 2146–2160. doi:10.1016/j.solener.2010.08.011

Ramachandran, S., Kedia, S. and Srivastava, R. 2012. Aerosol optical depth trends over different regions of India. *Atmos. Environ.* 49, 338–347. doi:10.1016/j.atmosenv.2011.11.017

Rehman, S. and Mohandes, M. 2008. Artificial neural network estimation of global solar radiation using air temperature and relative humidity. *Energy Policy 36*, 571–576. doi:10.1016/j.enpol.2007.09.033

Roy, S. S., Singh, R. B. and Kumar, M. 2011. An analysis of local spatial temperature patterns in the Delhi Metropolitan Area. *Phys. Geogr. 32*, 114–138. doi:10.2747/0272-3646.32.2.114

Selvin, S., Vinayakumar, R., Gopalakrishnan, E. A., Menon, V. K. and Soman, K. P. 2017. Stock price prediction using LSTM, RNN and CNN-sliding window model. In *2017 International Conference on Advances in Computing, Communications and Informatics (ICACCI)*. IEEE, pp. 1643–1647.

Singal, S. P., Gera, B. S. and Pahwa, D. R. 1994. Application of SODAR to air pollution meteorology. *Remote Sens.* 15, 427–441. doi:10.1080/01431169408954084

Soni, K. and Parmar, K. S. 2020. Soft computing applications in air pollution meteorology. In: *Intelligent Data Analytics for Decision-Support Systems in Hazard Mitigation*, Springer, Singapore, pp. 441–469.

Soni, K., Singh, S., Bano, T., Tanwar, R. S. and Nath, S. 2011. Wavelength dependence of the aerosol angstrom exponent and its implications over Delhi, India. *Aerosol Sci. Technol.* 45, 1488–1498. doi:10.1080/02786826.2011.601774

Stull, R. B. 2012. *An Introduction to Boundary Layer Meteorology*. Vol. 13. Springer Business Media.

Terradellas, E., Soler, M. R., Ferreres, E. and Bravo, M. 2005. Analysis of oscillations in the stable atmospheric boundary layer using wavelet methods. *Boundary Layer Meteorol.* 114, 489–518. doi:10.1007/s10546-004-1293-y

Unal, Y., Kindap, T. and Karaca, M. 2003. Redefining the climate zones of Turkey using cluster analysis. *Int. J. Climatol.* 23, 1045–1055. doi:10.1002/joc.910

Vivas, D. R., Sánchez, E. and Reina, J. H. 2020. Deep learning the atmospheric boundary layer height. *arXiv preprint arXiv: 2004.04353*. https://arxiv.org/pdf/2004.04353.pdf

Williamson, D. F., Parker, R. A. and Kendrick, J. S. 1989. The box plot: a simple visual method to interpret data. *Ann. Intern. Med.* 110, 916–921. doi:10.7326/0003-4819-110-11-916

Zaidi, S., Zela, A., Elsken, T., Holmes, C., Hutter, F. and co-authors. 2020. Neural ensemble search for performant and calibrated predictions. *arXiv preprint arXiv:2006.08573*.

Zhao, J., Wu, J., Guo, X., Han, J., Yang, K. and co-authors. 2019. Prediction of radar sea clutter based on LSTM. *J. Ambient Intell. Hum. Comput.* 1–8.

MAPAN-Journal of Metrology Society of India
https://doi.org/10.1007/s12647-021-00477-7

ORIGINAL PAPER

Design and Development of SODAR Antenna Structure

N. Kumar[1,2], K. Soni[2]* and R. Agarwal[1]

[1]Thapar Institute of Engineering and Technology, Patiala, India

[2]CSIR-National Physical Laboratory, New Delhi, India

Received: 03 February 2021 / Accepted: 31 May 2021

Abstract: The performance improvements of SOnic Detection And Ranging (SODAR) necessitate designing efficient acoustic antennas for the Atmospheric Boundary Layer (ABL) measurements to enhance the data availability of weak echoes. An efficient acoustic antenna needs to optimize electrical to acoustic and acoustic to electrical conversion efficiency measured at the antenna axis. It also needs to provide a good directional response and to handle atmospheric noise. Acoustic antennas designed using moving-coil transducers, parabolic dish and acoustic baffle should provide better characteristics. In the present research work, several types of Acoustic Composite Material (ACP) for acoustic baffle have been tested to their characteristics Sound Transmission Coefficient (STC) and Noise Reduction Coefficient (NRC). Based on these characteristics, the whole testing is performed in the reverberation chamber and a comparative study of transmission loss and absorption is elaborated. It is concluded that baffle (ACP sample 2 with foam) is the suitable material with STC (34) and NRC (0.98). Also, an acoustic antenna has been designed using ACP sheets with foam and tested all the components i.e. transducer, disc and baffles in the acoustic anechoic chamber and reverberation chamber, to analyse the axial transmit and receive conversion efficiencies and directional response.

Keywords: Atmospheric boundary layer; SODAR; Acoustical antenna; Acoustical baffle

1. Introduction

The Acoustic Sounder or SOnic Detection And Ranging (SODAR) system is an excellent tool for the study of the lower troposphere layer (i.e. Atmospheric Boundary Layer or ABL) [1]. This instrument is providing the wind profile, turbulence intensity and ABL structure or stability class [2]. It is a remote sensing device, based on the sound wave [3]. This instrument has advantages like lower cost, robustness over another instrument, which is used for ABL study. It has a limited range that depends on the acoustic frequency being used and on atmospheric attenuation [4, 5]. The SODAR estimates atmospheric structure and height by measuring the total acoustic energy scattered by the atmosphere. So, a basic component of the SODAR system is a transmitting system to illuminate the turbulent region with acoustic flux and a sensitive receiving system to detect the scattered flux [6]. In both cases, the SODAR antenna (acoustic antenna) is an important component. This antenna assists in transmitting the signal in the narrow beam and highly directive microphone in receiving mode [7]. The transmit and receive conversion efficiencies of the transducer have been measured in the return power. In addition to this, the atmospheric noise is one of the known components which degrade the functioning of SODAR [8]. For the operation of SODAR in a specific site, the atmospheric noise should be less than 35–40 dB. Further, the spatial resolution temperature structure increases at higher operating frequencies; however, the transmitting sound attenuation also increases [9, 10].

Based on antenna design, the SODAR system is divided into three types, namely Mono-static, Bi-static and Tri-axis [11]. These all types of Antenna need acoustic baffles or shield around the antenna for the removal of atmospheric noise [8, 12, 13]. The two primary non-random noise sources for a SODAR are reflections of the sound pulse from non-atmospheric substances ("fixed echoes" or "clutter") and environmental noise from vehicles, birds, construction, animals, etc., reaching the SODAR antenna.

The noise sources have been considerably reduced by using an acoustic baffle to shield the SODAR antenna. It is worth considering how small the sound intensity needs to

*Corresponding author, E-mail: 2006.kirti@gmail.com

Published online: 01 July 2021

be if reflected off a perfectly reflecting object, so as not to compete with the turbulence signal. Although commercial SODARs have marketed without covering acoustic baffle, SODAR systems have not been efficacious. The baffle must be designed to primarily absorb the noise (at least 30-dB absorption/transmission) and not to reduce the main beam [14]. The perfect baffle material should make a non-reflecting, absorbing and non-transmitting shield [2]. Commonly, fibreglass or marine plywood treated on the inside with acoustic foam is used [4]. Some of the acoustic baffles have a slim lead sheet joined to the fibreglass or wood substrate. This type of creation is generally adequate to stop any important sound energy from penetrating through the acoustic baffle walls.

With the SODAR dish, the acoustic baffle is a hexagonal or cylindrical frustum [10]. Maximum baffles have straight edges, though some past SODARs used horn-shaped baffles in which the uppermost rounded away from the SODAR perpendicular axis. Such type of configuration is probably based on the use of horns to a couple of small speaker drivers to the atmosphere. Though, the application is much changed from speaker horns, as the scales are much higher than a wavelength and acoustic impedance matching is not related [2]. In the case of mono-static SODAR, the acoustic baffle requirements to have a more wide-range departure to the slanted beams, which do not cross the baffle edges excessively. The topmost rim of the baffle is the adjacent field of the SODAR beam. Though, complete estimations have revealed that far-field estimates are usually adequate to improve a design [2, 4, 7].

The actual problem with recording appropriate data at a lower height is the antenna and the baffle shielding are possible to "ring" for some time afterwards the transmit pulse. It is not merely the time taken for sound to travel along with the baffle and back to the speakers, as a typical speed in a complex wooden baffle might be around 103 m s^{-1}, and for a length of 2 m, this would only give an arrival time of 4 ms [2], which is the best configurations effort to damp any reverberations. It has been achieved using "soft" ingredients for the acoustic baffle. Moreover, the difficulties with reverberations are likely to disturb data of the last 6–10 ms timespan [15].

Council of Scientific and Industrial Research-National Physical Laboratory (CSIR-NPL), being the National Measurement Institute (NMI) of India, has the statutory responsibility to create, continue and advance the national standards of calibration and testing facilities for different parameters [16, 17]. It has a strong base in the research and development of Acoustics and Vibration (A&V) metrology. A conventional mono-static SODAR or acoustic RADAR developed in India in 1975 then advanced to a computer-controlled SODAR system in 1981 [18]. It has been successfully operating at CSIR-NPL, New Delhi and Central Pollution Control Board (CPCB), New Delhi since its development [11, 19]. Now, CSIR-NPL has developed a LabVIEW-based software for a new design of mono-static SODAR, data acquisition and control system with minimized hardware elements. It is a user-friendly system that runs without problems like less sensitivity to ambient noise, noise from the rain hitting antenna, ground clutter and strong spurious signals from nearby objects and provides continuous real-time data on the dynamics of ABL thermal structures. The improved SODAR system has been integrated with a new acoustic antenna.

The preliminary study shows that a highly directional acoustic antenna, recording system, background noise and choice of frequency affect the operational efficiency of a SODAR system [2]. The directivity of the acoustic antenna determines the amount of energy from a transducer to project the scattering region for determining the amount of clutter and background noise in receiving mode. The present work aims to study the Aluminium Composite Panel (ACP) for antenna baffles. The samples have been assembled with different configurations of ACP sheet-mounted and acoustic foam. Acoustic baffles have been designed and fabricated using a suitable ACP sheet. Also, the design and construction details of the complete SODAR antenna have been described with salient features of a result obtained.

2. Mechanism of SODAR Echoes

For any volume of atmospheric air, it undergoes continuous small-scale refractive index variations [1]. These variations provide tracers for the scattering of the acoustic beam. The fluctuations usually arise when turbulence occurs within a region of refractive index gradient associated either with temperature inversion or with convective activity [9]. Energy has scattered from turbulent temperature fluctuations of half the acoustic wavelength. The scattering is most significant when the wavelength is minimum. Temperature inversions alone (without turbulence) probably do not have sufficiently strong temperature gradients to provide significant echoes directly [10]. Turbulence fluctuations proper scale accompanied with atmospheric stratification other than neutral is generally necessary to produce the scattering. It has been found that small-scale temperature variations produced by turbulence in a region of atmosphere having a vertical temperature gradient other than dry adiabatic are responsible for causing an acoustic echo [5]. The refractive index structure parameter represented by the temperature structure parameter C_T (^{0} K m^{-1}) and Richardson number R_i (a measure of turbulence and unitless number) are related as

$$C_T = z^{4/3}\left(\frac{\mathrm{d}\theta}{\mathrm{d}z}\right)^2 f(R_i) \quad (1)$$

$$\text{where } R_i = \frac{\left(\frac{g}{\theta}\right)\left(\frac{\mathrm{d}\theta}{\mathrm{d}z}\right)}{\left(\frac{\mathrm{d}u}{\mathrm{d}z}\right)^2} \quad (2)$$

g = acceleration due to gravity, θ = mean temperature

$\frac{\mathrm{d}\theta}{\mathrm{d}z}$ = mean potential temperature gradient

$\frac{\mathrm{d}u}{\mathrm{d}z}$ = mean wind speed gradient

where z = *height,* $f(R_i)$ = *function of Richardson number.* This relationship indicates that the variations of C_T involve the gradients of temperature and wind speed.

The received powers represent the echoes from random fluctuations of temperature at a scale size of half the wavelength of the interrogating waves and thereby provide information about the thermal in-homogeneities in the lower atmosphere [20]. If the signal is lost due to sound attenuation throughout the trip, then scattering volume and beam spreading has taken into account. The received power has given a measure of C_T which in turn provides a measure of the intensity of temperature fluctuations [1–5]. The backscattered acoustic energy in pascal is given by

$$P_r = P_t.\sigma.\frac{c\tau}{2}\frac{A.L}{R^2} \quad (3)$$

where σ is the scattering cross-section (m^2), c is the speed of sound (m s^{-1}), τ is the pulse width (s), R is the range (m), A is the antenna area (m^2), L is a factor containing the equipment efficiencies, antenna gain (dB) and the atmospheric absorption (dB), P_r is receiving power (Pa), P_t is the transmitting power (Pa). According to Eq. 3, the antenna is capable of transmitting or receiving energy in a narrow-angle with side lobes as low as possible [2, 7]. For this purpose, a parabolic dish with a horn-loaded transducer at its focus is used in the directional antennas [4]. The acoustic antenna has been divided into two parts, i.e. acoustic transducer and acoustic baffle, as shown in Fig. 1.

3. Aluminium Composite Panel and Their Acoustical Characteristics

The ACP sheet is a sandwich panel, constructed from two sheets of aluminium bonded to a core [21]. Figure 2 shows that a low-density core inserted between two relatively thin skin layers of aluminium. The core is commonly polyethene (PE) or polyurethane (PU) or mixes low-density polyethene and mineral material to exhibit fire-retardant properties [22]. This sandwich setup allows us to achieve excellent mechanical performance at minimal weight. This type of panel is frequently used for external cladding or facades of buildings, insulation and signage board. ACP sheets have been used owing to low cost, durability and efficiency. Also, it has the properties of flexibility, low weight and easy forming and processing allow for innovative design with increased rigidity and duration.

For the selection of acoustic antenna baffle material, two types of tests have been performed: sound transmission loss and sound absorption. In the first phase of the work, different kinds of ACP sheet are examined for their sound transmission loss properties in the reverberation chamber for the frequency range of 100–4000 Hz. From the sound transmission loss, Sound Transmission Coefficient (STC) has been calculated for different ACP sheets. STC has been introduced as the method for comparing different wall, ceiling, floor, door and window assemblies [23]. STC has been calculated by taking the transmission loss values tested at 16 standard frequencies over the range of 125 Hz–4000 Hz. The sound transmission loss of sound-insulating material has been measured in the laboratory through the measurement of the one-third octave band levels L_s and L_r at the source and receiver chambers, respectively, and reverberation time T of the latter.

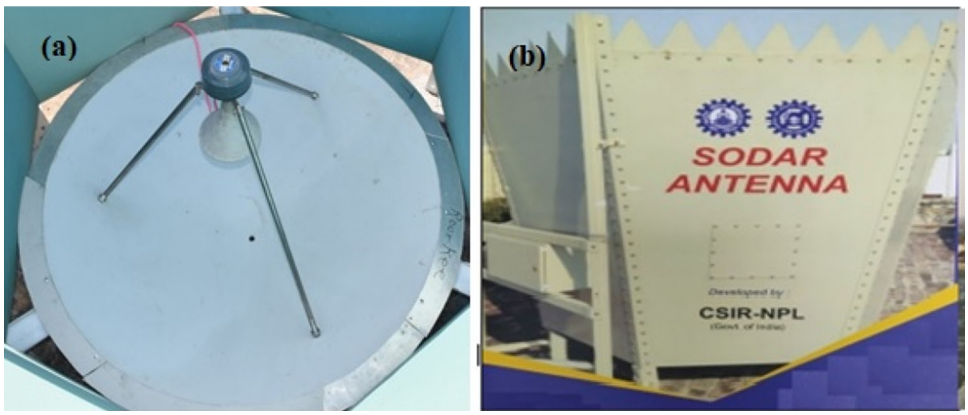

Fig. 1 Acoustic Antenna
a Acoustic Transducer
b Acoustic Baffle

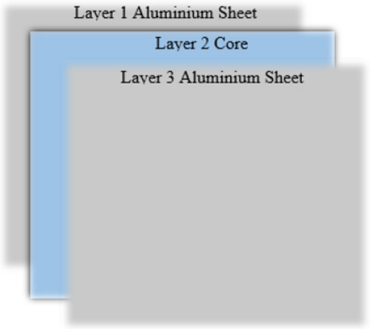

Fig. 2 Aluminium Composite Panel (ACP)

$$L = L_s - L_r + 10\ln\frac{T * A}{0.161 * V} \quad (4)$$

where L = Sound Transmission Loss, dB. A = area of the sample, m^2. V = volume of the receiver chamber, m^3.

In the second stage, the sound absorption property of panel and acoustic foam has been tested as per standards. For the sound absorption, Noise Reduction Coefficient (NRC) has been calculated for the sound-absorbent material (acoustic foam) with a selected ACP sheet. The NRC is a scalar representation of the amount of sound energy absorbed upon striking a particular surface. An NRC of 0 indicates perfect reflection; an NRC of 1 indicates excellent absorption. It is the arithmetic average, the absorption coefficients for a specific material and mounting condition are determined at the one-octave band centre frequencies of 250, 500, 1000 and 2000 Hz. Absorption coefficients have been used to calculate NRC to determine in the reverberation rooms of qualified acoustical laboratory test facilities. The sound absorption of sound-absorbing material has measured in the laboratory through the measurement of the one-octave band levels,

$$\text{Sound Absorption}, \alpha = \frac{55.3 * V}{s * (331 + 0.6 * t)}\left[\frac{1}{T_s} - \frac{1}{T_e}\right] \quad (5)$$

where V = Volume of Room, m^3.

s = test sample area, m^2.

t = Temperature of Room, ^{0}C.

T_s = Reverberation time with Sample, sec.

T_e = Reverberation Time without Sample (Empty Room), sec

$$NRC = \frac{\alpha_{250} + \alpha_{500} + \alpha_{1000} + \alpha_{2000}}{4} \quad (6)$$

NRC is most widely used to rate general acoustical properties of acoustic ceiling tiles, baffles, banners, office screens and acoustic wall panels. Higher STC and NRC are generally better, though not always due to low-frequency problem. Here, the material has been mainly used for a higher frequency; therefore, the high value of STC and NRC is needed.

4. Results and Discussion

The antenna is designed and fabricated to study the lower atmosphere. The fibre parabolic dish designs with an aperture diameter of 1.2 m, depth of dish 0.22 m for the antenna. A commercial driver unit (60 watts RMS/90 watts maximum) is fitted with a fibre exponential horn on a tripod stand at the focus of the dish with a height of 0.60 m from its apex. Figure 3 shows the whole combined dish, horn and driver unit. The directional response of this antenna system at frequencies of 1000 Hz, 2000 Hz and 2500 Hz is provided in Fig. 4. It shows that the ninety-degree side lobe suppression is around 15 dB, 20 dB and 25 dB at 1000 Hz, 2000 Hz and 2500 Hz, respectively. The main lobe has a width of $\pm 12^0$ at 1000 Hz. The maximum impulse output has been measured without the dish 110 dB for an input of 60 watts, and with the dish, it increases to 136 dB at 1000 Hz using a standard sound source. The receiving sensitivity of the system is 12.5 mv/μbar under free field conditions.

The characteristics of the parabolic dish show in a receiving transducer with a B&K pre-polarized free-field ½ inch microphone type 4189 of open-circuit sensitivity -26.9 dB (1 V/Pa) with 0.2 dB uncertainty (95% confidence level) fixed at its focus. It has been observed that the gain in the received signal due to the paraboloid reflecting surface is of the order of 25 dB (approximate). The received signal has been reduced by 10 dB in case the sounding source moves by an angle of $\pm 20^0$ on either side of the axial line of the paraboloid surface or 25 dB side-lobe rejections at 90^0. Calculations have been made [2] to determine the receiving and transmitting power efficiencies of the antenna transducer. It has been found that receiving and transmitting efficiencies are determined as 21.3% and 29%, respectively. To make the acoustic baffle, an ACP sheet has been used after calculating the acoustical characteristics (STC and NRC) of the ACP sheet.

For the calculation of STC (Fig. 5), the sample size is 0.63 m * 0.93 m * 0.002 m; with a working standard microphone (associated uncertainty ± 0.2 dB, traceable to national standards). As per requirement [24–30], the acoustical material has been tested for its airborne sound insulation by using two reverberation chambers under existing environmental conditions. The sample has fixed in the standard opening window between the two chambers. The volume of the source room was 257 m^3, and that of the receiving room was 271 m^3. Adequate diffusion has been excited in both chambers. Using filtered noise in 1/3 – octave band, the airborne sound insulation index has been

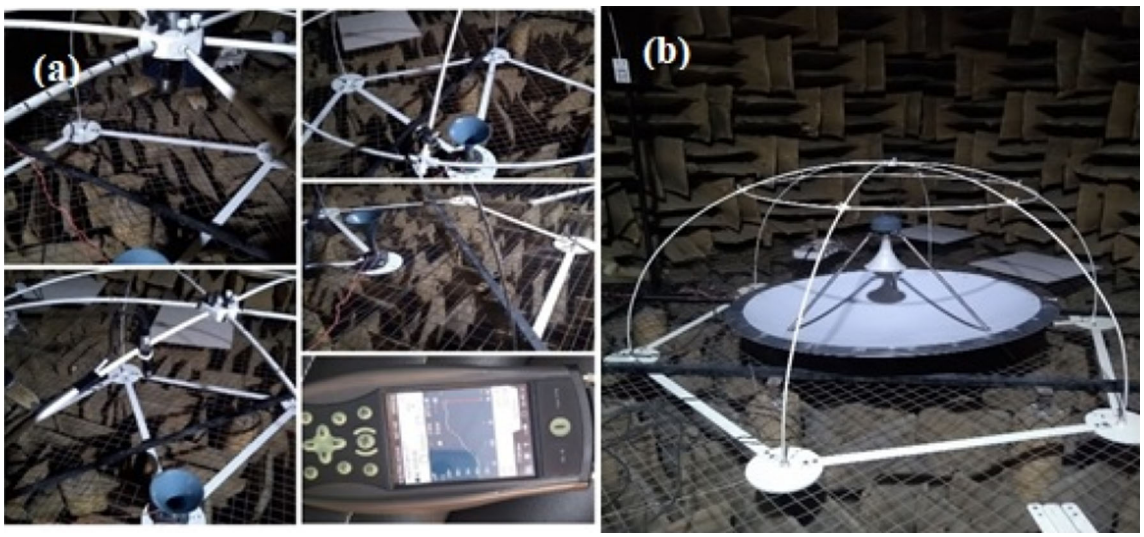

Fig. 3 Transducer testing in Anechoic chamber

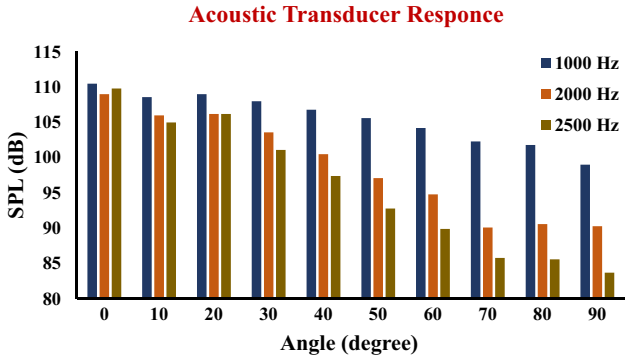

Fig. 4 Transducer response in transmitting mode

evaluated by measuring the average sound pressure levels generated in the source room and the receiver room, as shown in Table 1. The evaluated uncertainty in measurement is ± 1.0 dB which is at a coverage factor $k = 2$ and it corresponds to a coverage probability of approximately 95% for normal distribution.

To test the NRC (Fig. 5), acoustical material has been tested in one reverberation chamber under existing environmental conditions [24–30]. The sample has been fixed on the surface of the chamber with a rigid backing to get an exposed sample area of 12 m^2 and the chamber's volume has 257 m^3. A loudspeaker with uniform spherical radiation has been used as the source of sound suspended at a height of 2.5 m above the floor in one corner and the microphone has been kept at different locations near the other corners of the chamber at least 1 m away from any surface. The measurement has made by using 1/3-octave bands of random noise and several decay rates have been determined. The sound absorption coefficient has been calculated [Annexure I] as shown in Table 2. The evaluated

Table 1 Transmission loss (Frequency response) of ACP sheet

STC = 34			
Frequency	L_s	L_r	STL
100	99.3	73.5	13
125	104.4	78.1	15
160	107.2	74.6	19
200	107.4	74.2	20
250	105.3	70.9	20
315	103.6	65.7	24
400	104.4	63.6	28
500	103.4	57.8	33
630	102.2	53.9	35
800	101.3	49.3	39
1000	99.7	46.9	40
1250	100.8	44.5	43
1600	101.3	42.5	45
2000	99.2	37.5	47
2500	100.1	35.6	50
3150	96.6	30.3	51
4000	94.2	28.6	50

uncertainty in measurement is ± 5% which is at a coverage factor $k = 2$ and which corresponds to a coverage probability of approximately 95% for normal distribution.

Table 3 shows that STC and NRC of four different company's ACP sheet vary from 31- 34 and 0.04–0.07, respectively. Four samples of ACP sheet have been analysed for STC value and selected one of the best samples which has the highest STC (= 34) value and then made a combination of that sample with foam and got the most NRC's (= 0.98) value. When four combination of different STC samples with foam have been made, and it was found

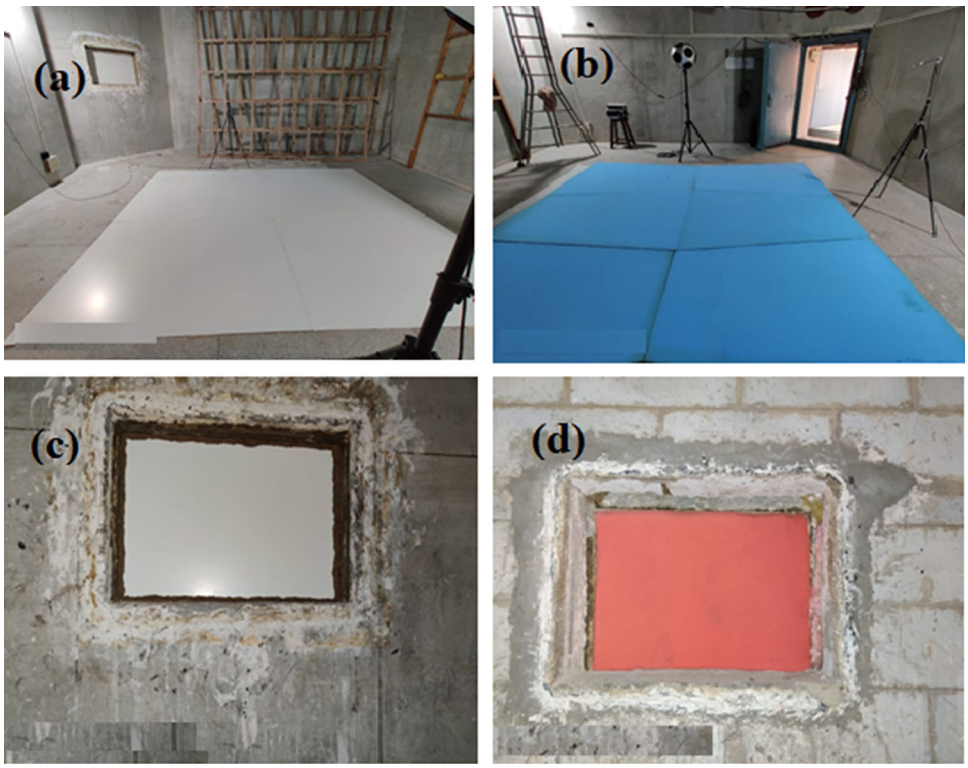

Fig. 5 Testing in a reverberation chamber **a** NRC testing of ACP sheet, **b** NRC testing of combined ACP sheet and Acoustic Foam, **c** STC testing of ACP Sheet, and **d** STC testing of Acoustic Foam

Table 2 Absorption of ACP sheet with acoustic foam

NRC = 0.98			
Frequency	T_e	T_s	Absorption
100	7.2	4.47	0.32
125	7.52	4.75	0.29
160	7.78	3.41	0.63
200	7.21	2.74	0.86
250	6.17	2.48	0.92
315	5.77	2.17	1.09
400	5.88	2.2	1.08
500	6.00	2.27	1.04
630	6.04	2.24	1.07
800	5.52	2.28	0.98
1000	5.37	2.26	0.97
1250	4.7	2.12	0.98
1600	4.4	2.04	1.00
2000	3.96	1.93	1.01
2500	3.54	1.81	1.02
3150	3.05	1.63	1.08
4000	2.6	1.51	1.05

that the value of the STC is the same, just the value of the NRC is changing. The combination ACP 2 plus Acoustic Foam is found suitable for the SODAR antenna baffle.

A hexagonal-shaped baffle with 1.98 m high walls and a 2.13 m diameter has been erected around the horn reflector

Table 3 Different ACP sheet STC and NRC

Sample No	STC	NRC
ACP 1	31	0.04
ACP 2	34	0.04
ACP 3	31	0.07
ACP 4	32	0.05
ACP 2 + Acoustic Foam	34	0.98

antenna. Each plank of the hexagon used a plain ACP sheet (1.21 m * 2.13 m) on the outer side and the inner side fixed with acoustic foam (density 40 kg m^{-3}; 0.10 m thickness). A hexagonal-shaped structure with its wall sloping slightly outwards (angle of the slope 9 degrees with the vertical) has been constructed to work as a baffle. The horn reflector antenna has been placed at the centre of this baffle. It has an inside base diameter of 1.53 m to fit the antenna and a 2.13 m diameter at the top. The height of assembly is determined by the size of panels and the slope by diameter on the parabolic dish, which is 1.28 m. However, it has been found that this baffle is very useful and hardly raised any ringing effects. Figure 6 shows that the testing of acoustic baffles with a dish in the reverberation chamber. The whole combined system has been tested in the reverberation chamber, and the noise level is found to be reduced by 32 dB. The baffle is tested in an open atmosphere and it has been observed that an ambient noise level

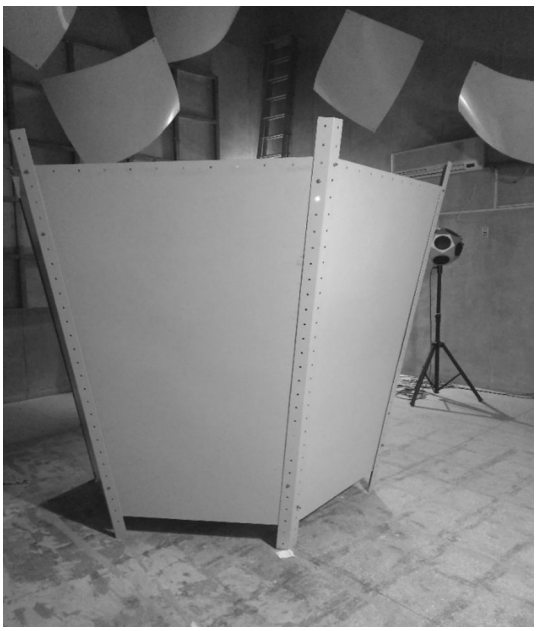

Fig. 6 SODAR baffle testing in a reverberation chamber

is reduced by 25–30 dB as compared to the measurement made inside the baffle.

In the last four decades, Monostatic SODAR has been operating under varying atmospheric conditions for 24 h [31–34], now a new SODAR system has been developed using new acoustical baffles (with ACP sheet). Previously it was observed that SODAR works on acoustic waves under-heavy ambient noise due to traffic, birds, etc. This noise merged with weak SODAR signals and pose a serious problem in the data processing. Conventionally, effective acoustical fibre-based baffles are used to surround the antenna to protect it from ambient noise. The fibre-based baffles are heavy in construction, less precise, more weight, costly, etc. Nowadays, the SODAR antenna is installed on the building floor; therefore, a lightweight acoustic baffle with high precision and cheaper are required. The ACP sheet-based baffles are more suited for the SODAR system. It has been tested to remove the 25–30 dB environmental noise in the open area. Its operation is carried out continuously for monitoring of ABL height with the new acoustical antenna. Figure 7 shows the stable and unstable conditions for the atmosphere on the echogram. These conditions are the manifestation of thermal in-homogeneities within the lower atmosphere caused by diverse meteorological phenomena.

5. Conclusion

A transmitting system to illuminate the highly directed signal into the turbulent region and a sensitive receiving

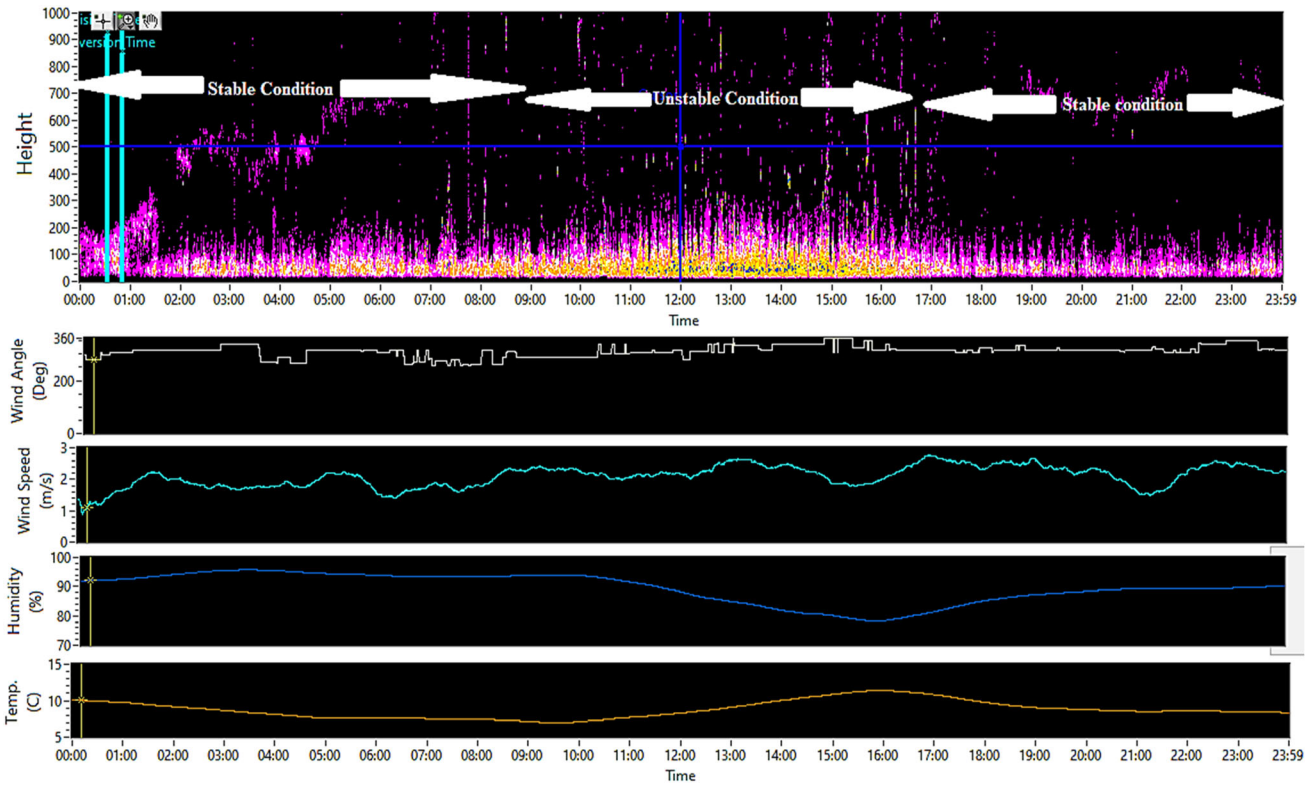

Fig. 7 SODAR echogram observation at Delhi

signal to detect the return scattered signal from the atmosphere are the basic needs of any SODAR system. In the SODAR system, this feature is provided via a precise acoustical antenna. For the optimal performance of the antenna, two factors must be considered: the antenna's structure for signal directivity, and the metal sheet of the antenna frame and the quality of the attached absorbent material for ambient noise cancellation. Using one moving-coil transducer, parabolic dish and acoustic ACP sheet baffle for a unique SODAR system for monitoring the lower atmosphere, the optimal combination of a new acoustical parabolic antenna has been devised. The new design offers economical SODAR system development and a lightweight acoustic baffle with high precision. The acoustical characteristics of baffles are calculated (STC = 34 and NRC = 0.98) in the reverberation chamber. ACP sheet with foam is the most suitable acoustic baffle for an acoustic antenna design. It is capable of radiating acoustic pressure as high as 135 dB into a narrow beam in the atmosphere. It has been observed that the newly designed antenna slightly improves receiving (21.3%) and transmitting (29%) efficiencies of the signal concerning earlier antenna. The new acoustical baffles remove the 25–30 dB environmental noise in the open area. The merits of a new antenna are very suitable for transportable SODAR application for different sites and field experiments.

References

[1] R. B. Stull, An introduction to boundary layer meteorology, Springer Business Media, vol 13, 2012. eBook ISBN 978-94-009-3027-8 doi: https://doi.org/10.1007/978-94-009-3027-8.

[2] S. Bradley, Atmospheric acoustic remote sensing: principles and applications, CRC Press, 2007. eBook ISBN 9781420005288 https://www.taylorfrancis.com/books/9781420005288.

[3] M.A. Kallistratova and R.L. Coulter, Application of sodars in the study and monitoring of the environment. Meteorol. Atmos. Phys., vol. 85, pp. 21–37, 2004.

[4] S.P. Singal, J.R. Anand, B.S. Gera and S.K. Agarwal, Design, fabrication & studies of the directional acoustic antennas for use in the acoustic sounding technique, indian journal of radio & space. Physics, vol 4, pp. 50–59, 1975.

[5] F.F. Hall Jr. and J.W. Wescott, Acoustic antennas for atmospheric echo sounding. J. Acoust. Soc. Am., vol. 56, pp. 1376–1382, 1974.

[6] S. G. Bradley, and N. L. Roberts, Design and evaluation of a compact Doppler acoustic sounder, in Proceedings of Fifth International Symposium on Acoustic Remote Sensing, New Delhi, pp. 141–146, 1990. Tata McGraw-Hill, New Delhi, India.

[7] R.M. Khanna, O. Sharma and S.C. Garg, Design of a high efficiency acoustic phased array antenna for an acoustic wind profiler. Meteorol. Atmos. Phys., vol. 71, pp. 35–41, 1999.

[8] R.L. Coulter and T.J. Martin, Results from a high-power, high-frequency sodar. Atmos. Res., vol. 20, pp. 257–269, 1986.

[9] H.E. Bass, L.C. Sutherland and A.J. Zuckerwar, Atmospheric absorption of sound: Update. J. Acoust. Soc. Am., vol. 88, pp. 2019–2021, 1990.

[10] W.D. Neff, Beamwidth effects on acoustic backscatter in the planetary boundary layer. J. Appl. Meteorol., vol. 17, pp. 1514–1520, 1978.

[11] N. Kumar, K. Soni, N. Garg, R. Agarwal, D. Saha, M. Singh and G. Singh, SODAR pattern classification and its dependence on meteorological parameters over a semiarid region of India. Int. J. Remote Sens., vol. 38, pp. 3466–3482, 2017.

[12] S.D. Danilov, A.E. Guryanov, M.A. Kallistratova, I.V. Petenko, S.P. Singal, D.R. Pahwa and B.S. Gera, Simple method of calibration of conventional sodar antenna system. Remote Sens., vol. 15, pp. 307–312, 1994.

[13] S.D. Danilov, A.E. Gur'yanov, M.A. Kallistratova, I.V. Petenko, S.P. Singal, D.R. Pahwa and B.S. Gera, Acoustic calibration of sodars. Measur. Sci. Technol., vol. 3, pp. 1001–1010, 1992.

[14] R.L. Coulter and M.A. Kallistratova, Two decades of progress in SODAR techniques: a review of 11 ISARS proceedings. Meteorol. Atmos. Phys., vol. 85 pp. 3–19, 2004.

[15] L.L. Beranek, Acoustic Measurements. John Wiley, New York, 1949.

[16] S. Yadav and D.K. Aswal, Redefined SI units and their implications. MAPAN, vol. 35, pp. 1–9, 2020.

[17] D.K. Aswal, Quality infrastructure of India and its importance for inclusive national growth. MAPAN, vol. 35, pp. 139–150, 2020.

[18] B.S. Gera and S.P. Singal, Design of a microcomputer-based monostatic SODAR system. Indian J. Radio Space Phys., vol. 22, pp. 296–300, 1993.

[19] B.S. Gera, T. Raghavendra, G. Singh, V.K. Ojha, J. Malik, N. Gera and N.C. Gupta, Instrumentation and computer capabilities for improving SODAR data acquisition. Int. J. Remote Sens., vol. 32, pp. 4807–4817, 2011.

[20] N. Kumar, K. Soni and R. Agarwal, A comprehensive study of different feature selection methods and machine-learning techniques for SODAR structure classification. Model. Earth Syst. Environ., vol. 6, pp. 1–12, 2020. https://doi.org/10.1007/s40808-020-00872-0.

[21] A. Zinno, E. Fusco, A. Prota and G. Manfredi, Multiscale approach for the design of composite sandwich structures for train application. Composite Struct., vol. 92, pp. 2208–2219, 2010.

[22] A. Paktiawal and A. Mehtab, An experimental study on effect of aluminium composite panel waste on performance of cement concrete. Ain Shams Eng. J. 2020. https://doi.org/10.1016/j.asej.2020.07.024.

[23] L E. Kinsler, A. R. Frey, A. B. Coppens and J. V. Sanders, Fundamentals of acoustics, 4th Edition, Wiley-VCH, 1999. ISBN 0-471-84789-5.

[24] ISO 3740:2019(en) Acoustics — Determination of sound power levels of noise sources.

[25] ISO 6926:2016(en) Acoustics — Requirements for the performance and calibration of reference sound sources used for the determination of sound power levels.

[26] ANSI/ASA S1.13-2005 (R2010) Measurement of Sound Pressure Levels in Air.

[27] ANSI S1.22-1992 (R2007) American National Standard Scales and Sizes for Frequency Characteristics and Polar Diagrams in Acoustics.

[28] ANSI/ASA S1.26-2014 Methods for Calculation of The Absorption of Sound by The Atmosphere.

[29] ISO 26101:2012 Acoustics — Test methods for the qualification of free-field environments.

[30] ISO 12001:1996 Acoustics — Noise emitted by machinery and equipment — Rules for the drafting and presentation of a noise test code.

[31] S. P. Singal, and S. K. Aggarwal, sodar & radiosonde studies of thermal structure of the lower atmosphere at Delhi, Indian J. Radio Space Phys., vol 8, 76–81, 1979. http://nopr.niscair.res.in/handle/123456789/37079

[32] N. Kumar, K.S. Parmar, K. Soni, N. Garg and R. Agarwal, Prediction of ventilation coefficient using a conjunction model of wavelet-Neuro-fuzzy model: a case study Delhi. India, Acad. J. Sci. Res., vol. 3, pp. 184–191, 2015.

[33] N. Kumar, K. Soni, R. Agarwal and M. Singh, SODAR as a diagnostics tool for urban air-quality and health care system. J. Acoust. Soc. India, vol. 44, pp. 213–222, 2017.

[34] N. Kumar, K. Soni, R. Agarwal and M. Singh, Preliminary analysis of operating conditions of acoustic sounder (SODAR) before the installation. J. Acoust. Soc. Am., vol. 146, 2997–2998, 2019.

A comprehensive study of different feature selection methods and machine-learning techniques for SODAR structure classification

Nishant Kumar, Kirti Soni & Ravinder Agarwal

Modeling Earth Systems and Environment

ISSN 2363-6203

Model. Earth Syst. Environ.
DOI 10.1007/s40808-020-00872-0

Springer

Modeling Earth Systems and Environment
https://doi.org/10.1007/s40808-020-00872-0

ORIGINAL ARTICLE

A comprehensive study of different feature selection methods and machine-learning techniques for SODAR structure classification

Nishant Kumar[1] · **Kirti Soni**[2] · **Ravinder Agarwal**[1]

Received: 18 April 2020 / Accepted: 24 June 2020

Abstract
Sonic detection and ranging (SODAR) echogram provides atmospheric boundary layer (ABL) structure and its height. In the present research, highly accurate and reliable machine-learning methods have been derived and successfully applied on the SODAR echogram for the ABL structure. Five feature selection methods and eight classification methods have been studied in terms of their performance. 133 statistical features have been calculated from 1698 SODAR echogram images. To ensure the unbiased estimation of different structures, machine-learning methods have been used. Furthermore, ten cross-validations have been used to find accuracy. It is found that the boosted tree classifier (overall prediction performance 52.02%) has the highest prognostic presentation with 133 features. After application of the Laplacian method for feature selection, the classifier (overall prediction performance 62.19%) has the highest prognostic presentation with 20 features. The large variability analysis indicates the choice of a classification method for performance variation. Identification of optimal machine-learning methods for SODAR echogram applications is a crucial step towards the ABL structure application, providing an automatic structure classification method for atmospheric and pollutants studies.

Keywords MATLAB · Boosted tree classifier · Laplacian feature selection · SODAR

Introduction

Amongst several methods such as SODAR, RASS, radiosonde, LIDAR, tethered ballon, instrumented tower, etc., it has been observed that acoustic remote sensing (i.e., SODAR) system of the lower atmosphere can be used to determine and forecast the atmospheric boundary layer (ABL) climatological parameters. Hazardous conditions in air pollution can various times be evaded in case short-term local weather-predicting of the boundary layer meteorology becomes available. In studies related to air pollution meteorology, information related to atmospheric stability and turbulence is essential. In this context, Council of Scientific and Industrial Research—National Physical Laboratory (CSIR-NPL), New Delhi, designed and developed monostatic SODAR (SOnic Detection And Ranging) system, which has been operating from last four decades to study the thermal stratification, ventilation coefficient, dispersion, mixing height, low-level disturbances, stability classification, depth of the planetary boundary layer, turbulence parameters, and diffusion characteristics, etc. (Singal et al. 1997; Stull 2012).

SODAR is an important equipment that measures the real-time ABL height and can be used as a diagnostics tool in the air quality management for air quality monitoring in different hazardous conditions which are directly related to human health problems. Environment impact assessment (EIA) has been made SODAR mandatory wherein the recommendations have been made (Central Pollution Control Board, 1992) to site-specific measurements of the ABL dynamics. SODAR is the only equipment that gives the pollution loading capacity of the region by measuring the ventilation coefficient. After the occurrence of the Bhopal Gas Tragedy, SODAR monitoring is necessary for improving and protecting the environment (Beyrich 1997;

✉ Kirti Soni
2006.kirti@gmail.com

Nishant Kumar
kumarnishant.kumar9@gmail.com

Ravinder Agarwal
ravinder_eeed@thapar.edu

[1] Thapar Institute of Engineering and Technology, Patiala 147004, Punjab, India

[2] CSIR-National Physical Laboratory, New Delhi 110012, Delhi, India

Published online: 09 July 2020

Stull 2012). Factors that govern the dilution, rise, and spread of pollutants include wind speed and direction, turbulence temperature, lapse rate, and ABL height (Little 1969; Singal et al. 1994; Soni et al. 2017; Makkhan et al. 2020). Thus, to understand local pollutants transfer and dispersion over an area, researchers should know the ABL height and the different types of ABL structure. During recent years the capacity of SODAR to map the different types of ABL structure has increased. The knowledge of these structures is of great use in air pollutant studies (Kumar et al. 2017b). SODAR is a comparatively cost-effective and real-time remote sensing technique employed to deal with all status of air pollution. SODAR echograms provide unprecedented opportunities for precision ABL structure studies (Choudhury and Mitra 2004). SODAR echogram is an emerging and promising field, hypothesizes that the ABL structure provides crucial information regarding the atmosphere to enhance pollution studies. In some studies, various ABL structure features in terms of their predictive abilities and reliability across different atmospheric conditions have been investigated (De et al. 1998; Choudhury and Mitra 2006; Narayan et al. 2010; Chandra et al. 2011). Some studies have reported the association between atmospheric structure and atmospheric stability for the atmosphere and pollution studies (Singal et al. 1997). The manual identification of various kinds of atmospheric structures is a tedious job and made by experienced personnel. Data mining and machine-learning techniques were developed to automatically discover knowledge and recognize patterns from these data.

Machine learning is a computation method, which provides training data (experience data) to improve performance or to make an accurate prediction (Mokarram et al. 2015; Parmar et al. 2015; Dezfooli et al. 2018; Nair et al. 2018; Verma et al. 2020; Zahraei et al. 2020). These methods are capable of learning data and automate to improve the prediction process (Martins et al. 2016; Zylshal et al. 2016; Dutta and Das 2019). In the present paper, an attempt has been made to compare the different machine-learning models for ABL structure identification based on the SODAR echograms and to remove noisy data from the SODAR echograms. Few studies suggest over SODAR structure classification has used such as algorithm using image processing and pattern recognition techniques or using fractal features (Kalogiros et al. 1995; Mukherjee et al. 2002) or neural network-based real-time system classification (De et al. 1998). Also, in the present work, a large panel of machine-learning approaches based on existence prediction for their predictive performance have been investigated for SODAR structure classification to describe the different types of structure in the ABL. This work helps in the identification of optimal machine-learning approaches for SODAR echograms structure-based predictive studies to enhance the applications of cost and time effectiveness for ABL studies.

Theory and data

Acoustic wave in the atmosphere and reflection

When a flexible diaphragm of a speaker moves, it creates small pressure fluctuations traveling outward from the speaker resulting in pressure fluctuations in the sound waves (Bass and Shields 1977). The speed (c), at which these waves travel is expected to depend on the mechanical properties atmospheric pressure and air density (Evans et al. 1972; Sutherland and Bass 2004).

When a sound wave meets an interface where the sound speed changes, some energy from it is reflected, and remaining energy proceeds over the interface yet with an adjustment in the direction (Gilman et al. 1946). According to the Huygens principle, each point on a wave front goes about a point wellspring of spherical wavelets and taking an unrelated bend to the wavelet before long to position the propagated wave front. There is no distinct interface when sound traveling through the air and there is a continuous change in sound speed due to a temperature gradient or wind shear (Ford and Meecham 1960).

On account of acoustic travel-time tomography where the engendering way is a couple of meters on the ground and reflections may be a major concern. In this case, reflection from the ground may combine with the direct line-of-sight signal, causing a much-reduced signal amplitude (Evans et al. 1972; Bass and Shields 1977). For this reason, continuous encoded-signal systems may experience difficulties and short pulses, and sound speed increases by 0.17% for every degree increment in air temperature (Knudsen 1946).

SODAR

SODAR is an all-around perceived acoustic remote-detecting method (Singal et al. 1985; Stull 2012) that continuously screens ABL thermal structures up to 340–3400 m heights (Garratt 1994). For this study, ABL height was been measured by using mono-static SODAR designed at CSIR-NPL at different frequencies (Singal et al. 1985; Gera et al. 2011; Kumar et al. 2017b). The technical specifications of CSIR-NPL mono-static SODAR are described below in Table 1 (Gera et al. 2011; Kumar et al. 2017a):

The SODAR framework was adjusted utilizing a calibration procedure in anechoic chambers at CSIR-NPL (Danilov et al. 1992). SODAR echogram reflexes pictures of the turbulence in the lower climate and accountability for the dispersion of pollutants. The height of the thermal plumes of SODAR during daytime gives an underestimated value unless they are covered by a low-level

Table 1 Characteristics of CSIR-NPL (New Delhi) mono-static SODAR

Parameters	Value
Transmitted power (electrical)	90 W
Transmitted power (acoustical)	15 W
Pulse width	100 ms
Pulse repetition period	6 s
Operational range	1000 m
Receiver bandwidth	50 Hz
Frequency of operation	2250 Hz
Acoustic velocity	330 m/s (average)
Receiver gain	80 dB
Transmit–receive antenna	Parabolic reflector dish surrounded by conical acoustic cuff
Receiver area	2.5 sq. m
Pre-amplifier sensitivity	The fraction of a micro-volt

elevated shear echo layer (Singal and Aggarwal 1979; Singal 2006; Bradley 2007). The below empirical relation gives the mixing height during the daytime (Singal and Aggarwal 1979; Gera et al. 2011; Kumar et al. 2017a):

$$y = 4.24x + 95, \quad (1)$$

where y is the ABL height (m) and x is the SODAR-measured thermal plume (m). An attempt was made to evaluate the feasibility of the ABL structure with the help of SODAR echogram and machine-learning techniques. The basic idea was to establish a standardized procedure for the ABL structure along with convention manual methods. Figure 1 shows the basic step followed for the development of the SODAR echogram-based classification model.

Data collection

Five thousand eight hundred and fifty (1-year dataset) SODAR echograms have been observed (CSIR-NPL, New Delhi) for various seasons and classified into different structures. Only clear structure echograms have been considered for investigation (1698 echograms). Mainly the ABL structures are divided into two classes: convective boundary layer (basically present in the daytime) and stable boundary layer (mostly in nighttime). Further, ABL structures are divided into a different category (12 classes) according to their structure and characteristics as shown in Table 2. Figure 2 shows a pie chart for different ABL structure under SODAR echograms (Singal and Gera 1982; Chaudhuri et al. 1990; Kalogiros et al. 1995; De et al. 1998; Choudhury and Mitra 2004, 2006; Singal 2006; Narayan et al. 2010; Chandra et al. 2011; Kallistratova et al. 2016; Kumar et al. 2017a).

The convection layer structure characteristic highlights the daytime unstable conditions, which disseminates after the beginning of the sunset and temperature profile changes its shape (Garratt 1994; Stull 2012). The height of the convection layer and the amount of dispersion depends on the different weather conditions. The nature of the inversion layer in the night depends on the daytime rising layer and convection height (Kallistratova et al. 2016).

Figure 3a, b, c displays the thermal plume with tall spikes which has observed during the daytime. These structures are more common in May due to the high temperature (or solar radiation), because high solar radiations uncover the height of thermal plumes (generally, 470 m and can go up to 625 m). In this period, ABL height is increased because dispersion areas of pollutants are more (Singal et al. 1994, 1997; Kumar et al. 2017b). As a result, this condition is more favorable for the industry and humans due to the high dispersion of pollutants (Singal et al. 1985). Figure 3d displays the thermal plume with spikes which has been observed during the daytime of winter season and these types of structure were observed in December and January (generally ABL height is less than 400 m).

Figure 3e–l displays the multilayer structure observed during the night-time. Figure 3g, l is commonly observed in May, due to more variation in temperature, wind speed, wind direction, and relative humidity (Garratt 1994). This is a stable class and unfavorable condition for the industry and humans (Singal et al. 1985). The height of the inversion layer is generally in the range of 100–600 m.

Waves structure (Fig. 3j) is another class of ABL structures, which have been found and grouped specifically on the SODAR echograms. The wave structures are observed in the April, May and June months, i.e., in the pre-monsoon season. This type of structure is essential in the area of wave movement (Stull 2012) and forms due to high wind speed and change of direction over time.

The inversion layer structure is the characteristic highlight of the night-time stable conditions, which disseminates in the morning after sunrise, and the temperature profile changes its shape. As mentioned earlier the daytime dispersion and formation of the rising layer also depend on the inversion height and types. During scattering, nighttime inversion demonstrates its essence as a rising layer ranges to specific most extreme tallness, and thereafter it disappears. This kind of structure is not seen every day in the morning time and immediate progress of the inversion layer changes to the plume structure. Also, during rainy spell and cloudy days, the inversion layer does not convert into the rising layer, resulting in less rising layer formation during the monsoon season.

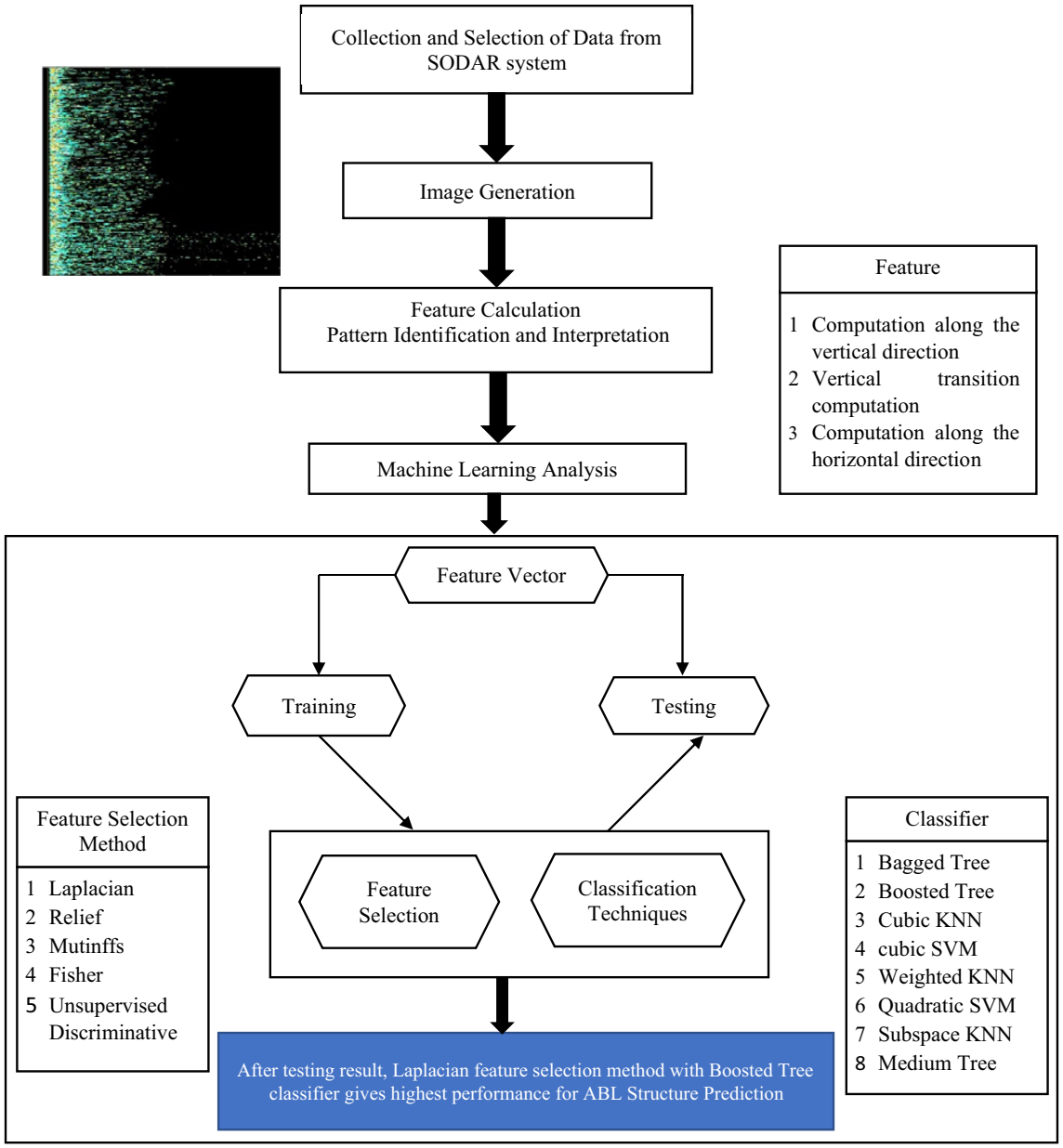

Fig. 1 General flowchart of SODAR echogram-based classification model

SODAR echograms image classification model

SODAR echograms image classification model was used to extract suitable features from the different types of ABL structure, so that chosen features can be extracted. Sub-steps for echograms image classification in the current research work are as follows (Fig. 1).

Statistical features extraction

Overall, 133 SODAR structure features have been used in the analysis of different structures of ABL. These features have been categorized into three feature groups namely computation along the vertical direction, vertical transition computation, and computation along the horizontal direction (Narayan et al. 2010). These feature sets include the mean,

Table 2 Description of SODAR structure and class numbers

Class	Description of SODAR structure
1	Inversion with force convection
2	Inversion with a tall spike
3	Inversion with a single elevated layer
4	Inversion with two elevated layers
5	Inversion with wave motion
6	Inversion with one or two elevated layers in motion
7	Inversion with a small spike
8	Stratified layer
9	Diffuse thermal plumes
10	Thermal plumes with normal days
11	Thermal plumes with a foggy layer
12	Transition structure

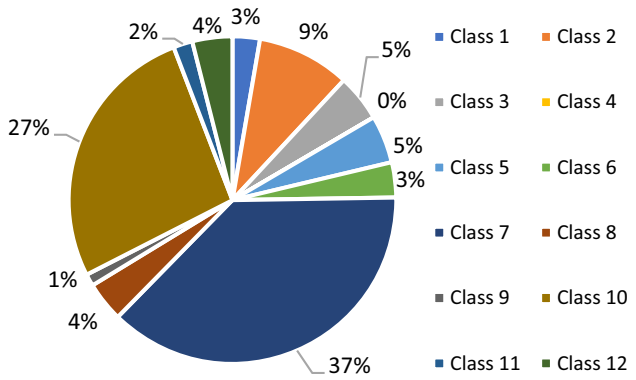

Fig. 2 Percentage distribution of SODAR echograms into 12 classes

maximum, and standard deviation of SODAR echograms (formula of feature calculation is given in detail—Annexure I).

Echogram intensity-based features estimate the statistics of the intensity graph, whereas shape features describe the structure of the ABL (De et al. 1998; Chandra et al. 2011). MATLAB 2017a software was used for SODAR echograms (size 640 × 560) image analysis. SODAR structure features have been automatically extracted by developing structure image analysis software and MATLAB for the pre-processing of ABL images (Chaudhuri et al. 1990; Chandra et al. 2011).

Feature selection methods

Five feature selection methods have been used for analysis (Laplacian, Relief, Mutinffs, Fisher, Unsupervised Discriminative feature selection (UDFS)) (Tang et al. 2014; Zaffalon and Hutter 2002). These methods have been chosen because of their popularity in literature, simplicity and computational efficiency, which rank the features using a scoring criterion (Biesiada et al. 2005; Tang et al. 2014; Wang et al. 2017).

Classifiers

In machine learning, the classification has been considered as a supervised learning task of inferring a function from labeled training data (Tang et al. 2014). The classification algorithm (classifier) analyzes the training data and infers a hypothesis (function), which can be used for predicting the labels of unseen observations (Parmar et al. 2015). In this study, Bagged Tree, Boosted Tree, Cubic KNN (K-Nearest Neighbors), cubic SVM (Support Vector Machine), Weighted KNN, Quadratic SVM, Subspace KNN, Medium Tree have used for machine-learning classifiers (Kriti and Virmani 2015; Kriti et al. 2017a, b; Parmar et al. 2015; Samant and Agarwal 2018). All the classifiers have been implemented using the classification learner app in MATLAB 2017, which provides a nice interface to access many machine-learning algorithms (Samant and Agarwal 2018; CLA 2018). Classifiers have been trained, tested, and validated using the repeated tenfold cross-validation technique. To investigate and compare different feature selection and classification methods, percentage recognition scores have been compared and analyzed.

Results and discussion

SODARs have been successfully used to study the microclimates and to provide an integrated approach to the meteorological classification of pollutant concentrations in major cities (McAllister et al. 1969; Little 1970; Asimakopoulos et al. 1976; Aggarwal et al. 1980; Gera and Singal 1993). The inversion or convection heights are a very important parameter for air pollution control and forecasting (Singal et al. 1994; Kumar et al. 2017b). The code developed for SODAR information has a good possibility of obtaining climatological information as well as a real-time picture of the spatial distribution of the ABL features (Little 1969; Beyrich 1997; Choudhury and Mitra 2004; Stull 2012; Kumar et al. 2017a). There are many studies on the prediction of ABL height and structure classification (De et al. 1998; Chandra et al. 2011). For the successful realization of ABL prediction analysis based on the SODAR echogram, it is important to evaluate and compare different feature selection methods for classification analysis. In the present study, five feature selection and eight classification methods have been employed. These methods have been selected based on previous studies (Bonacich 1987; Kalogiros et al. 1995; Guyon et al. 2002; Mukherjee et al. 2002; Biesiada et al. 2005; He et al. 2006; Narayan et al. 2010; Gu et al. 2012; Borah et al. 2014; Tang et al. 2014; Roffo et al. 2015; Gupta and Bhavsar

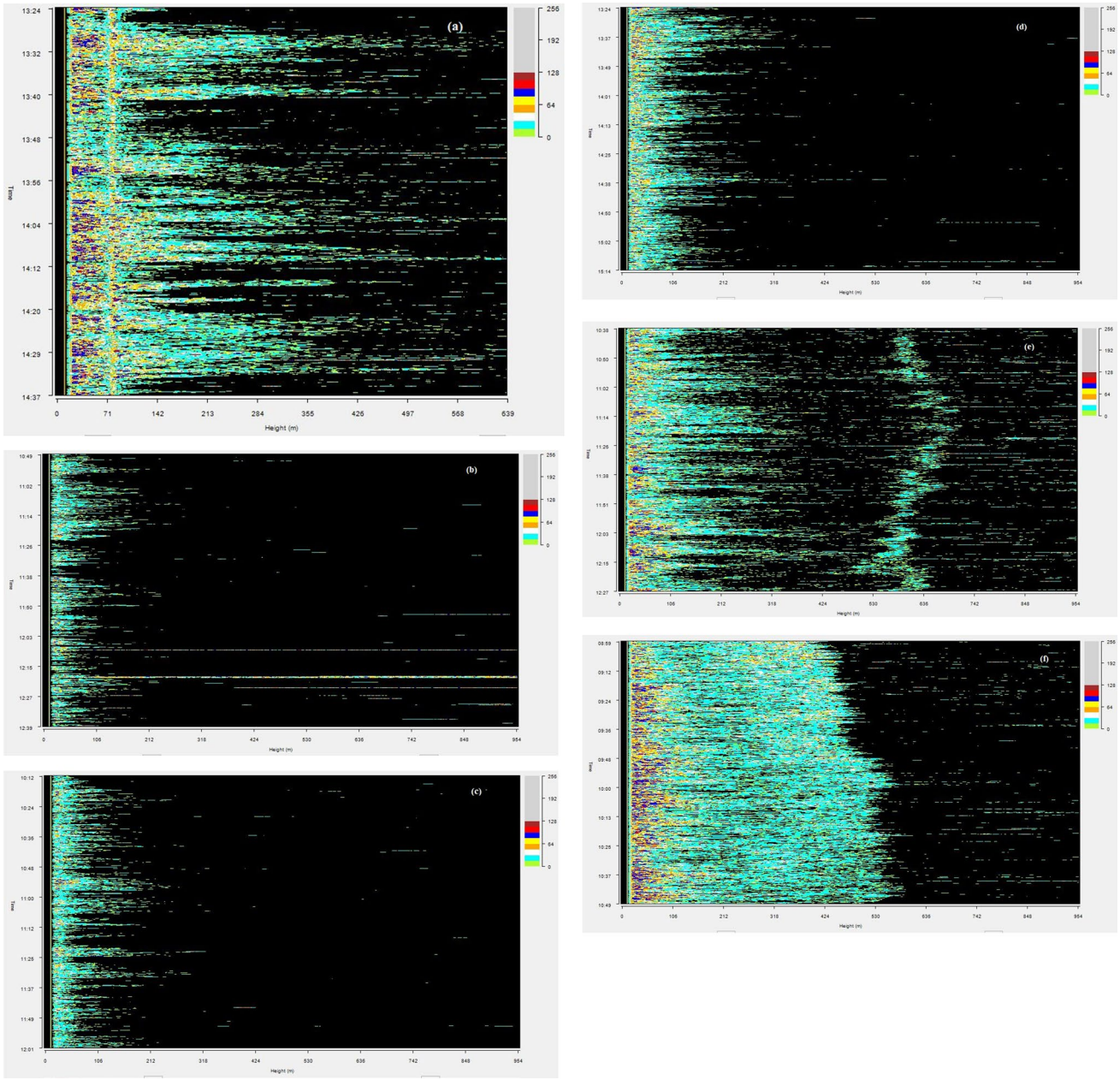

Fig. 3 Different structures of ABL: **a** thermal plume long; **b** thermal plume during rainy day; **c** thermal plume during before rainy day; **d** thermal plume during winter; **e** thermal plume with foggy; **f** rising layer during winter season; **g** inversion with long spikes; **h** winter inversion; **i** inversion with one or two elevated layers in motion; **j** inversion with wave motion; **k** inversion with fog; **l** multilayer

2017; Roffo and Melzi 2017; Samant and Agarwal 2018; Wang et al. 2017) to avoid over-fitting.

Chandra et al. (2011) applied neural network architecture that combines multilayer perceptron and graph-matching technique for classifying the different types of SODAR echograms and Choudhury and Mitra (2004, 2006) reported the multilayer perceptron-based model to classify the different SODAR patterns. This decreased dependence on human specialists for the recognizable proof process. A new classifier is proposed to compare with reference classifiers of the same family excluding the other classifier families (Parmar et al. 2015). New classifier gives best results for different families in comparison to the existing classifier. For the classification, the classifier app is used (MATLAB 2018 Classifier

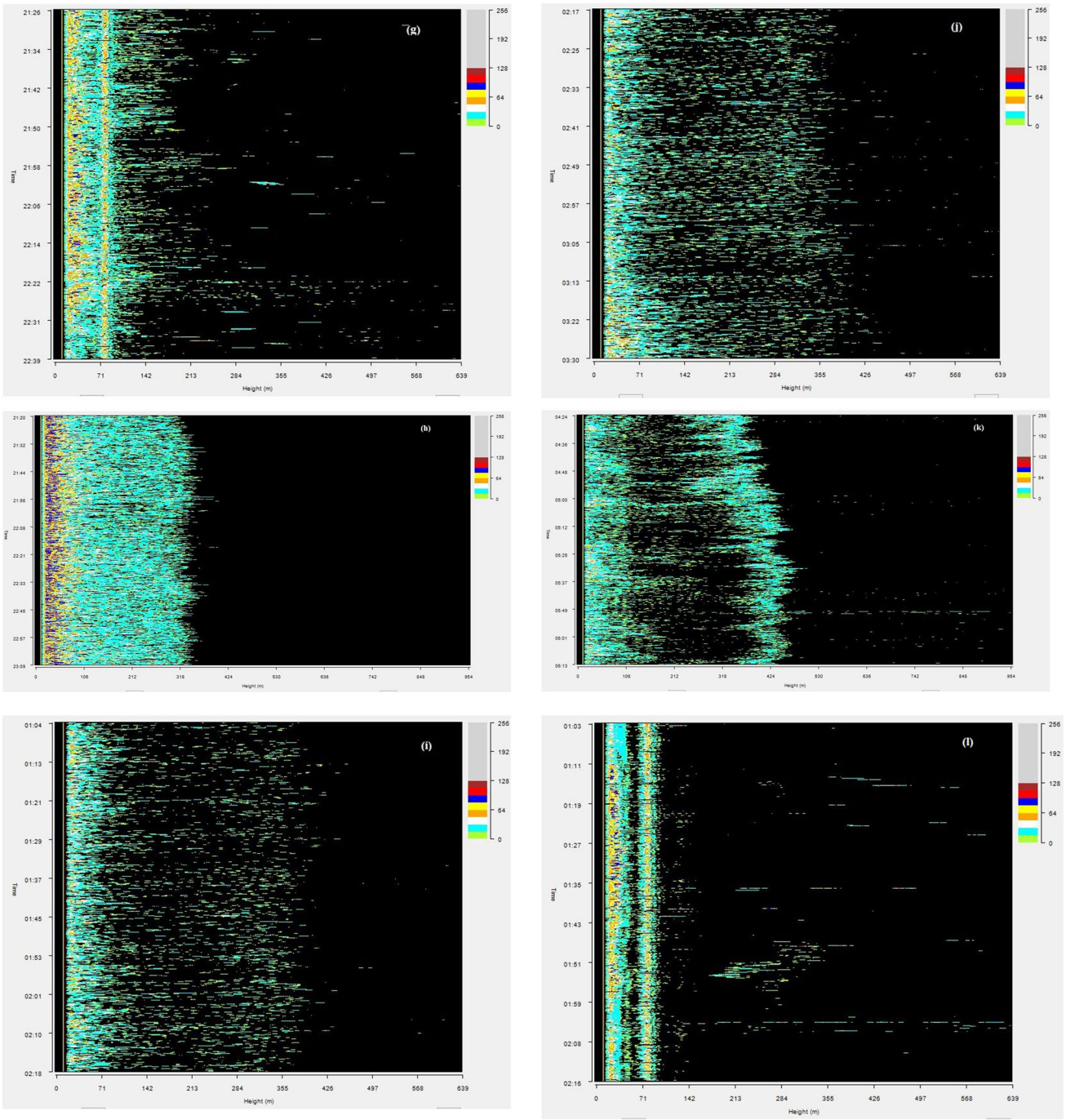

Fig. 3 (continued)

Learner App) for all (eight) the classifiers. For the classifier, the parameter configuration has been selected from the literature. Furthermore, in this study, the parameters have been tuned using the repeated ten cross-validations of training data only. Hence the work has been designed to evaluate different classification and different feature selection for the SODAR echograms.

A total of 133 statistical features have been calculated from a different structure of the pre-treatment SODAR echogram images of the Delhi region to investigate the machine-learning approaches for SODAR echogram and to find out the different structures present in the ABL. Feature selection, classification training, and testing have been done using SODAR echogram images (10—cross-validation). The predictive performance of different feature selection and classification methods has been assessed using the classification accuracies.

Table 3 Classifier accuracy (in percentage %)

	Bagged tree	Boosted tree	Cubic KNN	Cubic SVM	Weighted KNN	Quadratic SVM	Subspace KNN	Medium tree
1	47.82	54.34	33.3	21	22.22	33.33	26.67	44.44
2	49.35	66.02	36.53	46	33.97	67.3	39.74	37.17
3	46.83	44.3	40.5	31	27.84	40.5	34.17	50.63
5	43.75	51.25	23.75	38	28.75	30	28.75	42.5
6	25	38.95	35.59	35	35.59	42.37	20.33	35.59
7	32.91	84	45.61	68.96	77.27	76.33	61.28	77.42
8	42.64	44.11	44.77	26.87	32.83	34.32	32.83	46.26
9	50	25	25	25	35	25	40	40
10	67.54	80.57	57.39	46.13	56.29	64.01	42.16	76.37
11	40.62	37.5	25	21.87	21.87	37.5	34.37	40.62
12	41.79	46.26	32.83	29.98	38.8	44.77	17.91	46.26
Overall	44.38	52.02	36.38	35.43	37.31	45.03	34.38	48.84

Table 3 shows the classification accuracies for all eight classifiers. Boosted tree classifier has been found overall highest percentage recognition score (accuracy) with 52.02%. But individual accuracy of the classifier varies from 20% to 85%. From the results, the boosted tree classifier displayed the highest predictive performance. Therefore, boosted tree classification methods have been assessed for prediction performance of different feature selection methods.

Tables 4, 5, 6, 7 and Fig. 3 depict the performance of feature selection and boosted tree classification method using 5, 10, 20, 30, and 50 features, which are the top-ranked features resulted in feature selection. The results observed from Mutinffs and Fisher methods are the same, therefore only the Fisher method is shown above. The Laplacian feature selection method shows the highest predictive performance (61.15%) with 30 (thirty) features, whereas the UDFS method shows the lowest predictive performance (46.04%) with 30 features.

The prime motive for using different feature selection and classification methods was to investigate and compute suitable feature selection method and classifier according to the present data set. Depending upon the accuracy of each feature selection method, top 50 features were selected. Classifiers were trained using these features and applied on the testing data to predict the classes (Tables 4, 5, 6 and 7). Thereafter, accuracy was calculated to evaluate the performance of the classifiers. To generalize the classifier performance tenfold cross-validation technique was applied. From the detailed comparisons and analysis of feature selection (number of features 5, 10, 20, 30 and 50), it is observed

Table 4 Classifier accuracy with Fisher selection method (in %)

	Number of features				
	5	10	20	30	50
1	62.22	66.66	51.11	44.44	42.64
2	58.33	58.33	60.89	58.97	54.82
3	49.36	45.56	48.1	44.3	43.1
5	38.75	43.75	38.75	42.5	36.5
6	35.59	38.98	50.84	44.06	40.1
7	83.07	83.38	91.69	83.07	80.45
8	43.28	34.32	47.76	38.8	36.67
9	45	50	50	50	50
10	78.14	83.88	84.54	84.32	81.78
11	56.25	62.5	53.12	62.5	60.32
12	44.77	55.22	44.77	49.25	45.2
Overall	54.06	56.59	56.50	54.74	54.74

that when the number of features is increased, then after 20 features, the classification model takes more time and its accuracy decreases. Then more time is required to complete the iteration and model process. Accuracy and iteration time are very important parameters for performance evaluation of any classifier.

After the selection of the best classifier and feature selection method, monthly predictive performance was calculated using 20 selected features, which are 20 top-ranked features. Table 8 represents monthly predictive performance. The highest overall accuracy is shown for the October month (72.29%), whereas August month (31.62%) shows the lowest. Identification of atmospheric structures generated by a

Table 5 Classifier accuracy with Laplacian selection method (in %)

	Number of features				
	5	10	20	30	50
1	66.67	48.87	64.44	66.67	55.55
2	57.68	64.1	60.89	60.89	62.17
3	48.1	53.16	45.56	50.63	54.43
5	37.5	48.75	51.25	48.75	43.75
6	38.98	50.84	50.84	59.32	50.84
7	88.08	88.08	89.96	87.46	85.1
8	44.78	59.7	49.25	59.7	44.78
9	50	50	50	50	50
10	86.31	86.75	87.19	87.19	80.13
11	31.25	59.37	59.37	46.87	34.37
12	44.78	52.23	52.23	55.22	49.25
Overall	54.01	60.16	60.08	61.15	55.48

Table 6 Classifier accuracy with relief selection method (in %)

	Number of features				
	5	10	20	30	50
1	43.47	55.55	48.89	54.34	43.47
2	58.33	58.97	63.46	62.82	58.97
3	48.1	44.3	45.56	46.83	45.56
5	50	45	48.75	45	46.25
6	50.84	49.15	52.54	42.37	35.59
7	85.57	88.08	88.75	82.75	80.4
8	52.23	56.71	47.76	40.29	31.34
9	40	45	50	50	40
10	83.44	84.98	86.31	83.88	76.37
11	62.5	62.5	59.37	46.87	50
12	52.23	41.79	56.71	52.23	40.29
Overall	56.97	57.45	58.91	55.21	49.84

Table 7 Classifier accuracy with UDFS selection method (in %)

	Number of features				
	5	10	20	30	50
1	43.47	54.34	47.82	43.47	36.95
2	53.84	57.65	52.56	54.48	53.2
3	50.63	37.97	50.63	44.3	48.1
5	32.5	31.25	37.5	38.75	38.75
6	35.59	32.2	30.5	32.2	37.28
7	81.97	82.13	81.5	78.36	78.52
8	31.34	44.77	43.28	46.26	44.77
9	35	35	40	35	35
10	75.93	76.82	79.24	74.39	77.48
11	40.62	43.75	34.37	25	34.37
12	35.82	37.31	37.31	34.32	35.82
Overall	46.97	48.47	48.61	46.04	47.29

SODAR system and its observation completely depends on the knowledge, experience, and expertise in the system. The utility of information captured by the SODAR system has been restricted to a variety of persons having experience within the field. Therefore, correct utilization of SODAR information and potential use of SODAR observation demand for a computer-based SODAR structure recognition system which may be developed by incorporating human skilled information and experiences. For the effective realization of feature-based classification analysis, it is essential to evaluate and compare various classification methods, which is one of the key points of the analysis. Using the Laplacian method for feature selection and boosted tree classifier (overall prediction performance 62.19%), the highest prognostic presentation with 20 features for the ABL structure (using the SODAR echograms) classification is observed.

Conclusion

In the present paper an automated tool is developed using the machine-learning techniques to identify the different structures of ABL. The methodology presented here can be established as a powerful investigative tool along with the mainstream analysis methods. It has been observed that the Boosted Tree classifier method shows the highest prediction performance (overall preformation 52% with total 133 feature) among eight classifiers and along with the Laplacian feature selection method has the highest predictive accuracy (overall preformation 61% with 30 feature) in SODAR echograms/ABL structure identification. Also, it has been observed that with different feature selection methods and different parameter configurations, the performance of classifier can be improved further. Besides, these models can be applied as a monthly prediction model as October month has the highest predictive accuracy (overall preformation 72% with 20 feature), and August month has the lowest predictive performance (overall preformation 31% with 20 feature).

Table 8 Monthly predictive performance

	Months						
	January	February	March	April	May	June	July
1	62.5	33.33	NA	25	0	23	66.67
2	45.45	0	12.5	33.33	21.05	10.25	0
3	66.67	NA	50	NA	0	28.57	40
5	50	38.46	NA	25	40.74	40	33.3
6	66.67	0	0	46.67	37.5	46.15	0
7	76.62	71.42	80.95	48.78	42.85	48.07	81.18
8	40	40	50	37.5	33.33	50	40
9	33.33	50	50	NA	100	33.33	NA
10	45.16	39.02	20	72.97	71.25	53.12	73.43
11	52.38	NA	NA	40	0	NA	NA
12	25.92	27.27	NA	NA	100	40	0
Overall	51.34	33.28	37.64	41.16	40.61	37.25	37.17

	Months				
	August	September	October	November	December
1	25	25	NA	33.33	0
2	0	58.33	NA	40	51.72
3	33.33	50	50	38.89	58.82
5	11.11	0	NA	33.33	33.33
6	50	33.3	NA	33.33	57.14
7	57.3	65.38	88.63	63.63	59.03
8	40	33.33	NA	100	0
9	0	0	NA	NA	NA
10	66.19	50	78.26	55.55	66.67
11	NA	0	NA	NA	55.55
12	33.33	33.33	NA	0	33.33
Overall	31.63	31.7	72.3	44.23	41.559

Annexure I: Statistical feature formula

Feature	Formula
Feature computation along vertical direction	The average of the ith row, $y_i = \frac{1}{640}\sum_{j=1}^{640} a_{ij} \quad i = 1, 2, \ldots, 550$ mean, $y_{\text{mean}} = \frac{1}{550}\sum_{i=1}^{550} y_i$ Vertical maximum, $y_{\max} = \text{Max}_{i=1}^{550}\{y_i\}$ $\sigma_{\text{ver}} = \sqrt{\frac{1}{550}\sum_{i=1}^{640}\left(y_i - y_{\text{mean}}\right)^2}$ kth vertical average, $y_{\text{avg}_k} = \frac{1}{50}\sum_{i=1+50(k+1)}^{50k} y_i \quad \text{for} \quad k = 1, 2, \ldots, 11$
Vertical transition computation. Vertical transition of r (in percentage)	$y_r = \sum_{i=1}^{10} h_i^{(r)}\left(1 - h_{i+1}^{(r)}\right) + \sum_{i=11}^{2} h_i^{(r)}\left(1 - h_{i-1}^{(r)}\right)$ $h_i^{(r)} = \left\{\begin{array}{l} 1, \; y_{\text{avg}} \geq \frac{r}{100} \times y\max \\ 0, \quad \text{otherwise} \end{array}\right\}$
Feature computation along horizontal direction	The average of the jth column, $x_i = \frac{1}{550}\sum_{j=1}^{550} a_{ij} \quad j = 1, 2, \ldots, 640$ mean, $x_{\text{mean}} = \frac{1}{640}\sum_{i=1}^{640} x_i$ Horizontal maximum, $x_{\max} = \text{Max}_{i=1}^{640}\{x_i\}$ $\sigma_{\text{hor}} = \sqrt{\frac{1}{640}\sum_{i=1}^{550}\left(x_i - x_{\text{mean}}\right)^2}$ kth horizontal average, $x_{\text{avg}_k} = \frac{1}{50}\sum_{i=1+50(k+1)}^{50k} x_i \quad j = 1, 2, \ldots, 640$

References

Aggarwal SK, Singal SP, Kapoor RK, Adiga BB (1980) A study of atmospheric structures using SODAR in relation to land and sea breezes. Bound-Layer Meteorol 18(4):361–371

Asimakopoulos N, Cole RS, Caughey CJ, Crease BA (1976) A quantitative comparison between acoustic sounder returns and the direct measurement of atmospheric temperature fluctuations. Bound-Layer Meteorol 10(2):137–147

Bass HE, Shields FD (1977) Absorption of sound in air: high-frequency measurements. J Acoust Soc Ame 62(3):571–576

Beyrich F (1997) Mixing height estimation from SODAR data—a critical discussion. Atmos Environ 31(23):3941–3953

Biesiada J, Duch W, Kachel A, Maczka K, Palucha S (2005) Feature ranking methods based on information entropy with parzen windows. Int Conf Res Electrotechnol Appl Inform 2005:1–10

Bonacich P (1987) Power and centrality: a family of measures. Am J Sociol 92(5):1170–1182

Borah P, Ahmed HA, Bhattacharyya DK (2014) A statistical feature selection technique. Netw Model Anal Health Inform Bioinform 3(1):3–55

Bradley S (2007) Atmospheric acoustic remote sensing: principles and applications. CRC Press, Boca Raton

Chandra N, Kumar SR, Dutta HN (2011) SODAR pattern classification by graph matching. IEEE Geosci Remote Sens Lett 8(3):483–487

Chaudhuri B, Ganguli A, De AK, Das J (1990) Algorithm development for the machine recognition of SODAR structure. In: Conference proceeding. Acoustic remote sensing, pp 155–160

Choudhury S, Mitra S (2004) A connectionist approach to SODAR pattern classification. IEEE Geosci Remote Sens Lett 1(2):42–46

Choudhury S, Mitra S (2006) Feature extraction and connectionist classification of SODAR echograms. IEEE Geosci Remote Sens Lett 3(1):19–22

CLA (Classification Learner App) 2018. https://in.mathworks.com/help/stats/classification-learner-app.html

Danilov SD, Gur'yanov AE, Kallistratova MA, Petenko IV, Singal SP, Pahwa DR, Gera BS (1992) Acoustic calibration of sodars. Meas Sci Technol 3(10):1001–1010

De K, Mukherjee DP, Pal P, Das J (1998) SODAPRETER: a novel approach towards automatic SODAR data interpretation. Int J Remote Sens 19(15):2987–3002

Dezfooli D, Hosseini-Moghari S, Ebrahimi K, Araghinejad S (2018) Classification of water quality status based on minimum quality parameters: application of machine learning techniques. Model Earth Syst Environ 4:311–324. https://doi.org/10.1007/s40808-017-0406-9

Dutta I, Das A (2019) Modeling dynamics of peri-urban interface based on principal component analysis (PCA) and cluster analysis (CA): a study of English Bazar Urban Agglomeration, West Bengal. Model Earth Syst Environ 5:613–626. https://doi.org/10.1007/s40808-018-0554-6

Evans LB, Bass HE, Sutherland LC (1972) Atmospheric absorption of sound: theoretical predictions. J Acoust Soc Am 51(5B):1565–1575

Ford W, Meecham WC (1960) Scattering of sound by isotropic turbulence of large Reynolds number. J Acoust Soc Am 32(12):1668–1672

Garratt JR (1994) The atmospheric boundary layers. Earth Sci Rev 37(1–2):89–134

Gera BS, Singal SP (1993) Design of a microcomputer-based monostatic SODAR system. Indian J Radio Space Phys 22(5):296–300

Gera BS, Raghavendra T, Singh G, Ojha VK, Malik J, Gera N, Gupta NC (2011) Instrumentation and computer capabilities for improving SODAR data acquisition. Int J Remote Sens 32(17):4807–4817

Gilman W, Coxhead WB, Willis FH (1946) Reflection of sound signals in the troposphere. J Acoust Soc Am 18(2):274–283

Gu Q, Li Z, Han J (2012) Generalized fisher score for feature selection. https://arxiv.org/ftp/arxiv/papers/1202/1202.3725.pdf

Gupta V, Bhavsar A (2017) Breast cancer histopathological image classification: is magnification important? In: IEEE conference on computer vision and pattern recognition workshops (CVPRW)

Guyon JW, Barnhill S, Vapnik V (2002) Gene selection for cancer classification using support vector machines. Mach Learn 46(1–3):389–422

He X, Cai D, Niyogi P (2006) Laplacian score for feature selection. Adv Neural Inf Process Syst 2006:507–514

Kallistratova MA, Petenko IV, Kouznetsov RD, Kuznetsov DD, Lyulyukin VS, Perepelkin VG (2016) Kelvin-Helmholtz billows in rising morning inversions. In: 18th ISARS 6–9 June 2016, Varna, Bulgaria

Kalogiros JA, Helmis CG, Asimakopoulos DN, Papageorgas PG, Soilemes AT (1995) A layer detection and classification algorithm for SODAR facsimile records. Remote Sens 16(15):2939–2954

Knudsen VO (1946) The propagation of sound in the atmosphere—attenuation and fluctuations. J Acoust Soc Am 18(1):90–96

Kriti, Virmani J (2015) Breast density classification using Laws' mask texture features. Int J Biomed Eng Technol 19(3):279–302

Kriti, Kaur H, Virmani J (2017a) Evaluating the efficacy of multi-resolution texture features for prediction of breast density using mammographic images. Hybrid Intell Image Anal Understand 2:1–2. https://doi.org/10.1002/9781119242963.ch17

Kriti, Virmani J, Agarwal R (2017b) Characterization of breast tumors using selected laws' mask texture features. In: Image information processing (ICIIP), 2017 fourth international conference, IEEE, pp 1–6

Kumar N, Soni K, Agarwal R, Singh M (2017a) SODAR as a diagnostics tool for urban air-quality and health care system. J Acoust Soc India 44(4):213–222

Kumar N, Soni K, Garg N, Agarwal R, Saha D, Singh M, Singh G (2017b) SODAR pattern classification and its dependence on meteorological parameters over a semiarid region of India. Int J Remote Sens 38(11):3466–3482

Little CG (1969) Acoustic methods for the remote probing of the lower atmosphere. Proc IEEE 57(4):571–578

Little CG (1970) Acoustic sounding of the lower atmosphere. Meteorol Observ Instrum Am Meteorol Soc (Boston, MA) 11(33):397–404

Makkhan SJS, Parmar KS, Kaushal S, Soni K (2020) Correlation and time-series analysis of black carbon in the coal mine regions of India: a case study. Model Earth Syst Environ 6:659–669. https://doi.org/10.1007/s40808-020-00719-8

Martins S, Bernardo N, Ogashawara I, Alcantara E (2016) Support vector machine algorithm optimal parameterization for change detection mapping in Funil Hydroelectric Reservoir (Rio de Janeiro State, Brazil). Model Earth Syst Environ 2:138. https://doi.org/10.1007/s40808-016-0190-y

McAllister LG, Pollard JR, Mahoney AR, Shaw PJR (1969) Acoustic sounding—a new approach to the study of atmospheric structure. Proc IEEE 57(4):579–587

Mokarram M, Roshan G, Negahban S (2015) Landform classification using topography position index (case study: salt dome of Korsia-Darab plain, Iran). Model Earth Syst Environ 1(40):1–7. https://doi.org/10.1007/s40808-015-0055-9

Mukherjee DP, Pal P, Das J (2002) Classification of SODAR data using fractal features. In: ICVGIP

Nair HC, Joseph A, Padmakumari GV (2018) GIS Based landform classification using digital elevation model: a case study from two river basins of Southern Western Ghats, Kerala, India. Model Earth Syst Environ 4:1355–1363. https://doi.org/10.1007/s40808-018-0490-5

Narayan C, Pal S, Patranabis DC, Dutta HN (2010) A neurocomputing model for SODAR structure classification. Int J Remote Sens 31(11):2995–3018

Parmar P, Grossmann J, Bussink P, Lambin Aerts HJ (2015) Machine learning methods for quantitative radiomic biomarkers. Sci Rep 5(13087):1–11

Roffo G, Melzi S (2017) Ranking to learn: feature ranking and selection via eigenvector centrality, new frontiers in mining complex patterns. In: Fifth international workshop nfMCP2016

Roffo G, Melzi S, Cristani M (2015) Infinite feature selection. Proc IEEE Int Conf Comput Vis 2015:4202–4210

Samant P, Agarwal R (2018) Machine learning techniques for medical diagnosis of diabetes using iris images. Comput Methods Programs Biomed 157:121–128

Singal SP (2006) Acoustic remote sensing applications. Springer, vol 69, pp 1–39. https://link.springer.com/book/10.1007/BFb0009557?page=1

Singal SP, Aggarwal SK (1979) Sodar & radiosonde studies of thermal structure of the lower atmosphere at Delhi. Indian J Radio Space Phys 8(2):76–81. http://nopr.niscair.res.in/handle/123456789/37079

Singal SP, Gera BS (1982) Acoustic remote sensing of the boundary layer. Proc Indian Acad Sci Sect C: Eng Sci 5(2):131–157

Singal SP, Aggarwal SK, Pahwa DR, Gera BS (1985) Stability studies with the help of acoustic sounding. Atmos Environ 19(2):221–228. https://doi.org/10.1016/0004-6981(85)90090-3

Singal SP, Gera BS, Pahwa DR (1994) Application of SODAR to air pollution meteorology. Remote Sens 15(2):427–441

Singal SP, Gera BS, Saxena N (1997) Sodar: a tool to characterize hazardous situations in air pollution and communication. In: Singal SP (ed) Acoustic remote sensing applications, vol 69. Lecture notes in earth sciences. Springer, Berlin, Heidelberg, pp 325–384. https://doi.org/10.1007/BFb0009573

Soni K, Parmar KS, Agrawal S (2017) Modelling of air pollution in residential and industrial sites by integrating statistical and Daubechies wavelet (level 5) analysis. Model Earth Syst Environ 3:1187–1198. https://doi.org/10.1007/s40808-017-0366-0

Stull RB (2012) An introduction to boundary layer meteorology. Springer Science & Business Media. https://www.springer.com/gp/book/9789027727688

Sutherland LC, Bass HE (2004) Atmospheric absorption in the atmosphere up to 160 km. J Acoust Soc Am 115(3):1012–1032

Tang J, Alelyani S, Liu H (2014) Feature selection for classification: a review. Data classification: algorithms and applications, 37. https://www.cc.gatech.edu/hic/CS7616/Papers/Tang-et al-2014.pdf

Verma P, Raghubanshi A, Srivastava PK, Raghubanshi AS (2020) Appraisal of kappa-based metrics and disagreement indices of accuracy assessment for parametric and nonparametric techniques used in LULC classification and change detection. Model Earth Syst Environ 6:1045–1059. https://doi.org/10.1007/s40808-020-00740-x

Wang J, Wei JM, Yang Z, Wang SQ (2017) Feature selection by maximizing independent classification information. IEEE Trans Knowl Data Eng 29(4):828–841

Zaffalon M, Hutter M (2002) Robust feature selection by mutual information distributions. In: Proceedings of the eighteenth conference on uncertainty in artificial intelligence. Morgan Kaufmann Publishers Inc., pp 577–584. https://arxiv.org/abs/cs/0206006

Zahraei A, Poodineh MR, Panjekoubi P, Hosseini SA (2020) Analysis of soil depth temperature changes in Iran according to classification of atmospheric circulation patterns. Model Earth Syst Environ 6:865–877. https://doi.org/10.1007/s40808-020-00713-0

Zylshal Syyidah S, Yulianto F, Nugroho JT, Sofan P (2016) A support vector machine object-based image analysis approach on urban green space extraction using Pleiades-1A imagery. Model Earth Syst Environ 2:54. https://doi.org/10.1007/s40808-016-0108-8